



Delft University of Technology

Document Version

Final published version

Citation (APA)

Yan, Z. (2025). *Superelastic Response of Additively-Manufactured Nitinol Metamaterials*. [Dissertation (TU Delft), Delft University of Technology]. <https://doi.org/10.4233/uuid:0886b240-c7a6-44b5-9d3c-a86b41401a89>

Important note

To cite this publication, please use the final published version (if applicable).
Please check the document version above.

Copyright

In case the licence states "Dutch Copyright Act (Article 25fa)", this publication was made available Green Open Access via the TU Delft Institutional Repository pursuant to Dutch Copyright Act (Article 25fa, the Taverne amendment). This provision does not affect copyright ownership.

Unless copyright is transferred by contract or statute, it remains with the copyright holder.

Sharing and reuse

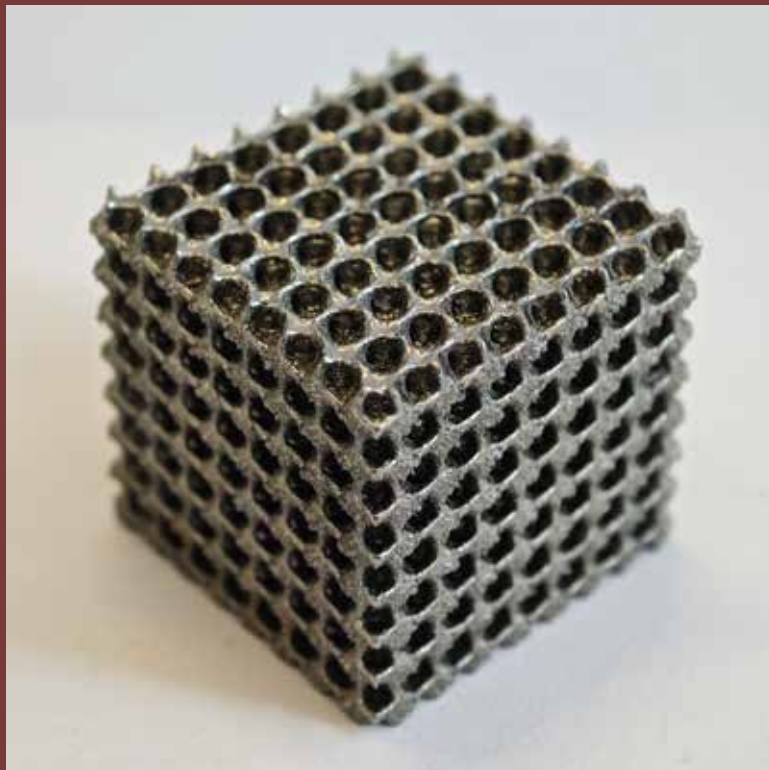
Other than for strictly personal use, it is not permitted to download, forward or distribute the text or part of it, without the consent of the author(s) and/or copyright holder(s), unless the work is under an open content license such as Creative Commons.

Takedown policy

Please contact us and provide details if you believe this document breaches copyrights.
We will remove access to the work immediately and investigate your claim.

This work is downloaded from Delft University of Technology.

Superelastic Response of Additively- Manufactured Nitinol Metamaterials



Zhaorui Yan

颜昭睿

Superelastic Response of Additively- Manufactured Nitinol Metamaterials

Zhaorui YAN 颜昭睿

Superelastic Response of Additively-Manufactured Nitinol Metamaterials

Dissertation

for the purpose of obtaining the degree of doctor
at Delft University of Technology
by the authority of the Rector Magnificus, Prof. dr.ir. T.H.J.J. van der Hagen
chair of the Board for Doctorates
to be defended publicly on
Thursday 22 May 2025 at 10:00 o'clock

by

Zhaorui YAN 颜昭睿
Master of Science in Mechanical Manufacture and Automation,
Dalian University of Technology, China
born in Guangdong, China

This dissertation has been approved by the promotores.

Composition of the doctoral committee:

Rector Magnificus,	chairperson
Dr. V. A. Popovich	Delft University of Technology, promotor
Dr. ir. M. J. M. Hermans	Delft University of Technology, promotor
Dr. J. Jovanova	Delft University of Technology, copromotor

Independent members:

Prof. dr. ir. M. Langelaar	Delft University of Technology
Prof. dr. ir. L.A.I. Kestens	Delft University of Technology
Prof. dr. M. Vedani	Politecnico di Milano, Italy
Prof. dr. I. Gibson	University of Twente, The Netherlands
Dr. P. Dey	Delft University of Technology, reserve member

The research described in this thesis was carried out in the Faculty of Mechanical Engineering, Delft University of Technology.

This research was financially supported by China Scholarship Council (CSC).



Keywords: Nickel-Titanium, shape memory alloys, additive manufacturing, metamaterials.

Copyright © 2025 by Zhaorui YAN 颜昭睿

Printed by: Ridderprint

All research data and code supporting the findings described in this thesis are available in

4TU.Centre for Research Data at: DOI 10.4121/4423107d-1f8b-4885-8182-65a29eb59e46

An electronic version of this dissertation is available at <https://repository.tudelft.nl/>

Contents

Summary	v
Samenvatting	ix
1 Introduction	1
1.1. Introduction	3
1.2. Challenges and motivations	4
1.2.1. Microscale: process-induced microstructural inhomogeneity	5
1.2.2. Mesoscale: constitutive behavior of additively manufactured NiTi and deformation mechanism	5
1.2.3. Macroscale: theoretical versus actual mechanical responses	6
1.2.4. Multiscale: modeling-experimental consistency for NiTi metamaterials	6
1.3. Outline of thesis	6
References	8
2 Background	11
2.1. Additive manufacturing of NiTi shape memory alloys	13
2.1.1. Martensitic transformation of NiTi	13
2.1.2. Metal additive manufacturing	16
2.1.3. Metallurgy of NiTi	16
2.1.4. Phenomenological constitutive models of shape memory alloys	18
2.2. A brief review of lattice-based metamaterials	19
2.2.1. Lattice-based structures	19
2.2.2. Mechanical properties	20
2.2.3. Early research on superelastic metamaterials	21
2.3. Current applications	21
2.4. Conclusions	22
References	23
3 Modeling superelasticity in truss-based metamaterials	31

3.1. Introduction	33
3.2. Geometric parameters and mechanical modeling	34
3.2.1. Relative density	34
3.2.2. Constitutive material model	35
3.2.3. Characterization of material properties	35
3.2.4. Analytical model	37
3.2.5. Unit-cell models	38
3.2.6. Multi-cell models	39
3.3. Experiments	40
3.3.1. Materials and additive manufacturing	40
3.3.2. Microstructural characterization	40
3.3.3. Mechanical testing	42
3.4. Results	42
3.4.1. Effective superelastic response	42
3.4.2. Microstructural characterization	47
3.4.3. Uniaxial compression tests	54
3.5. Discussion	56
3.5.1. Initial transformation surface	56
3.5.2. Recoverable energy absorption and deformation mechanism	59
3.6. Conclusions	61
Appendix A	63
References	65
4 Inhomogeneity in NiTi metamaterials	71
4.1. Introduction	73
4.2. Geometry and computational models	75
4.2.1. Conduction-based thermal modeling of melt pool during L-PBF processes	75
4.2.2. Mechanical models	77
4.3. Experiments	79
4.3.1. Materials and additive manufacturing	79
4.3.2. Microstructural characterization	79

4.3.3. Mechanical testing	80
4.4. Results	84
4.4.1. Melt pool profiles	84
4.4.2. Dependence of microstructures on geometrical dimensions	86
4.4.3. Phase transformation behavior	91
4.5. Discussion	94
4.5.1. Thermal effects on grain size and morphology	94
4.5.2. Edge effect	95
4.5.3. Laser turn region	98
4.5.4. Influence of inhomogeneous thermomechanical properties on macroscopic structural response	99
4.6. Conclusions	104
Appendix A	106
References	108
5 Origin of premature fracture and enhancement of superelasticity	115
5.1. Introduction	117
5.2. Geometry and computational models	118
5.3. Experiments	119
5.4. Results and discussion	120
5.4.1. Premature fracture in as-fabricated samples	120
5.4.2. Origin of premature fracture	124
5.4.3. Heat treatments	128
5.5. Conclusions	131
Appendix A	132
Appendix B	134
References	135
6 Tunable transformation stress-temperature relation in superelastic metamaterials	139
6.1. Introduction	141
6.2. Computational models	142

6.2.1. Base constitutive relation	142
6.2.2. Unit cell model with periodic boundary conditions	144
6.2.3. Estimation of inelastic deformation	145
6.2.4. Multi-cell models	146
6.3. Experimental methods	146
6.3.1. Additive manufacturing and heat treatments	146
6.3.2. Characterization	147
6.3.3. Thermal analysis and thermo-mechanical tests	147
6.4. Results	148
6.4.1. Anisotropic superelasticity and scaling of transformation stress	148
6.4.2. Manufacturing strategy of superelastic metamaterials	150
6.4.3. Experimental characterization of superelastic metamaterial	151
6.5. Discussion	154
6.5.1. Cyclic stability	154
6.5.2. Effective transformation stress-temperature relationship	159
6.6. Conclusions	161
Appendix A Thermomechanical properties for numerical models	162
Appendix B Supplementary details on parameter optimization and characterization	164
Appendix C Table of notation	166
References	167
7 General discussion, conclusions, and recommendations	171
7.1. General discussion	173
7.2. General conclusions	176
7.3. Recommendations	177
Curriculum Vitae	181
List of publications	183
Acknowledgements	185

Summary

This thesis describes an investigation in the modeling and manufacturing of Nitinol (NiTi) superelastic metamaterials. To achieve an accurate agreement between model and experiment regarding superelasticity in Ni-rich NiTi metamaterials, the research focuses particularly on the martensitic transformation behavior. Each chapter contributes to a better understanding of the entire additive manufacturing process chain, including constitutive modeling, heat treatments and structural design, to develop NiTi-based metamaterials with tunable superelastic properties.

NiTi shape memory alloys exhibit unique shape memory effect (SME) and superelasticity due to reversible martensitic transformations. These properties make NiTi a suitable material for adaptive structures, biomedical devices, and aerospace components. Though computational models can be used to design NiTi structures and metamaterials with superelasticity and SME, the successful additive manufacturing of these designs remains challenging. Achieving full superelasticity in complex geometries produced via laser powder bed fusion (L-PBF) is particularly difficult. Thus, aiming for model-experiment consistency of superelastic metamaterials, the main research gap lies in establishing clear qualitative and quantitative relationships between material models, properties, mesoscopic structures and the resulting macroscopic responses.

In Chapter 3, the research started with the development of analytical expressions for the effective transformation stress and numerical models to evaluate the superelastic behavior and energy dissipation of truss-based metamaterials. NiTi truss-based metamaterials with body-centered cubic (BCC) and octet structures were selected to represent bending- and stretching-dominated architectures, respectively. A detailed parametric finite element analysis was performed to study the relationship between relative density and effective transformation criteria. Using L-PBF, crack-free BCC and octet samples were successfully fabricated from Ni-rich NiTi powder. However, the as-fabricated samples exhibited only partial superelasticity and premature fracture.

In Chapter 4, the study is focused on inhomogeneity of microstructural and functional properties and the underlying reasons for partial superelasticity. Through both numerical and experimental approaches, the study investigated how geometric factors, such as relative density, affect microstructural inhomogeneity and thermomechanical properties of NiTi in body-centered cubic (BCC) structures. Geometric effects on melt pool behavior lead to different solidification textures and inhomogeneous response to indentation. The numerical simulation shows that inhomogeneous transformation temperatures cause narrow stress

hysteresis in the macroscopic response. This chapter reveals the interdependent relation between relative density, microstructure, localized properties of NiTi and the macroscopic response.

The focus in Chapter 5 is on understanding and mitigating premature fracture in Ni-rich NiTi metamaterials produced by L-PBF. To investigate the origins of fracture, a comparative analysis of two unit cell architectures, the a Gyroid network (bending-dominated) and a Diamond shell (stretching-dominated), was conducted. Due to the inherent tension-compression asymmetry of NiTi, the structural stability of these designs was found to be reversed compared to conventional elastic-plastic responses, leading to premature fracture and limited superelasticity in the as-fabricated samples. As large deformation can not be achieved through martensitic transformation or dislocation slip systems, partial superelasticity and low deformation recoverability were observed in the as-fabricated samples. Heat treatments were applied to address these issues and achieve qualitative agreement between experimental data and model predictions.

After the superelasticity was successfully achieved, the transformation stress-temperature relation and energy absorption in Ni-rich NiTi superelastic metamaterials were investigated in Chapter 6. Temperature dependence often restricts the practical use of superelasticity. In metallic metamaterials, energy absorption typically relies on the elastoplasticity of ductile metals; however, achieving energy absorption with recoverable deformation has not been fully explored. To address this, a numerical model of the Diamond shell structure was developed to predict temperature-dependent superelasticity and energy absorption. A heat treatment was applied to ensure agreement between the model and experimental results. The findings show that the transformation stress-temperature coefficient decreases from 9.5 MPa/°C for bulk samples to 0.9 MPa/°C for Diamond samples. Under uniaxial compression, the effective transformation stress can be controlled by relative density, with values of 41.8, 52.1, and 65.3 MPa for relative densities of 0.15, 0.2, and 0.25, respectively. A specific energy absorption of 3.5 J/g was achieved in cyclic compression tests with 15 cycles. The recoverable plateau-like response in the macroscopic stress-strain curves originated in a continuous transformation region forms along the macroscopic [100] direction under uniaxial compression. Post-yielding plasticity in the macroscopic stress-strain curves is related to a plastic shear band formed along the [110] direction.

In summary, this work successfully developed a model-manufacturing strategy for superelastic NiTi metamaterials. By addressing multiscale challenges such as microstructural inhomogeneity and tension-compression asymmetry, this study demonstrates that computation-based design and additive manufacturing can create functional NiTi structures with tunable thermomechanical properties. Multiscale issues often prevent computational

designs from being fully realized in experiments. By identifying and controlling variable interdependencies across scales, this research achieves largely tunable superelasticity in experiments. This approach provides a foundation for practical applications of NiTi metamaterials in fields such as biomedical devices, aerospace, and civil engineering.

Samenvatting

Deze thesis beschrijft het onderzoek naar het modelleren en vervaardigen van superelastische Nitinol-metamaterialen. Om een nauwkeurige overeenstemming tussen model en experiment met betrekking tot superelasticiteit te bereiken in een Ni-rijk NiTi-metamateriaal, richt het onderzoek zich met name op het martensitische transformatiedrag van NiTi-structuren. Elk hoofdstuk draagt bij tot een beter begrip van het gehele additieve vervaardigingsproces, inclusief warmtebehandelingen, constitutieve modellering en structureel ontwerp, om NiTi-gebaseerde metamaterialen te ontwikkelen met afstembare superelastische eigenschappen.

NiTi-geheugenmetaallegeringen vertonen een unieke vormgeheugeneigenschap (Shape Memory Effect, SME) en superelasticiteit, door omkeerbare martensitische transformaties. Deze eigenschappen maken NiTi een ideaal materiaal voor adaptieve structuren, medische apparatuur en lucht- en ruimtevaartcomponenten. Hoewel computermodellen kunnen worden gebruikt om NiTi-structuren en -metamaterialen met superelasticiteit en SME te ontwerpen, blijft het succesvol produceren van deze ontwerpen een uitdaging. Het realiseren van volledige superelasticiteit in complexe geometrieën geproduceerd via laser powder bed fusion (L-PBF) is bijzonder moeilijk. Daarom ligt de belangrijkste onderzoeksraagstuk in het vaststellen van eenduidige kwalitatieve en kwantitatieve relaties tussen zowel materiaalmodellen en eigenschappen als tussen mesoscopische structuren en de resulterende macroscopische respons.

Het onderzoek is gestart, zoals beschreven in Hoofdstuk 3, met het ontwikkelen van analytische uitdrukkingen voor het bepalen van de effectieve transformatiespanning en van numeriek modellen om het superelastische gedrag en de energieabsorptie van traliewerkgebaseerde metamaterialen te evalueren. NiTi-traliewerkmetamaterialen met een kubisch ruimtelijk gecentreerde structuur (body-centered cubic (BCC)) en octetstructuren zijn geselecteerd om respectievelijk buig- en trekgedomineerde constructies te vertegenwoordigen. Een gedetailleerde parametrische eindige-elementenanalyse is uitgevoerd om voor deze constructies de relatie tussen relatieve dichtheid en effectieve transformatiecriteria te bestuderen. Met behulp van L-PBF zijn scheurvrije BCC- en octetproefstukken succesvol uit Ni-rijk NiTi-poeder vervaardigd. De gefabriceerde proefstukken vertoonden echter slechts een gedeeltelijk superelastisch gedrag en faalden voortijdig.

In Hoofdstuk 4 richt het onderzoek zich op inhomogeniteiten in de microstructuur en eigenschappen van het geprinte materiaal en de effecten daarvan op superelasticiteit. Met

behulp van numerieke en experimentele benaderingen wordt onderzocht hoe geometrische factoren, zoals relatieve dichtheid, de microstructurele inhomogeniteit en thermomechanische eigenschappen van NiTi de eigenschappen van BCC-structuren beïnvloeden. Geometrische effecten op het smeltbadgedrag leiden tot verschillende stollingstexturen en een inhomogene respons onder compressie. Numerieke simulaties tonen aan dat inhomogene transformatietemperaturen resulteren in een kleine spanningshysterese in de macroscopische respons. In dit hoofdstuk wordt de onderlinge afhankelijkheid tussen relatieve dichtheid, metallurgische microstructuur, lokale eigenschappen van NiTi en de macroscopische respons beschreven.

De focus in Hoofdstuk 5 ligt op het begrijpen en verminderen van vroegtijdige breuk in Ni-rijk NiTi-metamateriaal geproduceerd door L-PBF. Om de oorsprong van het breukgedrag te onderzoeken is een vergelijkende analyse uitgevoerd van twee eenheidscelarchitecturen: het Gyroid-netwerk (buig-gedomineerd) en de Diamond-shell (rek-gedomineerd). Vanwege de inherente trek-druk-asymmetrie van NiTi is vastgesteld dat de structurele stabiliteit van deze structuren omgekeerd is ten opzichte van de conventionele elastisch-plastische respons, hetgeen leidt tot vroegtijdige breuk en beperkte superelasticiteit in de gefabriceerde proefstukken. Omdat grote vervormingen niet kunnen worden bewerkstelligd door een martensitische transformatie of door dislocatieglijsystemen, wordt slechts een gedeeltelijke superelasticiteit en een beperkt deformatieherstel waargenomen. Om deze problemen te verhelpen zijn warmtebehandelingen uitgevoerd om een kwalitatieve overeenstemming tussen experimentele gegevens en modelvoorspellingen te bereiken.

Na het succesvol bereiken van superelasticiteit zijn in Hoofdstuk 6 de transformatiespanning-temperatuurrelaties van Ni-rijk NiTi superelastische metamaterialen onderzocht. Temperatuurafhankelijkheid beperkt vaak het praktische gebruik van superelasticiteit. In metallische metamaterialen is de energieabsorptie doorgaans afhankelijk van de elastoplasticiteit van ductiele metalen; het realiseren van energieabsorptie met herstelbare vervorming is echter nog niet volledig onderzocht. Een numeriek model van de Diamond-shellstructuur is ontwikkeld om temperatuurafhankelijke superelasticiteit en energieabsorptie te voorspellen. Op basis van de in Hoofdstuk 5 behaalde superelasticiteit door middel van een warmtebehandeling is de consistentie tussen model en experiment gewaarborgd. De resultaten tonen aan dat een lage transformatiespanning-temperatuurcoëfficiënt van $0,9 \text{ MPa}^{\circ}\text{C}$ en een specifieke energieabsorptie van $3,5 \text{ J/g}$ kunnen worden verkregen in cyclische compressietests. De plateauachtige respons in de macroscopische spannings-rekcurves ontstaat door een continu transformatiegedrag langs de macroscopische [100]-richting bij axiale compressie. Plasticiteit na het bereiken van de vloeigens in de macroscopische spannings-rekcurves is gerelateerd aan een plastische afschuifband gevormd langs de [110]-richting.

Na het succesvol bereiken van superelasticiteit werden in Hoofdstuk 6 de transformatiespanning-temperatuurrelaties van Ni-rijk NiTi superelastische metamaterialen onderzocht. Een numeriek model van de Diamond-shellstructuur werd ontwikkeld om temperatuurafhankelijke superelasticiteit en energieabsorptie te voorspellen. Op basis van de in Hoofdstuk 5 behaalde superelasticiteit werd warmtebehandeling toegepast om consistentie tussen model en experiment te waarborgen. De resultaten tonen aan dat een lage transformatiespanning-temperatuurcoëfficiënt van 0,9 MPa/°C en een specifieke energieabsorptie van 3,5 J/g kunnen worden verkregen in cyclische compressietests. De herstelbare plateauachtige respons in de macroscopische spannings-rekcurves ontstaat door een continu transformatiegebied langs de macroscopische [100]-richting bij eenaxiale compressie. Post-vloeigrens plasticiteit in de macroscopische spannings-rekcurves is gerelateerd aan een plastische schuifband gevormd langs de [110]-richting. Dit hoofdstuk voltooit de model-productiestrategie voor superelastische metamaterialen.

Samenvattend kan gesteld worden dat in deze studie een model-productiestrategie succesvol is ontwikkeld voor superelastische NiTi-metamaterialen. Door uitdagingen over meerdere lengteschalen, zoals microstructurele inhomogeniteit en macroscopische trek-druk-asymmetrie te adresseren, laat dit onderzoek zien dat ontwerp op basis van computermodellen het mogelijk maakt additieve vervaardiging van functionele NiTi-structuren te creëren met aanpasbare thermomechanische eigenschappen. Deze 'multiscale' effecten belemmeren vaak de volledige realisatie van computergestuurd ontwerpen in experimenten. Door variabele onderlinge afhankelijkheden over verschillende lengteschalen te identificeren en te beheersen, is in dit onderzoek de gewenste mechanische prestaties gerealiseerd in geprinte producten. De in dit onderzoek gevolgde benadering biedt een basis voor praktische toepassingen van NiTi-metamaterialen in sectoren zoals medische apparatuur, lucht- en ruimtevaart, en civiele techniek. De succesvolle integratie van modellering, productie en testen zorgt ervoor dat NiTi-structuren met herstelbare deformatie gemaakt kunnen worden voor geavanceerde technische toepassingen.

Introduction

1

2

1.1. Introduction

In recent years, the rapid development of additive manufacturing (AM) for shape memory alloys (SMAs) has transitioned production from bulk materials to customized structures and metamaterials. Compared to conventional structural metals, SMAs have the unique ability to recover their original shape after significant deformation when exposed to stimuli such as thermal, magnetic, or electrical stimuli [1]. Additionally, SMAs exhibit higher stiffness, greater actuation stress, longer cyclic life, and better biocompatibility than shape memory polymers (SMPs). Among all SMAs, Nitinol (NiTi) is the most widely used due to its exceptional shape memory effect (SME) and superelasticity. These unique properties make NiTi a popular choice in a variety of engineering applications, including medical devices such as stents and orthodontic tools, aerospace components like actuators and sensors, adaptive robotic systems, and vibration dampers in civil engineering for seismic protection [1–4].

The SME and superelasticity of NiTi alloys originate from reversible martensitic transformation, a diffusionless solid state phase transformation [5]. The one-way shape memory effect occurs when NiTi is deformed in its martensitic state, retaining the deformation as long as the temperature is below the austenite start temperature (A_s). Upon heating above A_s the material recovers its original shape. Superelasticity, on the other hand, occurs under applied stress when the material is in the temperature range of thermally stable austenite. This property allows NiTi to undergo significant deformation during loading (up to 10% strain) with full shape recovery upon unloading [6].

To systematically design adaptive structures and metamaterials using NiTi and other SMAs, computational tools are required to capture the deformation and thermomechanical behavior of base SMAs [7,8]. From a continuum mechanics perspective, the thermomechanical behavior of SMAs can be described using phenomenological constitutive models. The thermomechanical properties used in phenomenological models are often characterized through uniaxial tensile or compression experiments [9,10]. Thus, the macroscopic functional response of the designed SMA structures and metamaterials can be designed and predicted through finite element analysis (FEA) with the constitutive model of SMAs.

Mechanical metamaterials are man-made structures with mechanical properties controlled by the geometry of the unit cell [11]. The effective properties of mechanical metamaterials are obtained by applying mechanical homogenization to unit cell models. These effective properties are determined by various mesoscale deformation mechanisms. The mechanical metamaterials in this thesis, based on fundamental material mechanics, are

associated with mechanical properties such as ultra-high strength-to-density ratios, shear/bulk moduli, and Poisson's ratio [12].

1

These customized structures, designed through computational modeling, are difficult to manufacture using conventional fabrication methods [13]. Therefore, laser powder bed fusion (L-PBF), an additive manufacturing technique (also known as 3D printing), is employed to produce components with complex geometries. Due to the flexibility of L-PBF, and the superelasticity of NiTi, superelastic metamaterials can be modeled and fabricated to achieve recoverable large deformations. Their high stiffness-density ratio and ability to recover large deformation make them ideal for extreme environments and adaptive applications, such as medical devices and aerospace components.

1.2. Challenges and motivations

To develop Nitinol metamaterials with superelastic responses, a comprehensive model-manufacturing-properties methodology is required. The challenges in controlling martensitic transformation arise at three length scales: inhomogeneous microstructures (metallurgical aspect) at the microscale, base properties and deformation mechanisms at the mesoscale, and homogenized functional responses at the macroscale.

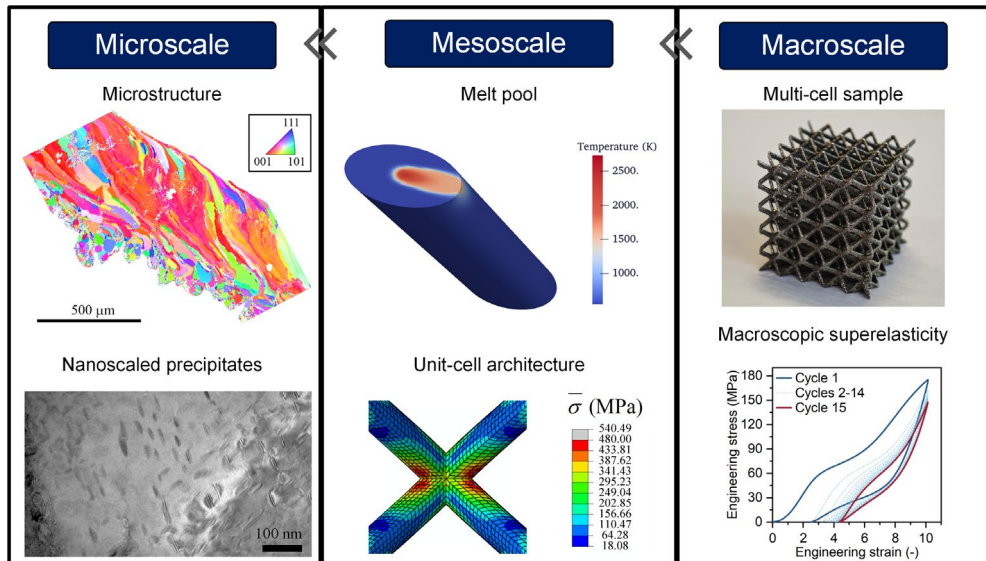


Figure 1.1 Schematic diagram of multiscale challenges in this thesis.

1.2.1. Microscale: process-induced microstructural inhomogeneity

The microstructure evolution during additive manufacturing of Ni-rich NiTi metamaterials is not fully understood. As the relative density of the unit cell decreases, the classical semi-infinite space assumption used in existing analytical thermal models no longer holds [14,15]. Solidification parameters such as temperature gradients, solidification rates, and undercooling become predominantly influenced by geometrical features, such as strut diameter and shell thickness in truss-based and shell structures. This leads to the formation of different solidification microstructures inside the unit cells. Given that microstructure data for laser powder bed fusion (L-PBF) NiTi metamaterials, including grain size, texture, compositions and precipitates, are sparse, critical experimental information is missing. Furthermore, the non-uniaxial stress states in NiTi metamaterials make it difficult to analyze the relationship between microstructure and thermomechanical properties based on uniaxial mechanical tests. Without advanced experimental tools to analyze local properties, it is challenging to understand how grain size, texture and composition affect the localized thermomechanical properties of the NiTi, and how that, in turn, affects the macroscopic behavior of NiTi metamaterials.

1.2.2. Mesoscale: constitutive behavior of additively manufactured NiTi and deformation mechanism

For conventionally manufactured NiTi shape memory alloys, constitutive models have been significantly developed over the last few decades [16]. However, adopting these constitutive models to predict the phenomenological thermo-mechanical behavior of L-PBF NiTi shape memory alloys needs further discussion. As new process-induced polycrystalline microstructures form and thermomechanical properties are tailored for specific applications, basic assumptions such as the continuum hypothesis, isotropic material behavior, and homogeneity require further consideration. Additionally, the unique geometrical dimensions in L-PBF NiTi samples require further adaption of standardized testing methods for conventional NiTi alloys. The lack of sufficient experimental data for characterizing the constitutive models means that this study must begin with basic one-dimensional reductions of material models and the development of testing setups for small-scale samples at the millimeter scale. After superelasticity can be obtained for bulk samples, the deformation mechanisms of superelastic structures at the mesoscale remain unclear.

1.2.3. Macroscale: theoretical versus actual mechanical responses

To derive theoretical effective properties of superelastic NiTi metamaterials, further modeling is needed. Specifically, understanding how the strengthening effect of martensite after transformation influences deformation in bending- and stretching-dominated structures remains a research gap. The anisotropy, effective martensitic transformation, energy dissipation, and multiaxial transformation criteria for the theoretically superelastic metamaterials are not fully understood. Moreover, although macroscopic compressive curves for superelastic structures are predicted within both the superelastic and plastic ranges, the actual response curves differ from the modeling results. It is still unclear to what extent the difference between numerical and experimental results can be explained by the martensitic transformation behavior.

1.2.4. Multiscale: modeling-experimental consistency for NiTi metamaterials

The challenges at three different length scales were introduced as independent factors, but the experimental variables involved in the length scales are interdependent. For instance, the relative density of mechanical metamaterials at the macroscale affects the microstructure by altering the strut diameter or shell thickness at the mesoscale. In turn, the microstructure influences the local thermomechanical properties and macroscopic stress-strain response. Due to these dependent relationships, multiple intermediate variables (e.g., texture, composition, localized properties, transformation localization and structural compliance) were introduced in the experimental design, although only one variable (relative density) was consistently used. As a result, establishing clear qualitative or quantitative relationships between relative density, material properties, and structural performance remains challenging.

This thesis aims to develop a path from additively manufactured solid NiTi to structural NiTi, focusing on mechanical modeling, manufacturing, and testing. Given interdependent variables present at multiscale, a detailed study was carried out to understand the impact of these variables, such as relative density, on the (meta)materials at different scales. By understanding the interdependency of the key variables on the superelasticity of the Ni-rich NiTi structure, the knowledge gap across length scales can be bridged. The quantitative superelastic behavior and effective properties of NiTi metamaterials can be achieved and controlled for both engineering applications.

1.3. Outline of thesis

In Chapter 2, the fundamental concepts of NiTi shape memory alloys and mechanical metamaterials are introduced. The chapter covers three topics: the process-microstructure-

properties relationship of additively manufactured NiTi shape memory alloys, the continuum mechanics and constitutive models of SMAs, and the basic knowledge of mechanical metamaterials.

In Chapter 3, analytical expressions and a parametric finite element study of superelastic NiTi metamaterials are presented, focusing on octet and BCC truss-based structures. Partial superelasticity with a recoverable engineering strain of 2.8% and damping properties was achieved.

In Chapter 4, the correlation between microstructural inhomogeneity and the macroscopic mechanical response of NiTi metamaterials fabricated via L-PBF is investigated. Inhomogeneity in transformation temperatures causes partial superelasticity and pseudo-linear mechanical responses at the macroscale.

In Chapter 5, the origin of premature fracture in Ni-rich NiTi metamaterials is explained, and heat treatment is proposed as a method for enhancing superelasticity. Consistency between the model and experimental results was achieved in the macroscopic superelastic curves.

In Chapter 6, the transformation stress-temperature relationship in superelastic NiTi metamaterials is shown to be controllable by tuning microstructure and mesostructure. The reduction of the effective transformation stress-temperature coefficient to as low as 0.9 MPa/°C and specific energy absorption of 3.5 J/g can be obtained in cyclic compression.

In Chapter 7, the key findings of the thesis are summarized and the broader implications of the research are discussed.

References

[1] J. Mohd Jani, M. Leary, A. Subic, M.A. Gibson, A review of shape memory alloy research, applications and opportunities, *Mater. Des.* 56 (2014) 1078–1113. <https://doi.org/10.1016/j.matdes.2013.11.084>.

[2] J. Van Humbeeck, Non-medical applications of shape memory alloys, *Mater. Sci. Eng. A* 273–275 (1999) 134–148.

[3] N.B. Morgan, Medical shape memory alloy applications - The market and its products, *Mater. Sci. Eng. A* 378 (2004) 16–23. <https://doi.org/10.1016/j.msea.2003.10.326>.

[4] M.H. Elahinia, M. Hashemi, M. Tabesh, S.B. Bhaduri, Manufacturing and processing of NiTi implants: A review, *Prog. Mater. Sci.* 57 (2012) 911–946. <https://doi.org/10.1016/j.pmatsci.2011.11.001>.

[5] K. Otsuka, X. Ren, Physical metallurgy of Ti-Ni-based shape memory alloys, *Prog. Mater. Sci.* 50 (2005) 511–678. <https://doi.org/10.1016/j.pmatsci.2004.10.001>.

[6] J.P. Oliveira, R.M. Miranda, F.M. Braz Fernandes, Welding and Joining of NiTi Shape Memory Alloys: A Review, *Prog. Mater. Sci.* 88 (2017) 412–466. <https://doi.org/10.1016/j.pmatsci.2017.04.008>.

[7] D. Lagoudas, D. Hartl, Y. Chemisky, L. MacHado, P. Popov, Constitutive model for the numerical analysis of phase transformation in polycrystalline shape memory alloys, *Int. J. Plast.* 32–33 (2012) 155–183. <https://doi.org/10.1016/j.ijplas.2011.10.009>.

[8] F. Auricchio, R.L. Taylor, J. Lubliner, Shape-memory alloys: macromodelling and numerical simulations of the superelastic behavior, *Comput. Methods Appl. Mech. Eng.* 146 (1997) 281–312. [https://doi.org/10.1016/S0045-7825\(96\)01232-7](https://doi.org/10.1016/S0045-7825(96)01232-7).

[9] D.J. Hartl, D.C. Lagoudas, F.T. Calkins, J.H. Mabe, J.T. Mooney, D.C. Lagoudas, F.T. Calkins, J.H. Mabe, Use of a Ni60Ti shape memory alloy for active jet engine chevron application: I. thermomechanical characterization, *Smart Mater. Struct.* 19 (2010). <https://doi.org/10.1088/0964-1726/19/1/015021>.

[10] D.C. Lagoudas, Shape memory alloys: modeling and engineering applications, Springer, 2008.

[11] X. Yu, J. Zhou, H. Liang, Z. Jiang, L. Wu, Mechanical metamaterials associated with stiffness, rigidity and compressibility: A brief review, *Prog. Mater. Sci.* 94 (2018) 114–173. <https://doi.org/10.1016/j.pmatsci.2017.12.003>.

[12] P. Jiao, J. Mueller, J.R. Raney, X.R. Zheng, A.H. Alavi, Mechanical metamaterials and beyond, *Nat. Commun.* 14 (2023) 6004. <https://doi.org/10.1038/s41467-023-41679-8>.

[13] M. Elahinia, N. Shayesteh Moghaddam, M. Taheri Andani, A. Amerinatanzi, B.A. Bimber, R.F. Hamilton, Fabrication of NiTi through additive manufacturing: A review, *Prog. Mater. Sci.* 83 (2016) 630–663. <https://doi.org/10.1016/j.pmatsci.2016.08.001>.

[14] T.W. Eagar, N.S. Tsai, Temperature Fields Produced By Traveling Distributed Heat Sources., *Weld. J. (Miami, Fla)* 62 (1983) 346–355.

[15] Y. Yang, F. van Keulen, C. Ayas, A computationally efficient thermal model for selective laser melting, *Addit. Manuf.* 31 (2020) 100955. <https://doi.org/10.1016/j.addma.2019.100955>.

[16] C. Cisse, W. Zaki, T. Ben Zineb, A review of constitutive models and modeling techniques for shape memory alloys, *Int. J. Plast.* 76 (2016) 244–284. <https://doi.org/10.1016/j.ijplas.2015.08.006>.

2

2

Background

Three parts of background knowledge used in this thesis are briefly reviewed in this chapter, including metallurgy and additive manufacturing of NiTi shape memory, continuum mechanics for shape memory alloys, and lattice-based mechanical metamaterials.

2.1. Additive manufacturing of NiTi shape memory alloys

2.1.1. Martensitic transformation of NiTi

This thesis is organized within the framework of the martensitic transformation in NiTi alloys. These alloys exhibit two distinct crystallographic phases: austenite (B2 phase with a cubic structure) at elevated temperatures, and martensite (B19' phase with a monoclinic structure) at lower temperatures. The transformation from austenite to martensite, referred to as the martensitic transformation, occurs through a shear-induced lattice distortion. During this transformation, each martensitic crystal can adopt a different orientation, referred to as a variant. The assembly of martensitic variants can exist in two forms: twinned martensite, where the combination of “self-accommodated” martensitic variants coexist, and detwinned or reoriented martensite where a specific variant is dominant in the system [1,2].

As shown in Figure 2.1, the crystal structure of NiTi changes from austenite to martensite during cooling without an external load. The phase transformation from austenite to martensite is known as forward transformation, resulting in the formation of twinned martensite. When the material is subsequently heated from the martensite, the crystal structure reverts to austenite, and it is called reverse transformation, during which no shape change occurs. In this temperature-induced and stress-free martensitic transformation, four critical temperatures can be defined. During the forward transformation, austenite begins to transform to twinned martensite at the martensitic start temperature (M_s) and completes the transformation at the martensitic finish temperature (M_f). During heating, the reverse transformation starts at the austenitic start temperature (A_s) and is completed at the austenitic finish temperature (A_f).

Two fundamental phenomenological behaviors are associated with the martensitic transformation in NiTi shape memory alloys: the shape memory effect (SME) and superelasticity (SE). The stress-strain-temperature of the shape memory effect in the NiTi sample is shown in Figure 2.2. The SME is observed when an SMA is deformed in its twinned martensitic phase and then unloaded at a temperature below the austenitic start temperature (A_s). Upon subsequent heating above the austenitic finish temperature (A_f), the “shape memory” is triggered by recovering its original shape through reverse transformation.

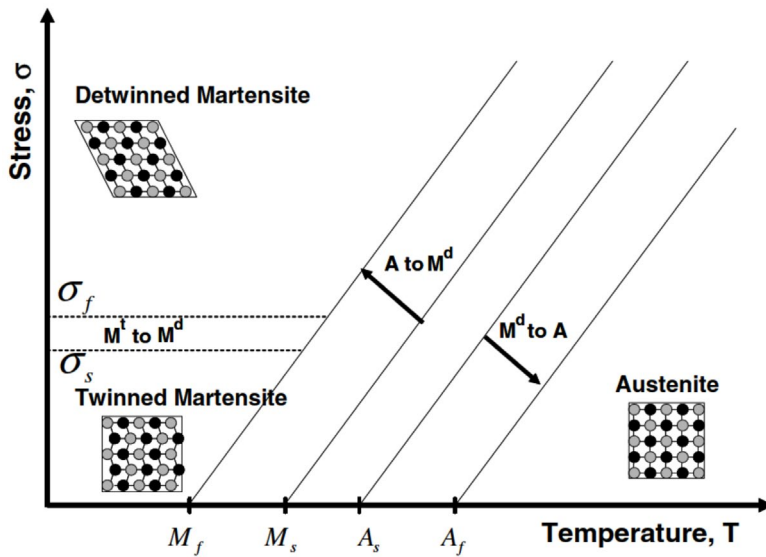


Figure 2.1 Schematic diagram illustrating the stress–temperature relationship during phase transformation in NiTi SMAs [1].

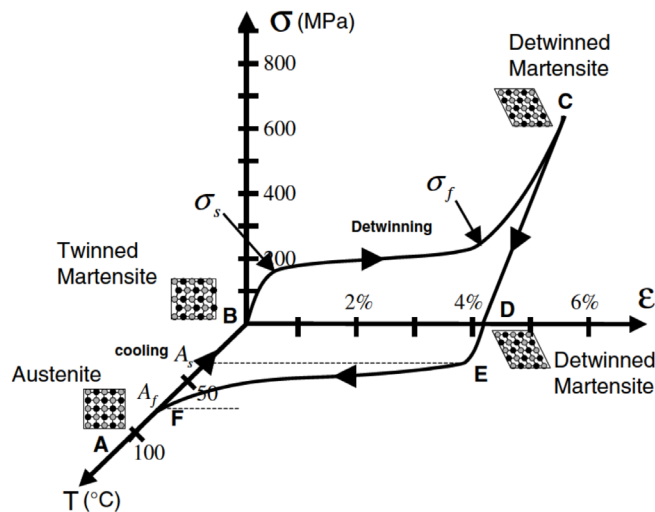


Figure 2.2 Schematic representation of the shape memory effect in NiTi SMAs, demonstrating deformation in the martensitic phase and subsequent recovery upon heating [1].

A schematical diagram of the superelasticity response is shown in Figure 2.3. A superelastic thermomechanical loading path generally starts at a temperature above austenitic finish temperature A_f , where stable austenite exists. Under applied load, the material progressively transforms into martensite where detwinned martensite becomes stable and then reversely changes back to the austenitic phase upon unloading back to a zero-stress state.

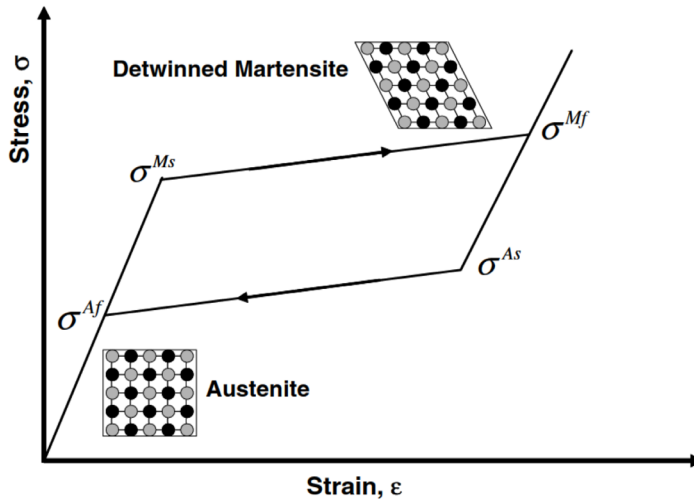


Figure 2.3 Schematic diagram illustrating the superelastic behavior of NiTi SMAs [1].

Due to their unique functionalities, NiTi and other SMAs are increasingly applied across various industrial sectors, including automotive and aerospace, soft robotics, civil engineering, and biomedical industries [3,4]. In the automotive and aerospace sectors, NiTi is used in adaptive actuators, damping systems, and lightweight shape-morphing components [5,6]. Its energy dissipation properties also make NiTi suitable for civil engineering applications, such as seismic dampers, which enhance structural resilience against vibrations [3,7]. The high actuation force and energy density of NiTi alloys enable flexible and responsive movements that mimic biological behaviors, making them ideal for applications in soft robotics [8]. In the biomedical industry, as the largest market share, NiTi is widely used for its biocompatibility and adaptability, particularly in devices such as stents, orthodontic wires, and minimally invasive surgical tools [4,9].

2.1.2. Metal additive manufacturing

A definition of AM is introduced by ASTM standard, that AM is a process of joining materials to make parts from 3D model data, usually layer upon layer, as opposed to subtractive manufacturing and formative [10–13]. The AM processes include seven main categories defined by ASTM F2792 as directed energy deposition (DED), material extrusion, material jetting, powder bed fusion (PBF), sheet lamination, and vat photopolymerization. A further categorization can be defined as the influence of heat source and material feedstock. The heat source integrated into the AM process includes a laser, electron beam, plasma arc, and gas metal arc [12].

The PBF process is particularly suitable for printing metal structures with high feature resolution and accuracy, making it a preferred AM technique for producing metal metamaterials. Within PBF, laser powder bed fusion (L-PBF) stands out as an important technique for manufacturing complex structures, including closed-cell unit architectures, with acceptable geometrical precision [14,15]. Key process parameters in L-PBF, including laser power, scanning speed, hatch distance, scanning strategy, preheat temperature, and powder layer thickness can be controlled to suppress macroscopic defects and achieve mechanical properties [2,16].

However, L-PBF shows several challenges that remain incompletely addressed. First, although high-fidelity modeling and synchrotron imaging have recently explained keyhole and pore formation mechanisms [17,18], porosity in as-fabricated metamaterials still exist, and basic parameter optimization alone does not ensure defect suppression [19–21]. Due to the path-by-path and layer-by-layer scanning process, the staircase effect can lead to discrepancies between intended and fabricated geometries [22]. Partially melted powder particles may adhere to the surfaces of metamaterials, further influencing the geometrical accuracy and performance. Third, the current L-PBF process focuses on geometrical accuracy, often assuming uniform microstructure and material properties across the structure. However, achieving microstructural consistency and control within the L-PBF process remains a significant challenge [23–25].

2.1.3. Metallurgy of NiTi

Chemical composition

The phase composition and martensitic transformation of NiTi alloys have been widely discussed since the shape memory effect of equiatomic NiTi alloy was first found by Buehler et al [26]. The phase diagram of nearly equiatomic NiTi alloy was developed after a long-term discussion as shown in Figure 2.4 [27].

Martensitic transformation temperature (MTT) is sensitive to the Ni content in the NiTi matrix, which is mainly controlled by process parameters and elements ratio in raw powder. Generally, an increase of Ni content in the matrix by 0.1 at% leads to the decrease of transformation temperatures by up to 20 °C [2,27]. These conclusions are typically drawn under the assumption of homogeneity, where thermomechanical properties are averaged across test samples. However, when compositional inhomogeneity is present, these general conclusions become less reliable, as limited characterization techniques are available to perform point-wise measurements of composition and properties. Contradictory findings have been reported, showing that compositional gradients in NiTi can both increase [28] and decrease stress hysteresis [29,30], suggesting that further investigation is needed to understand these effects.

Texture

It is known that the superelasticity of NiTi alloys is influenced by crystallographic texture and loading direction [31,32]. Xue et al found that the strong (101) texture // tensile direction crystallographic texture in the as-printed tension samples, and reported that the tensile superelastic properties are orientation-dependent [33]. Zhu et al. observed that superelasticity could be achieved in equiaxial NiTi samples with a (100) texture [34]. However, the effects of crystallographic texture remain unclear for NiTi samples, both textured and non-textured, subjected to complex stress states, suggesting that further investigation is needed to fully understand these dependencies.

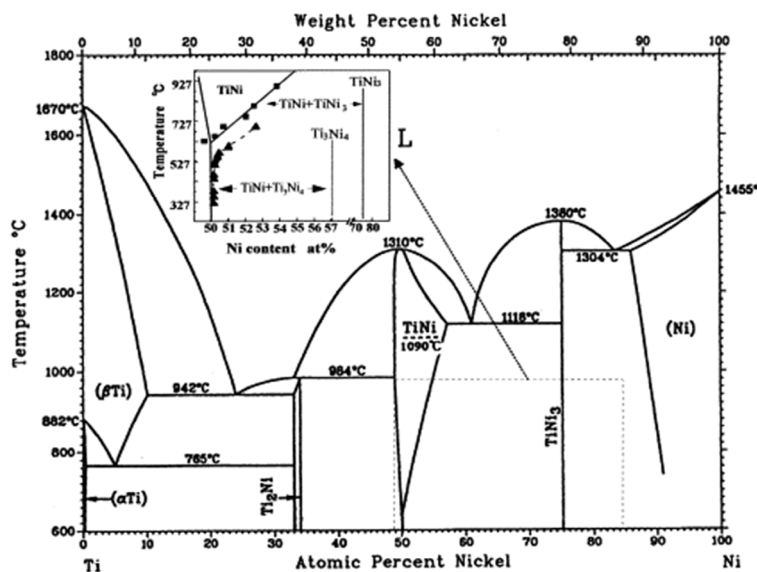


Figure 2.4 Phase diagram of NiTi alloy [27].

Precipitates

Ni_4Ti_3 precipitates are commonly observed in Ni-rich fabricated using DED or WAAM [35], or L-PBF samples after aging heat treatment [31,36]. The formation of Ni-depletion regions around the precipitates Ni_4Ti_3 could cause a Ni concentration gradient in the B2 matrix. A higher initial Ni concentration leads to a wider temperature window for the R phase transformation [37]. Ni_4Ti_3 can effectively improve transformation strain due to the saturation of formed dislocations and the interaction between Ni_4Ti_3 and formed dislocations [36].

2.1.4. Phenomenological constitutive models of shape memory alloys

Material models have been developed to understand and predict the complex behaviors and underlying physical mechanisms of shape memory alloys (SMAs) [38]. These foundational models span various length scales, including microscopic thermodynamic models [30,37], micro-macro constitutive models [39,40], and macroscopic models based on experimental phenomena [41–46]. For designing and computing NiTi structures with complex unit cell architectures at the mesoscale, macroscopic models based on phenomenological descriptions and generalized plasticity are reviewed.

Following the early development of macroscopic models describing the martensitic transformation phenomenon, phenomenological models have paved the way for the design and simulation of SMAs [47–49]. In macroscopic phenomenological models, martensitic transformation and detwinning are governed by loading functions and flow rules similar to those used in classical plasticity. Auricchio et al. developed a macroscopic model to describe the superelastic behavior of SMAs under both small and finite strains [44,45]. Souza et al. proposed a 3D phenomenological model that can simulate the behavior of polycrystalline CuZnAlMn [46]. With progressive algorithmic improvements and adjustments for characteristics such as tension-compression asymmetry, these models are now widely applied in the numerical modeling of superelastic behavior [50].

Boyd and Lagoudas developed a phenomenological SMA model derived from Gibbs free energy [49]. This model was subsequently refined by introducing factors such as the definition of mixing energy [43], the decaying function of maximum transformation strain [51,52], the introduction of transformation-induced plasticity [53,54], or nonlinear hardening functions [1].

2.2. A brief review of lattice-based metamaterials

2.2.1. Lattice-based structures

The design of unit cells in lattice-based metamaterials can follow various approaches, including topological optimization, biomimetic design, and crystalline analogs. These approaches aim to achieve specific mechanical properties such as strength, stiffness, or energy absorption. Selecting an appropriate unit cell design depends on the desired performance and deformation behavior of the metamaterial.

Truss and plate lattice-based structures

The common unit cell types in truss-based lattice metamaterials are often designed based on analogous crystalline structures. Typical unit cell structures, such as body-centered cubic (BCC) and face-centered cubic (FCC), follow similar crystalline symmetries, as shown in [55,56]. In truss-based lattice structures, the Maxwell criterion offers a theoretical basis for identifying deformation modes by considering the system's degrees of freedom (DOF) [57]. The lattice structure is treated as a pin-jointed truss with b struts and j frictionless joints, and the Maxwell number M is given by:

$$M = s - 3n + 6. \quad (2.1)$$

For $M < 0$, the structure is under-constrained and behaves as a truss or mechanism when loaded. For $M = 0$, the structure is stretching-dominated and becomes bending-dominated when $M < 0$. Stretching-dominated strut-based cell structure provides high Young's modulus and strength such as octet cell structure [58–60]. Tancogne-Dejean et al. [61] investigate the compression response of octet architecture through uniaxial compression experiments and finite element simulation. Results show an exceptional energy absorption capacity compared to traditional honeycomb cellular structures [61]. Body-centered cubic is a typical bending-dominated structure that exhibits a stress plateau for energy absorption [62].

Plate lattice structures are designed by intersecting plates along the closest planes of crystal structure. Tancogne-Dejean et al. designed plate lattices with optimal isotropic stiffness consisting of anisotropic single cubic(SC), BCC, and FCC elements structures [15]. The stiffness and yield strength of plate lattice structures are close to the theoretical limit of isotropic elastic cellular structures. However, The main obstacle to manufacturing this class of structure is the closed-cell structure traps the excess liquid and powder during manufacturing [14].

TPMS-type structures

Another type of cell structure is mathematically derived triply periodic minimal surfaces (TPMSs) [31]. TPMSs are smooth infinite non-self-intersecting surfaces intertwined in a 3D

design space and periodic in three distinct directions [63]. These topologies are generated using mathematical formulae that define the surface boundary between solid and void sections of the structure [22].

2.2.2. Mechanical properties

2

Relative density

Relative density is the most common parameter to describe the lattice-based metamaterials. The relative density is usually independent of the unit cell architecture that controls the family of structures. In practice, the relative density increases with the decrease in the unit cell size due to shorter scanning lengths in the L-PBF process [64]. The relative density is defined as the ratio of structural density to the density of constituent materials.

$$\bar{\rho} = \frac{\rho}{\rho_s}. \quad (2.2)$$

Stiffness and elastoplastic properties

The relation between relative density and relative modulus/strength can be described by the notable Gibson-Ashby model [59]:

$$\frac{E}{E_s} = C_1 \left(\frac{\rho}{\rho_s} \right)^n \quad (2.3)$$

$$\frac{\sigma}{\sigma_s} = C_2 \left(\frac{\rho}{\rho_s} \right)^m \quad (2.4)$$

where E and E_s are the static modulus of cellular structure and constituent material. σ , σ_s is the strength of the metamaterials and yielding stress of base material. Gibson-Ashby model provides a scaling relation of the approximated mechanical properties of different architectures and the experiment data given in [22].

Energy absorption

Energy absorption refers to a metamaterial's ability to absorb and dissipate energy when subjected to external loading. This capability is critical for applications such as impact protection, crashworthiness, and vibration damping. Traditional lattice-based metamaterials rely on plastic dissipation for energy absorption at cut-off or densification strains. Neglecting elastic energy, the specific energy absorption can be expressed as:

$$\psi = \frac{W}{\rho} = \frac{1}{\rho} \int_{\varepsilon=0}^{\varepsilon_{\max}} \bar{\sigma} d\bar{\varepsilon}. \quad (2.5)$$

For energy absorption applications, bending-dominated structures, such as the BCC architecture, are particularly advantageous. The crushing of BCC trusses provides a smooth, monotonically increasing plateau-like response without mesoscale instability. In contrast, FCC trusses, such as the octet structure, show stress oscillations during the plateau stage due to inelastic buckling and the formation of plastic hinges [62,65]. For octet structures, higher specific energy absorption than commercial honeycomb structures can be achieved [61,66].

2.2.3. Early research on superelastic metamaterials

Early modeling and manufacturing of superelastic metamaterials began with the successful development and fabrication of superelastic honeycomb structures, which demonstrated a clear plateau-like response and high deformation recoverability [67]. Stability investigations by Michailidis et al. revealed that deformation initially localized to individual cells and then returned to a regular pattern under continuous loading [68]. After the development of metallic additive manufacturing, numerous efforts have been made to develop superelastic NiTi metamaterials using Ni-rich NiTi [69–72]. Despite these attempts, only partial superelasticity has been achieved, often without a distinct plateau stress. Dadbakhsh et al. in [69] found that high laser power and scanning speed could enhance superelasticity by lowering the austenitic finish temperature (A_f). However, these studies also reported anomalies: structures manufactured from Ni-rich NiTi powder demonstrated higher deformation recoverability when the temperature increased compared to direct recovery [71–73]. This suggests that the shape memory effect (SME) of as-fabricated samples may surpass their superelastic performance. In cyclic compression tests, leaf-shape response or quasi-linear response were reported with observing no clear plateau stress.

2.3. Current applications

Current applications of NiTi shape memory alloys includes many traditional industrial sectors as illustrated in Figure 2.5. In the automotive industry, NiTi SMAs are employed in actuators, sensors, and active safety systems, such as vehicle locking mechanisms. In aerospace, applications include adaptive morphing wings, variable geometry nozzles, vibration dampers, and other adaptive structural components [5–6]. Robotic applications leverage NiTi alloys as artificial muscles, micro-actuators, bio-inspired structures, and

miniature manipulation devices [5]. Furthermore, NiTi's excellent biocompatibility, high recoverable deformation, corrosion resistance, and high mechanical reliability make it particularly suitable for biomedical applications, including vascular stents, orthodontic wires, orthopedic implants, and minimally invasive surgical instruments [4,74]. NiTi alloys are also effectively used in aerospace engineering for adaptive structures responding to dynamic flight conditions. However, due to the high machine hardening of NiTi, these conventional applications heavily relies on simple geometry such as wire, foil, tube and spring. Hence, additive manufacturing paves the way toward new potential applications with complex geometries and multifunctional responses.

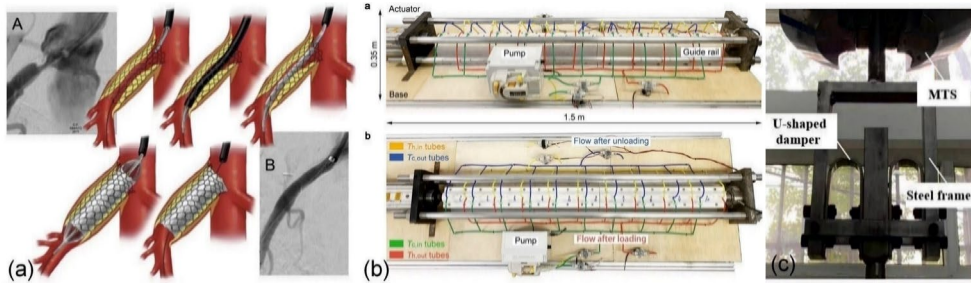


Figure 2.5 Current applications of shape memory alloys: (a) stent [74], (b) elastocaloric cooling device [75], and (c) damper [76].

2.4. Conclusions

This thesis is built upon three foundational areas of knowledge: (1) the metallic additive manufacturing techniques and metallurgy of NiTi shape memory alloys, (2) the continuum mechanics and phenomenological modeling of NiTi shape memory alloys, and (3) the mechanical modeling and mechanical properties of lattice-based metamaterials. The research gap can be summarized as follows: In modeling, it is significant to define the effective properties and mesoscopic deformation behaviors of NiTi superelastic metamaterials using the generalized plasticity model of NiTi and the Gibson-Ashby model of effective properties in metallic metamaterials. Experimentally, the challenge lies in developing a manufacturing strategy to achieve a consistent superelastic response in NiTi metamaterials. Once these challenges are overcome, it will enable the development of new designs for advanced lightweight structures with tailored superelastic properties, optimized for applications in fields such as aerospace, biomedical implants, and energy absorption systems.

References

[1] D.C. Lagoudas, Shape memory alloys: modeling and engineering applications, Springer, 2008.

[2] J.P. Oliveira, R.M. Miranda, F.M. Braz Fernandes, Welding and Joining of NiTi Shape Memory Alloys: A Review, *Prog. Mater. Sci.* 88 (2017) 412–466. <https://doi.org/10.1016/j.pmatsci.2017.04.008>.

[3] J. Mohd Jani, M. Leary, A. Subic, M.A. Gibson, A review of shape memory alloy research, applications and opportunities, *Mater. Des.* 56 (2014) 1078–1113. <https://doi.org/10.1016/j.matdes.2013.11.084>.

[4] N.B. Morgan, Medical shape memory alloy applications - The market and its products, *Mater. Sci. Eng. A* 378 (2004) 16–23. <https://doi.org/10.1016/j.msea.2003.10.326>.

[5] I.D. McCue, G.M. Valentino, D.B. Trigg, A.M. Lennon, C.E. Hebert, D.P. Seker, S.M. Nimer, J.P. Mastandrea, M.M. Trexler, S.M. Storck, Controlled shape-morphing metallic components for deployable structures, *Mater. Des.* 208 (2021) 109935. <https://doi.org/10.1016/j.matdes.2021.109935>.

[6] J. Van Humbeeck, Non-medical applications of shape memory alloys, *Mater. Sci. Eng. A* 273–275 (1999) 134–148.

[7] F. Fraternali, F. Santos, Mechanical modeling of superelastic tensegrity braces for earthquake-proof structures, *Extrem. Mech. Lett.* 33 (2019) 100578. <https://doi.org/10.1016/j.eml.2019.100578>.

[8] Y. Yang, Y. Wang, Snapping for 4D-Printed Insect-Scale Metal-Jumper, *Adv. Sci.* 2307088 (2023) 1–10. <https://doi.org/10.1002/advs.202307088>.

[9] M.H. Elahinia, M. Hashemi, M. Tabesh, S.B. Bhaduri, Manufacturing and processing of NiTi implants: A review, *Prog. Mater. Sci.* 57 (2012) 911–946. <https://doi.org/10.1016/j.pmatsci.2011.11.001>.

[10] A. 52900:2015, Standard Terminology for Additive Manufacturing – General Principles – Terminology, ASTM Int. i (2015) 1–9. http://compass.astm.org/EDIT/html_annot.cgi?ISOASTM52900+15.

[11] C.R. Cunningham, J.M. Flynn, A. Shokrani, V. Dhokia, S.T. Newman, Invited review article: Strategies and processes for high quality wire arc additive manufacturing, *Addit. Manuf.* 22 (2018) 672–686. <https://doi.org/10.1016/j.addma.2018.06.020>.

[12] T. DebRoy, H.L. Wei, J.S. Zuback, T. Mukherjee, J.W. Elmer, J.O. Milewski, A.M. Beese, A. Wilson-Heid, A. De, W. Zhang, Additive manufacturing of metallic components

– Process, structure and properties, *Prog. Mater. Sci.* 92 (2018) 112–224. <https://doi.org/10.1016/j.pmatsci.2017.10.001>.

[13] H.L. Wei, T. Mukherjee, W. Zhang, J.S. Zuback, G.L. Knapp, A. De, T. DebRoy, Mechanistic models for additive manufacturing of metallic components, *Prog. Mater. Sci.* 116 (2021). <https://doi.org/10.1016/j.pmatsci.2020.100703>.

[14] J.B. Berger, H.N.G. Wadley, R.M. McMeeking, Mechanical metamaterials at the theoretical limit of isotropic elastic stiffness, *Nature* 543 (2017) 533–537. <https://doi.org/10.1038/nature21075>.

[15] T. Tancogne-Dejean, M. Diamantopoulou, M.B. Gorji, C. Bonatti, D. Mohr, 3D Plate-Lattices: An Emerging Class of Low-Density Metamaterial Exhibiting Optimal Isotropic Stiffness, *Adv. Mater.* 30 (2018) 1–6. <https://doi.org/10.1002/adma.201803334>.

[16] M. Elahinia, N. Shayesteh Moghaddam, M. Taheri Andani, A. Amerinatanzi, B.A. Bimber, R.F. Hamilton, Fabrication of NiTi through additive manufacturing: A review, *Prog. Mater. Sci.* 83 (2016) 630–663. <https://doi.org/10.1016/j.pmatsci.2016.08.001>.

[17] A.A. Martin, N.P. Calta, S.A. Khairallah, J. Wang, P.J. Depond, A.Y. Fong, V. Thampy, G.M. Guss, A.M. Kiss, K.H. Stone, C.J. Tassone, J. Nelson Weker, M.F. Toney, T. van Buuren, M.J. Matthews, Dynamics of pore formation during laser powder bed fusion additive manufacturing, *Nat. Commun.* 10 (2019) 1–10. <https://doi.org/10.1038/s41467-019-10009-2>.

[18] C. Zhao, N.D. Parab, X. Li, K. Fezzaa, W. Tan, A.D. Rollett, T. Sun, Critical instability at moving keyhole tip generates porosity in laser melting, *Science* (80-.). 370 (2020) 1080–1086. <https://doi.org/10.1126/science.abd1587>.

[19] D. Melancon, Z.S. Bagheri, R.B. Johnston, L. Liu, M. Tanzer, D. Pasini, Mechanical characterization of structurally porous biomaterials built via additive manufacturing: experiments, predictive models, and design maps for load-bearing bone replacement implants, *Acta Biomater.* 63 (2017) 350–368. <https://doi.org/10.1016/j.actbio.2017.09.013>.

[20] X. Cao, Y. Jiang, T. Zhao, P. Wang, Y. Wang, Z. Chen, Y. Li, D. Xiao, D. Fang, Compression experiment and numerical evaluation on mechanical responses of the lattice structures with stochastic geometric defects originated from additive-manufacturing, *Compos. Part B Eng.* 194 (2020) 108030. <https://doi.org/10.1016/j.compositesb.2020.108030>.

[21] L. Liu, P. Kamm, F. García-Moreno, J. Banhart, D. Pasini, Elastic and failure response of imperfect three-dimensional metallic lattices: the role of geometric defects induced by

Selective Laser Melting, J. Mech. Phys. Solids 107 (2017) 160–184. <https://doi.org/10.1016/j.jmps.2017.07.003>.

[22] T. Maconachie, M. Leary, B. Lozanovski, X. Zhang, M. Qian, O. Faruque, M. Brandt, SLM lattice structures: Properties, performance, applications and challenges, Mater. Des. 183 (2019) 108137. <https://doi.org/10.1016/j.matdes.2019.108137>.

[23] N.M. della Ventura, C.Q. Dong, S.A. Messina, R.R. Collino, G.H. Balbus, S.P. Donegan, J.D. Miller, D.S. Gianola, M.R. Begley, Heterogeneity in millimeter-scale Ti-6Al-4V lattice primitives: Challenges in defining effective properties for metamaterial design, Mater. Des. 238 (2024). <https://doi.org/10.1016/j.matdes.2024.112695>.

[24] P. Delroisse, P.J. Jacques, E. Maire, O. Rigo, A. Simar, Effect of strut orientation on the microstructure heterogeneities in AlSi10Mg lattices processed by selective laser melting, Scr. Mater. 141 (2017) 32–35. <https://doi.org/10.1016/j.scriptamat.2017.07.020>.

[25] N.S. Johnson, M. Strantza, M.J. Matthews, J.S. Park, P. Kenesei, B. Clausen, D.W. Brown, J.S. Carpenter, C.A. Brice, A.P. Stebner, Direct measurement of the effective properties of an additively manufactured titanium octet truss unit cell using high energy X-ray diffraction, Mater. Charact. 209 (2024). <https://doi.org/10.1016/j.matchar.2024.113755>.

[26] W.J. Buehler, J. V. Gilfrich, R.C. Wiley, Effect of Low-Temperature Phase Changes on the Mechanical Properties of Alloys near Composition TiNi, J. Appl. Phys. 34 (1963) 1475–1477. <https://doi.org/10.1063/1.1729603>.

[27] K. Otsuka, X. Ren, Physical metallurgy of Ti-Ni-based shape memory alloys, Prog. Mater. Sci. 50 (2005) 511–678. <https://doi.org/10.1016/j.pmatsci.2004.10.001>.

[28] X. Wang, M. Speirs, S. Kustov, B. Vrancken, X. Li, J.P. Kruth, J. Van Humbeeck, Selective laser melting produced layer-structured NiTi shape memory alloys with high damping properties and Elinvar effect, Scr. Mater. 146 (2018) 246–250. <https://doi.org/10.1016/j.scriptamat.2017.11.047>.

[29] Y. Yang, J.B. Zhan, J.B. Sui, C.Q. Li, K. Yang, P. Castany, T. Gloriant, Functionally graded NiTi alloy with exceptional strain-hardening effect fabricated by SLM method, Scr. Mater. 188 (2020) 130–134. <https://doi.org/10.1016/j.scriptamat.2020.07.019>.

[30] J. Zhu, D. Wang, Y. Gao, T.Y. Zhang, Y. Wang, Linear-superelastic metals by controlled strain release via nanoscale concentration-gradient engineering, Mater. Today 33 (2020) 17–23. <https://doi.org/10.1016/j.mattod.2019.10.003>.

[31] Y. Cao, X. Zhou, D. Cong, H. Zheng, Y. Cao, Z. Nie, Z. Chen, S. Li, N. Xu, Z. Gao, W. Cai, Y. Wang, Large tunable elastocaloric effect in additively manufactured Ni-Ti shape

memory alloys, *Acta Mater.* 194 (2020) 178–189. <https://doi.org/10.1016/j.actamat.2020.04.007>.

[32] Z. Pu, D. Du, K. Wang, G. Liu, D. Zhang, X. Wang, B. Chang, Microstructure, phase transformation behavior and tensile superelasticity of NiTi shape memory alloys fabricated by the wire-based vacuum additive manufacturing, *Mater. Sci. Eng. A* 812 (2021). <https://doi.org/10.1016/j.msea.2021.141077>.

2

[33] L. Xue, K.C. Atlı, C. Zhang, N. Hite, A. Srivastava, A.C. Leff, A.A. Wilson, D.J. Sharar, A. Elwany, R. Arroyave, I. Karaman, Laser Powder Bed Fusion of Defect-Free NiTi Shape Memory Alloy Parts with Superior Tensile Superelasticity, *Acta Mater.* 229 (2022) 117781. <https://doi.org/10.1016/j.actamat.2022.117781>.

[34] J.N. Zhu, K. Liu, T. Riemslag, F.D. Tichelaar, E. Borisov, X. Yao, A. Popovich, R. Huizinga, M. Hermans, V. Popovich, Achieving superelasticity in additively manufactured Ni-lean NiTi by crystallographic design, *Mater. Des.* 230 (2023) 111949. <https://doi.org/10.1016/j.matdes.2023.111949>.

[35] J. Wang, Z. Pan, G. Yang, J. Han, X. Chen, H. Li, Location dependence of microstructure, phase transformation temperature and mechanical properties on Ni-rich NiTi alloy fabricated by wire arc additive manufacturing, *Mater. Sci. Eng. A* 749 (2019) 218–222. <https://doi.org/10.1016/j.msea.2019.02.029>.

[36] H.Z. Lu, H.W. Ma, W.S. Cai, X. Luo, Z. Wang, C.H. Song, S. Yin, C. Yang, Stable tensile recovery strain induced by a Ni₄Ti₃ nanoprecipitate in a Ni50.4Ti49.6 shape memory alloy fabricated via selective laser melting, *Acta Mater.* 219 (2021). <https://doi.org/10.1016/j.actamat.2021.117261>.

[37] J. Zhu, H.H. Wu, Y. Wu, H. Wang, T. Zhang, H. Xiao, Y. Wang, S.Q. Shi, Influence of Ni₄Ti₃ precipitation on martensitic transformations in NiTi shape memory alloy: R phase transformation, *Acta Mater.* 207 (2021). <https://doi.org/10.1016/j.actamat.2021.116665>.

[38] C. Cisse, W. Zaki, T. Ben Zineb, A review of constitutive models and modeling techniques for shape memory alloys, *Int. J. Plast.* 76 (2016) 244–284. <https://doi.org/10.1016/j.ijplas.2015.08.006>.

[39] J.K. Joy, T. Umale, D. Zhao, A. Solomou, K. Xie, I. Karaman, D.C. Lagoudas, Effects of microstructure and composition on constitutive response of high temperature shape memory alloys: Micromechanical modeling using 3-D reconstructions with experimental validation, *Acta Mater.* 232 (2022) 117929. <https://doi.org/10.1016/j.actamat.2022.117929>.

[40] C. Yu, G. Kang, Q. Kan, Crystal plasticity based constitutive model of NiTi shape memory alloy considering different mechanisms of inelastic deformation, *Int. J. Plast.* 54 (2014) 132–162. <https://doi.org/10.1016/j.ijplas.2013.08.012>.

[41] B. Haghgouyan, C. Hayrettin, T. Baxevanis, I. Karaman, D.C. Lagoudas, Fracture toughness of NiTi—Towards establishing standard test methods for phase transforming materials, *Acta Mater.* 162 (2019) 226–238. <https://doi.org/10.1016/j.actamat.2018.09.048>.

[42] M. Simoes, C. Braithwaite, A. Makaya, E. Martínez-Pañeda, Modelling fatigue crack growth in shape memory alloys, *Fatigue Fract. Eng. Mater. Struct.* 45 (2022) 1243–1257. <https://doi.org/10.1111/ffe.13638>.

[43] D. Lagoudas, D. Hartl, Y. Chemisky, L. MacHado, P. Popov, Constitutive model for the numerical analysis of phase transformation in polycrystalline shape memory alloys, *Int. J. Plast.* 32–33 (2012) 155–183. <https://doi.org/10.1016/j.ijplas.2011.10.009>.

[44] F. Auricchio, R.L. Taylor, Shape-memory alloys: modelling and numerical simulations of the finite-strain superelastic behavior, *Comput. Methods Appl. Mech. Eng.* 143 (1997) 175–194. [https://doi.org/10.1016/S0045-7825\(96\)01147-4](https://doi.org/10.1016/S0045-7825(96)01147-4).

[45] F. Auricchio, R.L. Taylor, J. Lubliner, Shape-memory alloys: macromodelling and numerical simulations of the superelastic behavior, *Comput. Methods Appl. Mech. Eng.* 146 (1997) 281–312. [https://doi.org/10.1016/S0045-7825\(96\)01232-7](https://doi.org/10.1016/S0045-7825(96)01232-7).

[46] A.C. Souza, E.N. Mamiya, N. Zouain, Three-dimensional model for solids undergoing stress-induced phase transformations, *Eur. J. Mech. A/Solids* 17 (1998) 789–806. [https://doi.org/10.1016/S0997-7538\(98\)80005-3](https://doi.org/10.1016/S0997-7538(98)80005-3).

[47] L.C. Brinson, One-dimensional constitutive behavior of shape memory alloys: Thermomechanical derivation with non-constant material functions and redefined martensite internal variable, *J. Intell. Mater. Syst. Struct.* 4 (1993) 229–242. <https://doi.org/10.1177/1045389X9300400213>.

[48] J. Lubliner, F. Auricchio, Generalized plasticity and shape-memory alloys, *Int. J. Solids Struct.* 33 (1996) 991–1003. [https://doi.org/10.1016/0020-7683\(95\)00082-8](https://doi.org/10.1016/0020-7683(95)00082-8).

[49] J.G. Boyd, D.C. Lagoudas, A thermodynamical constitutive model for shape memory materials. Part I. The monolithic shape memory alloy, *Int. J. Plast.* 12 (1996) 805–842. [https://doi.org/10.1016/S0749-6419\(96\)00030-7](https://doi.org/10.1016/S0749-6419(96)00030-7).

[50] F. Auricchio, L. Petrini, Improvements and algorithmical considerations on a recent three-dimensional model describing stress-induced solid phase transformations, *Int. J. Numer. Methods Eng.* 55 (2002) 1255–1284. <https://doi.org/10.1002/nme.619>.

[51] D.J. Hartl, J.T. Mooney, D.C. Lagoudas, F.T. Calkins, J.H. Mabe, Use of a Ni60Ti shape memory alloy for active jet engine chevron application: II. Experimentally validated numerical analysis, *Smart Mater. Struct.* 19 (2010). <https://doi.org/10.1088/0964-1726/19/1/015021>.

[52] D.J. Hartl, D.C. Lagoudas, F.T. Calkins, J.H. Mabe, J.T. Mooney, D.C. Lagoudas, F.T. Calkins, J.H. Mabe, Use of a Ni60Ti shape memory alloy for active jet engine chevron application: I. thermomechanical characterization, *Smart Mater. Struct.* 19 (2010). <https://doi.org/10.1088/0964-1726/19/1/015021>.

[53] D.C. Lagoudas, P.B. Entchev, Modeling of transformation-induced plasticity and its effect on the behavior of porous shape memory alloys. Part I: Constitutive model for fully dense SMAs, *Mech. Mater.* 36 (2004) 865–892. <https://doi.org/10.1016/j.mechmat.2003.08.006>.

[54] L. Xu, A. Solomou, T. Baxevanis, D. Lagoudas, Finite strain constitutive modeling for shape memory alloys considering transformation-induced plasticity and two-way shape memory effect, *Int. J. Solids Struct.* 221 (2021) 42–59. <https://doi.org/10.1016/j.ijsolstr.2020.03.009>.

[55] Q. Feng, Q. Tang, Y. Liu, R. Setchi, S. Soe, S. Ma, L. Bai, Quasi-static analysis of mechanical properties of Ti6Al4V lattice structures manufactured using selective laser melting, *Int. J. Adv. Manuf. Technol.* 94 (2018) 2301–2313. <https://doi.org/10.1007/s00170-017-0932-7>.

[56] R. Gümrük, R.A.W. Mines, Compressive behaviour of stainless steel micro-lattice structures, *Int. J. Mech. Sci.* 68 (2013) 125–139. <https://doi.org/10.1016/j.ijmecsci.2013.01.006>.

[57] C.M. Portela, J.R. Greer, D.M. Kochmann, Impact of node geometry on the effective stiffness of non-slender three-dimensional truss lattice architectures, *Extrem. Mech. Lett.* 22 (2018) 138–148. <https://doi.org/10.1016/j.eml.2018.06.004>.

[58] L.J. Gibson, M.F. Ashby, Mechanics of Three-Dimensional Cellular Materials., *Proc. R. Soc. London, Ser. A Math. Phys. Sci.* 382 (1982) 43–59. <https://doi.org/10.1098/rspa.1982.0088>.

[59] M.F. Ashby, The properties of foams and lattices, *Philos. Trans. R. Soc. A Math. Phys. Eng. Sci.* 364 (2006) 15–30. <https://doi.org/10.1098/rsta.2005.1678>.

[60] N.A. Fleck, V.S. Deshpande, M.F. Ashby, Micro-architected materials: Past, present and future, *Proc. R. Soc. A Math. Phys. Eng. Sci.* 466 (2010) 2495–2516. <https://doi.org/10.1098/rspa.2010.0215>.

[61] T. Tancogne-Dejean, A.B. Spierings, D. Mohr, Additively-manufactured metallic micro-lattice materials for high specific energy absorption under static and dynamic loading, *Acta Mater.* 116 (2016) 14–28. <https://doi.org/10.1016/j.actamat.2016.05.054>.

[62] T. Tancogne-Dejean, D. Mohr, Stiffness and specific energy absorption of additively-manufactured metallic BCC metamaterials composed of tapered beams, *Int. J. Mech. Sci.* 141 (2018) 101–116. <https://doi.org/10.1016/j.ijmecsci.2018.03.027>.

[63] Z. Alomar, F. Concli, A Review of the Selective Laser Melting Lattice Structures and Their Numerical Models, *Adv. Eng. Mater.* 22 (2020) 1–17. <https://doi.org/10.1002/adem.202000611>.

[64] C. Yan, L. Hao, A. Hussein, D. Raymont, Evaluations of cellular lattice structures manufactured using selective laser melting, *Int. J. Mach. Tools Manuf.* 62 (2012) 32–38. <https://doi.org/10.1016/j.ijmachtools.2012.06.002>.

[65] K. Ushijima, W.J. Cantwell, R.A.W. Mines, S. Tsopanos, M. Smith, An investigation into the compressive properties of stainless steel micro-lattice structures, *J. Sandw. Struct. Mater.* 13 (2011) 303–329. <https://doi.org/10.1177/1099636210380997>.

[66] L. Dong, V. Deshpande, H. Wadley, Mechanical response of Ti-6Al-4V octet-truss lattice structures, *Int. J. Solids Struct.* 60 (2015) 107–124. <https://doi.org/10.1016/j.ijsolstr.2015.02.020>.

[67] J.A. Shaw, D.S. Grummon, J. Foltz, Superelastic NiTi honeycombs: fabrication and experiments, *Smart Mater. Struct.* 16 (2007) S170–S178. <https://doi.org/10.1088/0964-1726/16/1/S17>.

[68] P.A. Michailidis, N. Triantafyllidis, J.A. Shaw, D.S. Grummon, Superelasticity and stability of a shape memory alloy hexagonal honeycomb under in-plane compression, *Int. J. Solids Struct.* 46 (2009) 2724–2738. <https://doi.org/10.1016/j.ijsolstr.2009.03.013>.

[69] S. Dadbakhsh, M. Speirs, J.P. Kruth, J. Van Humbeeck, Influence of SLM on shape memory and compression behaviour of NiTi scaffolds, *CIRP Ann. - Manuf. Technol.* 64 (2015) 209–212. <https://doi.org/10.1016/j.cirp.2015.04.039>.

[70] Z. Gorgin Karaji, M. Speirs, S. Dadbakhsh, J.P. Kruth, H. Weinans, A.A. Zadpoor, S.A. Yavari, Additively manufactured and surface biofunctionalized porous nitinol, *ACS Appl. Mater. Interfaces* 9 (2017) 1293–1304. <https://doi.org/10.1021/acsami.6b14026>.

[71] S. Saedi, S.E. Saghalian, A. Jahadakbar, N. Shayesteh Moghaddam, M. Taheri Andani, S.M. Saghalian, Y.C. Lu, M. Elahinia, H.E. Karaca, Shape memory response of porous NiTi shape memory alloys fabricated by selective laser melting, *J. Mater. Sci. Mater. Med.* 29 (2018). <https://doi.org/10.1007/s10856-018-6044-6>.

2. Background

[72] H.Z. Lu, H.W. Ma, X. Luo, Y. Wang, J. Wang, R. Lupoi, S. Yin, C. Yang, Microstructure, shape memory properties, and in vitro biocompatibility of porous NiTi scaffolds fabricated via selective laser melting, *J. Mater. Res. Technol.* 15 (2021) 6797–6812. <https://doi.org/10.1016/j.jmrt.2021.11.112>.

[73] X. Yang, Q. Yang, Y. Shi, L. Yang, S. Wu, C. Yan, Y. Shi, Effect of volume fraction and unit cell size on manufacturability and compressive behaviors of Ni-Ti triply periodic minimal surface lattices, *Addit. Manuf.* 54 (2022) 102737. <https://doi.org/10.1016/j.addma.2022.102737>.

[74] T. Tallarita, G.S. Oderich, T.A. Macedo, P. Głowiczki, S. Misra, A.A. Duncan, M. Kalra, T.C. Bower, Reinterventions for stent restenosis in patients treated for atherosclerotic mesenteric artery disease, *J. Vasc. Surg.* 54 (2011) 1422-1429.e1.

[75] G. Zhou, L. Zhang, Z. Li, P. Hua, Q. Sun, S. Yao, Achieving kilowatt-scale elastocaloric cooling by a multi-cell architecture, *Nature* 639 (2025).

[76] Z.X. Zhang, J. Zhang, C. Fang, Y. Zhang, Y. Li, Emerging steel frames with Fe-SMA U-shaped dampers for enhancing seismic resilience, *J. Infrastruct. Preserv.* 4 (2023).

3

Modeling superelasticity in truss-based metamaterials

3

Truss-based metamaterials typically exhibit well-defined analytical expressions for homogenized elastic stiffness and strength based on their deformation mechanisms. Before exploring alternative design paradigms, it is essential to derive the effective properties of these structures using analytical expressions and numerical modeling based on a superelastic material model. In this chapter, BCC and octet structures are selected to represent bending-dominated and stretching-dominated unit cell architectures, respectively. A parametric finite element analysis is conducted to establish a foundational relationship between density and mechanical properties, as well as effective transformation criteria for the homogenized unit cell with ideal superelasticity. Crack-free BCC and octet samples were successfully additively manufactured using L-PBF from $\text{Ni}_{51.4}\text{Ti}_{48.6}$ powder. Uniaxial compression experiments conducted at temperatures above the austenite finish temperature revealed that only partial superelasticity was achieved in the as-fabricated samples. The energy dissipation and engineering stress-strain curves were validated using data obtained from cyclic compression experiments.

This chapter is based on the scientific publication: Z. Yan, J. Zhu, E. Borisov, T. Riemsdag, S. Paul, M. Hermans, J. Jovanova, V. Popovich, Superelastic response and damping behavior of additively manufactured Nitinol architected materials, *Addit. Manuf.* 68 (2023) 103505. <https://doi.org/10.1016/j.addma.2023.103505>.

3

3.1. Introduction

Recent developments in metallic metamaterials illustrate the successful creation of 3D lattice-based metamaterials with a high strength-weight ratio [1], tunable anisotropy [2–4], and energy absorption [5]. For energy absorption applications, bending-dominated structures are known to exhibit a stable plateau stress, making them more favorable for shock protection [6]. However, such structures typically rely on plastic deformation, meaning they are not reusable after initial use. In applications like shock protection, where multiple load cycles may occur, recoverability of deformation in energy dissipation is essential [7]. Here, a combination of superelastic NiTi and mechanical metamaterials provides a feasible solution to design and additively manufacture reusable energy-absorbing metamaterial. Due to the nature of dissipative energy in damping behavior, energy dissipation in cyclic loading can be formulated as damping. Golovin and co-workers attributed high damping capacity in stochastic cellular material to stress hysteresis caused by local yielding behavior, but this damping property can lead to crack initiation and premature failure [8,9]. For NiTi metamaterials, the damping behavior can be considered as a martensitic transformation loss factor, and further analysis is needed to explain the mesoscale deformation mechanisms underlying energy absorption and damping.

Building on early works [10,11], analytical and computational studies have explored the designed parameter space by relating the nonlinear response of different cell architectures to external loading conditions [6,12,13]. Numerical studies have focused on understanding the complex relations between elastoplastic constituent materials and different structures [12,14–17]. In studies where NiTi is used as a constituent material, some researchers simplify it as an elastoplastic material [18,19]. Ravari et al. [20] investigated the macroscopic stress response of the NiTi body centered cubic (BCC) lattice and experimentally validated it. Viet et al. [21] developed a model for the effective response of the NiTi primitive unit cell based on the Zaki and Moumni model [22]. However, the interaction between NiTi constitutive models and the macroscopic thermomechanical response remains underexplored. Given the temperature-dependent functionalities of NiTi, rescaling property-density relationships is crucial for discovering new design paradigms and achieving customizable functionalities.

The fast development of L-PBF for NiTi provides controllable process parameters allowing to mitigate macroscopic defects and tailor its functional properties. Successful additive manufacturing of NiTi samples demands careful optimization of process parameters and choice of raw powder [23–26]. NiTi structures with complicated shapes were successfully manufactured based on parametric studies on bulk material [27–30]. Several works have explored the optimized parameters for NiTi 2D honeycomb [18], micro-lattice [31], and micro stent with a one-way shape memory effect using an equiatomic raw powder. Yang et al. [32] investigated the effect of volume fraction on the compressive behavior of

NiTi Gyroid structures. However, for cyclic loading conditions, cyclic stability and immediate recovery without external stimulus are required. Achieving stabilized superelasticity in metamaterials directly from the L-PBF process remains challenging. The influence of microstructure on the functional properties of NiTi lattices is widely neglected and mechanical properties of polycrystalline NiTi are simplified as phenomenological models in numerical simulation [33,34]. To the best of our knowledge, most of the current research is focused on process optimization and functionality in AM process. The relation between L-PBF NiTi mesoscopic deformation modes and the macroscopic thermomechanical response has not been dealt with in depth. Therefore, a comprehensive work, which combines phenomenological modeling, microstructure characterization, and experimentally validated stabilized superelastic behavior is needed.

3

This chapter aims to explore the superelastic response space and damping properties of lattice-based NiTi metamaterials. BCC and octet structures are chosen to represent bending-dominated and stretching-dominated deformation modes, respectively. The macroscopic superelastic response of both structures is modeled and compared. An effective initial transformation surface with temperature effect is developed based on the extended Hill's model. Partial superelasticity with a leaf-shaped response was achieved in lattice samples fabricated via L-PBF. Simulations were validated under quasi-static compressive loading following cyclic compression. Energy absorption with recoverable deformation and damping properties were achieved in cyclic compression tests. Comparative studies among bulk, bending-dominated, and stretching-dominated structures were conducted to illustrate the consistency and deviations in composition, microstructure, and local superelasticity.

3.2. Geometric parameters and mechanical modeling

3.2.1. Relative density

To explore the ideal superelastic response of lattice-based metamaterials, body centered cubic (BCC) structures, and octet structures are chosen as the architecture cases to represent bending- and stretching-dominated modes along the $<100>$ loading direction [35]. The macroscale mechanical properties of both structures vary with relative density, which is defined by the ratio of their density to the density of the base material. For a latticed-based structure composed of solid beams [6,12], the relative density $\bar{\rho}$ can be given by the second- or $3\sqrt{3}\pi$ der approximate equation:

$$\bar{\rho} = C_1 \left(\frac{R}{l} \right)^2 - C_2 \left(\frac{R}{l} \right)^3, \quad (3.1)$$

where R and l are the radius and length of the beam. C_1 and C_2 are structure-dependent constants, which are $18\sqrt{2}\pi$ for a BCC structure, and $6\sqrt{2}\pi$ and 54.6 for an octet structure.

3.2.2. Constitutive material model

The superelastic behavior of NiTi is modeled based on the phenomenological model developed by Auricchio [36]. Austenite and Martensite are assumed to follow isotropic linear elasticity. The stress-induced forward and reverse phase transformation surfaces are modeled using the Drucker-Prager loading surface:

$$F^t(\sigma, T) = \|\sigma_{\text{dev}}\| + \frac{1}{3} \text{tr}(\sigma) \tan(\beta), \quad (3.2)$$

where σ_{dev} is the deviatoric part of the stress, β is material constants estimated from the tensile and compressive transformation stress levels, the uniaxial transformation strain, and the volumetric transformation strain. The transformation surface is linearly dependent on temperature T , which is described by Clausius–Clapeyron relation

$$C_s^{\text{fwd}} = C_s^{\text{rev}} = \frac{d\sigma_s^{\text{fwd}}}{dT} = \frac{\Delta S}{\varepsilon^{\text{tr}}}, \quad (3.3)$$

where C_s^{fwd} and C_s^{rev} are coefficients defined as the slopes of the stress-temperature boundaries for forward and reverse transformations respectively. σ_s^{fwd} is the transformation stress, ΔS is the entropy variation and ε^{tr} is the transformation strain. Transformation-induced plasticity is neglected and martensite fraction ξ_s is the internal variable used to describe the evolution of transformation strain in the flow rule.

3.2.3. Characterization of material properties

NiTi thermomechanical properties need to be carefully calibrated for the phenomenological material model because NiTi exhibits functional degradation during the cyclic loading test. In order to mitigate the statistical deviation of thermomechanical properties resulting from different cycles, the material properties were calibrated from the cyclic compression tests on bulk samples. Calibration methods are introduced in detail. To determine the temperature required for subsequent mechanical testing, transformation temperatures (TTs) were measured from the differential scanning calorimetry (DSC) curves as shown in Figure 3.1(a). The testing temperature for uniaxial compression was determined to be 6 °C higher than the austenite finish temperature A_f , which ensures a fully austenitized

parent phase. Cyclic compression tests were conducted until superelasticity was completely stabilized (Figure 3.1 (b)). As can be seen, the superelastic response of bulk material can be stabilized after 10 cycles with the residual strain lower than 0.038% (Figure 3.1 (c)) [37]. In the 10th cycle, the statistical deviation of mechanical properties under 54 °C is negligible, and the main mechanical properties of additively manufactured NiTi bulk samples are calibrated in the 10th cycle of cyclic compression tests (Figure 3.1(d) and Table 3.1). Young's modulus of austenite and martensite is determined using the tangent line. The initial transformation stress is measured using the parallel line at the strain of 0.2%. The low Young's modulus of austenite likely resulted from either R-phase transformation, or a strong [001] texture parallel to BD and residual martensite generated in the L-PBF process and cyclic compression [38,39].

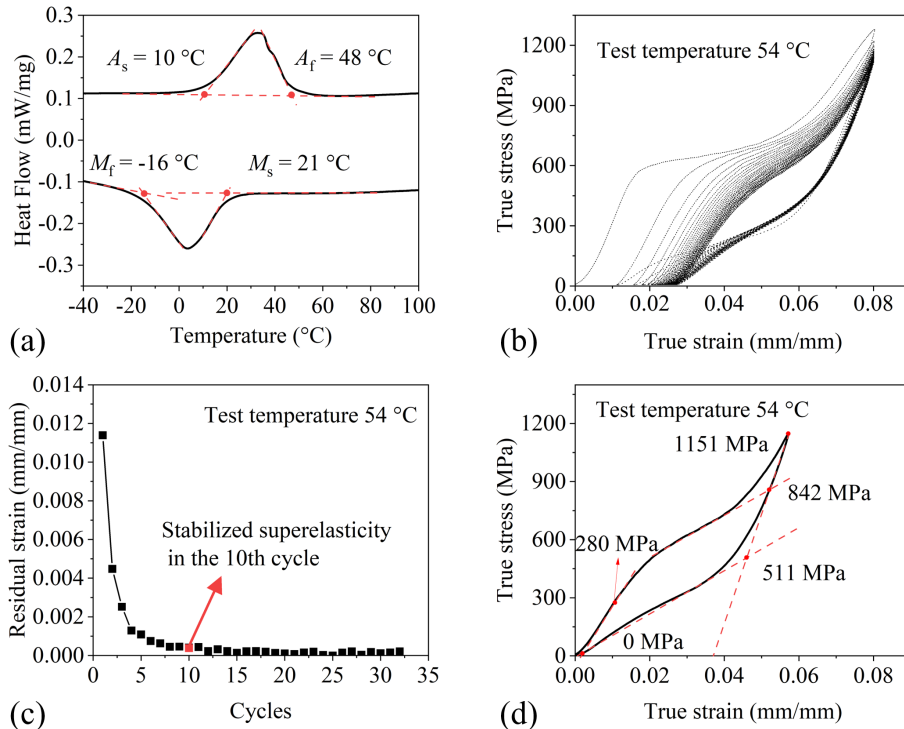


Figure 3.1 Thermomechanical properties of NiTi bulk material: (a) DSC curve, (b) cyclic compression, (c) stabilization in the 10th cycle, (d) transformation stress.

Table 3.1 Summary of thermomechanical experimental results used for calibration of NiTi constitutive relations.

Thermomechanical properties	Unit	Value
Austenite Young's modulus (E_A)	GPa	32.584
Austenite Poisson ratio (ν_A)	-	0.33
Martensite Young's modulus (E_M)	GPa	56.592
Martensite Poisson ratio (ν_M)	-	0.33
Transformation strain ($\varepsilon_s^{\text{fwd}}$)	-	0.037
Martensite start stress (σ_s^{fwd})	MPa	280
Martensite finish stress	MPa	842
Austenite start stress	MPa	511
Austenite finish stress	MPa	0
Clausius–Clapeyron relation (C_s^{fwd} and C_s^{fwd}) [40]	MPa/°C	6.5
Reference temperature (T_0)	°C	54

3.2.4. Analytical model

To understand the temperature effect on the effective transformation stress of both structures, the effective transformation stress is expressed as a function of relative density. Macroscopic plastic strain is substituted by the initial martensitic transformation of NiTi. Using the first-order approximation equation of relative density, the initial transformation stress of the BCC and octet structures under uniaxial compressive response can be obtained using slender beam theory:

$$\sigma^{\text{fwd}} = k \left(\bar{\rho} \right)^p \sigma_s^{\text{fwd}}, \quad (3.4)$$

where k and p are the architecture (strut orientation) dependent coefficients. $k=0.47$ and $p=1.5$ for BCC structure, and $k=1/3$ and $p=1$ for octet structure under uniaxial compression based on free body method [11,41]. The 1-dimensional reduction of forward transformation stress is

$$\sigma_s^{\text{fwd}}(T) = \sigma_s^{\text{fwd}}(T_0) - C_s^{\text{fwd}} T. \quad (3.5)$$

The temperature-influenced term can be decomposed from effective transformation stress and expressed as

$$\sigma^{\text{fwd}} = k(\bar{\rho})^p \sigma_s^{\text{fwd}} - C^{\text{fwd}} T, \text{ with } C^{\text{fwd}} = k(\bar{\rho})^p C_s^{\text{fwd}}, \quad (3.6)$$

where C^{fwd} is the effective Clausius–Clapeyron relation. This material property can be controlled by relative density under uniaxial compression. To account for the influence of non-slender beams, the power law relation is modeled numerically using RVEs.

3

3.2.5. Unit-cell models

The effective superelastic behavior of representative volume element (RVE) is predicted using a unit cell model with periodic boundary conditions (PBC). Applying PBC on structures with nonlinear material behavior was discussed in earlier research [42]. The unit cell model is discretized using first-order block elements (C3D8R) to ensure symmetric meshes on the paired surfaces. The displacement of nodes on the paired surfaces is coupled with the displacement of dummy nodes using constraint equations [43]. Nodes located on the edges and vertices are also considered in constraint equations excluding redundant equations. The displacement components of nodes in PBC are formulated as

$$u_i^{j+}(x, y, z) - u_i^{j-}(x, y, z) = c_i^j \quad (i, j = 1, 2, 3), \quad (3.7)$$

where $j+$ and $j-$ denote the positive and negative normal of paired surfaces, and i is the displacement component in Cartesian coordinates.

Simulations for BCC and octet RVEs with a unit cell size of 4 mm and a relative density ranging from 0.1 to 0.6 are performed to understand the density-properties relation. Three displacement loading conditions are applied to dummy points of the RVEs to simulate superelastic behaviors in a stabilized cycle as shown in Figure 3.2. Uniaxial compression is applied along the [100] direction with a maximum displacement of 0.3 mm to simulate the uniaxial transformation stress. Pure shear with a maximum displacement of 0.1 mm is applied along the 1-2 plane and 2-1 plane to simulate the shear response: $\mathbf{F} = \mathbf{I} + \varepsilon_{\text{max}} (\mathbf{e}_1 \otimes \mathbf{e}_2 + \mathbf{e}_2 \otimes \mathbf{e}_1)$. Hydrostatic compression with a maximum displacement of 0.1 mm is applied in three normal directions. Constant temperature loading $T = (54, 70, 90, \text{ and } 110^{\circ}\text{C})$ is applied on all RVEs to simulate the effect of temperature T on transformation stress.

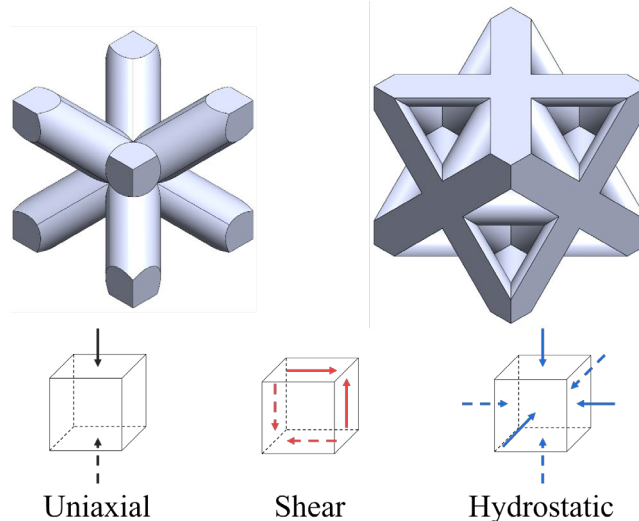
After the numerical solution of the RVEs, the effective stress of RVEs is obtained by the reaction forces \mathbf{RF} on the 3 dummy nodes and the unit cell size L :

$$\bar{\sigma}_{ij} = \frac{\mathbf{e}_i \cdot \mathbf{R} \mathbf{F}_j}{L^2}. \quad (3.8)$$

The effective martensite fraction $\bar{\xi}$ is determined by the volumetric average of the martensite fraction over the whole RVE:

$$\bar{\xi} = \frac{1}{V} \int_V \xi_s dV, \quad (3.9)$$

where V is the volume of the RVE.



3

Figure 3.2 RVEs with a relative density of 0.4 and loading conditions.

3.2.6. Multi-cell models

The uniaxial compression response of both structures with $5 \times 5 \times 5$ cells tessellation is modeled to simulate the stabilized cycling of NiTi metamaterials. Both structures are compressed quasi-statically by two horizontal rigid planes. The contact between rigid planes and the metamaterial is assumed to be a surface-to-surface contact with a tangential frictional coefficient of 0.2. The bottom plane was completely fixed by the reference point and the top plane moved downward until the macroscopic strain reached the maximum value before returning to the initial position. The same C3D8R element with an approximate seed size smaller than 0.14 mm is used to discretize the geometry model after the mesh convergence study. A one-quarter model with x - z and y - z plane symmetry is used to reduce computational

time. The macroscopic engineering stress and strain were calculated from the reaction force and displacement of the reference point of the top plane.

3.3. Experiments

3.3.1. Materials and additive manufacturing

The NiTi metamaterials and cylindrical bulk samples were manufactured by a laser-based powder bed fusion (L-PBF) process using an Aconity3D Midi printer equipped with a fiber ytterbium laser (1060 nm wavelength). Cylindrical samples of 13 mm diameter and 20 mm length were fabricated for material properties calibration. The $20 \times 20 \times 20$ mm³ metamaterial samples with $5 \times 5 \times 5$ tessellation were manufactured for microstructural characterization and subsequent mechanical tests. Commercial Ni_{51.4}Ti_{48.6} powder prepared by gas atomization was used as powder bed feedstock. The process chamber was filled with high-purity Argon. A stripe scanning strategy with a rotation of 67.5° between layers was used to heat and fuse the powder bed as shown in Figure 3.3 (a) and (b). The process parameters were optimized to mitigate macroscopic defects such as cracks, warping, and delamination. Based on our earlier research [24,44]. The process parameters, resulting in a defect-free sample were selected for this chapter and are listed in Table 3.2.

Table 3.2 L-PBF process parameters used in this chapter.

Laser power (W)	Scanning speed (mm/s)	Hatch distance (mm)	Layer thickness (mm)	Volume energy density (J/mm ³)
400	1250	0.120	0.030	88.9

3.3.2. Microstructural characterization

The actual relative density of additively manufactured metamaterials was calculated by the ratio of their measured density to the theoretical density of NiTi material (6.450 g/cm³). Strut diameter was measured using a Keyence VHX-5000 optical microscope. Metallographic samples were cut using Electrical Discharge Machining (EDM) with exposed surfaces as shown in Figure 3.3 (a). EDS (Energy Dispersive Spectroscopy) samples use the macroscopic (110) surface of the BCC structure and (100) surface of the octet structure because compositional deviations along the struts were taken into account. The macroscopic (100) surfaces, which are parallel to the building direction of the L-PBF process, were further

used for microstructural characterization. These samples were ground and polished following standard procedures used for the metallographic preparation of metal samples. Samples were subsequently etched using a solution consisting of 120 ml distilled water, 15 ml HCl, 15 g Na₂S₂O₅, 10 g K₂S₂O₅, and 2 g NH₄-HF to identify austenite grains. Austenite grains were visualized by linearly polarized light (LEICA DML 5000 light optical microscope). The grain size of columnar grains is estimated using the image software ImageJ. EDS analysis (using SEM, JEOL JSM 6500F) was performed on seven different locations and calculated as the mean and deviation. Phase transformation temperatures were measured by differential scanning calorimetry (DSC, Perkin Elmer DSC 800) in a nitrogen atmosphere with a cooling and heating rate of 10 °C/min over a temperature range of -50 to +150 °C. The austenite start temperature (A_s), austenite finish temperature (A_f), martensite start temperature (M_s), and martensite finish temperature (M_f) were determined using the tangential lines.

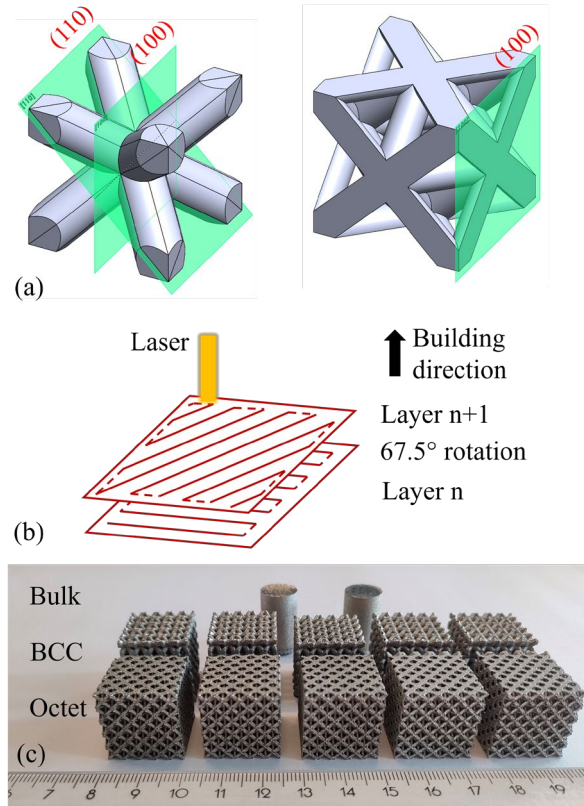


Figure 3.3 (a) Definition of macroscopic planes on BCC and octet structures, (b) CAD coordinate for L-PBF coordinate system and scanning strategy, and (c) as-fabricated samples.

3.3.3. Mechanical testing

To characterize the printed NiTi bulk material, cuboid samples (cross-section 4.2 mm \times 4.2 mm, height 8 mm) were cut from the as-fabricated cylindrical samples with a diameter of 13 mm, using EDM. Compression tests were conducted at a strain rate of 1.0×10^{-4} s $^{-1}$, using a 25 kN MTS 858 hydraulic test machine, equipped with a high temperature extensometer (632.53F-14, MTS). A sample temperature of 54 °C was maintained by locating the sample inside the coil of an induction heating system with the temperature being controlled by a K-type thermocouple (spot welded to the specimen). Displacement-controlled cyclic loading was applied to the sample with a maximum strain of 8%.

3

The cyclic compressive response of NiTi metamaterials was investigated using universal mechanical tests (Zwick Z100). The samples were placed inside a heating chamber with a constant temperature of 54 °C. To determine the recoverable strain accurately, engineering strains of metamaterials were measured using a contact extensometer (Zwick DigiClip with a gauge length of 24 mm). Cyclic compression tests were conducted three times, with each test containing 10 cycles so that the superelasticity of metamaterials was stabilized. Displacement-controlled loading was applied with a maximum displacement of 0.7 mm and a strain rate of 5×10^{-4} s $^{-1}$. The fracture behavior of designed NiTi metamaterials was investigated using compressive deformation until fracture. The fracture images were taken using a high speed camera. The engineering strain was measured using a contact extensometer (MakroExtensometer BTC EXMACRO.001).

The local mechanical properties of different NiTi samples were tested using instrumented indentation (Zwick ZHU2.5) at room temperature. A spherical ball indenter with a diameter of 0.5 mm was used to reduce the strain gradient. Hold time at the maximum force was set at 2 s and the indentation rate was 0.05 N/s. Indentation forces of 5, 10, 20, and 40 N were used to test the superelastic behavior and recoverability under indentation.

3.4. Results

3.4.1. Effective superelastic response

The superelastic response of RVEs with different relative densities ranging from 0.1 to 0.6 are modeled. Examples of effective stress and strain graphs of both RVEs with a relative density of 0.4 for uniaxial compression, shear, and hydrostatic loading conditions are shown in Figure 3.4. The octet structure shows higher stiffness and larger stress hysteresis than the BCC structure under uniaxial compression. Under hydrostatic loading, each strut in the structures is subjected to axial compression and both structures show a similar response. The BCC structure exhibits higher shear stiffness than the octet structure.

3.4. Results

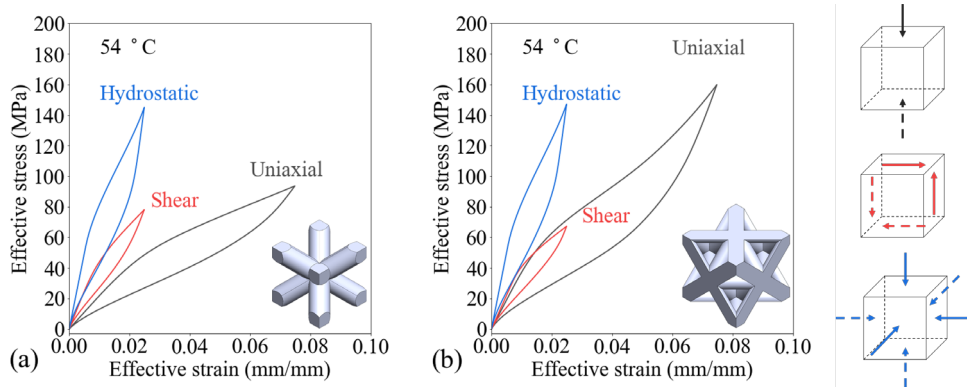


Figure 3.4 Effective stress and strain diagrams of (a) BCC and (b) octet RVEs for uniaxial, shear and hydrostatic loadings at 54 °C.

At the relative density of 0.1, the transition of the mesoscopic deformation mode is observed in the octet structure. An additional superelastic hinge is generated at the middle of the beam as shown in Figure 3.5. Due to the superelastic buckling of the slender NiTi strut, the octet structure at the relative density of 0.1 loses stability. However, the elastic deformation of martensite can mitigate the twist of the lattice and reinforce the stability of the octet structure [12].

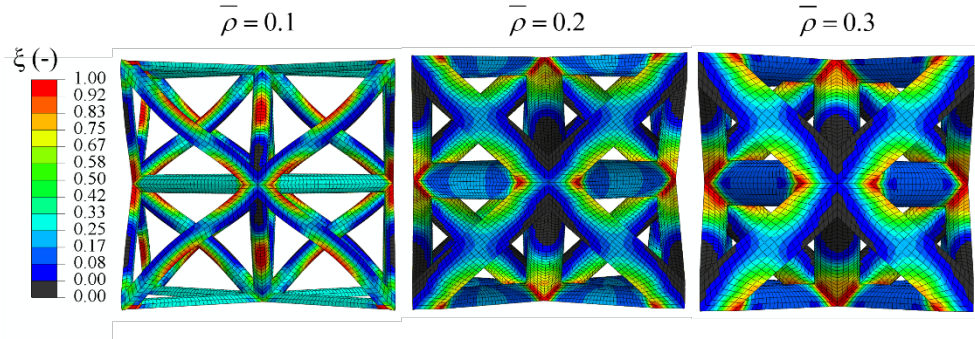


Figure 3.5 Transition of deformation mode due to the formation of superelastic hinges.

Initial transformation behavior under different loading conditions requires additional attention. The initial transformation stress, including uniaxial martensite transformation stress σ_M , shear martensite transformation stress τ_M , and hydrostatic martensite transformation stress σ_{HM} were obtained using effective stress and strain curves of RVEs. All initial

transformation stress are determined based on the effective martensite volume fraction $\bar{\xi} \geq 10^{-4}$ to reduce the numerical sensitivity of the single element. The uniaxial martensitic transformation stress σ_M obtained using RVE simulation is shown in Figure 3.6 and the shear martensite transformation stress τ_M and hydrostatic martensite transformation σ_{HM} are shown in Figure 3.7 and Figure 3.8. It was found that the effective transformation stress is linearly dependent on environmental temperature as shown in Figure 3.6-Figure 3.8. For superelastic metamaterials with high relative density, the effective transformation-temperature relation is fitted based on unit-cell models with different relative densities. The transformation stress is fitted to a power law, including the temperature effect:

$$\sigma^{\text{fwd}} = k_1 (\bar{\rho})^{p_1} \sigma_s^{\text{fwd}} - C^{\text{fwd}} T, \text{ with } C^{\text{fwd}} = k_2 (\bar{\rho})^{p_2} C_s^{\text{fwd}}. \quad (3.10)$$

3

The rescaled relation returns to the power dependence of uniaxial yield stress of traditional BCC and octet structures with high relative density [13] after the temperature effect is separated in the second term on the right-hand side. Both structure exhibits higher power law factors due to the non-slender beam used in unit cell structures with high relative density (Table 3.3). With increasing beam slenderness, this effective transformation stress-density power law can be varied [35]. For both structures with low relative density, the analytical model of initial transformation stress is derived based on the slender beam theory. These numerical results illustrate NiTi metamaterial exhibiting effective transformation stress tailororable by adapting the relative density and cell architecture, which is rarely found in bulk NiTi alloys [45].

Table 3.3 Power-law parameters for transformation stress of BCC and octet structures.

	k_1	p_1	k_2	p_2
BBC				
Uniaxial	0.424	1.92	0.426	1.96
Shear	0.178	1.23	0.157	1.21
Hydrostatic	0.563	1.25	0.519	1.22
Octet				
Uniaxial	0.368	1.31	0.254	1.27
Shear	0.351	1.34	0.270	1.29
Hydrostatic	0.654	1.30	0.530	1.17

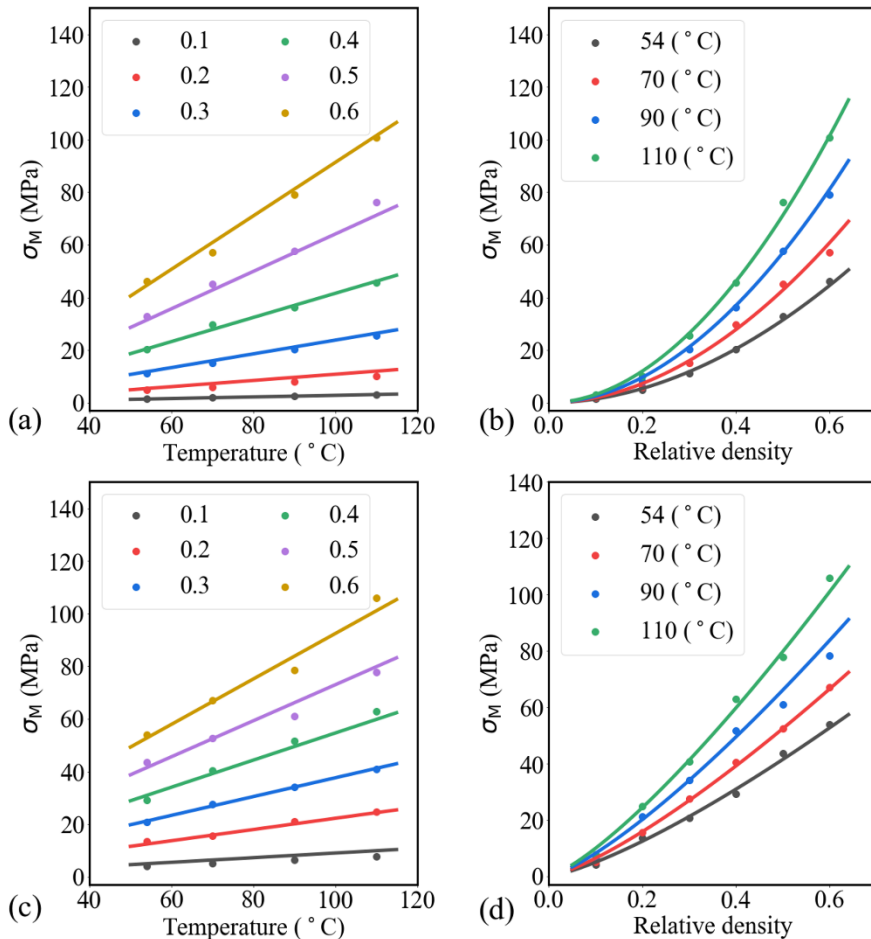


Figure 3.6 Effect of temperature loadings and relative densities on martensite start stress under uniaxial loading of (a)(b) BCC and (c)(d) octet RVEs.

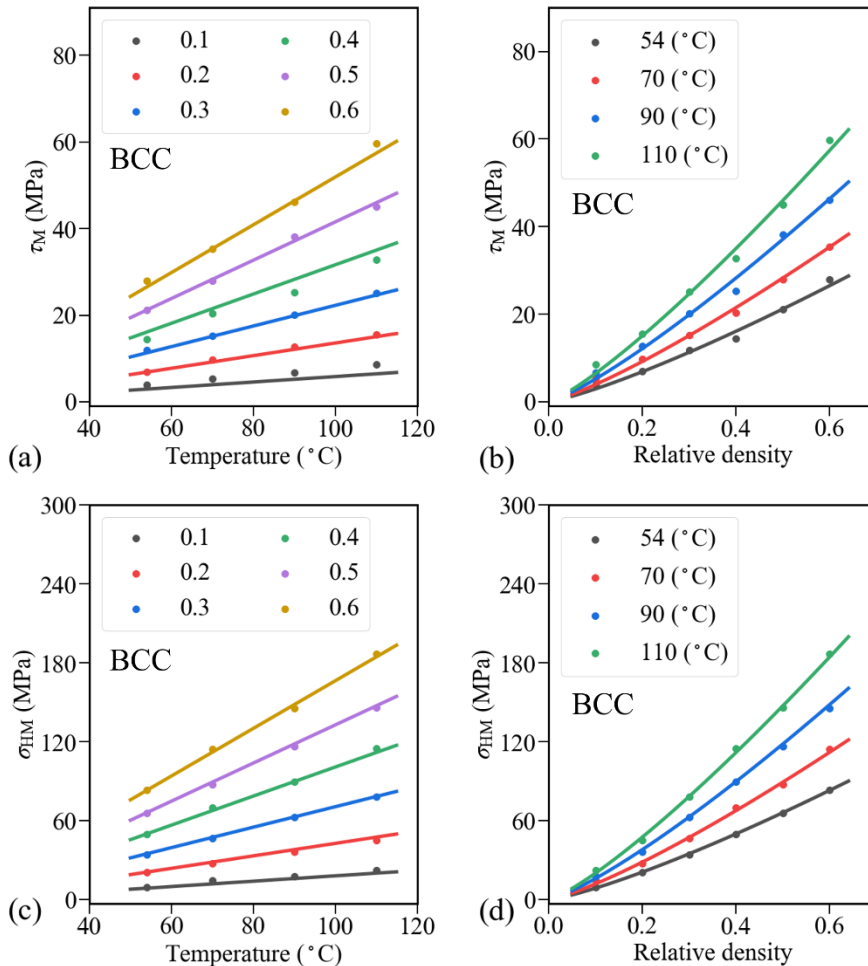


Figure 3.7 Effect of temperature loadings and relative densities on martensite start stress under (a)(b) pure shear and (c)(d) hydrostatic loading of BCC RVEs.

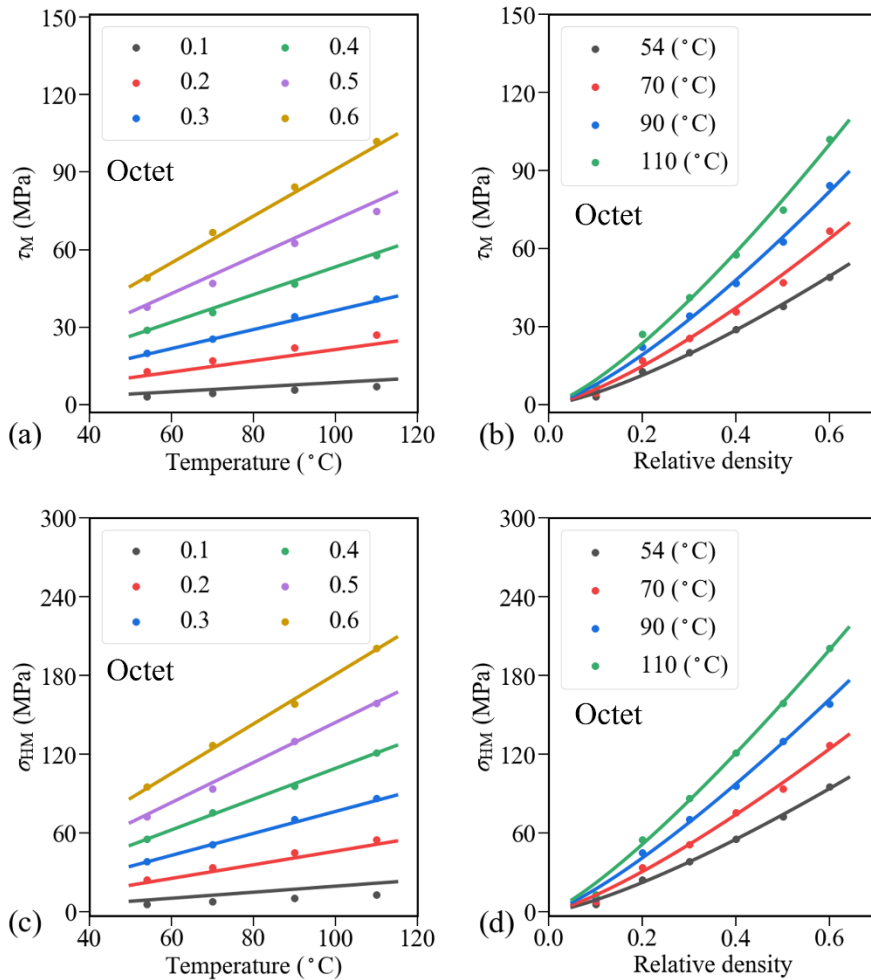


Figure 3.8 Effect of temperature loadings and relative densities on martensite start stress under (a)(b) pure shear and (c)(d) hydrostatic loading of octet RVEs..

3.4.2. Microstructural characterization

In order to reduce the influence of microstructure in a single track, BCC and octet structures with a relative density of 0.4 were additively manufactured and tested (Figure 3.3 (c)). With this relative density, each strut contained multiple scanning tracks and layers. The dimensional accuracy of both L-PBFed metamaterials is shown in Table 3.4. The dimensional discrepancy between the nominal and measured geometry of as-fabricated materials is due to partially molten powders, resulting in the waviness and roughness of struts [46]. The ‘staircase effect’ is another common AM phenomenon that influences the geometrical inaccuracy of as-fabricated metamaterials [32].

Table 3.4 Dimensions and density of as-designed compared with L-PBFed samples.

Metamaterials	Strut diameter (mm)	Volume (mm ³)	Mass (g)	Relative density (-)
As-designed BCC	1.30	8000.00	20.6	0.4
As-fabricated BCC	1.67±0.08	7910.67±22.02	24.8±0.9	0.486±0.021
As-designed octet	0.84	8000.00	20.6	0.4
As-fabricated octet	1.11±0.06	7982.41±8.97	25.4±0.2	0.494±0.004

The martensitic transformation of NiTi is known to be sensitive to Ni evaporation at high heat input in the L-PBF process [45]. EDS analyses were conducted on the (110) cross-section of BCC structures and (100) cross-section of octet structures and similar compositional ratios were detected, as shown in Table 3.5. Similar elemental composition results in less variation of superelastic behavior of constituent NiTi material in different structures. Martensitic transformation temperatures are obtained by DSC curves and shown in Table 3.6. As can be seen in Figure 3.9, L-PBF metamaterials show a broader transformation temperature range and higher transformation temperatures compared to bulk samples. Higher reversed transformation temperatures are found in the octet structure than in the BCC structure.

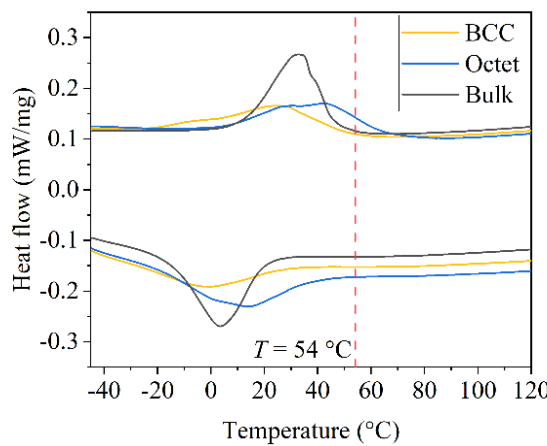


Figure 3.9 DSC curves for bulk, BCC, and octet samples.

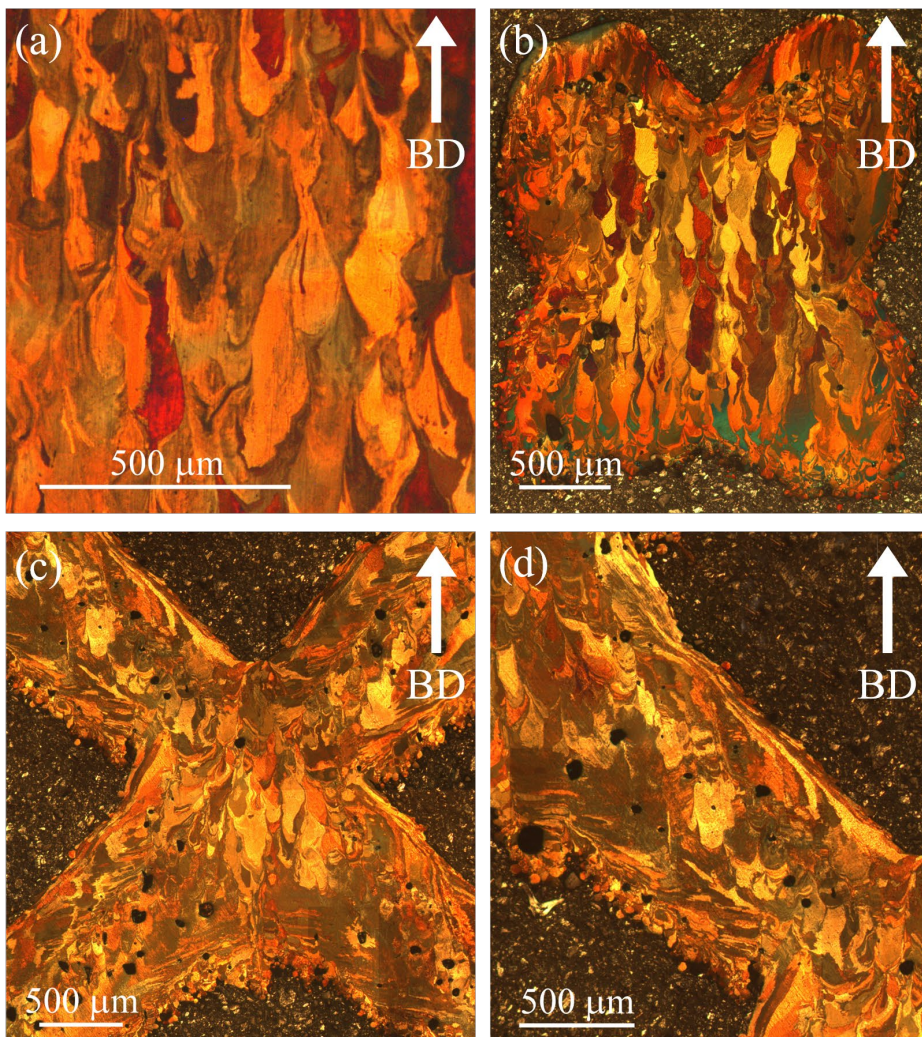
Table 3.5 EDS compositional analysis of different NiTi structures.

Samples	Ni (at. %)	Ti (at. %)
Powder	50.60±0.10	49.40±0.10
Bulk	50.30±0.15	49.70±0.15
BCC	50.20±0.10	49.80±0.10
Octet	50.20±0.15	49.80±0.15

Table 3.6 Martensitic transformation temperature of different structures (obtained by DSC).

Sample	A_s (°C)	A_f (°C)	M_s (°C)	M_f (°C)
Bulk	10	48	21	-16
BCC	-19	53	27	-42
Octet	4	69	38	-19

The microstructure on the (100) cross-section parallel to the building direction (BD) of bulk, BCC, and octet samples is shown in Figure 3.10. NiTi samples printed with high Ni-rich raw powder ($\text{Ni}_{51.4}\text{Ti}_{48.6}$, at. %) show more macroscopic defects such as cracking, warping, and delamination due to the change of element ratios [26]. In this chapter, high energy input (88.9 J/mm^3) was successfully used to mitigate these macroscopic defects based on bulk process optimization, as shown in Figure 3.10 (a). Pores defects are observed in as-fabricated metamaterials although bulk samples with low porosity were fabricated using the same process parameters. Coarse columnar grains epitaxially grow along the building direction (BD) in the bulk sample due to heat sinking into the as-fabricated layers [47]. Columnar grains growing along BD have an average length of $0.46 \pm 0.08 \text{ mm}$, which surpasses multiple deposition layers (0.030 mm per layer). Similar epitaxial growth of coarse columnar grains is shown at the nodes of BCC and octet structures, which implies similar thermal dissipation conditions in bulk samples and nodes of metamaterials (Figure 3.10(b) and (c)). The average length of columnar grain is $0.24 \pm 0.05 \text{ mm}$ in the BCC node and $0.15 \pm 0.05 \text{ mm}$ in the octet node. Figure 3.10(d) illustrates the microstructure of a strut of octet structure, which is on the macroscopic (100) cross-section and 45° to the BD. Three different areas of grains with different growth orientations are distinguishable. At both edges of the strut, thin columnar grains grow along the orientation of the strut. The growth direction of columnar grains gradually transforms to BD around the middle axis.



Sample	Grain size (mm)
Bulk	0.46 ± 0.08
BCC	0.24 ± 0.05
Octet	0.15 ± 0.05

Figure 3.10 Optical images of the microstructure for (a) Bulk (b) BCC structure (c) octet structure and (d) magnified strut in octet structure and corresponding grain size.

Inhomogeneous microstructure results in the variation of mechanical properties of the base NiTi material. This variation of mechanical properties leads to discrepancies between numerical simulation and validation experiments. To reveal the local mechanical properties of the base NiTi material, instrumented indentation was conducted under room temperature and low loading conditions. Indentation force and depth curves of different structures with varying maximum forces of 5 N, 10 N, 20 N, and 40 N are shown in Figure 3.11 and Figure 3.12. For the bulk sample, residual depth increased with indentation force because the superelastic deformation could not recover at a room temperature lower than A_f . Higher recovery capacities are found in the center of BCC and octet cross-section samples due to the inhomogeneous microstructure and martensitic transformation temperatures. The indentation force of 5 N is chosen to estimate the indentation elastic modulus due to the high proportion of elastic deformation. The estimation of the indentation elastic modulus is based on Kumar's simplification of the classical Hertz model [48]. Within the restriction condition of the Hertz model [49], the indentation force and depth relation for the ball indenter is

$$P_{\text{ind}} = \frac{4}{3} R_{\text{eff}}^{1/2} E_{\text{ind}} h_{\text{R}}^{3/2}, \quad (3.11),$$

where R_{eff} is the effective radius of curvature at the contact. R_{eff} can be given as

$$\frac{1}{R_{\text{eff}}} = \frac{1}{R} - \frac{1}{R_{\text{S}}}, \quad (3.12),$$

where R is the radius of the ball indenter and R_{S} is the residual radius of indentation. To apply this method to superelastic NiTi, high-depth recoverability is required, and elastic deformation is dominant as shown in Figure 3.11 [50]. R_{eff} is approximated to R and h_{R} is approximated to the maximum indentation depth h_{max} . The indentation force is approximated to

$$P_{\text{ind}} = \frac{4}{3} R^{1/2} E_{\text{ind}} h_{\text{max}}^{3/2}. \quad (3.13)$$

This method provides an approximated comparison of local mechanical properties at the mesoscale between different NiTi samples. Material thermomechanical properties used in FEM should be carefully calibrated using uniaxial loading tests.

3.4. Results

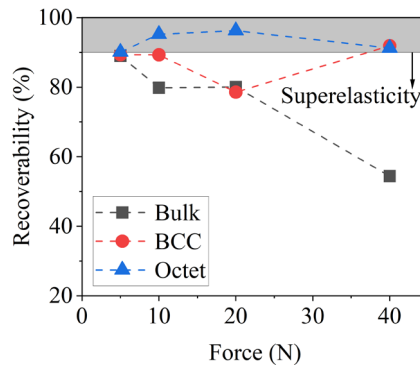


Figure 3.11 Recoverability of instrumented indentation.

The indentation force and depth curves of bulk, BCC, and octet samples are shown in Figure 3.12. Indentation with a force of 5 N is repeated in four different locations and the estimated elastic modulus of the bulk and structural samples are shown in Figure 3.12 (d). The indentation elastic modulus of BCC and octet structures are comparable with the indentation elastic modulus of the bulk sample. The variation of indentation modulus is likely influenced by local microstructure in different locations.

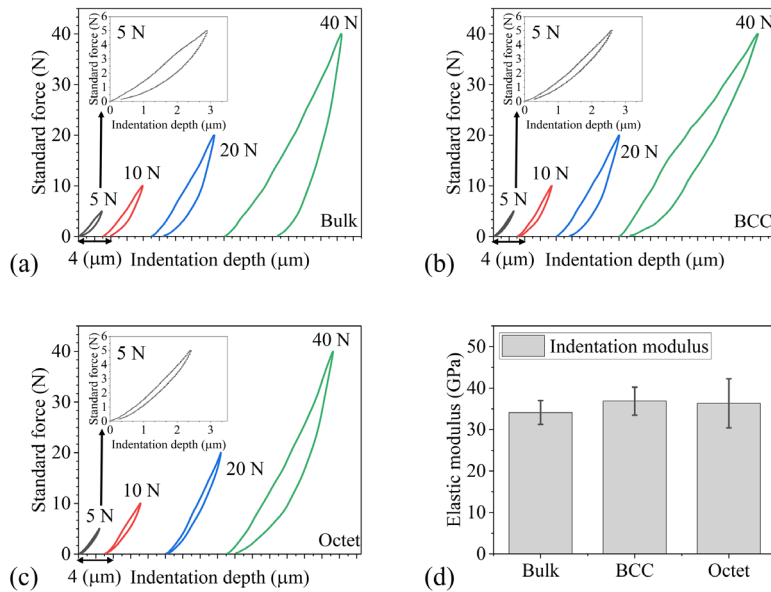


Figure 3.12 Instrumented indentation force and depth curves of (a) bulk, (b) BCC, and (c) octet samples and (d) indentation modulus.

3.4.3. Uniaxial compression tests

The superelastic response of both structures was tested using three batches of cyclic compression tests under the displacement loading of 0.7 mm, as shown in Figure 3.13 (a) and (b). In each training batch, the superelastic response of NiTi metamaterials was achieved with a large recoverable strain. The recoverable strain and stress hysteresis increased in the second and third training, while hardening behavior was observed in the first cycle. To distinguish the hardening behavior and stress plateau in both structures, the von Mises stress distribution of $5 \times 5 \times 5$ cells simulation after symmetric operation in post-processing is shown in Figure 3.13 (c). The von Mises stress of the relative density of ideal structures is approximated as 0.5 considering the geometrical inaccuracy of as-fabricated metamaterial as shown in Table 3.4. The printed NiTi does not reach plastic yield until 1151 MPa as shown in Figure 3.1 (d), and as can be seen in the stress contour, no stress-concentration-induced plastic stress is shown. The stress plateau and hardening in the training process are mainly attributed to the stress-induced martensitic transformation and transformation-induced plasticity. After 10 training cycles, the stress plateau disappears and a partial superelastic response is achieved. Due to the inhomogeneous stress distribution in NiTi metamaterials, insufficient martensitic transformation in the first cyclic test results in low recoverable strain. It is likely due to the incompatibility of preferred martensite variants and the nonuniform stress distribution in NiTi structures. The experimental and numerical results are compared in Figure 3.13 (d) and (e). Due to the hardening behavior in the training process, the tested samples show higher stiffness than the numerical results.

3.4. Results

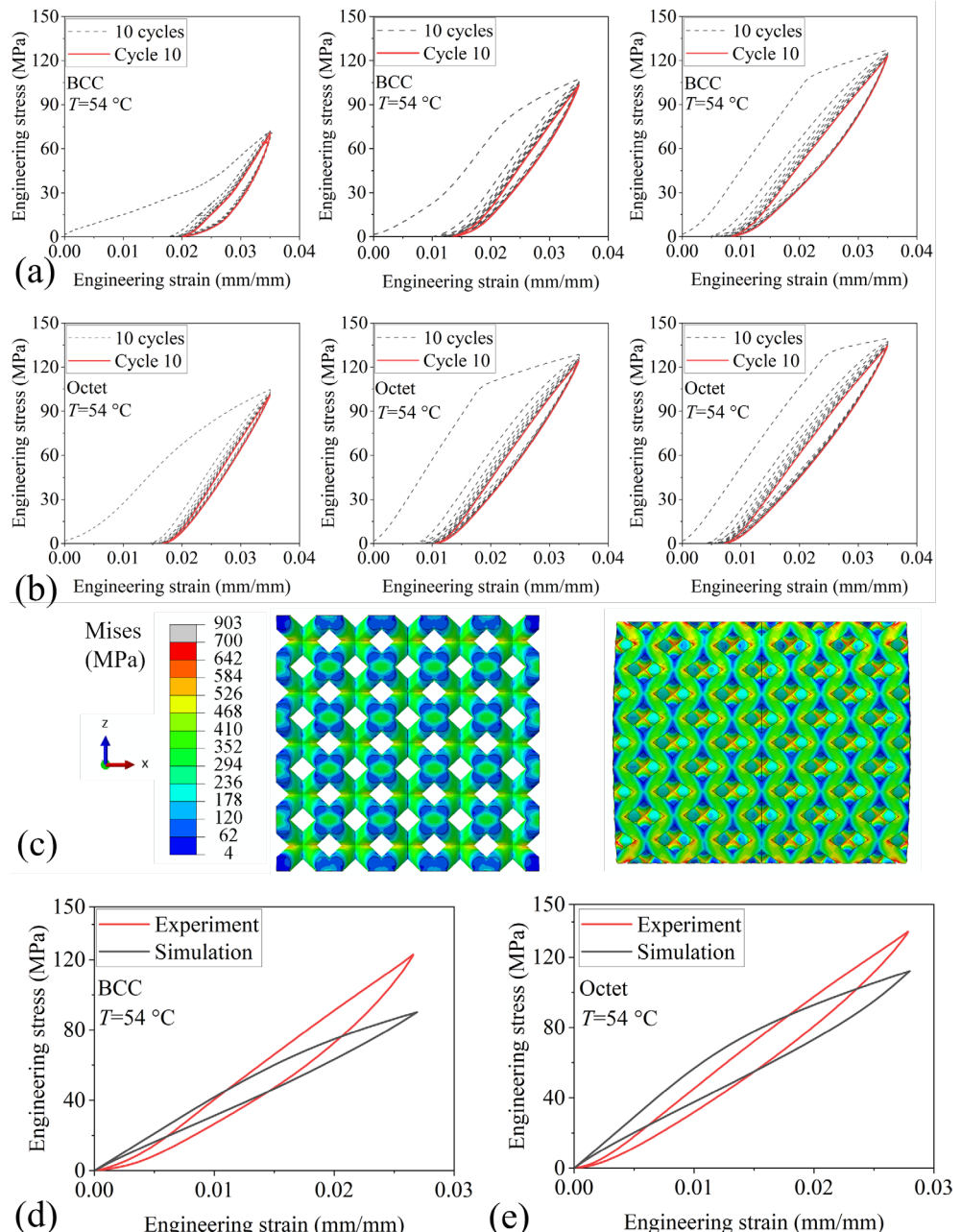


Figure 3.13 Cyclic compression tests on (a) BCC and (b) octet structure, (c) von Mises stress distribution after symmetric operation in post-processing, and (d) validation of simulation in the 10th cycle under cyclic compression tests.

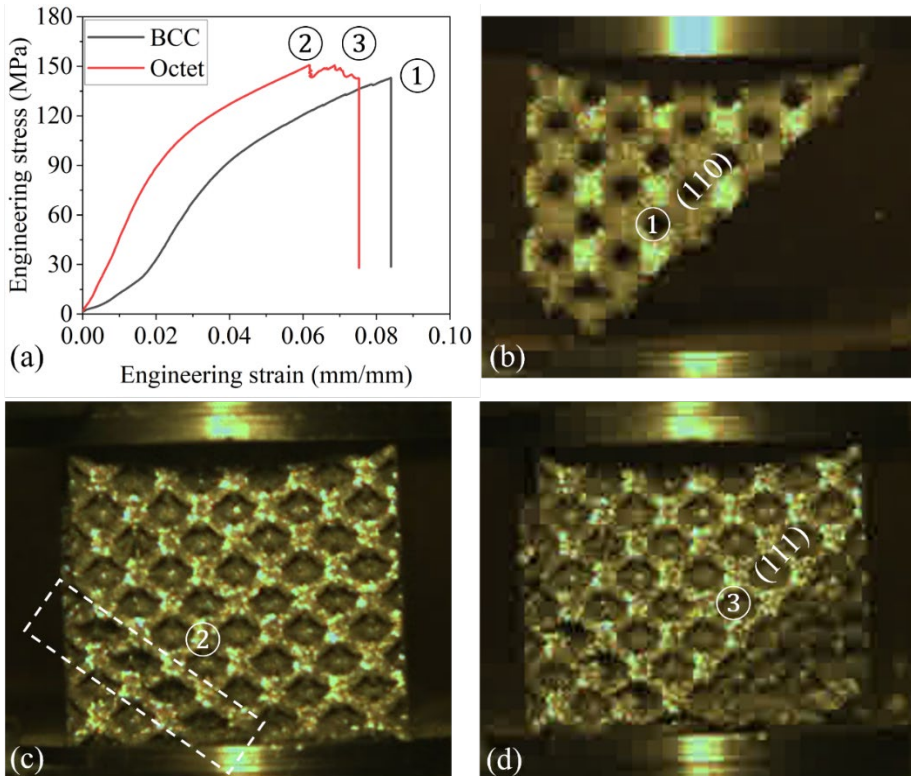


Figure 3.14 (a) Uniaxial fracture compression tests and high speed camera images of (b) BCC structure and (c) (d) octet structure.

3.5. Discussion

3.5.1. Initial transformation surface

For metamaterials with orthotropic symmetry, the multiaxial transformation criteria for forward transformation is described using the extended Hill's model [10]:

$$A(\sigma_{11} - \sigma_{22})^2 + B(\sigma_{22} - \sigma_{33})^2 + C(\sigma_{22} - \sigma_{33})^2 + D\sigma_{12}^2 + E\sigma_{23}^2 + F\sigma_{13}^2 + G\sigma_H^2 = 1, \quad (3.14)$$

where $A-G$ are anisotropy coefficients that are obtained by curve fitting under uniaxial, shear, and hydrostatic loading conditions. Because the environmental temperature is considered as the temperature loading, multiaxial stress is not directly normalized using uniaxial transformation stress. G is obtained under hydrostatic loading, $A=B=C$ is obtained under

uniaxial loading and $D=E=F$ are obtained under shear loading conditions. For the choice of $\bar{\rho} = 0.4$, $A-G$ are given explicitly:

For the BCC structure,

$$\begin{aligned} G &= \left(0.563(\bar{\rho})^{1.25} \sigma_s^{\text{fwd}} + 0.519(\bar{\rho})^{1.22} C_s^{\text{fwd}} (T - T_0) \right)^{-2} \\ A &= \frac{4}{9} \left(0.424(\bar{\rho})^{1.92} \sigma_s^{\text{fwd}} + 0.426(\bar{\rho})^{1.96} C_s^{\text{fwd}} (T - T_0) \right)^{-2} . \\ D &= \left(0.178(\bar{\rho})^{1.23} \sigma_s^{\text{fwd}} + 0.157(\bar{\rho})^{1.21} C_s^{\text{fwd}} (T - T_0) \right)^{-2} \end{aligned} \quad (3.15)$$

For the octet structure,

$$\begin{aligned} G &= \left(0.654(\bar{\rho})^{1.30} \sigma_s^{\text{fwd}} + 0.530(\bar{\rho})^{1.17} C_s^{\text{fwd}} (T - T_0) \right)^{-2} \\ A &= \frac{4}{9} \left(0.368(\bar{\rho})^{1.31} \sigma_s^{\text{fwd}} + 0.254(\bar{\rho})^{1.27} C_s^{\text{fwd}} (T - T_0) \right)^{-2} , \\ D &= \left(0.351(\bar{\rho})^{1.34} \sigma_s^{\text{fwd}} + 0.270(\bar{\rho})^{1.29} C_s^{\text{fwd}} (T - T_0) \right)^{-2} \end{aligned} \quad (3.16)$$

where T_0 is the reference temperature. For the BCC and octet structures with $\bar{\rho} = 0.4$, a multiaxial transformation criterion is shown in Figure 3.15. Projecting $(\sigma_{11}, \sigma_{12}, T)$ transformation surface onto (σ_{11}, T) plane, the anisotropic transformation surface reduces to the linear dependent relation between uniaxial stress and temperature. The transformation stress and linear dependence relation can be tailored by relative density and unit cell structure. The proposed rescaled density-properties graph and effective transformation behaviors provide a physical understanding of the design parameters of NiTi metamaterials.

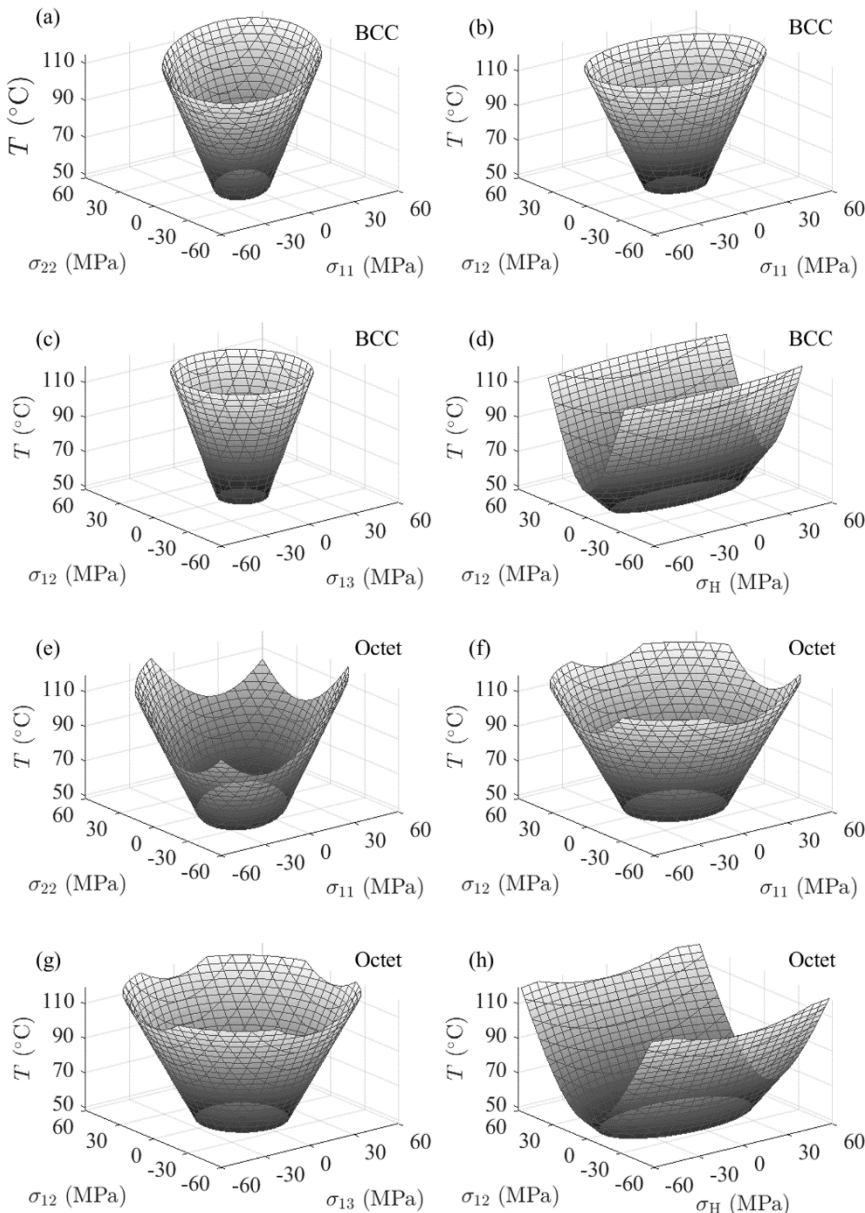


Figure 3.15 Anisotropic initial transformation surface in (a)(e) (σ_{11}, σ_{22}), (b)(f) (σ_{11}, σ_{12}), (c)(g) (σ_{12}, σ_{13}), (d)(h) (σ_{12}, σ_H) and T loading space of BCC and octet structures.

3.5.2. Recoverable energy absorption and deformation mechanism

The superelastic response of NiTi metamaterials is modeled and experimentally obtained. This superelastic stress hysteresis can be used for cyclic energy absorption. Energy dissipation is defined as the closed integration of the effective stress and strain curve and the specific energy dissipation is formulated as

$$\varphi = \frac{\Delta W}{\rho} = \frac{\oint \bar{\sigma} d\bar{\varepsilon}}{\rho}, \quad (3.17)$$

where ρ is the density of metamaterials and ΔW is the energy dissipation. Cyclic energy dissipation can be formulated as damping due to the nature of dissipative energy. For metallic damping cases, the loss factor η is defined from the uniaxial compression test as

$$\eta = \frac{\Phi}{2\pi}, \text{ with } \Phi = \frac{\Delta W}{W} = \frac{\oint \bar{\sigma} d\bar{\varepsilon}}{\int_0^{\varepsilon_{\max}} \bar{\sigma} d\bar{\varepsilon}}, \quad (3.18)$$

where Φ is the specific damping capacities and W is the storage energy [52].

Conventional metallic metamaterials exhibit energy absorption due to permanent plastic deformation [12,53]. NiTi metamaterials can provide stable nonlinear stiffness and recoverable energy dissipation under cyclic compressive loading as shown in Figure 3.13 (d), (e), and Figure 3.16. Damping in cellular material is amplitude-dependent, but mainly results from the irreversible process of microplastic deformation. Due to the strain concentration in truss-based metamaterials, microplastic strain occurs at the strut junctions before the effective stress reaches macroscopic yield stress [8,9]. This microplastic strain results in irreversible damage instead of a reversible stress hysteresis. In NiTi metamaterials, detwinning deformation is used to replace dislocation deformation to obtain damping. For metamaterials with high relative density, structures are interconnected by non-slender beams, and stable structure configuration under uniaxial compression is supported by strut intersection (without rotation and buckling of struts). Different from the nearly homogeneous transformation in NiTi bulk sample, martensitic transformation in NiTi metamaterials is inhomogeneous and induced by stress concentration at the nodes. Similar to the plastic deformation behavior of both structures, superelastic hinges first form at the nodes and are further connected by a progressive martensitic transformation zone along the struts. Progressive martensitic transformation contributes to the recoverable strain and energy dissipation.

Due to the large recoverable strain and energy dissipation in NiTi constitutive relation, the advantages of classic deformation modes need to be further discussed. One clear conclusion from theoretical results is that stretching-dominated deformation enables sufficient martensitic transformation and broader stress hysteresis. Bending-dominated

deformation enhances compliance of base NiTi but the superelastic deformation is constrained by the stress concentration and yield stress of base NiTi. Comparative numerical results between BCC and octet structures validate this basic conclusion for NiTi structure by illustrating larger energy dissipation in stretching-dominated octet structure. Future design research can choose the main deformation mode compatible with the hysteresis or compliant application of NiTi structure.

The experiments illustrate that BCC structures exhibit comparable energy dissipation and higher loss factor than octet structures, which is different from the prediction based on the numerical model. The indentation modulus of bulk, BCC, and octet samples are comparable as shown in Figure 3.12, which proves the effectiveness of using bulk samples in calibration.

3

The phenomenological model cannot capture the local variations in the TTs due to the inhomogeneous nature of the L-PBF process. Although the same process strategy and raw powder are used, different thermal history induced by path-by-path laser scanning in different structures results in the variation of Ni evaporation and microstructure in the deposition layer, as shown in Table 3.5 and Figure 3.9. Comparable Ni contents were found in both structures, while the BCC structure has a larger grain size than the octet structure. It is reported that TTs generally decrease with the increase in grain size [54]. Lower TTs in the BCC structure result in a larger portion of stress-induced martensite when the same $T = 54$ °C was used in compression tests, so a larger stress hysteresis area can be obtained in the BCC structure. From the view of the deformation mode, the octet structures exhibit higher energy dissipation capacity and damping capacity, but a higher loss factor was illustrated in the BCC structure. The influence of NiTi local microstructure surpasses the deformation modes, and thus further research should be conducted to control microstructure-sensitive thermomechanical properties of NiTi metamaterials. This chapter illustrates the importance of accounting for the effect of local microstructure variations on the thermomechanical properties of NiTi metamaterial, which is still to be further investigated.

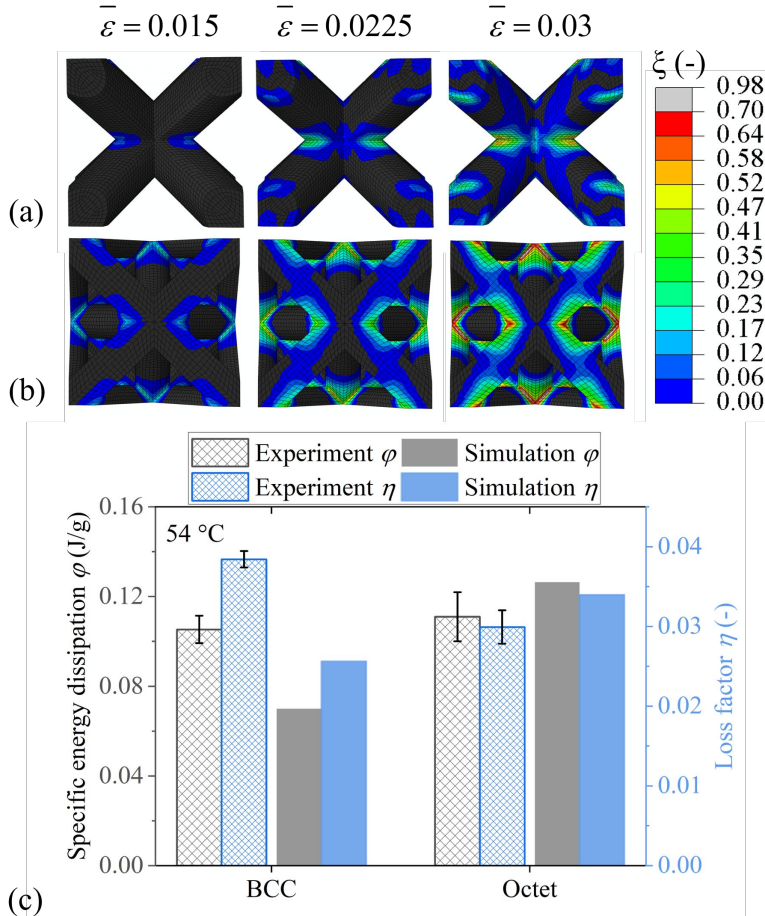


Figure 3.16 Progressive martensitic transformation in (a) the BCC and (b) the octet structures, and (c) specific energy dissipation and loss factor of BCC and octet NiTi structures.

3.6. Conclusions

In this chapter, Ni-rich NiTi BCC and octet structures with superelasticity and damping behavior are modeled and fabricated using L-PBF. Temperature-dependent superelasticity of NiTi BCC and octet structures are investigated using FEM and uniaxial compression testing. The following conclusions can be drawn:

- Effective transformation stress of NiTi BCC and octet structures was found to be dependent on relative density and temperature. The martensitic transformation surface for NiTi BCC

and octet structures was approximated using extended Hills criteria considering the temperature effect.

- NiTi BCC and octet structures, designed herein, were successfully fabricated by L-PBF and mechanically tested. High energy input (88.9 J/mm³) was used to mitigate macroscale cracking and warping. EDS results show a comparable Ni/Ti ratio between bulk, BCC, and octet samples. Coarse columnar grains were found to grow epitaxially in the bulk and at the nodes of the metamaterial.
- NiTi BCC and octet structures exhibit stabilized superelasticity with recoverable strain up to 2.8 %. The BCC structure shows fracture along (110), while the octet structure shows fracture along (111) surface under large deformation. The underlying reasons for the partial superelasticity in as-fabricated samples need further investigation.
- Stretching-dominated deformation enables sufficient martensitic transformation and broader stress hysteresis. Bending-dominated deformation enhances compliance of base NiTi but the superelastic deformation is constrained by the stress concentration and yield stress of base NiTi.
- NiTi BCC and octet structures exhibit reversible energy dissipation and damping due to progressive martensitic transformation. Under uniaxial compression loading, superelastic hinges form at the nodes and martensitic transformation gradually extends from the node along the struts. Different from theoretical prediction, BCC structure shows higher comparable energy dissipation and higher loss factor due to lower transformation temperatures. Further research will be conducted to control the superelastic response by tailoring the microstructure.

Appendix A Table of notation

Structural parameters	
$\bar{\rho}$	Relative density of mechanical metamaterial
ρ	Density of mechanical metamaterial
ρ_s	Density of solid NiTi
C_1	Structure-dependent constant
C_2	Structure-dependent constant
R	Radius of the beam
l	Length of the beam
L	Size (edge length) of a unit cell
Base NiTi model	
$F^t(\sigma, T)$	Drucker-Prager loading surface for forward transformation
σ_{dev}	Deviatoric part of the stress
C_s^{fwd}	Slopes of the stress-temperature base NiTi
T	External temperature
ε^{tr}	Transformation strain of NiTi
ΔS	Entropy variation NiTi
ξ_s	Martensitic volume fraction
E_A	Austenite Young's modulus of NiTi
ν_A	Austenite Poisson ratio of NiTi
E_M	Martensite Young's modulus of NiTi
ν_M	Martensite Poisson ratio of NiTi
σ_s^{fwd}	Martensite start stress of NiTi
Variables of superelastic metamaterials	
σ^{fwd}	Martensite start stress of NiTi lattice under uniaxial compression
k	Coefficient for Gibson-Ashby model
p	Coefficient for Gibson-Ashby model
u_i^j	Displacement component of surface nodes for periodic boundary conditions
c_i^j	Displacement component of dummy nodes

$\bar{\sigma}$	Effective stress of RVE
$\bar{\varepsilon}$	Effective strain of RVE
$\bar{\xi}$	Effective martensitic fraction of RVE
V	The volume of the RVE
φ	Specific energy dissipation
ΔW	Dissipated energy
W	Storage energy
η	Loss factor for damping
Φ	Specific damping

References

[1] X. Zhang, A. Vyatskikh, H. Gao, J.R. Greer, X. Li, Lightweight, flaw-tolerant, and ultrastrong nanoarchitected carbon, *Proc. Natl. Acad. Sci. U. S. A.* 116 (2019) 6665–6672. <https://doi.org/10.1073/pnas.1817309116>.

[2] J. Feng, B. Liu, Z. Lin, J. Fu, Isotropic octet-truss lattice structure design and anisotropy control strategies for implant application, *Mater. Des.* 203 (2021) 109595. <https://doi.org/10.1016/j.matdes.2021.109595>.

[3] T. Tancogne-Dejean, M. Diamantopoulou, M.B. Gorji, C. Bonatti, D. Mohr, 3D Plate-Lattices: An Emerging Class of Low-Density Metamaterial Exhibiting Optimal Isotropic Stiffness, *Adv. Mater.* 30 (2018) 1–6. <https://doi.org/10.1002/adma.201803334>.

[4] K. Karami, A. Blok, L. Weber, S.M. Ahmadi, R. Petrov, K. Nikolic, E. V. Borisov, S. Leeflang, C. Ayas, A.A. Zadpoor, M. Mehdipour, E. Reinton, V.A. Popovich, Continuous and pulsed selective laser melting of Ti6Al4V lattice structures: Effect of post-processing on microstructural anisotropy and fatigue behaviour, *Addit. Manuf.* 36 (2020) 101433. <https://doi.org/10.1016/j.addma.2020.101433>.

[5] L. Zhang, S. Feih, S. Daynes, S. Chang, M.Y. Wang, J. Wei, W.F. Lu, Energy absorption characteristics of metallic triply periodic minimal surface sheet structures under compressive loading, *Addit. Manuf.* 23 (2018) 505–515. <https://doi.org/10.1016/j.addma.2018.08.007>.

[6] T. Tancogne-Dejean, D. Mohr, Stiffness and specific energy absorption of additively-manufactured metallic BCC metamaterials composed of tapered beams, *Int. J. Mech. Sci.* 141 (2018) 101–116. <https://doi.org/10.1016/j.ijmecsci.2018.03.027>.

[7] A. du Plessis, S.M.J. Razavi, M. Benedetti, S. Murchio, M. Leary, M. Watson, D. Bhate, F. Berto, Properties and applications of additively manufactured metallic cellular materials: A review, *Prog. Mater. Sci.* 125 (2022) 100918. <https://doi.org/10.1016/j.pmatsci.2021.100918>.

[8] I.S. Golovin, H.R. Sinning, I.K. Arhipov, S.A. Golovin, M. Bram, Damping in some cellular metallic materials due to microplasticity, *Mater. Sci. Eng. A* 370 (2004) 531–536. <https://doi.org/10.1016/j.msea.2003.08.089>.

[9] I.S. Golovin, H.R. Sinning, J. Göken, W. Riehemann, Fatigue-related damping in some cellular metallic materials, *Mater. Sci. Eng. A* 370 (2004) 537–541. <https://doi.org/10.1016/j.msea.2003.08.090>.

[10] V.S. Deshpande, N.A. Fleck, M.F. Ashby, Effective properties of the octet-truss lattice material, *J. Mech. Phys. Solids* 49 (2001) 1747–1769. [https://doi.org/10.1016/S0022-5096\(01\)00010-2](https://doi.org/10.1016/S0022-5096(01)00010-2).

[11] L. Dong, V. Deshpande, H. Wadley, Mechanical response of Ti-6Al-4V octet-truss lattice structures, *Int. J. Solids Struct.* 60 (2015) 107–124. <https://doi.org/10.1016/j.ijsolstr.2015.02.020>.

[12] T. Tancogne-Dejean, A.B. Spierings, D. Mohr, Additively-manufactured metallic micro-lattice materials for high specific energy absorption under static and dynamic loading, *Acta Mater.* 116 (2016) 14–28. <https://doi.org/10.1016/j.actamat.2016.05.054>.

[13] N. Jin, F. Wang, Y. Wang, B. Zhang, H. Cheng, H. Zhang, Failure and energy absorption characteristics of four lattice structures under dynamic loading, *Mater. Des.* 169 (2019) 107655. <https://doi.org/10.1016/j.matdes.2019.107655>.

[14] M. Dallago, S. Raghavendra, V. Luchin, G. Zappini, D. Pasini, M. Benedetti, The role of node fillet, unit-cell size and strut orientation on the fatigue strength of Ti-6Al-4V lattice materials additively manufactured via laser powder bed fusion, *Int. J. Fatigue* 142 (2021) 105946. <https://doi.org/10.1016/j.ijfatigue.2020.105946>.

[15] D. Qi, H. Yu, M. Liu, H. Huang, S. Xu, Y. Xia, G. Qian, W. Wu, Mechanical behaviors of SLM additive manufactured octet-truss and truncated-octahedron lattice structures with uniform and taper beams, *Int. J. Mech. Sci.* 163 (2019) 105091. <https://doi.org/10.1016/j.ijmecsci.2019.105091>.

[16] L. Liu, P. Kamm, F. García-Moreno, J. Banhart, D. Pasini, Elastic and failure response of imperfect three-dimensional metallic lattices: the role of geometric defects induced by Selective Laser Melting, *J. Mech. Phys. Solids* 107 (2017) 160–184. <https://doi.org/10.1016/j.jmps.2017.07.003>.

[17] X. Li, C.C. Roth, T. Tancogne-Dejean, D. Mohr, Rate- and temperature-dependent plasticity of additively manufactured stainless steel 316L: Characterization, modeling and application to crushing of shell-lattices, *Int. J. Impact Eng.* 145 (2020) 103671. <https://doi.org/10.1016/j.ijimpeng.2020.103671>.

[18] Z. Xiong, M. Li, S. Hao, Y. Liu, L. Cui, H. Yang, C. Cui, D. Jiang, Y. Yang, H. Lei, Y. Zhang, Y. Ren, X. Zhang, J. Li, 3D-Printing Damage-Tolerant Architected Metallic Materials with Shape Recoverability via Special Deformation Design of Constituent Material, *ACS Appl. Mater. Interfaces* 13 (2021) 39915–39924. <https://doi.org/10.1021/acsami.1c11226>.

[19] W. Chen, D. Gu, J. Yang, Q. Yang, J. Chen, X. Shen, Compressive mechanical properties and shape memory effect of NiTi gradient lattice structures fabricated by laser powder bed fusion, *Int. J. Extrem. Manuf.* 4 (2022) 045002. <https://doi.org/10.1088/2631-7990/ac8ef3>.

[20] M.R. Karamooz Ravari, S. Nasr Esfahani, M. Taheri Andani, M. Kadkhodaei, A. Ghaei, H. Karaca, M. Elahinia, On the effects of geometry, defects, and material asymmetry on the mechanical response of shape memory alloy cellular lattice structures, *Smart Mater. Struct.* 25 (2016). <https://doi.org/10.1088/0964-1726/25/2/025008>.

[21] N. Van Viet, R. Abu Al-Rub, W. Zaki, Mechanical Behavior of Shape-Memory Alloy Triply Periodic Minimal Surface Foam Based on Schwarz Primitive, *J. Eng. Mech.* 148 (2022) 1–12. [https://doi.org/10.1061/\(asce\)em.1943-7889.0002130](https://doi.org/10.1061/(asce)em.1943-7889.0002130).

[22] W. Zaki, Z. Moumni, A three-dimensional model of the thermomechanical behavior of shape memory alloys, *J. Mech. Phys. Solids* 55 (2007) 2455–2490. <https://doi.org/10.1016/j.jmps.2007.03.012>.

[23] S. Saedi, N. Shayesteh Moghaddam, A. Amerinatanzi, M. Elahinia, H.E. Karaca, On the effects of selective laser melting process parameters on microstructure and thermomechanical response of Ni-rich NiTi, *Acta Mater.* 144 (2018) 552–560. <https://doi.org/10.1016/j.actamat.2017.10.072>.

[24] J.N. Zhu, E. Borisov, X. Liang, E. Farber, M.J.M. Hermans, V.A. Popovich, Predictive analytical modelling and experimental validation of processing maps in additive manufacturing of nitinol alloys, *Addit. Manuf.* 38 (2021) 101802. <https://doi.org/10.1016/j.addma.2020.101802>.

[25] L. Xue, K.C. Atli, S. Picak, C. Zhang, B. Zhang, A. Elwany, R. Arroyave, I. Karaman, Controlling martensitic transformation characteristics in defect-free NiTi shape memory alloys fabricated using laser powder bed fusion and a process optimization framework, *Acta Mater.* 215 (2021) 117017. <https://doi.org/10.1016/j.actamat.2021.117017>.

[26] L. Xue, K.C. Atli, C. Zhang, N. Hite, A. Srivastava, A.C. Leff, A.A. Wilson, D.J. Sharar, A. Elwany, R. Arroyave, I. Karaman, Laser Powder Bed Fusion of Defect-Free NiTi Shape Memory Alloy Parts with Superior Tensile Superelasticity, *Acta Mater.* 229 (2022) 117781. <https://doi.org/10.1016/j.actamat.2022.117781>.

[27] T. Gustmann, F. Gutmann, F. Wenz, P. Koch, R. Stelzer, W.G. Drossel, H. Korn, Properties of a superelastic NiTi shape memory alloy using laser powder bed fusion and adaptive scanning strategies, *Prog. Addit. Manuf.* 5 (2020) 11–18. <https://doi.org/10.1007/s40964-020-00118-6>.

[28] Z. Gorgin Karaji, M. Speirs, S. Dadbakhsh, J.P. Kruth, H. Weinans, A.A. Zadpoor, S.A. Yavari, Additively manufactured and surface biofunctionalized porous nitinol, *ACS Appl. Mater. Interfaces* 9 (2017) 1293–1304. <https://doi.org/10.1021/acsami.6b14026>.

[29] P. Jamshidi, C. Panwisawas, E. Langi, S.C. Cox, J. Feng, L. Zhao, M.M. Attallah, Development, characterisation, and modelling of processability of nitinol stents using laser powder bed fusion, *J. Alloys Compd.* 909 (2022) 164681. <https://doi.org/10.1016/j.jallcom.2022.164681>.

[30] C. Tan, J. Zou, S. Li, P. Jamshidi, A. Abena, A. Forsey, R.J. Moat, K. Essa, M. Wang, K. Zhou, M.M. Attallah, Additive manufacturing of bio-inspired multi-scale hierarchically strengthened lattice structures, *Int. J. Mach. Tools Manuf.* 167 (2021) 103764. <https://doi.org/10.1016/j.ijmachtools.2021.103764>.

[31] Z. Xiong, H. Li, H. Yang, Y. Yang, Y. Liu, L. Cui, X. Li, Micro laser powder bed fusion of NiTi alloys with superior mechanical property and shape recovery function, *Addit. Manuf.* 57 (2022) 102960. <https://doi.org/10.1016/j.addma.2022.102960>.

[32] X. Yang, Q. Yang, Y. Shi, L. Yang, S. Wu, C. Yan, Y. Shi, Effect of volume fraction and unit cell size on manufacturability and compressive behaviors of Ni-Ti triply periodic minimal surface lattices, *Addit. Manuf.* 54 (2022) 102737. <https://doi.org/10.1016/j.addma.2022.102737>.

[33] D.C. Lagoudas, Shape memory alloys: modeling and engineering applications, Springer, 2008.

[34] C. Cisse, W. Zaki, T. Ben Zineb, A review of constitutive models and modeling techniques for shape memory alloys, *Int. J. Plast.* 76 (2016) 244–284. <https://doi.org/10.1016/j.ijplas.2015.08.006>.

[35] C.M. Portela, J.R. Greer, D.M. Kochmann, Impact of node geometry on the effective stiffness of non-slender three-dimensional truss lattice architectures, *Extrem. Mech. Lett.* 22 (2018) 138–148. <https://doi.org/10.1016/j.eml.2018.06.004>.

[36] F. Auricchio, R.L. Taylor, J. Lubliner, Shape-memory alloys: macromodelling and numerical simulations of the superelastic behavior, *Comput. Methods Appl. Mech. Eng.* 146 (1997) 281–312. [https://doi.org/10.1016/S0045-7825\(96\)01232-7](https://doi.org/10.1016/S0045-7825(96)01232-7).

[37] S. Saedi, A.S. Turabi, M.T. Andani, C. Haberland, H. Karaca, M. Elahinia, The influence of heat treatment on the thermomechanical response of Ni-rich NiTi alloys manufactured by selective laser melting, *J. Alloys Compd.* 677 (2016) 204–210. <https://doi.org/10.1016/j.jallcom.2016.03.161>.

[38] P. Šittner, L. Heller, J. Pilch, C. Curfs, T. Alonso, D. Favier, Young's modulus of austenite and martensite phases in superelastic NiTi wires, *J. Mater. Eng. Perform.* 23 (2014) 2303–2314. <https://doi.org/10.1007/s11665-014-0976-x>.

[39] P. Šittner, M. Landa, P. Lukáš, V. Novák, R-phase transformation phenomena in thermomechanically loaded NiTi polycrystals, *Mech. Mater.* 38 (2006) 475–492. <https://doi.org/10.1016/j.mechmat.2005.05.025>.

[40] G. Machado, H. Louche, T. Alonso, D. Favier, Superalastic cellular NiTi tube-based materials: Fabrication, experiments and modeling, *Mater. Des.* 65 (2015) 212–220. <https://doi.org/10.1016/j.matdes.2014.09.007>.

[41] K. Ushijima, W.J. Cantwell, R.A.W. Mines, S. Tsopanos, M. Smith, An investigation into the compressive properties of stainless steel micro-lattice structures, *J. Sandw. Struct. Mater.* 13 (2011) 303–329. <https://doi.org/10.1177/1099636210380997>.

[42] D. Garoz, F.A. Gilabert, R.D.B. Sevenois, S.W.F. Spronk, W. Van Paepegem, Consistent application of periodic boundary conditions in implicit and explicit finite element simulations of damage in composites, *Compos. Part B Eng.* 168 (2019) 254–266. <https://doi.org/10.1016/j.compositesb.2018.12.023>.

[43] W. Wu, J. Owino, A. Al-Ostaz, L. Cai, Applying periodic boundary conditions in finite element analysis, in: SIMULIA Community Conf. Provid., 2014: pp. 707–719.

[44] E. Borisov, K. Starikov, A. Popovich, T. Tihonovskaya, Investigation of the possibility of tailoring the chemical composition of the NiTi alloy by selective laser melting, *Metals (Basel)* 11 (2021) 1–11. <https://doi.org/10.3390/met11091470>.

[45] M. Elahinia, N. Shayesteh Moghaddam, M. Taheri Andani, A. Amerinatanzi, B.A. Bimber, R.F. Hamilton, Fabrication of NiTi through additive manufacturing: A review, *Prog. Mater. Sci.* 83 (2016) 630–663. <https://doi.org/10.1016/j.pmatsci.2016.08.001>.

[46] X. Cao, Y. Jiang, T. Zhao, P. Wang, Y. Wang, Z. Chen, Y. Li, D. Xiao, D. Fang, Compression experiment and numerical evaluation on mechanical responses of the lattice structures with stochastic geometric defects originated from additive-manufacturing, *Compos. Part B Eng.* 194 (2020) 108030. <https://doi.org/10.1016/j.compositesb.2020.108030>.

[47] T. DebRoy, H.L. Wei, J.S. Zuback, T. Mukherjee, J.W. Elmer, J.O. Milewski, A.M. Beese, A. Wilson-Heid, A. De, W. Zhang, Additive manufacturing of metallic components – Process, structure and properties, *Prog. Mater. Sci.* 92 (2018) 112–224. <https://doi.org/10.1016/j.pmatsci.2017.10.001>.

[48] S.K. S, I.A. Kumar, L. Marandi, I. Sen, Assessment of small-scale deformation characteristics and stress-strain behavior of NiTi based shape memory alloy using nanoindentation, *Acta Mater.* 201 (2020) 303–315. <https://doi.org/10.1016/j.actamat.2020.09.080>.

[49] W.C. Oliver, G.M. Pharr, Measurement of hardness and elastic modulus by instrumented indentation: Advances in understanding and refinements to methodology, *J. Mater. Res.* 19 (2004) 3–20. <https://doi.org/10.1557/jmr.2004.19.1.3>.

[50] Y. Zhang, Y.T. Cheng, D.S. Grummon, Finite element modeling of indentation-induced superelastic effect using a three-dimensional constitutive model for shape memory materials with plasticity, *J. Appl. Phys.* 101 (2007). <https://doi.org/10.1063/1.2436928>.

[51] J. Zhang, R.J. Perez, E.J. Lavernia, Documentation of damping capacity of metallic, ceramic and metal-matrix composite materials, *J. Mater. Sci.* 28 (1993) 2395–2404. <https://doi.org/10.1007/BF01151671>.

[52] J. Zhang, H. Huang, G. Liu, H. Zong, C. Zhang, Stiffness and energy absorption of additive manufactured hybrid lattice structures, *Virtual Phys. Prototyp.* 16 (2021) 428–443. <https://doi.org/10.1080/17452759.2021.1954405>.

[53] J.P. Oliveira, R.M. Miranda, F.M. Braz Fernandes, Welding and Joining of NiTi Shape Memory Alloys: A Review, *Prog. Mater. Sci.* 88 (2017) 412–466. <https://doi.org/10.1016/j.pmatsci.2017.04.008>.

4

Inhomogeneity in NiTi metamaterials

Chapter 3 identified two challenges in achieving superelastic NiTi metamaterials: partial superelasticity and premature fracture. This chapter focuses on partial superelasticity in as-fabricated Ni-rich NiTi metamaterials. To address this, the common assumption of homogeneity in modeling and additive manufacturing is examined, as geometric-dependent melt pool behavior results in significant microstructural and thermomechanical inhomogeneities. Numerical and experimental results demonstrate that mesoscale property inhomogeneity is one cause of pseudo-linear response and partial superelasticity observed in the fabricated NiTi body-centered cubic (BCC) metamaterials. Using a phenomenological constitutive relation the macroscopic response of NiTi metamaterials with varying relative densities was simulated using a multi-cell model. Samples with relative densities of 0.1, 0.4, and 0.6 were then additively manufactured for single-variable experiments. These fabricated samples showed distinct microstructural textures and compositions that affected their local recoverability. Edge effects and laser turn regions were identified as the causes underlying the observed microstructural inhomogeneity. This chapter provides valuable information on achieving rigorous experimental/computational consistency in future work.

4

This chapter is based on the scientific publication: Z. Yan, J.N. Zhu, D. Hartl, T. Riemsdag, S.P. Scott, R. Petrov, M. Hermans, J. Jovanova, V. Popovich, Correlation between microstructural inhomogeneity and architectural design in additively manufactured NiTi shape memory alloys, *Virtual Phys. Prototyp.* 19 (2024) 1–20. <https://doi.org/10.1080/17452759.2024.2396065>.

4

4.1. Introduction

The specific architectures and dimensions of the unit cell can significantly influence the as-fabricated microstructure and compositional distribution, due to interactions between the powder, melt pool, and fabricated geometry of the metamaterials [1,2]. This inhomogeneous microstructure can result in inconsistent thermomechanical properties of the NiTi, which causes the performance of NiTi metamaterials to deviate from the intended designs and properties-relative density relation [3]. Thus, a deeper understanding of the impact of geometric factors of additively manufactured NiTi metamaterials on the melt pool, solidification microstructure, and macroscopic mechanical responses is crucial for developing a reliable design methodology and manufacturing.

In the laser-based AM of bulk samples, the melt pool and microstructure can be controlled by adjusting various process parameters, with a dominant heat dissipation occurring along the building direction (BD). Numerous experiments have demonstrated that superior shape memory effects and superelasticity can be achieved by parameter optimization when the melt pool is minimally influenced by geometrical edges [4–8]. For instance, Xue et al. [9] fabricated a textured Ni-rich NiTi sample exhibiting a tensile superelasticity of 6%. Zhu et al. [10] achieved unprecedented superelasticity in a Ni-lean Ni (49.4 at.%)–Ti in the $\langle 001 \rangle$ textured additively manufactured NiTi. Safdel et al. [7] illustrated the tensile-compression asymmetry of additively manufactured NiTi bulk samples with a $\langle 001 \rangle$ texture and proposed optimal process parameters to minimize the asymmetry.

In laser powder bed fusion (L-PBF) of metallic metamaterials, the process optimization strategy aims to achieve geometric features [11–13]. However, the L-PBF process often results in inhomogeneous microstructures and varied local mechanical properties due to different heat dissipation from the melt pool to the fabricated materials. Several studies have reported the influence of macroscopic dimensions and unit cell architecture on the microstructure of base materials, focusing primarily on elastoplastic metals such as stainless steel [14,15], Al-based [2,16], Ni-based [17], and Ti-based [18,19] alloys. Johnson et al. reported the elastic stiffness of struts varies from 44 ± 4 MPa to 89 ± 38 MPa using high-energy X-ray diffraction [20]. Despite this variation in material properties, elastoplasticity constitutive relations, such as J2 plasticity and Johnson-Cook plasticity are reasonably accurate in the design and model, as elastoplastic behaviors are generally validated across local microstructures. However, this assumption of homogeneity needs further examination for additively manufactured NiTi metamaterials, given that the martensitic transformation and re-orientation are highly sensitive to compositional distribution, texture, and precipitates [21–25].

In the modeling of NiTi and other shape memory alloys (SMA) with martensitic transformation, the constitutive models have been significantly developed for conventionally manufactured SMAs [26–28]. These models enable the design and manufacturing of SMA devices with reasonably accurate simulations. [27,29–31]. When using the constitutive model in structural analysis, a common calibration approach is based on a one-dimensional reduction of the constitutive model and uniaxial loading tests conducted on wire or bulk samples, often assuming homogeneous and consistent properties across tested samples and other fabricated samples [13,32,33]. In our previous research, we found that the effective transformation stress of metamaterials is a function of relative density based on this assumption [34]. However, narrow stress hysteresis and partial superplasticity were observed in experiments, as widely reported in the literature [34–37]. These experimental findings suggest that the inhomogeneity of base NiTi in additive manufacturing of metamaterials needs re-examination.

4

To address this issue in the L-PBF of NiTi metamaterials, it is crucial to investigate the formation of microstructure inhomogeneities [38]. A recent study reported by Jiang et al. [39] illustrated a significant size effect on the microstructure and decrease of martensitic transformation temperatures of thin-wall samples. A different hatching distance was used in this study for the manufacturing of different thin wall samples. Dadbakhsh et al. [40] achieved improved superelastic behavior by using a combination of high laser power and high scanning speed but the inhomogeneous properties were not fully discussed. For L-PBF of NiTi metamaterials using the same process parameters, the key factor is the geometrically dependent interaction between the melt pool, powder bed, and as-fabricated strut of metamaterials. Martin et al. [41] revealed that overheating at laser turn regions leads to increased evaporation of alloying elements due to the changes in scanning speed. Numerous studies, building on the classical Rosenthal solution, have investigated heat transfer in both single-track and bulk manufacturing [42–45]. Given the potential edge effects of struts, it is necessary to analyze the relative measure of the melt pool and geometric dimension, and its correlation to the thermal field during L-PBF of truss-based metamaterials.

In this chapter, a potential cause for the pseudo-linear response and partial superelasticity observed in NiTi metamaterials is explained. The influence of geometric relative density on the inhomogeneous microstructure and the spatial variation in thermomechanical properties are analyzed, in NiTi metamaterials with a body-centered cubic (BCC) structure and relative densities of 0.1, 0.4, and 0.6. The thermal model with dimensional analysis was conducted to explain the edge effect and transition from strut-based to bulk-based printing mode. The mechanical model with unified constitutive law was developed to predict the impact of inhomogeneous transformation temperatures on the macroscopic response of fabricated NiTi BCC metamaterials.

4.2. Geometry and computational models

4.2.1. Conduction-based thermal modeling of melt pool during L-PBF processes

BCC structures with nominal relative densities of 0.02 (extreme condition), 0.05, 0.1, 0.2, 0.3, 0.4, 0.5, and 0.6 were chosen to understand the geometric effect on heat transfer during the L-PBF process. The unit strut, each with respective diameters of 0.24, 0.40, 0.60, 0.84, 1.08, 1.30, 1.50, and 1.70 mm, was calculated using a second-order approximation equation of relative density $\bar{\rho}$ [46],

$$\bar{\rho} = 3\sqrt{3}\pi\left(\frac{R}{l}\right)^2 - 18\sqrt{2}\pi\left(\frac{R}{l}\right)^3, \quad (4.1)$$

where R and l are the radius and length of the beam. The geometrical parameters used in the geometrical and computational models are shown in Figure 4.1.

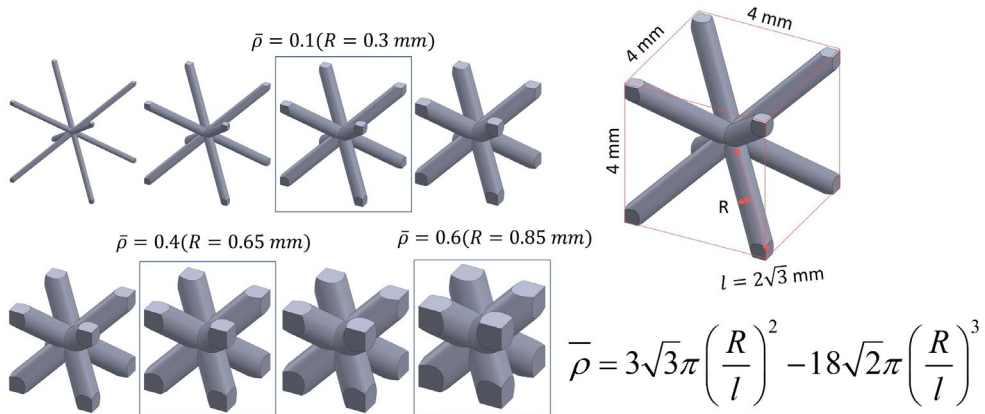


Figure 4.1 Second-order approximation equation of relative density in the structural design [46].

To understand the geometric effect on the melt pool during L-PBF processes, finite element simulations are carried out using the commercial framework Abaqus/Standard 2019. The multiscale problem in space, between the size of the melt pool and the structure, can lead to a trade-off between solution accuracy and computational time. For this consideration, heat transfer in the beam is modeled using the heat conduction equation [47]:

$$\rho_s(T)c_p(T)\frac{\partial T}{\partial t} = \nabla \cdot (k(T)\nabla T), \quad (4.2)$$

where T is the temperature, ρ_s , c_p and k are the temperature-dependent density, the constant pressure specific heat, and conductivity, respectively. The laser beam is modeled using a simple ellipsoid model derived from the double ellipsoid model by Goldak [48]:

$$Q = \frac{2\eta P}{c_1 c_2 c_3 \pi \sqrt{\pi}} \exp \left[- \left(\frac{x_1^2}{c_1^2} + \frac{(x_2 + vt)^2}{c_2^2} + \frac{x_3^2}{c_3^2} \right) \right], \quad (4.3)$$

where Q is the heat flux density of the laser beam, η is the absorptivity of the material, P is laser power, c_1 , c_2 , and c_3 are the ellipsoid semi-axis respectively and v is the scanning speed. The laser penetration c_3 is 130 μm and η is 0.50 based on validation experiments.

The adiabatic boundary condition is applied on the edge of the strut due to the weak heat conduction from the as-fabricated structure to the powder [49–51]. The temperature-dependent thermal properties ρ_s , c_p , and k are provided in Figure 4.2. The temperature-dependent thermal properties used in the thermal model were taken from the literature for conventionally manufactured NiTi [52] or calculated by using Thermo-Calc software (Version 2020a, Thermo-Calc, Stockholm, Sweden) based on TCHEA2 (High Entropy Alloys version 2.1) database in our early study [10,53,54]. The material states (powder and solid) are considered using solution-dependent variables in the UMATHT subroutine [47,55]. More discussion on the thermal properties used in the thermal model is provided in the supplementary documents. Melt pool convection is defined using enhanced thermal conductivity, set to 5 in this work [47]. Heat dissipation due to radiation and convection are considered, using a combined heat transfer coefficient of 20 $\text{W/m}^2 \text{K}$ [48].

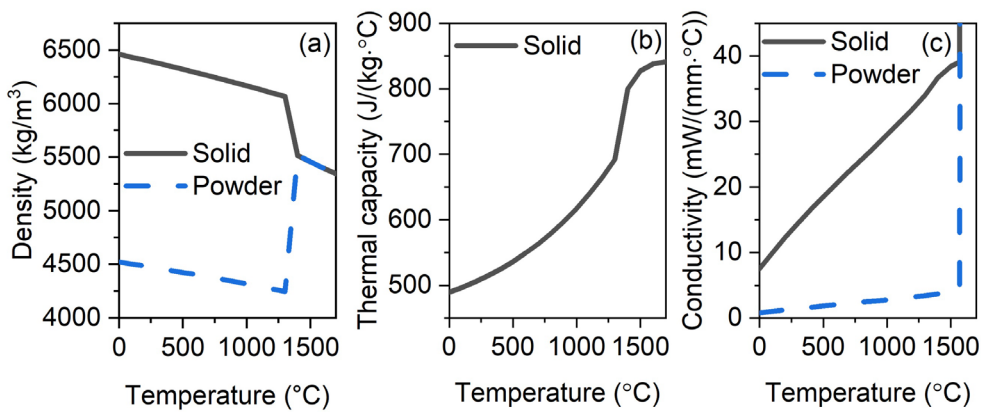


Figure 4.2 Thermal properties of NiTi used in the thermal model: (a) Density, (b) thermal capacity, and (c) conductivity.

The heat accumulation induced by as-fabricated deposition is treated as residual temperature. It has been reported that residual temperature reaches a steady condition after a few layers of material are deposited, thus residual temperature is modeled using an analytical equation to expedite the computation [56,57]. The initial conditions are set to the residual temperature after the deposition of 50 layers, as given by

$$T_{\text{res}}(r, N_A) = T_{\text{in}} + \frac{1}{\rho_s c_p \sqrt{4\pi \kappa}} \cdot \sum_{N=1}^{N_A} \frac{Q_{1D}}{\sqrt{(N/f)^{n_D}}} \cdot \exp\left(-\frac{f}{N} \cdot \frac{(r-Nd)^2}{4\kappa}\right), \quad (4.4)$$

where T_{res} is the residual temperature, T_{in} is the initial temperature before processing, Q_{1D} is the one-dimensional heat source, N_A is the number of energy inputs, f is the frequency of repetitive energy input, κ is the thermal diffusivity, $r-Nd$ is the conversion of coordinates for the moving heat source. The constant material properties for this linearized equation such as density, heat capacity, and thermal diffusivity are chosen at a temperature close to the melting point [50].

The strut and validation models are discretized using 3D 8-node linear elements (DC3D8R). The powder layer is meshed with an approximate size of $20 \mu\text{m} \times 20 \mu\text{m} \times 10 \mu\text{m}$, while the deposition layer is gradually meshed from $20 \mu\text{m} \times 20 \mu\text{m} \times 10 \mu\text{m}$ to $20 \mu\text{m} \times 20 \mu\text{m} \times 60 \mu\text{m}$. The mesh size is determined to balance mesh convergence, the geometric accuracy of the melt pool, and computational time. After obtaining the numerical results, they were converted to the .vtk (Visualization Toolkit) format and further post-processed using the open-source framework Paraview.

4.2.2. Mechanical models

Mechanical models of uniaxial compression on full samples are developed to understand the influence of inhomogeneous thermomechanical properties on the macroscopic response of the NiTi BCC metamaterials using the commercial framework Abaqus/Standard 2019. Here, the constitutive model of the thermomechanical behavior of NiTi is recalled [28,30,58]. The total infinitesimal strain is the sum of elastic, thermal, and transformation strain:

$$\boldsymbol{\varepsilon} = \mathbf{S}(\xi_s) \boldsymbol{\sigma} + \boldsymbol{\alpha}(T - T_0) + \boldsymbol{\varepsilon}^{\text{tr}}, \quad (4.5)$$

where $\boldsymbol{\alpha}$ is the thermal expansion tensor, T_0 is a reference temperature, and $\mathbf{S}(\xi)$ is the compliance tensor calculated based on the martensite volume fraction ξ_s using the rule of mixtures. The evolution equation of transformation strain $\boldsymbol{\varepsilon}^{\text{tr}}$ is given by a function of the rate of martensitic volume fraction $\dot{\xi}_s$ and the transformation direction tensor $\mathbf{A}^{\text{tr}}(\boldsymbol{\sigma})$:

$$\dot{\boldsymbol{\varepsilon}}^{\text{tr}} = \dot{\xi}_s \mathbf{A}^{\text{tr}}(\boldsymbol{\sigma}) \cdot \quad (4.6)$$

For forward and reverse transformation, the transformation direction tensor is defined as follows:

$$A^{\text{tr}}(\sigma) = \begin{cases} A_{\text{fwd}}^{\text{tr}} = \frac{3}{2} H^{\text{cur}}(\bar{\sigma}) \frac{\sigma'}{\bar{\sigma}} & \text{if } \dot{\xi}_s > 0 \\ A_{\text{rev}}^{\text{tr}} = \frac{\epsilon^{\text{tr-r}}}{\xi^r} & \text{if } \dot{\xi}_s < 0 \end{cases}, \quad (4.7)$$

where $\bar{\sigma}_{\text{Mises}}$ is the equivalent stress expressed from von Mises plasticity as $\sigma_{\text{Mises}} = \sqrt{(3/2)\sigma' : \sigma'}$, and σ' denotes the deviatoric part of Cauchy stress. $\epsilon^{\text{tr-r}}$ and ξ^r are the transformation strain tensor and martensite volume fraction at the reversal of the most recent forward transformation. The magnitude of the full transformation $H^{\text{cur}}(\bar{\sigma})$ is using a decaying exponential function once the equivalent stress exceeds a critical value σ_{crit} :

$$H^{\text{cur}}(\bar{\sigma}) = \begin{cases} H_{\text{min}} & \text{if } \bar{\sigma} \leq \bar{\sigma}_{\text{crit}} \\ H_{\text{min}} + (H_{\text{sat}} - H_{\text{min}}) \left(1 - \exp(-k_{\text{tr}}(\bar{\sigma} - \bar{\sigma}_{\text{crit}}))\right) & \text{if } \bar{\sigma} > \bar{\sigma}_{\text{crit}} \end{cases}. \quad (4.8)$$

4

The transformation function is determined for forward and reverse transformation as

$$\dot{\xi}_s \Phi^{\text{tr}} = 0, \quad \text{with } \Phi^{\text{tr}} = \begin{cases} \Phi_{\text{fwd}}^{\text{tr}} = \pi^{\text{tr}} - Y & \text{if } \dot{\xi}_s > 0 \\ \Phi_{\text{rev}}^{\text{tr}} = -\pi^{\text{tr}} - Y & \text{if } \dot{\xi}_s < 0 \end{cases}, \quad (4.9)$$

where Y is the critical thermodynamic driving force. The thermodynamic driving force for transformation π^{tr} , work conjugate to ξ , is given as

$$\pi^{\text{tr}} = \sigma : A^{\text{tr}} + \frac{1}{2} \sigma : \Delta S \sigma + \rho_s \Delta s_0 T - \rho_s \Delta u_0 - f^{\text{tr}}(\xi_s), \quad (4.10)$$

where the operator Δ denotes the difference in material constant between martensite and austenite (e.g., $\Delta S = S_M - S_A$, and s_0 and u_0 are the specific entropy and specific internal energy at the reference state. In practice, Δs_0 and Δu_0 are defined as model parameters. Finally, $f^{\text{tr}}(\xi)$ is the transformation hardening function, which is described as follows:

$$f^{\text{tr}}(\xi_s) = \begin{cases} f_{\text{fwd}}^{\text{tr}}(\xi_s) = \frac{1}{2} a_1 \left(1 + \xi_s^{n_1} - (1 - \xi_s)^{n_2}\right) + a_3 & \text{if } \dot{\xi}_s > 0 \\ f_{\text{rev}}^{\text{tr}}(\xi_s) = \frac{1}{2} a_2 \left(1 + \xi_s^{n_3} - (1 - \xi_s)^{n_4}\right) - a_3 & \text{if } \dot{\xi}_s < 0 \end{cases}, \quad (4.11)$$

where parameters a_1 , a_2 and a_3 are computed from material properties and exponents n_1 , n_2 , n_3 and n_4 are real numbers in the interval $(0,1]$ that govern the “smoothness” of the transformation curves. The material model above is implemented using the UMAT subroutine with a return mapping algorithm [28]. The calibration of thermomechanical

properties of NiTi with homogeneity assumption is shown in Figure 4.3, Table 4.2 and Chapter 3 [34].

The $5 \times 5 \times 5$ unit cell samples with a unit cell size of 4 mm were investigated in numerical models and experiments. The BCC metamaterials are subjected to uniaxial compression between two rigid planes with a frictional coefficient of 0.2. Due to the changes in thermomechanical properties, both the superelasticity and one-way shape memory effect are considered in simulations. The functional response is modeled using displacement loading applied to a rigid plane with the same maximum displacement used in uniaxial compression tests. The geometry is discretized using linear solid element C3D8R with a seed size smaller than 0.25 mm after convergence analysis. The reaction force and displacement of the upper rigid plane are used to compute the engineering stress and strain of the full-tessellated simulations along the loading direction.

4.3. Experiments

4.3.1. Materials and additive manufacturing

BCC structures of $5 \times 5 \times 5$ cells and cylindrical bulk samples were manufactured by L-PBF using an Aconity3D Midi machine equipped with a fiber ytterbium laser (1060 nm wavelength). All samples were manufactured using a laser power of 400 W, a scanning speed of 1250 mm/s, a hatching space of 120 μm , and a powder thickness of 30 μm . The scanning strategy employed was the stripe scanning strategy, with a rotation of 67.5° between layers. High-purity Argon gas was used as an inert gas to prevent oxidation during the manufacturing process. The feedstock used for the powder bed was commercial $\text{Ni}_{51.4}\text{Ti}_{48.6}$ powder, which had a spherical shape and D-values of 23 μm (D_{10}), 40 μm (D_{50}), and 67 μm (D_{90}). This powder was fabricated through gas atomization. Cylindrical bulk samples with a diameter of 13 mm and a height of 20 mm, and BCC structures with nominal relative densities of 0.1, 0.4, and 0.6 were manufactured for microstructural characterization and mechanical tests. The relative density of the manufactured samples is selected based on the relative dimensions between the strut size (refer to Table 4.1) and the melt pool.

4.3.2. Microstructural characterization

Cross-sectional samples were obtained by cutting along the macroscopic (110) plane // BD, as shown in Figure 4.4(a), using Electrical Discharge Machining (EDM). All samples were then ground and mechanically polished using a solution consisting of 70 ml OPS and 30 ml H_2O_2 . To recover any polished-induced residual martensite, the polished samples were heated using hot water at a temperature up to 100°C, followed by cooling to room temperature.

The images used for thermal model validation and measurement of the laser return region were characterized using scanning electron microscopy (SEM, JSM-IT100). The length of the laser return region was determined by the change of the surface morphology at the laser return region. Texture analysis was conducted using a scanning electron microscopy (SEM, Helios G4) equipped with an electron backscatter diffraction (EBSD) detector with a step size of 2 μm . Grains were characterized using OIM analysis, where grains were considered as ellipses, partitioned with a tolerance angle of 5°. Only grains with more than 30 pixels were considered in the calculation, and those at the edges were excluded from the analysis. Two repetitions of EBSD were performed on each sample for statistical significance. The Phase analysis was carried out using X-ray diffraction (XRD), using a Bruker D8 Advance diffractometer (Cu Ka radiation) with a step size of 0.043° and a counting time of 4 s per step. For measuring the transformation temperatures, Differential scanning calorimetry (DSC, TA Instruments DSC250) was employed at a heating/cooling rate of 10 °C/min over a temperature range of −70 to +150 °C.

4

Table 4.1 Geometrical parameters of bulk and BCC architectured samples.

Sample	Nominal relative density (-)	Unit cell size (mm)	Nominal strut diameter (mm)	As-fabricated strut diameter (mm)
BCC 0.1	0.1	4	0.6	0.68±0.04
BCC 0.4	0.4	4	1.3	1.28±0.27
BCC 0.6	0.6	4	1.7	1.69±0.18

4.3.3. Mechanical testing

The thermomechanical properties used in the phenomenological constitutive model of NiTi were calibrated based on the uniaxial compression tests of bulk samples, assuming a homogeneous microstructure and compositional distribution. Cylindrical bulk samples, measuring 13 mm in diameter and 20 mm in height, were manufactured using consistent process parameters. Cuboid samples with a size of 4 mm×4 mm×8 mm were produced using EDM for quasi-static compression tests along the [100] crystallographic orientation. Cyclic compression tests, comprising 30 cycles, were conducted at 54°C until the superelastic response stabilized. The Young's modulus for austenite and martensite E_A , E_M , and maximum transformation strain H_{\max} were measured during the 10th cycle when the residual strain remained below 0.038%. The Clausius-Clapeyron coefficients C^A and C^M were assumed to be identical for both forward and reverse transformations. Quasi-static compression tests were subsequently conducted on the same sample after training at

temperatures of 44, 54, 64, 74, and 84 °C (Figure 4.3 (a)). The martensitic starting stresses were determined using the tangent line method, and C^A and C^M were calculated by linearly fitting the temperature-start stress data for the forward martensitic transformation. Constants n_1 , n_2 , n_3 , and n_4 , which capture the smooth hardening formulation during transformation, were determined by fitting the numerical results of the uniaxial compression model to the experimental responses (Figure 4.3(b) and Table 4.2).

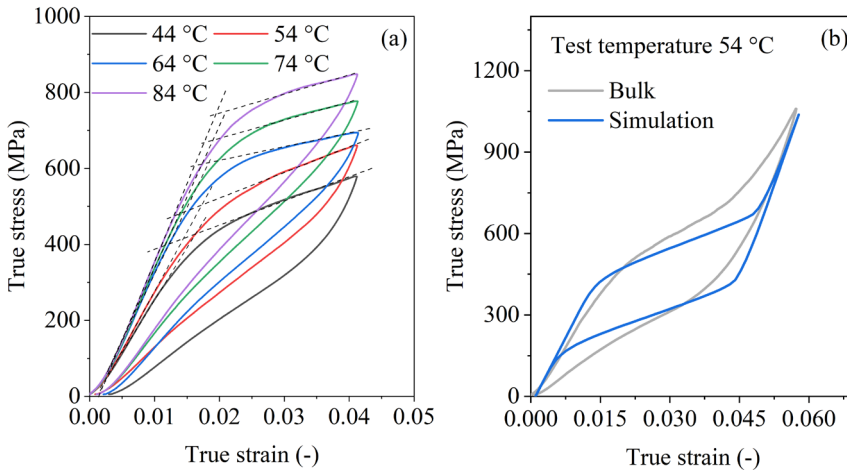


Figure 4.3 (a) Calibration of Clausius Clapeyron relation based on uniaxial compression on the bulk sample and (b) Calibration of uniaxial compression curves.

Table 4.2 Thermo-mechanical properties used in the mechanical model.

E_A (MPa)	E_M (MPa)	n_A	ν_M	α (K^{-1})
32600	48307	0.33	0.33	0
H_{\min}	H_{sat}	k_{tr}	$\bar{\sigma}_{\text{crit}}$ (MPa)	
0.037	0.037	N/A	N/A	
C_s^{fwd} (MPa K^{-1})	C_s^{fwd} (MPa K^{-1})	M_s (K)	M_f (K)	A_s (K)
8.2	8.2	Table 4.3	Table 4.3	Table 4.3
n_1	n_2	n_3	n_4	
0.17	0.9	0.25	0.75	

The cyclic compressive tests on NiTi BCC metamaterials were conducted using universal mechanical tests (Zwick Z100) with a heating chamber at a constant temperature

of 54 °C. Displacement and engineering strain of metamaterials were measured using a contact extensometer. Cyclic compression tests contain 10 cycles, corresponding to the number of stabilized cycle used in calibration experiments. Displacement-controlled loading was applied, with a maximum displacement of 0.8 mm for the BCC 0.1 sample and 0.7 mm for the BCC 0.4 and 0.6 samples, at a strain rate of $5 \times 10^{-4} \text{ s}^{-1}$.

To evaluate the local mechanical response, instrumented indentation was conducted using a Zwick ZHU2.5 at room temperature. A spherical ball indenter with a diameter of 0.5 mm was used to avoid plastic deformation. The indentation was controlled to produce a constant increment of 0.1 N/s until reaching the maximum force of 20 N. The hold time at the maximum force was set at 10 s.

In summarizing the methodology, three coordinate systems are used in this chapter, as depicted in Figure 4.4 (b). The first coordinate system is the cylindrical coordinate system used for the strut at the mesoscale, specifically referring to the axial direction (AD) of the strut. The second one is the Cartesian coordinate system employed in L-PBF, corresponding to the building direction (BD), scanning direction (SD), and hatching direction (HD) of the laser head. The Cartesian coordinate system x_1 , x_2 and x_3 is used in the numerical model. The last coordinate system is the Cartesian coordinate system utilized in texture analysis at the microscale, referencing Miller indices in crystallography.

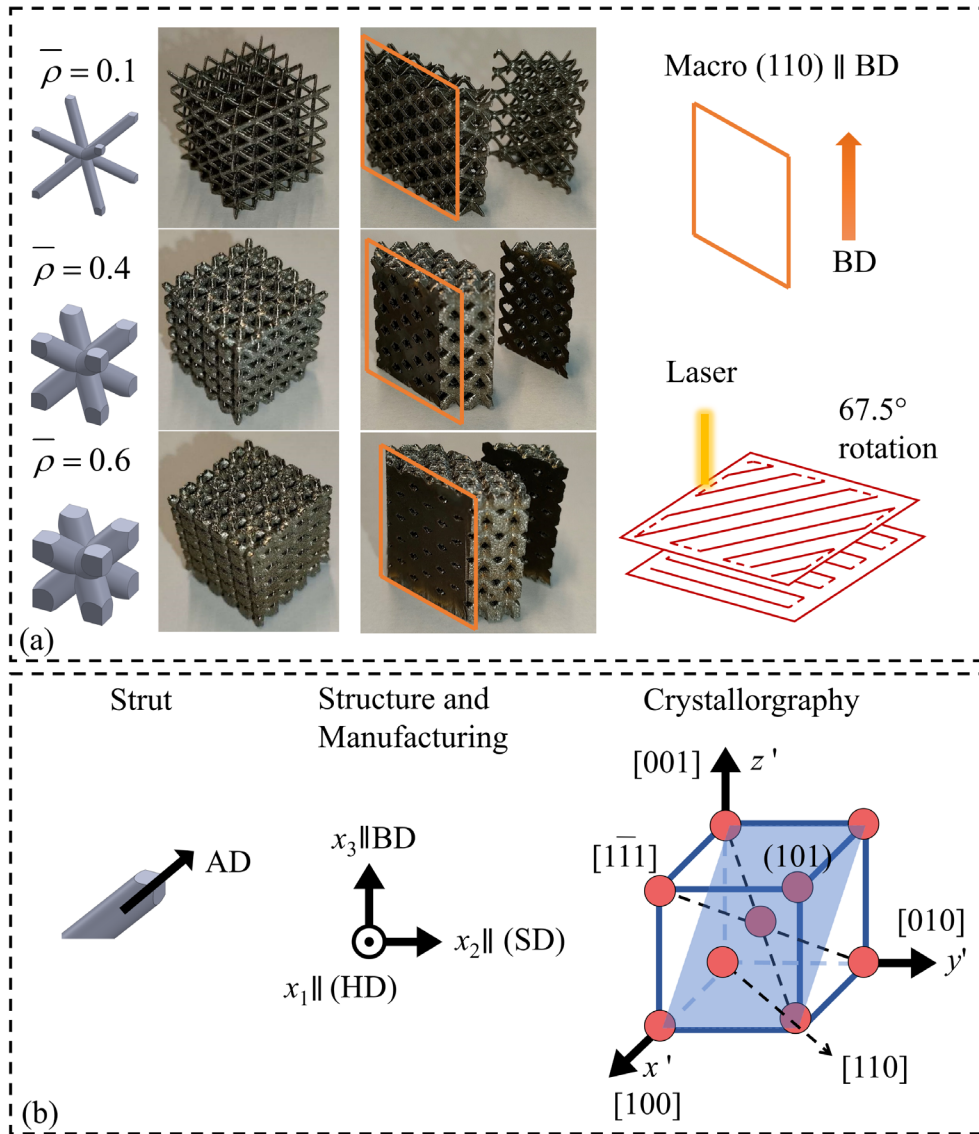


Figure 4.4 (a) Schematic diagram of macroscopic (110) cutting plane of as-fabricated samples (b) coordinate systems used in the current chapter.

4.4. Results

4.4.1. Melt pool profiles

The melt pool profiles for the parameters used in the current chapter are shown in Figure 4.5 and Figure 4.6. The melt pool depth ($155\pm10\ \mu\text{m}$) surpasses multiple layer thickness (30 μm), resulting in remelting and re-solidification of as-fabricated material (Figure 4.5 (b) and Figure 4.6). To ensure the accuracy of the heat source and UMATHT subroutine, the validation of the thermal model is performed using the geometrical dimensions of the melt pool. As illustrated in Figure 4.5 (b) and (c), the melt pool profile is consistent with the prediction of the simulation. The predicted width of the melt pool is closely validated by the experimental results. The simulated depth of the melt pool is 141 μm , 9% smaller than the average value in experiments (Figure 4.5 (a)).

4

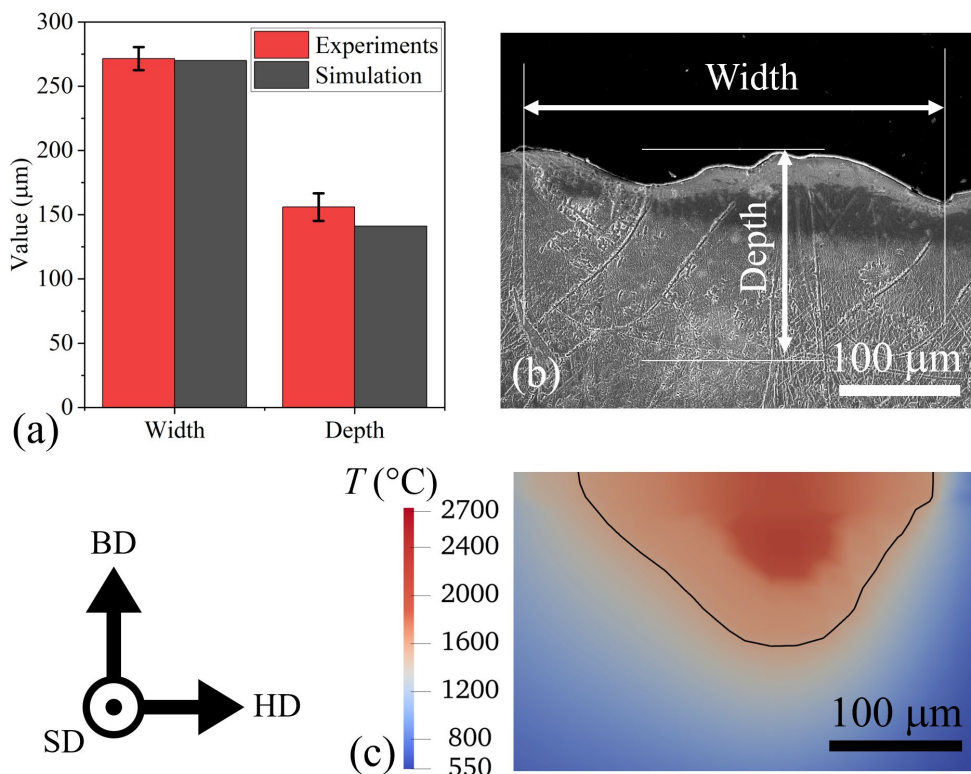


Figure 4.5 (a) Validation of thermal simulation by comparing the width and depth of the melt pool, (b) experimental melt pool profile, and (c) corresponding melt pool profile from thermal simulation.

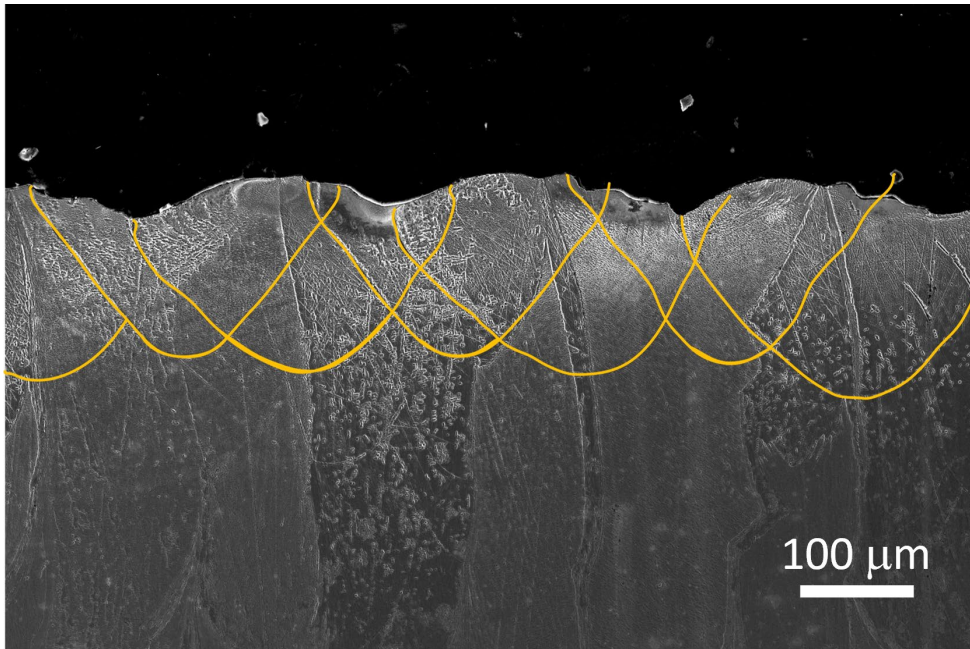


Figure 4.6 Melt pool profile for simulation validation.

The validated simulations were extended to thermal simulation for manufacturing BCC structures as shown in Figure 4.7 (a). The influence of strut dimensions on heat flux is illustrated in Figure 4.7 (b). In the BCC structure with low density (nominal relative density of 0.02 and 0.1), the heat dissipation is restricted by the low conductivity between the solid strut and the powder bed [51]. The small strut dimension also constrains the extension of the melt pool in the scanning direction, resulting in a puddle-like shape of the melt pool. Consequently, the temperature gradient and high conductivity in the as-fabricated strut direct the dominant heat flow close to the axial direction of the strut. Conversely, in BCC structures with higher relative densities (0.4 and 0.6), the dimple-like melt pool extends into a long and flat morphology due to the increased scanning distance. The effect of low conductivity of powder on the heat transfer in the strut is attenuated. Heat transfer in the manufacturing of a thick strut can be approximated to that of a bulk sample, with the dominant direction of heat flux at the melt pool bottom close to the building direction [42].

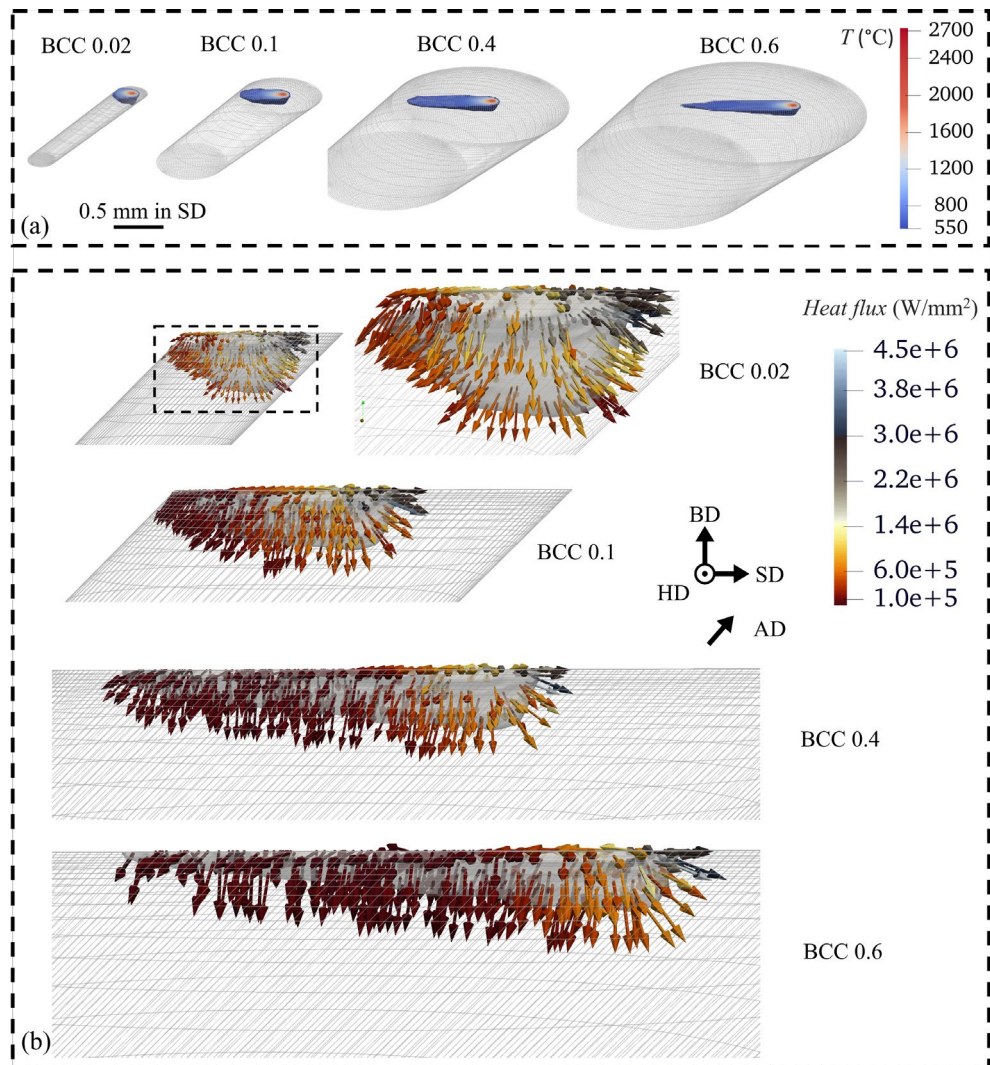


Figure 4.7 (a) Melt pool profile and (b) heat flow at the solid-liquid zone of melt pool during L-PBF of BCC metamaterials with the relative density of 0.02 (an extreme case), 0.1, 0.4, and 0.6.

4.4.2. Dependence of microstructures on geometrical dimensions

As shown in the XRD pattern (Figure 4.8), the B2 parent phase with a BCC crystal structure is the predominant phase for all BCC samples at room temperature. The BCC samples exhibit three strong diffraction peaks corresponding to (110), (200) and (211) Miller indices. Variations of peaks among samples with different relative densities are attributed to the different sampling areas of diffraction beam projecting on the samples.

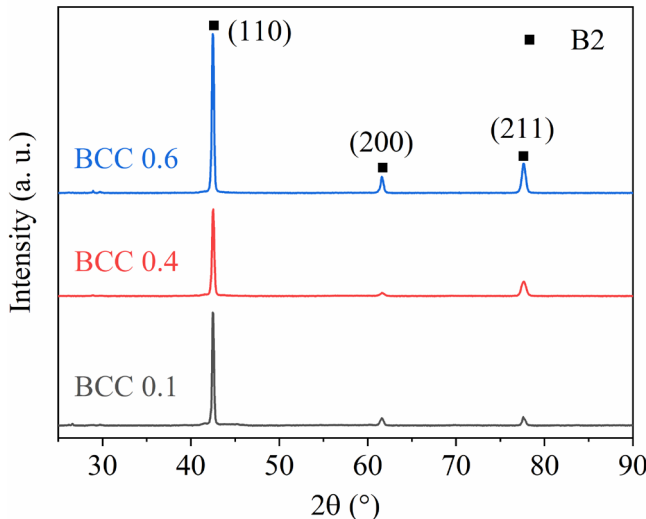


Figure 4.8 XRD patterns of BCC 0.1, 0.4, and 0.6 NiTi samples at room temperature.

The homogeneous microstructure and texture of the bulk sample were analyzed using EBSD, as illustrated in Figure 4.9. Inverse Pole Figures (IPF) for the building direction (IPF-BD), showing the sample cross-sections perpendicular and parallel to the BD, are presented in Figure 4.9 (a) and (b) with a colormap corresponding to the BD in the manufacturing coordinate system. It was observed that most grains exhibit a strong $\langle 001 \rangle$ orientation aligned with the BD, and columnar grains epitaxially grow along the BD. The corresponding pole figure (PF) further confirms these results as shown in Figure 4.9 (c) and (d). The highly $\langle 001 \rangle$ textured microstructure is attributed to the vertical maximum heat flux direction in the bulk sample and the insignificant edge effect, consistent with findings reported in previous studies [7,22]. Given the homogeneous microstructure at the sample scale, homogeneous mechanical properties were achieved across the bulk sample.

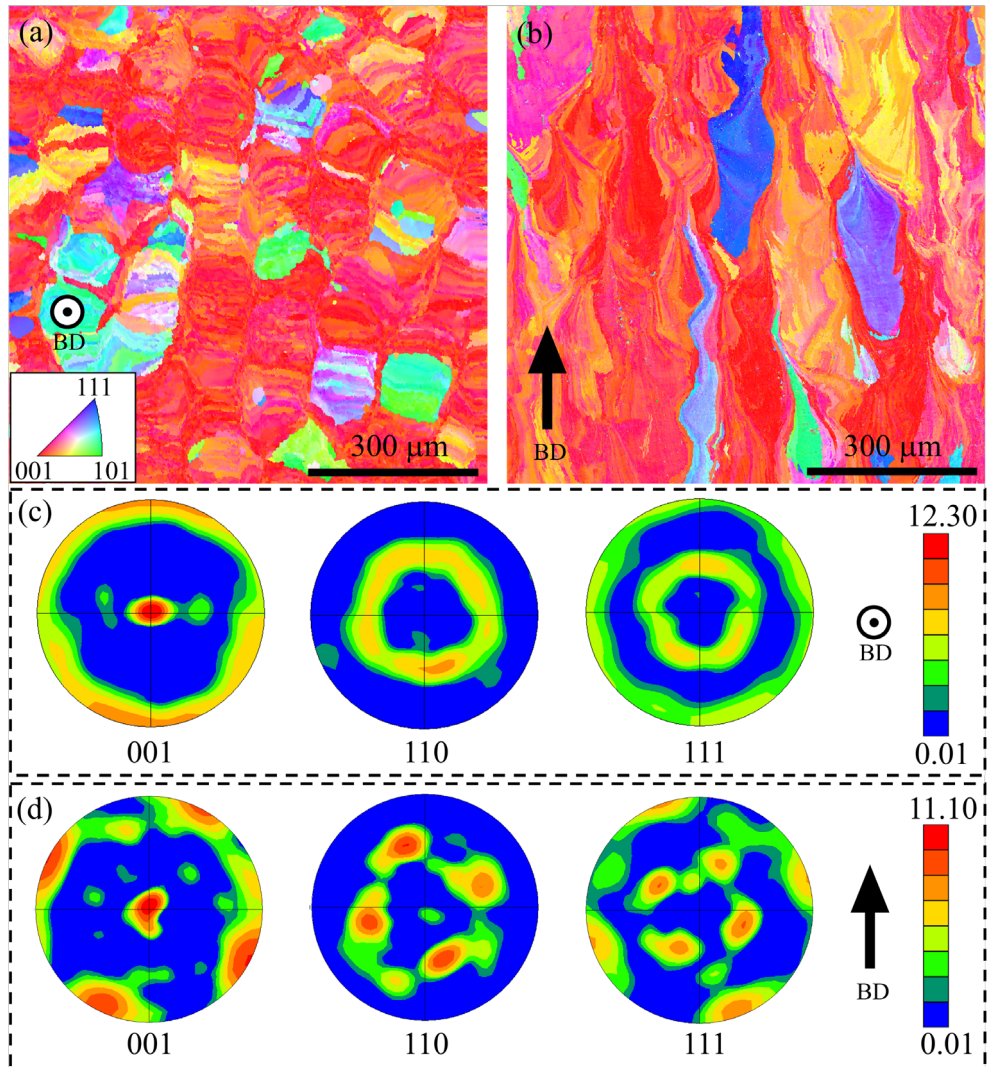


Figure 4.9 Images of EBSD data represented as inverse pole figure (IPF) map and pole figure maps of the bulk sample: (a) (c) perpendicular and (b) (d) parallel to the building direction.

4.4. Results

Texture analysis was conducted using EBSD on selected areas of BCC samples with relative densities of 0.1, 0.4, and 0.6, as shown in Figure 4.10 (a). Three distinct textures are observed in three samples fabricated using the same process parameters. Figure 4.10 (b) presents an IPF of the macroscopic $\langle 110 \rangle$ cross-section for sample BCC 0.1, using a color map corresponding to the axial direction (IPF-AD). In this sample, cellular grains are observed in the lower portion of the strut, while columnar grains dominate the central and upper regions. The elongation of the columnar grains in the upper area was promoted along the axial direction, gradually transitioning towards the vertical direction at the center of the strut. This columnar area exhibits a distinct texture parallel to the AD. Figure 4.10 (f) shows the corresponding Pole Figure (PF) for the same region, confirming the texture orientation observed in the IPF-AD.

For the sample BCC 0.4, Figure 4.10 (c) illustrates the IPF of the strut with the colormap corresponding to the BD (IPF-BD). In the central and bottom regions, a strong $\langle 001 \rangle // BD$ texture is observed, which is further confirmed in the corresponding PF (Figure 4.10 (f)). In the upper portion of the strut, columnar grains with shorter elongation were observed, and the growth direction shifted from the building direction to the strut AD. At the top area of the strut, columnar grains with less elongation are observed, and the elongation of the grains deviates from BD to AD of the strut. Figure 4.10 (d) and (e) illustrate the IPF of the macroscopic $\langle 110 \rangle$ cross-section of the strut and node in the sample BCC 0.6, with colormap aligned with the BD (IPF-BD). Coarse columnar grains are observed in the node area, characterized by elongation along the building direction. However, a comparably weaker texture is observed, differing from the results of BCC 0.4 and 0.1 samples.

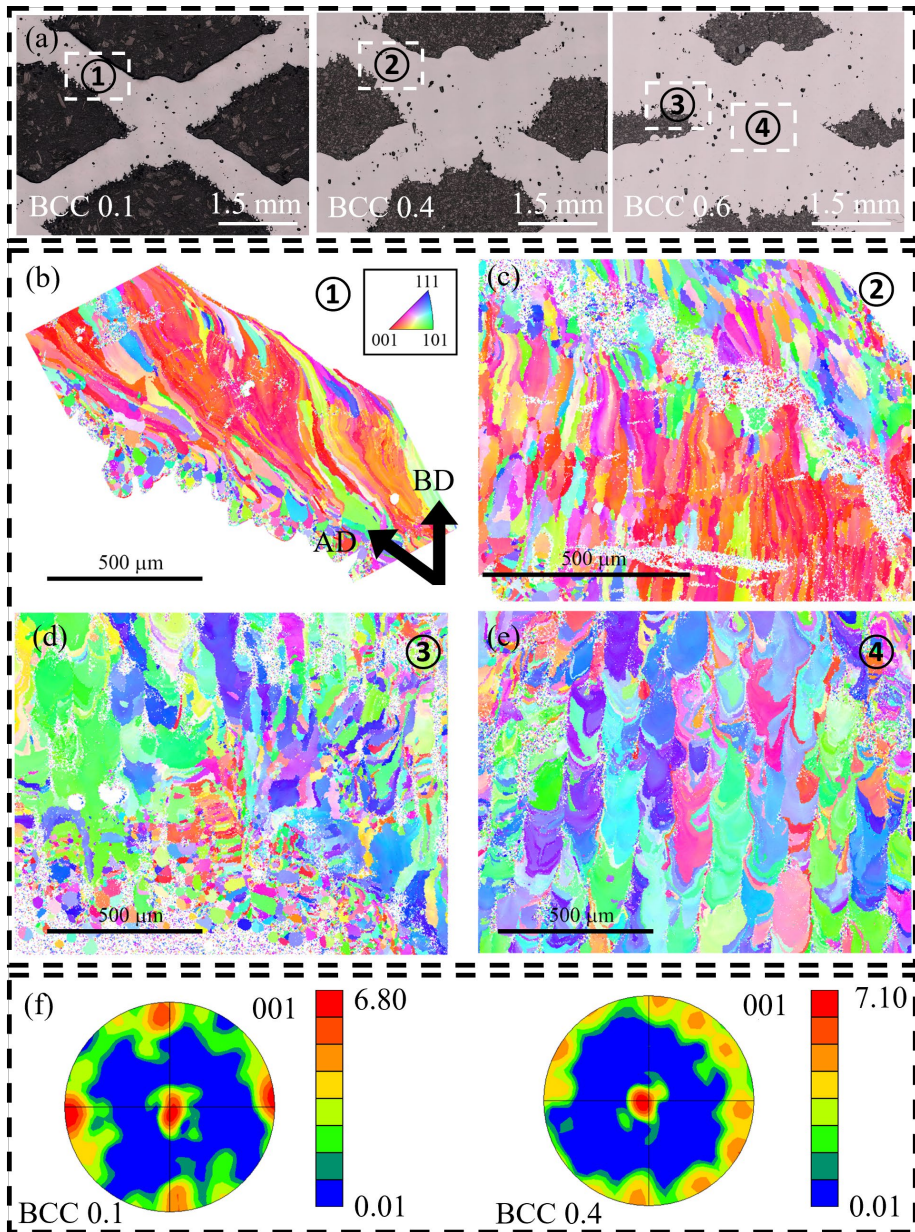


Figure 4.10 (a) Selected areas of BCC samples with relative densities of 0.1, 0.4, and 0.6. (b) Inverse Pole Figure (IPF) of the macroscopic cross-section for the BCC 0.1 sample. (c) IPF of the strut for the BCC 0.4 sample. (d, e) IPF of the macroscopic cross-section of the strut and node for the BCC 0.6 sample. (f) Corresponding Pole Figure (PF) for the BCC 0.1 and 0.4 samples.

4.4. Results

The grain morphology was defined as ellipses with major axis and minor axis for statistical analysis. The effect of relative density on the major axis and minor axis is presented in Figure 4.11. The EBSD analyses were performed twice on samples with identical relative density, and the results were subsequently combined. These replicates were adopted to encompass a sufficient number of grains within the statistical analysis. In total, the quantitative analysis comprised 915, 1355, and 2773 grains for the BCC 0.1, BCC 0.4, and BCC 0.6 samples, respectively. The averaged fraction corresponding to these morphology parameters is calculated, in the figure legend. The largest average major axis of the elongated grains was observed in the BCC 0.1 samples (36.5 μm) (Figure 4.11 (a)). The minor axis of the grains showed a consistent average value across the samples, which slightly increased from 7.2 to 7.9 μm (Figure 4.11 (b)).

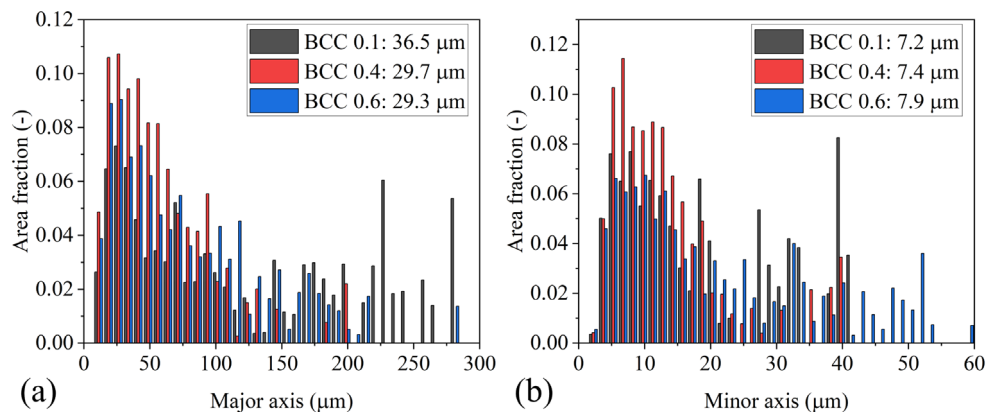


Figure 4.11 Grain size measured by EBSD with a (a) major axis and (b) minor axis of BCC samples with different relative densities. Averages are reported in the legend.

4.4.3. Phase transformation behavior

EDS was conducted on seven different locations in samples with two replicates for statistical significance, and the mean and standard deviation of the measurements are illustrated in Figure 4.12 (a). The mean Ni content increases with the increase of relative density. The variability in Ni content is related to the occurrence of Ni evaporation during the L-PBF process.

The DSC curves of BCC metamaterials after 4 cycles are shown in Figure 4.12 (b). The corresponding transformation temperatures (martensite start temperature M_s , martensite finish temperature M_f , austenite start temperature A_s , and austenite finish temperature A_f) are determined using tangent lines, as shown in Table 4.3. All as-fabricated BCC metamaterials

samples underwent single B2 to B19' transformation during cooling, and reverse transformation during heating. With the increase of relative density from 0.1 to 0.6, the span of the transformation temperature range ($A_f - M_f$) decreased, and the peaks became sharper. BCC 0.6 sample exhibited the lowest A_f of 35 °C.

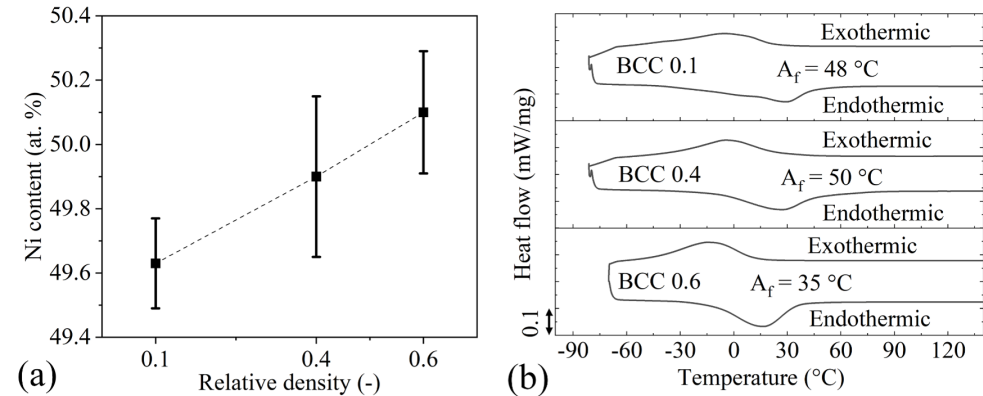


Figure 4.12 Ni content from (a) EDS and (b) DSC results of the BCC metamaterials with relative densities of 0.1, 0.4, and 0.6.

Table 4.3 Martensitic transformation temperatures for BCC metamaterials with relative densities of 0.1, 0.4, and 0.6.

Sample	M_s (°C)	M_f (°C)	A_s (°C)	A_f (°C)
BCC 0.1	24	-63	-42	48
BCC 0.4	28	-34	-9	50
BCC 0.6	12	-42	-12	35

The indentation force-depth responses from instrumented indentation are illustrated in Figure 4.13. The location dependence of recoverability for BCC 0.1, BCC 0.4, and BCC 0.6 samples at room temperature is illustrated in Figure 4.14. The BCC 0.6 sample exhibits on average higher recoverability under instrumented indentation with a maximum force of 20 N. This higher recoverability at room temperature could be attributed to the lowest austenite finish temperature (A_f) in the BCC 0.6 sample. The BCC 0.1 and BCC 0.4 samples showed a larger deviation in recoverability at room temperature, mainly due to the wider span of transformation temperatures as shown in Figure 4.12 (b). It has been reported that an increase of 0.1 at.% Ni could decrease transformation temperatures by approximately 20 °C for Ni-

4.4. Results

rich NiTi [59,60]. A higher Ni content in the BCC 0.6 sample decreased the A_f to approximately 35 °C, enabling greater recoverability under indentation at room temperature.

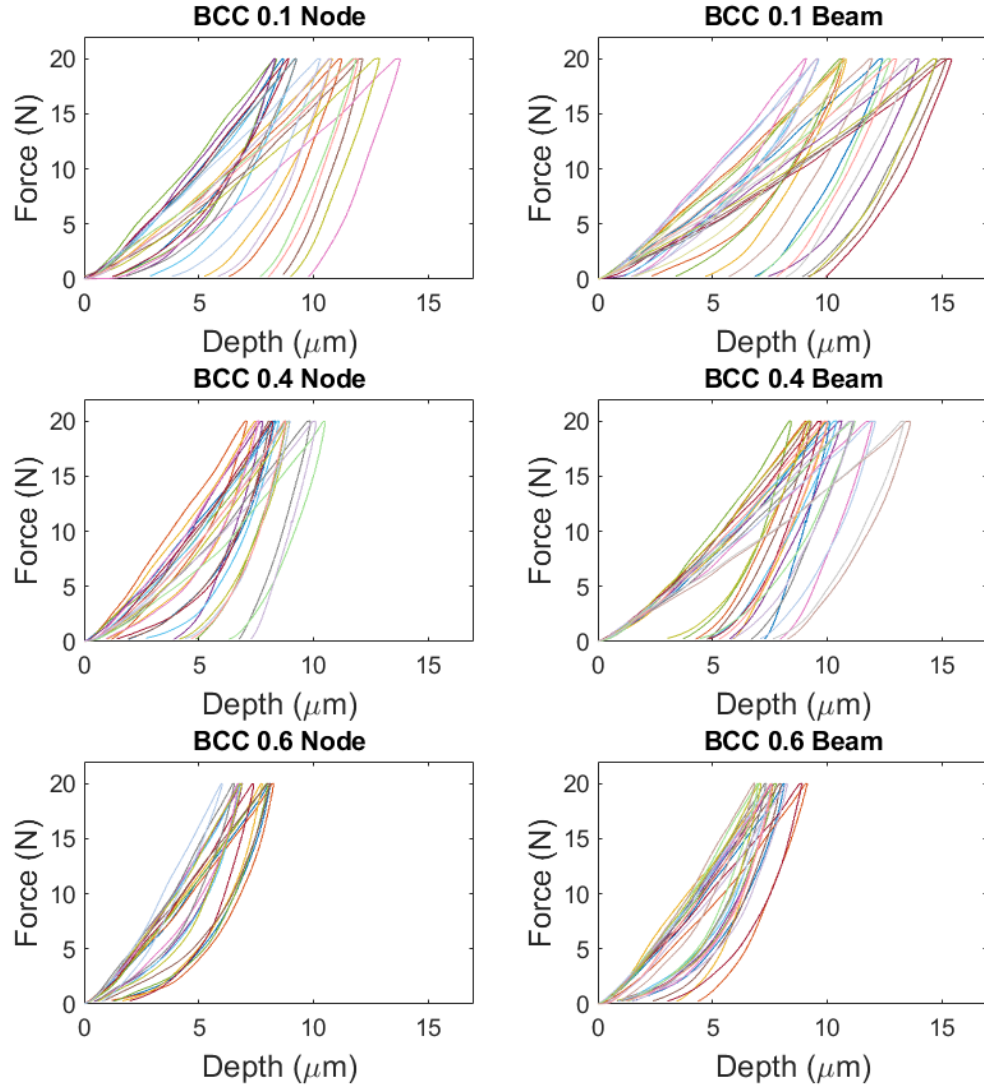


Figure 4.13 Indentation force-depth response for BCC 0.1, 0.4 and 0.6 samples.

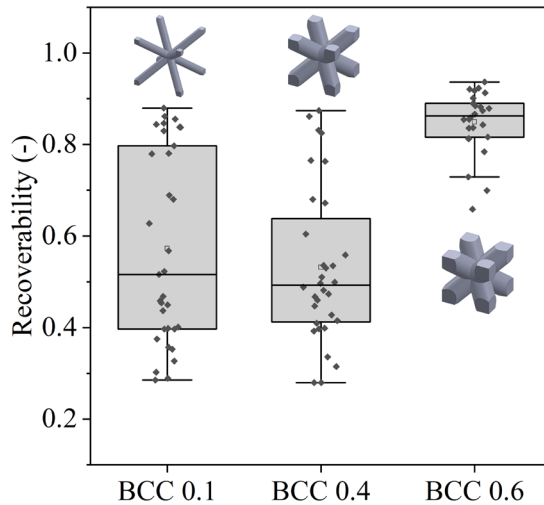


Figure 4.14 Recoverability in the instrumented indentation of BCC 0.1, 0.4, and 0.6 samples, including statistical mean, median, and range.

4

4.5. Discussion

4.5.1. Thermal effects on grain size and morphology

The inhomogeneity was observed in three BCC samples with different relative densities, and the formation mechanisms of this unexpected inhomogeneity are discussed. As shown in Figure 4.15, grain morphology varies with the relative density of the BCC metamaterials, even when using the same process parameters. Grain morphology is controlled by temperature gradient G and solidification rate R_s , as proposed by Güaumann et al [61]. For cases of high temperature gradient in the L-PBF process, the columnar to equiaxed transition is given as follows [61]:

$$\frac{G^n}{R_s} = a \left\{ \sqrt[3]{\frac{-4\pi N_0}{3 \ln[1-\varphi]}} \times \frac{1}{n+1} \right\}^n, \quad (4.12)$$

where $a = 1.25 \times 10^6$ (K^{3.4}/m·s) and $n = 3.4$ are material-dependent constants, $N_0 = 2 \times 10^{15}$ m⁻³ is the nuclei density and $\varphi = 0.05$ is a grain morphology factor, which was calibrated in our early studies [10]. As shown in Figure 4.15, the $G-R_s$ area in the equiaxed region corresponds to the upper region of the melt pool, which is subjected to remelting by successive layers. The area of $G-R_s$ in the central and bottom regions promotes the formation

of columnar grains at the bottom area of the melt pool. The columnar grains elongated along the maximum heat flux direction, which can vary from the BD direction to the AD of the strut with the increasing edge effect (Figure 4.10). Hence, considering the epitaxial growth of columnar grains and the spatiotemporal variation of the direction of the temperature gradient at the solid-liquid interface, the elongation direction of columnar grains in BCC metamaterials with different relative density deviates from building direction to the axial direction of the strut.

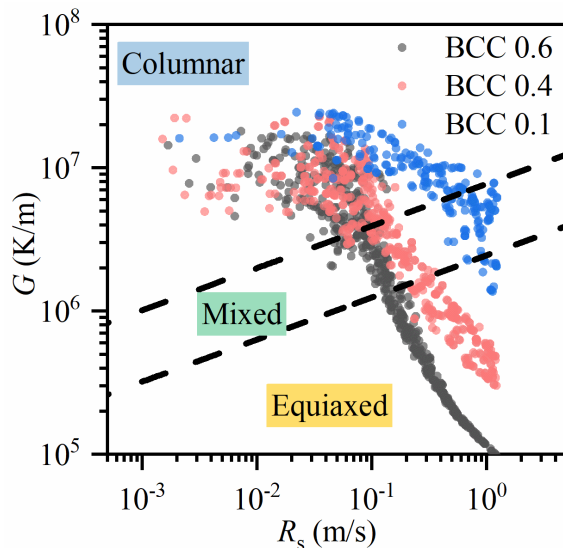


Figure 4.15 Columnar to equiaxed transition of L-PBF NiTi, where G is the temperature gradient and R_s is the solidification rate.

4.5.2. Edge effect

As strut dimensions decrease in the L-PBF process using consistent process parameters, the edge effect becomes more pronounced. The structural parameters are provided in Figure 4.1. An extreme case is shown in Figure 4.7(b), Figure 4.16 (b), and (c) for BCC structure with a relative density of 0.02, in which the melt pool occupies the entire cross-section of a unit strut. The temperature history of the central point of the strut during the laser scanning is shown in Figure 4.16 (b). For low-density BCC structures, the extension and movement of the melt pool along the scanning direction are limited by the strut's dimensions, keeping the central point molten even after one scanning finish. Consequently, the steady state of the moving melt pool cannot be achieved. Conversely, for a BCC structure with a relative density

above 0.2, the melt pool progresses along the scanning direction, allowing the central point to begin solidifying once laser scanning ends, as shown in Figure 4.16 (c).

The evolution of the melt pool is influenced by process parameters, scanning strategy, and geometrical parameters as shown in our simulations. To evaluate the edge effect for L-PBF of truss-based metamaterials, we applied the Fourier number (Fo) to analyze it in the scanning direction [44]:

$$Fo = \frac{\kappa\tau}{\delta^2} = \frac{\kappa}{v\delta}, \quad (4.13)$$

where δ is the characteristic length, which is defined by the characteristic length of the melt pool. κ is the thermal diffusivity of NiTi and τ is the characteristic time. Due to the change in melt pool morphology with different scanning lengths in different layers, the characteristic length of the melt pool is calculated as half the track that was scanned. The Fourier number describes the change in thermal dissipation along the scanning direction.

4

As shown in Figure 4.16 (d), the dimensional analysis shows how Fo varies with relative density and non-dimensional heat input, due to the combined influence of process parameters and geometrical parameters during L-PBF process. Considering the process parameters used in our experiments, the variation of Fo with relative density is shown in Figure 4.16 (e). For BCC structures with a relative density higher than 0.3, Fo remains relatively constant, suggesting a stable relationship between heat input and heat dissipation. The printing process can be defined as a bulk-based mode. Conversely, for a BCC structure with a relative density of less than 0.3, the edge effect becomes pronounced, and Fo increases with the decrease of relative density, indicating a transition to a strut-based printing mode.

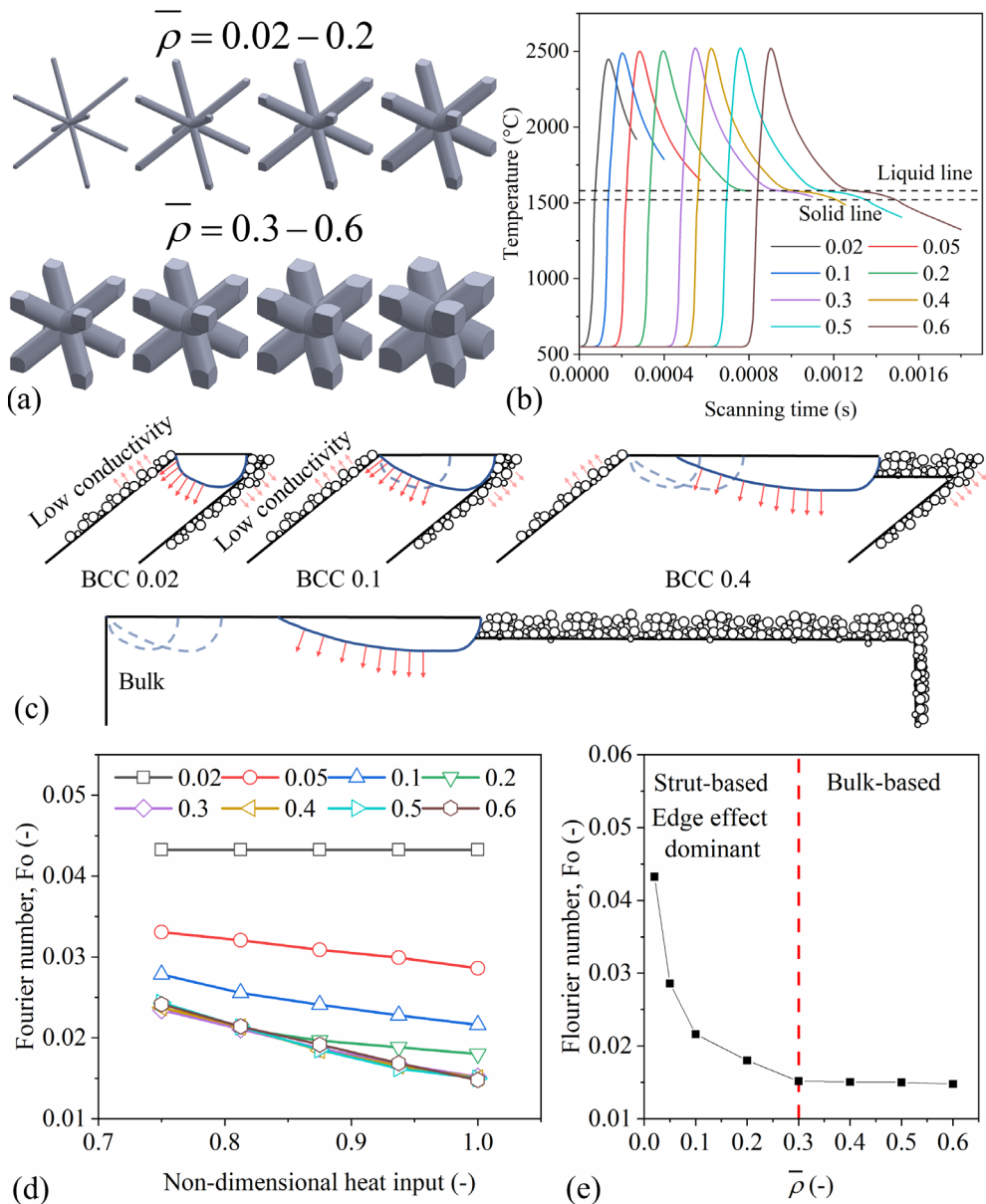


Figure 4.16 Edge effect in L-PBF of NiTi BCC metamaterials: (a) CAD model of unit cells, (b) temperature history at the central point of the strut, (c) schematic diagram of edge effect, (d) the effect of non-dimensional heat input on the Fourier number, and (e) The effect of relative density of Fourier number for the parameters used in the current chapter.

4.5.3. Laser turn region

Fourier number provides a heat conduction-based insight into the geometric effect on the melt pool and the evolution of microstructure. Another mechanism related to geometrical dependence is the overheat at the laser turn region during the L-PBF process. Recent studies reported that acceleration/deceleration at laser start/end points can result in overheat and unexpected defects during laser-based welding and additive manufacturing. In-situ observations and multi-physics simulations have shown that overheat at the laser turn region results in increased metal evaporation and collapse of the melt pool surface [62,63]. For the L-PBF of bulk samples, overheat at the laser turn region is insignificant to the properties because the relative size between the laser turn region and the sample is small. However, the impact of the laser turn region becomes more pronounced when the size of the geometry is reduced to the same scale as the laser turn region (Figure 4.17 (a)).

As shown in Figure 4.17 (b), the laser turn region leads to a transition in the surface morphology of the fabricated layer. The average length, measured by an average across twelve scanning tracks, is $636\pm38\text{ }\mu\text{m}$ for one endpoint of a scanning track (Figure 4.17 (c)). Overheat at the turn point region leads to the over-evaporation of Ni in a low-density structure (Figure 4.12 (a)), contributing to an increased A_f of $48\text{ }^\circ\text{C}$ in sample BCC 0.1 and $50\text{ }^\circ\text{C}$ in sample BCC 0.4. This observation explains the low A_f of $35\text{ }^\circ\text{C}$ and an average high indentation recoverability of 84% in sample BCC 0.6 (Figure 4.14). The significance of the laser turn region is influenced by the different relative lengths between the laser turn region and the scanning length. When the scanning length is less than twice the length of the turning region, the overheat region mainly occupies the printing scanning track. Decreased laser power and adaptive control of heat input can be applied to improve the consistency of NiTi properties.

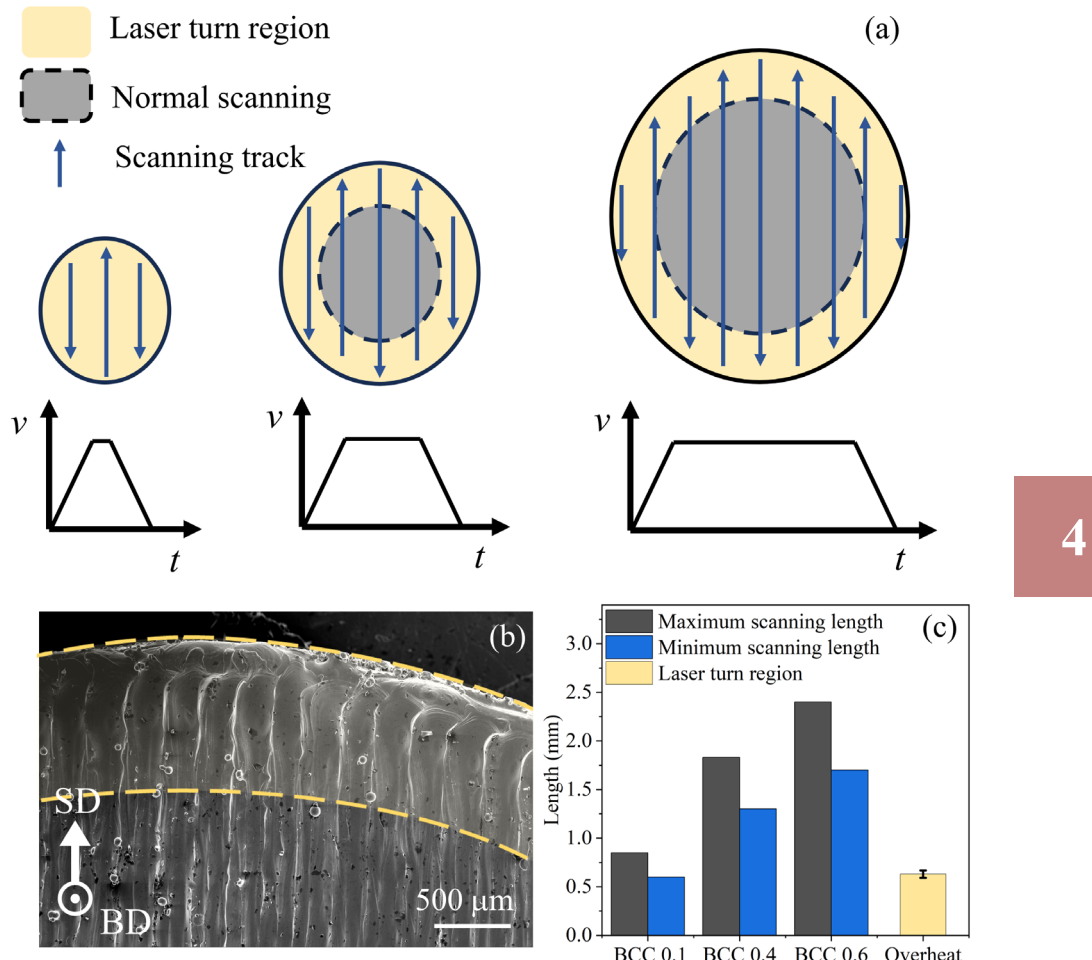


Figure 4.17 Representation of the laser turn region: (a) schematical diagram (b) SEM picture, and (c) the comparison of scanning length and length of laser turn region.

4.5.4. Influence of inhomogeneous thermomechanical properties on macroscopic structural response

The significance of inhomogeneous microstructure and thermomechanical properties has been underestimated in previous studies due to limited testing methods [34]. To better understand this effect, we evaluate the influence of changing transformation temperatures on the macroscopic stress and strain response of BCC metamaterials. In the absence of sufficient

experimental data, we first assume that global changes in transformation temperatures are inhomogeneous and follow a multivariate Gaussian distribution:

$$\begin{aligned}
 M_s &= M_{s0} + \Delta M_s \prod_{i=1}^3 \frac{1}{s_i \sqrt{2\pi}} \exp \left[-\frac{(x_i - \mu_i)^2}{s_i^2} \right] \\
 M_f &= M_{f0} + \Delta M_f \prod_{i=1}^3 \frac{1}{s_i \sqrt{2\pi}} \exp \left[-\frac{(x_i - \mu_i)^2}{s_i^2} \right], \\
 A_s &= A_{s0} + \Delta A_s \prod_{i=1}^3 \frac{1}{s_i \sqrt{2\pi}} \exp \left[-\frac{(x_i - \mu_i)^2}{s_i^2} \right] \\
 A_f &= A_{f0} + \Delta A_f \prod_{i=1}^3 \frac{1}{s_i \sqrt{2\pi}} \exp \left[-\frac{(x_i - \mu_i)^2}{s_i^2} \right]
 \end{aligned} \tag{4.14}$$

where M_{s0} , M_{f0} , A_{s0} , and A_{f0} are the calibrated transformation temperatures obtained using DSC under the assumption of homogeneity. ΔM_s , ΔM_f , ΔA_s , and ΔA_f are the differences in transformation temperatures, used to evaluate the global inhomogeneity, which is estimated from DSC curves. The inhomogeneous transformation temperatures are spatially distributed in a global coordinate system that coincides with the manufacturing coordinate system, represented by variables COORD in subroutine UMAT. Future work will extend these efforts to consider the complete heterogeneous assignment of thermomechanical properties.

The calibration is shown in Figure 4.3 under the assumption of homogeneity and consistency. The transformation temperatures were derived from DSC tests performed on regions from each of the three fabricated BCC lattices (Table 4.2). The inhomogeneity is estimated from differences in transformation temperatures, which are 30 °C for BCC 0.1 and BCC 0.4 samples, and 10 °C for BCC 0.6 samples. The response of the printed samples is predicted at an ambient temperature of 54 °C, consistent with the conditions of the uniaxial compression tests.

The numerical study in Figure 4.18 and experimental data in Figure 4.21 show that the inhomogeneous transformation temperatures in BCC samples lead to a pseudo-linear behavior and a narrow hysteresis across all samples. The expected effective transformation stress for NiTi metamaterials is not obviously observed in both numerical and experimental results [34]. Only partial superelasticity is achieved due to a partial martensitic transformation or reorientation as shown in Figure 4.20. Higher equivalent stress and lower martensitic fraction are observed in all BCC samples with inhomogeneous transformation temperatures (Figure 4.19).

The numerical and experimental results suggest that both unit cell design and local thermomechanical properties contribute to macroscopic deformation recoverability, as shown in Figure 4.19 and Figure 4.20. The BCC 0.6 sample, which has smaller transformation temperature differences of 10°C , shows low recoverable deformation due to the high structural stiffness, despite a higher reverse martensitic transformation of the base NiTi (Figure 4.19 (c) and Figure 4.20 (c)). Conversely, the BCC 0.1 sample, with a larger transformation temperature difference of 30°C , exhibits larger deformation recoverability due to its structural compliance, while martensite volume fraction is relatively low due to inhomogeneous transformation temperatures (Figure 4.18 (a), Figure 4.20 (a) and Figure 4.21 (a)). Thus, macroscopic compression on metamaterials cannot fully reflect the properties of base NiTi without assuming homogeneity and consistency.

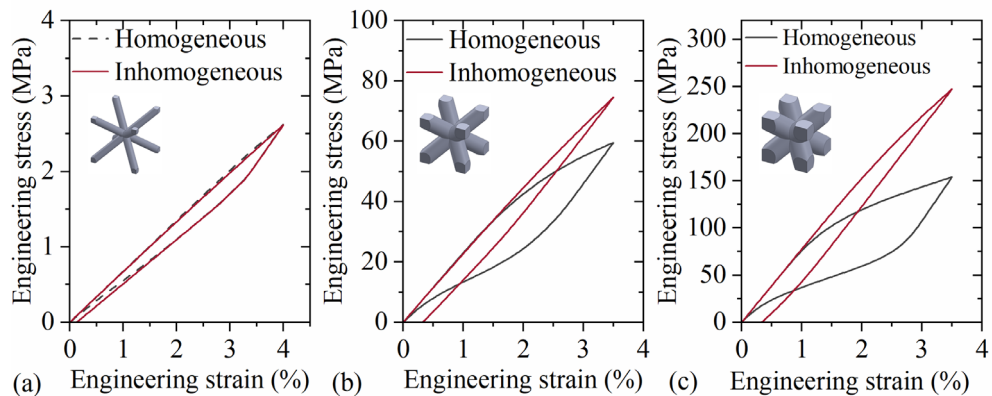


Figure 4.18 Engineering stress-strain response of NiTi metamaterials with inhomogeneous and homogeneous martensitic transformation temperatures: (a) BCC 0.1, (b) BCC 0.4, and (c) BCC 0.6.

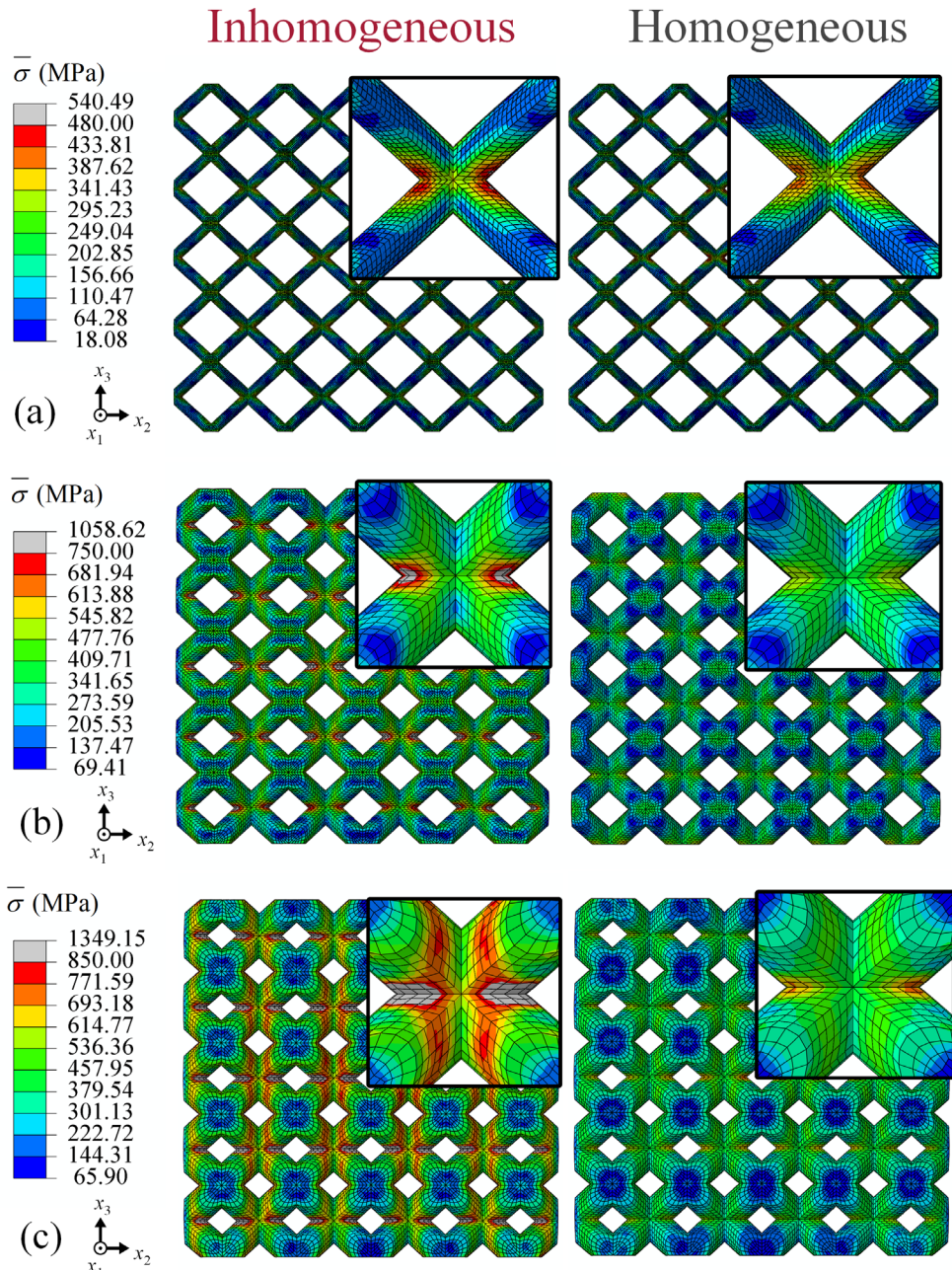


Figure 4.19 Contour plots of equivalent (von Mises) stress resulting from the inhomogeneous and homogeneous martensitic transformation temperatures in (a) BCC 0.1, (b) BCC 0.4, and (c) BCC 0.6 samples under maximum loading.

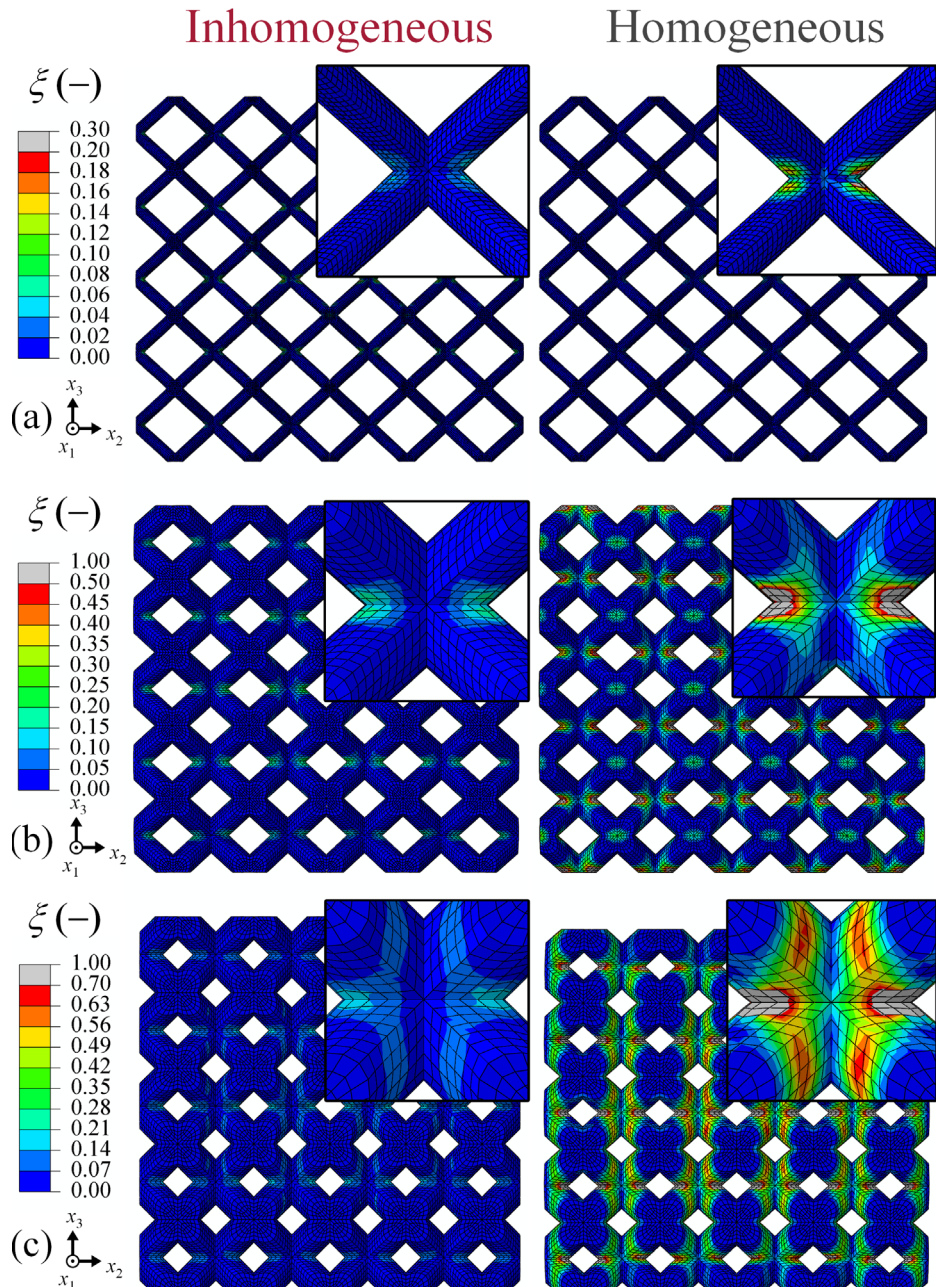


Figure 4.20 Contour plots of martensitic volume fraction resulting from the inhomogeneous and homogeneous martensitic transformation temperatures in (a) BCC 0.1, (b) BCC 0.4 and (c) BCC 0.6 samples under maximum loading.

From the above computational and experimental study, one can observe the strong impact of inhomogeneous transformation temperatures on macroscopic mechanical response. However, the transformation temperatures assigned to each of the three structural forms were taken from sample-specific DSC experiments with an effective resolution of 10 mm^2 . The discussion of inhomogeneity implies a possible variation in properties throughout the samples (e.g., due to the laser turn region, etc.) at the length scale of $500 \mu\text{m}$. The corresponding sample errors cannot be completely eliminated due to their high inhomogeneity. Therefore, we do not expect the computational predictions in Figure 4.18 to be fully accurate.

The observed narrow hysteresis and partial superelasticity in NiTi metamaterials are likely attributed to an inhomogeneous microstructure and spatial variations in properties. While macroscopic compression tests provide valuable trends, they do not confirm that the functionality of the as-fabricated samples aligns with the design objective. This motivates a more rigorous experimental/computational study regarding the specifics of process-induced material heterogeneity in future works.

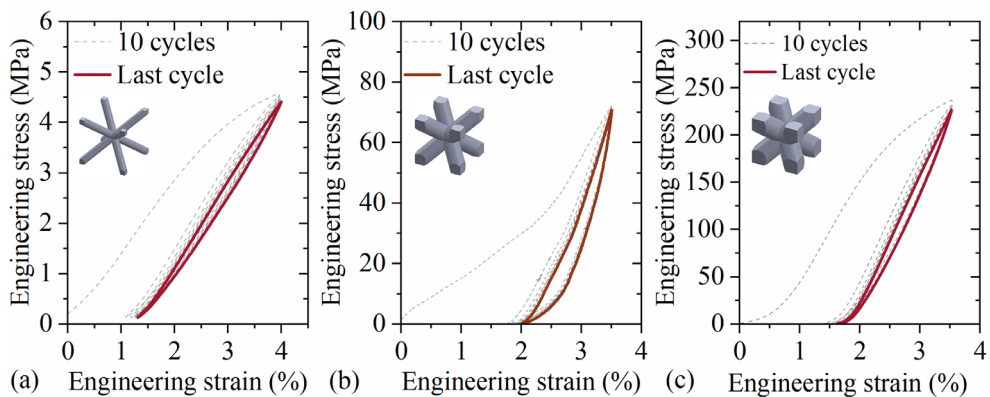


Figure 4.21 Cyclic compression tests on fabricated BCC metamaterials at 54°C : (a) BCC 0.1, (b) BCC 0.4, and (c) BCC 0.6 samples.

4.6. Conclusions

In the present chapter, the inhomogeneity phenomenon in NiTi metamaterials was investigated. The influence of relative density on microstructure, local indentation response, and the macroscopic thermomechanical response of as-fabricated body-centered cubic (BCC) structures are discussed. The main findings can be summarized as follows:

- The thermomechanical response of NiTi BCC metamaterials is modeled using a phenomenological constitutive model of shape memory alloys. The highly inhomogeneous martensitic transformation temperatures at the mesoscale could lead to a pseudo-linear response and narrow stress hysteresis. The partial superelasticity in NiTi metamaterials is related to microstructure and thermomechanical properties inhomogeneity at the mesoscale.
- In low-density, bending-dominated structures, deformation recoverability is jointly attributed to both structural compliance and the recoverable strain of NiTi. The compliance of low-density BCC structures enhances the overall deformation recoverability when superelasticity of the base NiTi is suppressed.
- Strut dimensions of metamaterials significantly influence the interaction between the powder bed, melt pool, and as-fabricated layers during the L-PBF process. Short scanning tracks and the low conductivity of the powder bed collectively limit the extension of the melt pool along the scanning direction. Changes in the dominant heat flux direction from axial to building directions influence the growth of columnar grains and textures. This results in distinct textures across the three fabricated BCC samples, varying with strut size.
- Excessive evaporation of Ni content occurs during printing, becoming more pronounced when geometrical dimensions are reduced to the scale of the laser turn region. In instrumented indentation, the BCC 0.6 sample shows the highest recoverability (84% at room temperature) due to lower martensite finish temperature A_f .
- The edge effect of the strut during L-PBF is clarified using dimensional analysis. The transition from strut-based to bulk-based printing modes is defined using a dimensionless Fourier number.

Appendix A Table of notation

Structural parameters	
$\bar{\rho}$	Relative density of mechanical metamaterial
ρ	Density of mechanical metamaterial
ρ_s	Density of solid NiTi
R	Radius of the beam
l	Length of the beam
L	Size (edge length) of a unit cell
Thermal model	
c_p	Constant pressure specific heat
k	Thermal conductivity
Q	Heat flux density of the laser beam
η	Absorptivity of the material
P	Laser power
c_1, c_2, c_3	Ellipsoid semi-axis
v	Scanning speed
T_{res}	Residual temperature
T_{in}	Initial temperature
Q_{1D}	One-dimensional heat source
N_A	Number of energy inputs
κ	Thermal diffusivity
f	Frequency of repetitive energy input
$r - Nd$	Conversion of coordinates for the moving heat source
G	Temperature gradient
R_s	Solidification rate
N_0	Nuclei density
a, n	Material-dependent constants
φ	Grain morphology factor
Fo	Fourier number
τ	Characteristic time
δ	Characteristic length

Appendix A

T	External temperature
NiTi constitutive model	
ϵ^{tr}	Transformation strain of NiTi
ΔS	entropy variation NiTi
ξ_s	Martensitic volume fraction
E_A	Austenite Young's modulus NiTi
ν_A	Austenite Poisson ratio NiTi
E_M	Martensite Young's modulus NiTi
ν_M	Martensite Poisson ratio NiTi

References

[1] A. Großmann, J. Felger, T. Frölich, J. Gosmann, C. Mittelstedt, Melt pool controlled laser powder bed fusion for customised low-density lattice structures, *Mater. Des.* 181 (2019) 108054. <https://doi.org/10.1016/j.matdes.2019.108054>.

[2] P. Delroisse, P.J. Jacques, E. Maire, O. Rigo, A. Simar, Effect of strut orientation on the microstructure heterogeneities in AlSi10Mg lattices processed by selective laser melting, *Scr. Mater.* 141 (2017) 32–35. <https://doi.org/10.1016/j.scriptamat.2017.07.020>.

[3] L.J. Gibson, M.F. Ashby, Mechanics of Three-Dimensional Cellular Materials., *Proc. R. Soc. London, Ser. A Math. Phys. Sci.* 382 (1982) 43–59. <https://doi.org/10.1098/rspa.1982.0088>.

[4] S. Saedi, N. Shayesteh Moghaddam, A. Amerinatanzi, M. Elahinia, H.E. Karaca, On the effects of selective laser melting process parameters on microstructure and thermomechanical response of Ni-rich NiTi, *Acta Mater.* 144 (2018) 552–560. <https://doi.org/10.1016/j.actamat.2017.10.072>.

[5] L. Xue, K.C. Atli, S. Picak, C. Zhang, B. Zhang, A. Elwany, R. Arroyave, I. Karaman, Controlling martensitic transformation characteristics in defect-free NiTi shape memory alloys fabricated using laser powder bed fusion and a process optimization framework, *Acta Mater.* 215 (2021) 117017. <https://doi.org/10.1016/j.actamat.2021.117017>.

[6] X. Wang, J. Yu, J. Liu, L. Chen, Q. Yang, H. Wei, J. Sun, Z. Wang, Z. Zhang, G. Zhao, J. Van Humbeeck, Effect of process parameters on the phase transformation behavior and tensile properties of NiTi shape memory alloys fabricated by selective laser melting, *Addit. Manuf.* 36 (2020) 101545. <https://doi.org/10.1016/j.addma.2020.101545>.

[7] A. Safdel, N. Zaker, G.A. Botton, M.A. Elbestawi, The role of texture and restoration mechanisms in defining the tension-compression asymmetry behavior of aged NiTi alloys fabricated by laser powder bed fusion, *Mater. Sci. Eng. A* 864 (2023) 144592. <https://doi.org/10.1016/j.msea.2023.144592>.

[8] H.Z. Lu, L.H. Liu, X. Luo, H.W. Ma, W.S. Cai, R. Lupoi, S. Yin, C. Yang, Formation mechanism of heterogeneous microstructures and shape memory effect in NiTi shape memory alloy fabricated via laser powder bed fusion, *Mater. Des.* 232 (2023) 112107. <https://doi.org/10.1016/j.matdes.2023.112107>.

[9] L. Xue, K.C. Atli, C. Zhang, N. Hite, A. Srivastava, A.C. Leff, A.A. Wilson, D.J. Sharar, A. Elwany, R. Arroyave, I. Karaman, Laser Powder Bed Fusion of Defect-Free NiTi Shape Memory Alloy Parts with Superior Tensile Superelasticity, *Acta Mater.* 229 (2022) 117781. <https://doi.org/10.1016/j.actamat.2022.117781>.

[10] J.N. Zhu, K. Liu, T. Riemslag, F.D. Tichelaar, E. Borisov, X. Yao, A. Popovich, R. Huizinga, M. Hermans, V. Popovich, Achieving superelasticity in additively manufactured Ni-lean NiTi by crystallographic design, *Mater. Des.* 230 (2023) 111949. <https://doi.org/10.1016/j.matdes.2023.111949>.

[11] C. Tan, S. Li, K. Essa, P. Jamshidi, K. Zhou, W. Ma, M.M. Attallah, Laser Powder Bed Fusion of Ti-rich TiNi lattice structures: Process optimisation, geometrical integrity, and phase transformations, *Int. J. Mach. Tools Manuf.* 141 (2019) 19–29. <https://doi.org/10.1016/j.ijmachtools.2019.04.002>.

[12] P. Jamshidi, C. Panwisawas, E. Langi, S.C. Cox, J. Feng, L. Zhao, M.M. Attallah, Development, characterisation, and modelling of processability of nitinol stents using laser powder bed fusion, *J. Alloys Compd.* 909 (2022) 164681. <https://doi.org/10.1016/j.jallcom.2022.164681>.

[13] A. Safdel, H. Torbati-Sarraf, M.A. Elbestawi, Laser powder bed fusion of differently designed NiTi stent structures having enhanced recoverability and superelasticity, *J. Alloys Compd.* 954 (2023) 170196. <https://doi.org/10.1016/j.jallcom.2023.170196>.

[14] T. Niendorf, F. Brenne, M. Schaper, Lattice structures manufactured by SLM: On the effect of geometrical dimensions on microstructure evolution during processing, *Metall. Mater. Trans. B Process Metall. Mater. Process. Sci.* 45 (2014) 1181–1185. <https://doi.org/10.1007/s11663-014-0086-z>.

[15] C. Britt, C.J. Montgomery, M.J. Brand, Z.K. Liu, J.S. Carpenter, A.M. Beese, Effect of processing parameters and strut dimensions on the microstructures and hardness of stainless steel 316L lattice-emulating structures made by powder bed fusion, *Addit. Manuf.* 40 (2021) 101943. <https://doi.org/10.1016/j.addma.2021.101943>.

[16] M. Liu, N. Takata, A. Suzuki, M. Kobashi, Development of gradient microstructure in the lattice structure of AlSi10Mg alloy fabricated by selective laser melting, *J. Mater. Sci. Technol.* 36 (2020) 106–117. <https://doi.org/10.1016/j.jmst.2019.06.015>.

[17] S. Banait, C. Liu, M. Campos, M.S. Pham, M.T. Pérez-Prado, Coupled effect of microstructure and topology on the mechanical behavior of Inconel718 additively manufactured lattices, *Mater. Des.* 224 (2022) 111294. <https://doi.org/10.1016/j.matdes.2022.111294>.

[18] R. Wauthle, B. Vrancken, B. Beynaerts, K. Jorissen, J. Schrooten, J.P. Kruth, J. Van Humbeeck, Effects of build orientation and heat treatment on the microstructure and mechanical properties of selective laser melted Ti6Al4V lattice structures, *Addit. Manuf.* 5 (2015) 77–84. <https://doi.org/10.1016/j.addma.2014.12.008>.

[19] J. Zhang, Y. Liu, B.B. Babamiri, Y. Zhou, M. Dargusch, K. Hazeli, M.X. Zhang, Enhancing specific energy absorption of additively manufactured titanium lattice structures through simultaneous manipulation of architecture and constituent material, *Addit. Manuf.* 55 (2022) 102887. <https://doi.org/10.1016/j.addma.2022.102887>.

[20] N.S. Johnson, M. Strantza, M.J. Matthews, J.S. Park, P. Kenesei, B. Clausen, D.W. Brown, J.S. Carpenter, C.A. Brice, A.P. Stebner, Direct measurement of the effective properties of an additively manufactured titanium octet truss unit cell using high energy X-ray diffraction, *Mater. Charact.* 209 (2024). <https://doi.org/10.1016/j.matchar.2024.113755>.

[21] J.P. Oliveira, R.M. Miranda, F.M. Braz Fernandes, Welding and Joining of NiTi Shape Memory Alloys: A Review, *Prog. Mater. Sci.* 88 (2017) 412–466. <https://doi.org/10.1016/j.pmatsci.2017.04.008>.

[22] K. Safaei, M. Nematollahi, P. Bayati, F. Kordizadeh, M.T. Andani, H. Abedi, B. Poorganji, M. Elahinia, On the crystallographic texture and torsional behavior of NiTi shape memory alloy processed by laser powder bed fusion: Effect of build orientation, *Addit. Manuf.* 59 (2022) 103184. <https://doi.org/10.1016/j.addma.2022.103184>.

[23] B. Li, L. Wang, B. Wang, D. Li, R. Cui, B. Su, L. Yao, L. Luo, R. Chen, Y. Su, J. Guo, H. Fu, Solidification characterization and its correlation with the mechanical properties and functional response of NiTi shape memory alloy manufactured by electron beam freeform fabrication, *Addit. Manuf.* 48 (2021) 102468. <https://doi.org/10.1016/j.addma.2021.102468>.

[24] M. Mehrpouya, A. Gisario, A. Brotzu, S. Natali, Laser welding of NiTi shape memory sheets using a diode laser, *Opt. Laser Technol.* 108 (2018) 142–149. <https://doi.org/10.1016/j.optlastec.2018.06.038>.

[25] H.Z. Lu, H.W. Ma, W.S. Cai, X. Luo, Z. Wang, C.H. Song, S. Yin, C. Yang, Stable tensile recovery strain induced by a Ni₄Ti₃ nanoprecipitate in a Ni50.4Ti49.6 shape memory alloy fabricated via selective laser melting, *Acta Mater.* 219 (2021). <https://doi.org/10.1016/j.actamat.2021.117261>.

[26] C. Cisse, W. Zaki, T. Ben Zineb, A review of constitutive models and modeling techniques for shape memory alloys, *Int. J. Plast.* 76 (2016) 244–284. <https://doi.org/10.1016/j.ijplas.2015.08.006>.

[27] F. Auricchio, R.L. Taylor, J. Lubliner, Shape-memory alloys: macromodelling and numerical simulations of the superelastic behavior, *Comput. Methods Appl. Mech. Eng.* 146 (1997) 281–312. [https://doi.org/10.1016/S0045-7825\(96\)01232-7](https://doi.org/10.1016/S0045-7825(96)01232-7).

[28] D. Lagoudas, D. Hartl, Y. Chemisky, L. MacHado, P. Popov, Constitutive model for the numerical analysis of phase transformation in polycrystalline shape memory alloys, *Int. J. Plast.* 32–33 (2012) 155–183. <https://doi.org/10.1016/j.ijplas.2011.10.009>.

[29] D.C. Lagoudas, *Shape memory alloys: modeling and engineering applications*, Springer, 2008.

[30] D.J. Hartl, D.C. Lagoudas, F.T. Calkins, J.H. Mabe, J.T. Mooney, D.C. Lagoudas, F.T. Calkins, J.H. Mabe, Use of a Ni60Ti shape memory alloy for active jet engine chevron application: I. thermomechanical characterization, *Smart Mater. Struct.* 19 (2010). <https://doi.org/10.1088/0964-1726/19/1/015021>.

[31] N. An, M. Li, J. Zhou, Modeling SMA-enabled soft deployable structures for kirigami/origami reflectors, *Int. J. Mech. Sci.* 180 (2020). <https://doi.org/10.1016/j.ijmecsci.2020.105753>.

[32] T. Tancogne-Dejean, A.B. Spierings, D. Mohr, Additively-manufactured metallic micro-lattice materials for high specific energy absorption under static and dynamic loading, *Acta Mater.* 116 (2016) 14–28. <https://doi.org/10.1016/j.actamat.2016.05.054>.

[33] G. Machado, H. Louche, T. Alonso, D. Favier, Superelastic cellular NiTi tube-based materials: Fabrication, experiments and modeling, *Mater. Des.* 65 (2015) 212–220. <https://doi.org/10.1016/j.matdes.2014.09.007>.

[34] Z. Yan, J. Zhu, E. Borisov, T. Riemslag, S. Paul, M. Hermans, J. Jovanova, V. Popovich, Superelastic response and damping behavior of additively manufactured Nitinol architected materials, *Addit. Manuf.* 68 (2023) 103505. <https://doi.org/10.1016/j.addma.2023.103505>.

[35] H.Z. Lu, H.W. Ma, X. Luo, Y. Wang, J. Wang, R. Lupoi, S. Yin, C. Yang, Microstructure, shape memory properties, and in vitro biocompatibility of porous NiTi scaffolds fabricated via selective laser melting, *J. Mater. Res. Technol.* 15 (2021) 6797–6812. <https://doi.org/10.1016/j.jmrt.2021.11.112>.

[36] X. Yang, Q. Yang, Y. Shi, L. Yang, S. Wu, C. Yan, Y. Shi, Effect of volume fraction and unit cell size on manufacturability and compressive behaviors of Ni-Ti triply periodic minimal surface lattices, *Addit. Manuf.* 54 (2022) 102737. <https://doi.org/10.1016/j.addma.2022.102737>.

[37] S. Saedi, S.E. Saghalian, A. Jahadakbar, N. Shayesteh Moghaddam, M. Taheri Andani, S.M. Saghalian, Y.C. Lu, M. Elahinia, H.E. Karaca, Shape memory response of porous NiTi shape memory alloys fabricated by selective laser melting, *J. Mater. Sci. Mater. Med.* 29 (2018). <https://doi.org/10.1007/s10856-018-6044-6>.

[38] X. Li, Q. Li, M. Nie, D. Kong, Z. Liu, Z. Zhang, Evading the strength-ductility trade-off dilemma in steel-nickel heterostructured material by bionic crossed-lamellar structures, *Virtual Phys. Prototyp.* 18 (2023). <https://doi.org/10.1080/17452759.2023.2266640>.

[39] H. Jiang, X. Wang, R. Xi, G. Li, H. Wei, J. Liu, B. Zhang, S. Kustov, K. Vanmeensel, J. Van Humbeeck, G. Zhao, Size effect on the microstructure, phase transformation behavior, and mechanical properties of NiTi shape memory alloys fabricated by laser powder bed fusion, *J. Mater. Sci. Technol.* 157 (2023) 200–212. <https://doi.org/10.1016/j.jmst.2023.02.026>.

[40] S. Dadbakhsh, M. Speirs, J.P. Kruth, J. Van Humbeeck, Influence of SLM on shape memory and compression behaviour of NiTi scaffolds, *CIRP Ann. - Manuf. Technol.* 64 (2015) 209–212. <https://doi.org/10.1016/j.cirp.2015.04.039>.

[41] A.A. Martin, N.P. Calta, S.A. Khairallah, J. Wang, P.J. Depond, A.Y. Fong, V. Thampy, G.M. Guss, A.M. Kiss, K.H. Stone, C.J. Tassone, J. Nelson Weker, M.F. Toney, T. van Buuren, M.J. Matthews, Dynamics of pore formation during laser powder bed fusion additive manufacturing, *Nat. Commun.* 10 (2019) 1–10. <https://doi.org/10.1038/s41467-019-10009-2>.

[42] T. DebRoy, H.L. Wei, J.S. Zuback, T. Mukherjee, J.W. Elmer, J.O. Milewski, A.M. Beese, A. Wilson-Heid, A. De, W. Zhang, Additive manufacturing of metallic components – Process, structure and properties, *Prog. Mater. Sci.* 92 (2018) 112–224. <https://doi.org/10.1016/j.pmatsci.2017.10.001>.

[43] S.M. Thompson, L. Bian, N. Shamsaei, A. Yadollahi, An overview of Direct Laser Deposition for additive manufacturing; Part I: Transport phenomena, modeling and diagnostics, *Addit. Manuf.* 8 (2015) 36–62. <https://doi.org/10.1016/j.addma.2015.07.001>.

[44] T. Mukherjee, V. Manvatkar, A. De, T. DebRoy, Dimensionless numbers in additive manufacturing, *J. Appl. Phys.* 121 (2017). <https://doi.org/10.1063/1.4976006>.

[45] M. McMillan, M. Leary, M. Brandt, Computationally efficient finite difference method for metal additive manufacturing: A reduced-order DFAM tool applied to SLM, *Mater. Des.* 132 (2017) 226–243. <https://doi.org/10.1016/j.matdes.2017.06.058>.

[46] T. Tancogne-Dejean, D. Mohr, Stiffness and specific energy absorption of additively-manufactured metallic BCC metamaterials composed of tapered beams, *Int. J. Mech. Sci.* 141 (2018) 101–116. <https://doi.org/10.1016/j.ijmecsci.2018.03.027>.

[47] B. Cheng, S. Price, J. Lydon, K. Cooper, K. Chou, On Process Temperature in Powder-Bed Electron Beam Additive Manufacturing: Model Development and Validation, *J. Manuf. Sci. Eng. Trans. ASME* 136 (2014) 1–12. <https://doi.org/10.1115/1.4028484>.

[48] S. Hocine, H. Van Swygenhoven, S. Van Petegem, Verification of selective laser melting heat source models with operando X-ray diffraction data, *Addit. Manuf.* 37 (2021) 101747. <https://doi.org/10.1016/j.addma.2020.101747>.

[49] A.J. Wolfer, J. Aires, K. Wheeler, J.P. Delplanque, A. Rubenchik, A. Anderson, S. Khairallah, Fast solution strategy for transient heat conduction for arbitrary scan paths in additive manufacturing, *Addit. Manuf.* 30 (2019) 100898. <https://doi.org/10.1016/j.addma.2019.100898>.

[50] Y. Yang, F. van Keulen, C. Ayas, A computationally efficient thermal model for selective laser melting, *Addit. Manuf.* 31 (2020) 100955. <https://doi.org/10.1016/j.addma.2019.100955>.

[51] L.C. Wei, L.E. Ehrlich, M.J. Powell-Palm, C. Montgomery, J. Beuth, J.A. Malen, Thermal conductivity of metal powders for powder bed additive manufacturing, *Addit. Manuf.* 21 (2018) 201–208. <https://doi.org/10.1016/j.addma.2018.02.002>.

[52] C. Zanotti, P. Giuliani, G. Riva, A. Tuissi, A. Chrysanthou, Thermal diffusivity of Ni-Ti SMAs, *J. Alloys Compd.* 473 (2009) 231–237. <https://doi.org/10.1016/j.jallcom.2008.05.040>.

[53] A.K. Rai, H. Trpathy, R.N. Hajra, S. Raju, S. Saroja, Thermophysical properties of Ni based super alloy 617, *J. Alloys Compd.* 698 (2017) 442–450. <https://doi.org/10.1016/j.jallcom.2016.12.183>.

[54] J.N. Zhu, E. Borisov, X. Liang, R. Huizenga, A. Popovich, V. Bliznuk, R. Petrov, M. Hermans, V. Popovich, Controlling microstructure evolution and phase transformation behavior in additive manufacturing of nitinol shape memory alloys by tuning hatch distance, *J. Mater. Sci.* 57 (2022) 6066–6084. <https://doi.org/10.1007/s10853-022-07007-z>.

[55] N. An, G. Yang, K. Yang, J. Wang, M. Li, J. Zhou, Implementation of Abaqus user subroutines and plugin for thermal analysis of powder-bed electron-beam-melting additive manufacturing process, *Mater. Today Commun.* 27 (2021) 102307. <https://doi.org/10.1016/j.mtcomm.2021.102307>.

[56] Z. Yan, W. Liu, Z. Tang, X. Liu, N. Zhang, M. Li, H. Zhang, Review on thermal analysis in laser-based additive manufacturing, *Opt. Laser Technol.* 106 (2018) 427–441. <https://doi.org/10.1016/j.optlastec.2018.04.034>.

[57] C. Hagenlocher, P. O'Toole, W. Xu, M. Brandt, M. Easton, A. Molotnikov, Analytical modelling of heat accumulation in laser based additive manufacturing processes of metals, *Addit. Manuf.* 60 (2022) 103263. <https://doi.org/10.1016/j.addma.2022.103263>.

[58] D.J. Hartl, J.T. Mooney, D.C. Lagoudas, F.T. Calkins, J.H. Mabe, Use of a Ni60Ti shape memory alloy for active jet engine chevron application: II. Experimentally validated numerical analysis, *Smart Mater. Struct.* 19 (2010). <https://doi.org/10.1088/0964-1726/19/1/015021>.

[59] J. Khalil Allafi, X. Ren, G. Eggeler, The mechanism of multistage martensitic transformations in aged Ni-rich NiTi shape memory alloys, *Acta Mater.* 50 (2002) 793–803. [https://doi.org/10.1016/S1359-6454\(01\)00385-8](https://doi.org/10.1016/S1359-6454(01)00385-8).

[60] M. Mehrpouya, A. Gisario, M. Elahinia, Laser welding of NiTi shape memory alloy: A review, *J. Manuf. Process.* 31 (2018) 162–186. <https://doi.org/10.1016/j.jmapro.2017.11.011>.

[61] M. Gäumann, C. Bezençon, P. Canalis, W. Kurz, Single-crystal laser deposition of superalloys: Processing-microstructure maps, *Acta Mater.* 49 (2001) 1051–1062. [https://doi.org/10.1016/S1359-6454\(00\)00367-0](https://doi.org/10.1016/S1359-6454(00)00367-0).

[62] P.A. Hooper, Melt pool temperature and cooling rates in laser powder bed fusion, *Addit. Manuf.* 22 (2018) 548–559. <https://doi.org/10.1016/j.addma.2018.05.032>.

[63] C.L.A. Leung, S. Marussi, R.C. Atwood, M. Towrie, P.J. Withers, P.D. Lee, In situ X-ray imaging of defect and molten pool dynamics in laser additive manufacturing, *Nat. Commun.* 9 (2018) 1–9. <https://doi.org/10.1038/s41467-018-03734-7>.

5

Origin of premature fracture and enhancement of superelasticity

This chapter investigates the premature fracture observed in Ni-rich NiTi metamaterials manufactured by L-PBF. To address this issue, a comparative analysis was conducted on two structures: the Gyroid network and Diamond shell TPMS-type unit cell architectures. Numerical and experimental results reveal that, due to the tension-compression asymmetry of NiTi, the structural stability of bending- and stretching-dominated designs is reversed compared to typical elastic-plastic responses. The premature fracture and partial superelasticity in the as-fabricated samples are attributed to the limited ability to accommodate tensile stress of base NiTi, caused by a lack of martensitic transformation and slip systems. Based on these findings, a heat treatment introducing Ni_4Ti_3 precipitates was employed, successfully achieving macroscopic superelasticity in the NiTi metamaterials, with consistency between model prediction and experiments.

5

This chapter is based on publication Z. Yan, J.-N. Zhu, Y.-C. Yang, H. Brouwer, T. Riemslag, J.R. Jinschek, M. Hermans, J. Jovanova, V. Popovich, Origin of premature fracture and enhancement of superelasticity in laser additively manufactured Ni-rich NiTi metamaterials, *Scr. Mater.* 259 (2025) 116558.

5.1. Introduction

It is widely reported that recoverable large deformation in NiTi metamaterials can be successfully achieved using shape memory effect of Ti-rich or equiatomic NiTi, rather than the superelasticity of Ni-rich NiTi [1–4]. Though researchers have attempted to manufacture superelastic metamaterials using Ni-rich NiTi alloys, only partial superelasticity can be achieved and premature fracture has been widely reported [5,6]. In Chapter 4, it is found that the heterogeneous microstructure causes narrow hysteresis and low recoverability during uniaxial compression on NiTi metamaterials. Thus, this chapter focuses on the fracture mechanisms of Ni-rich NiTi metamaterials fabricated using laser powder bed fusion (L-PBF) and further provides a solution for achieving superelasticity in NiTi metamaterials.

Numerous studies have investigated the fracture behaviors of superelastic NiTi alloys produced through conventional manufacturing methods [7–10]. However, the failure criteria and fracture mechanisms of additively manufactured NiTi base materials under various loading directions and stress states remain unclear. Failure theories, such as the von Mises and Johnson-Cook criteria, which are commonly applied to metallic metamaterials made from ductile metals, are not directly applicable to the modeling of NiTi structures [11,12]. Therefore, the fracture mechanism of NiTi metamaterials has yet to be explained [13].

The macroscopic properties of NiTi metamaterials are influenced by the interaction between the NiTi functionalities and the structural stiffness [5,14]. The former, originating from reversible martensitic transformation, is sensitive to the local microstructure and compositions (As discussed in Chapter 4). The structural stiffness is determined by the unit cell architecture and the relative density [15]. This interaction between microstructure, mesoscale architectures, and macroscopic response indicates that the premature fracture mechanism could be considered as material-related or structure-related.

Based on the structure-stiffness relationship in mechanical metamaterials, the deformation modes are categorized into two types: bending-dominated and stretching-dominated behaviors [16–18]. By generalizing the Gibson-Ashby theory to martensitic transformation, bending-dominated structures exhibit higher deformation recoverability than stretching-dominated structures due to their structural compliance [5,14,19]. Among different design paradigms of mechanical metamaterials, two TPMS-type structures were chosen: Diamond shell structure, which exhibits typical stretching-dominated behavior, and the Gyroid network structure, which is typically bending-dominated [20,21]. The rationale behind this choice is to investigate whether the premature fracture observed Ni-rich NiTi structure is related to the structure configuration, as premature fracture is not observed in bulk samples when the same process parameters are used in the manufacturing of all samples [5].

5.2. Geometry and computational models

In this chapter, TPMS-type architectures are chosen due to their geometrical smoothness to reduce stress concentration. In TPMS architectures, the Diamond shell and Gyroid network structures are used to exemplify stretching-dominated and bending-dominated behaviors. The geometry of the selected surfaces is described by the following level-set functions [22]:

For the Diamond surface,

$$\mathcal{O}_D(x, y, z) = \cos(X) \cos(Y) \cos(Z) + \sin(X) \sin(Y) \sin(Z) = c . \quad (5.1)$$

And for Gyroid surface:

$$\mathcal{O}_G(x, y, z) = \sin(X) \cos(Y) + \sin(Z) \cos(X) + \sin(Y) \cos(Z) = c , \quad (5.2)$$

where $X = (k \cdot 2\pi/L)x$, $Y = (k \cdot 2\pi/L)y$, and $Z = (k \cdot 2\pi/L)z$. k represents the tessellation number, and l is the dimension of the entire surface. This study uses a unit cell size of 5 mm and a configuration of $4 \times 4 \times 4$ (64) unit cells to consider the periodicity of metamaterials. The Diamond shell structure was generated by thickening a minimal surface into a shell structure with a nominal relative density of 0.25. The Gyroid network structure was modeled by dividing the solid volume using a single minimal surface, aiming for a nominal relative density of 0.3. Geometric operations were performed using an open-source package in Matlab 2024a and converted to STL format [23]. As a reference, the Gyroid network and Diamond shell structures with varying relative densities are presented in Figure 5.1. The nominal relative density is selected to limit structural compliance and match the actual relative density in the as-fabricated samples.

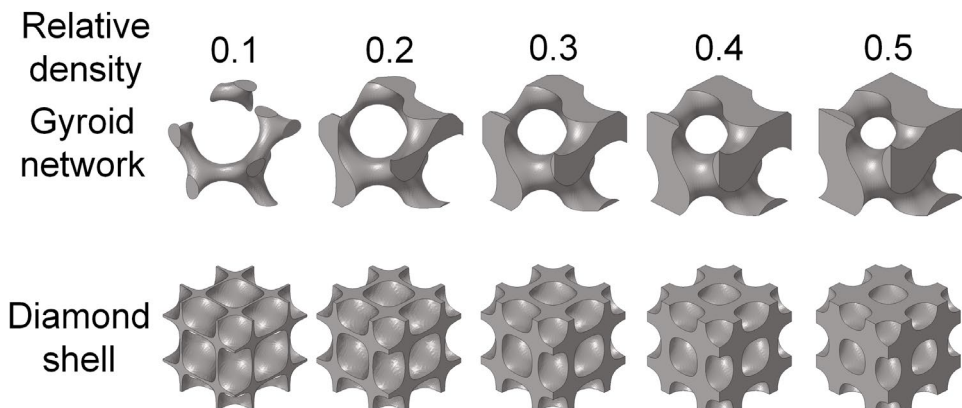


Figure 5.1 The geometrical model of the Gyroid network and Diamond shell structures.

For multi-cell simulation, the tetrahedral mesh with an average size of 0.12 mm was generated from the triangular mesh of these geometries. A phenomenological material model developed by Auricchio is used for numerical computations [24,25]. The potential plastic deformation due to yield was also considered. The increment of total strain $\Delta\epsilon$ is defined as the sum of elastic strain increment $\Delta\epsilon^{\text{el}}$ and the increment of equivalent transformation strain $\Delta\epsilon^{\text{tr}}$ and equivalent plastic strain $\Delta\epsilon^{\text{pl}}$:

$$\Delta\epsilon = \Delta\epsilon^{\text{el}} + \Delta\epsilon^{\text{tr}} + \Delta\epsilon^{\text{pl}} \quad (5.3)$$

The increment of equivalent transformation strain $\Delta\epsilon^{\text{tr}}$ is defined by:

$$\Delta\epsilon^{\text{tr}} = \Delta\xi_s \frac{\partial G^{\text{tr}}}{\partial \sigma}, \quad (5.4)$$

where G^{tr} is the transformation flow potential, ξ the martensitic volume fraction, and σ the Cauchy stress tensor. The numerical samples were compressed between two rigid planes, with the upper plane moving downward by 0.066 mm, and a tangential friction coefficient of 0.2 assumed for all contacts. The numerical solution was completed using the commercial package Abaqus/Explicit 2019. A semi-automatic mass scaling method, with a target of 2,500,000 steps was used after monitoring the kinetic energy in an explicit solution.

5.3. Experiments

Samples were fabricated using laser powder bed fusion (Aconity 3D Midi) from $\text{Ni}_{51.4}\text{Ti}_{48.6}$ powder prepared by gas atomization in a high-purity argon-filled chamber. Optimized process parameters were employed, including a laser power of 400 W, scanning speed of 1250 mm/s, hatch distance of 0.120 mm, layer thickness of 0.030 mm, and a stripe scanning strategy with a 67.5° rotation [26]. Following printing, some samples underwent heat treatment including solution annealed at 950 °C for 60 min followed by air cooling for 20 minutes, aging treatment at 450 °C for 90 minutes followed by air cooling to room temperature. All samples were sealed in vacuum quartz ampoules to prevent oxidation during heat treatment.

For measuring the transformation temperatures, differential scanning calorimetry (DSC, TA Instruments DSC250) was employed at a heating/cooling rate of 10 °C/min over a temperature range of -70 to +150 °C. A quasi-static tensile test was performed on mini-scaled dogbone samples using a contact extensometer with a 7 mm gauge length (Sample design is shown in Figure 5.2). Cyclic tension tests were carried out consisting of 15 cycles with a constant maximum displacement of 0.22 mm. Quasi-static compression tests were carried out on Gyroid and Diamond structures using a contact extensometer using a contact

extensometer with a maximum displacement of 4.4 mm. The samples were quasi-statically compressed until complete structural failure. All quasi-static uniaxial tests were conducted on a Zwick 100 universal mechanical testing platform, equipped with a high-temperature chamber set to 54 °C, under quasi-static conditions with a strain rate of $2 \times 10^{-4} \text{ s}^{-1}$. Fracture analysis was performed using a Scanning Electron Microscope (JSM-IT100) on samples from uniaxial compression tests. EBSD samples were prepared using electropolishing (Struers LectroPol5) on the macroscopic (100) cross-section aligned with the building direction (BD).

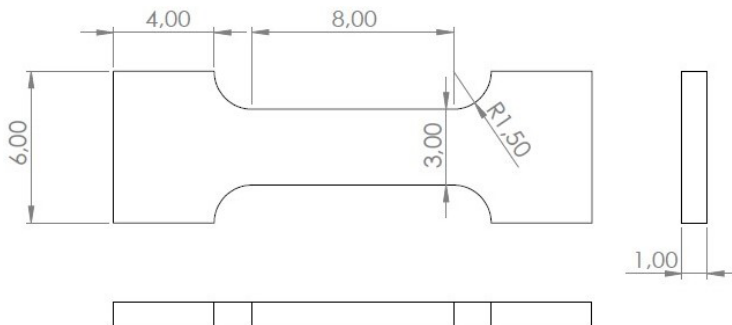


Figure 5.2 Dimension of dog-bone sample used in tensile tests.

5

Texture analysis was conducted using a scanning electron microscope (SEM) equipped with an electron backscatter diffraction (EBSD) detector (Helios G4) with a step size of 1.5 μm . Characterization using both bright-field transmission electron microscopy (TEM) TEM and scanning transmission electron microscopy (STEM) was conducted with spherical aberration-corrected transmission electron microscopes at an accelerating voltage of 300 kV. TEM experiments utilized an image-corrected Titan TEM 80-300 (Thermo Fisher Scientific Inc.) with a OneView camera (Gatan Inc.). STEM and EDS experiments were performed with a Spectra 300 S/TEM (Thermo Fisher Scientific Inc.), equipped with high-angle annular dark field (HAADF) and an Ultra-X EDS detector. For the STEM experiment, a probe semi-convergence angle of 28.7 mrad and a camera length of 342 mm were used.

5.4. Results and discussion

5.4.1. Premature fracture in as-fabricated samples

All mechanical tests are conducted at the test temperature of 54 °C, higher than the austenite finish temperature as shown in Figure 5.3. Compressive fracture tests were conducted on the as-fabricated samples (Figure 5.4 (a)) with loading direction (LD) aligned

with the building direction (BD) at a temperature of 54 °C. The engineering stress-strain curves from fracture tests are compared in Figure 5.4 (c). The engineering stress-strain curves show a reversed trend compared to the deformation behavior of metamaterials made from ductile metals (Figure 5.4 (b)) [17,20,27]. Diamond shell structures, which are stretching-dominated, exhibit an increasing effective stress and plateau-like response after initial elasticity. The Gyroid network structure shows typical elastic-brittle behavior [16]. The stress oscillates after the elasticity stage and the deformation mode is brittle fracture. The initial damage strain of the Gyroid structure is 3.7%, with a collapse strain of 7.3%. In contrast, the Diamond structure exhibits an initial damage strain of 12.5% and a collapse strain of 15.9%. The stability of the stretching-dominated Diamond structure makes it more attractive for load-bearing applications. This reversed trend in large deformation compression implies a need for a reexamination of the constitutive NiTi behaviors.

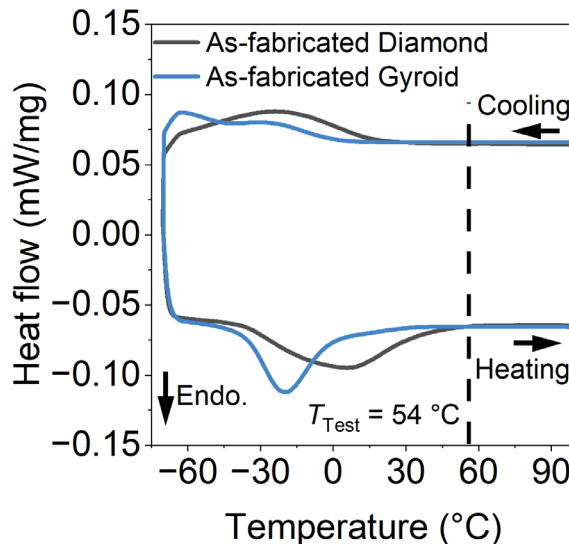


Figure 5.3 DSC curves for as-fabricated Gyroid network and Diamond shell structures.

Generally, the fracture of mechanical metamaterials involves the formation and propagation of cracks. To analyze the premature fracture, experiments were interrupted before the final collapse of the structures (Figure 5.4 (c)). The SEM images of crack initiation and propagation are shown in Figure 5.4 (d) and (e). The crack formation exhibits a repeated pattern in different unit cells (Figure 5.5 and Figure 5.6 (a)). In the Gyroid network unit cell, two discrete crack formations are observed (Figure 5.4 (d) ② ③), while three discrete crack initiations are observed in the Diamond structure (Figure 5.4 (e) ④ ⑤ ⑥).

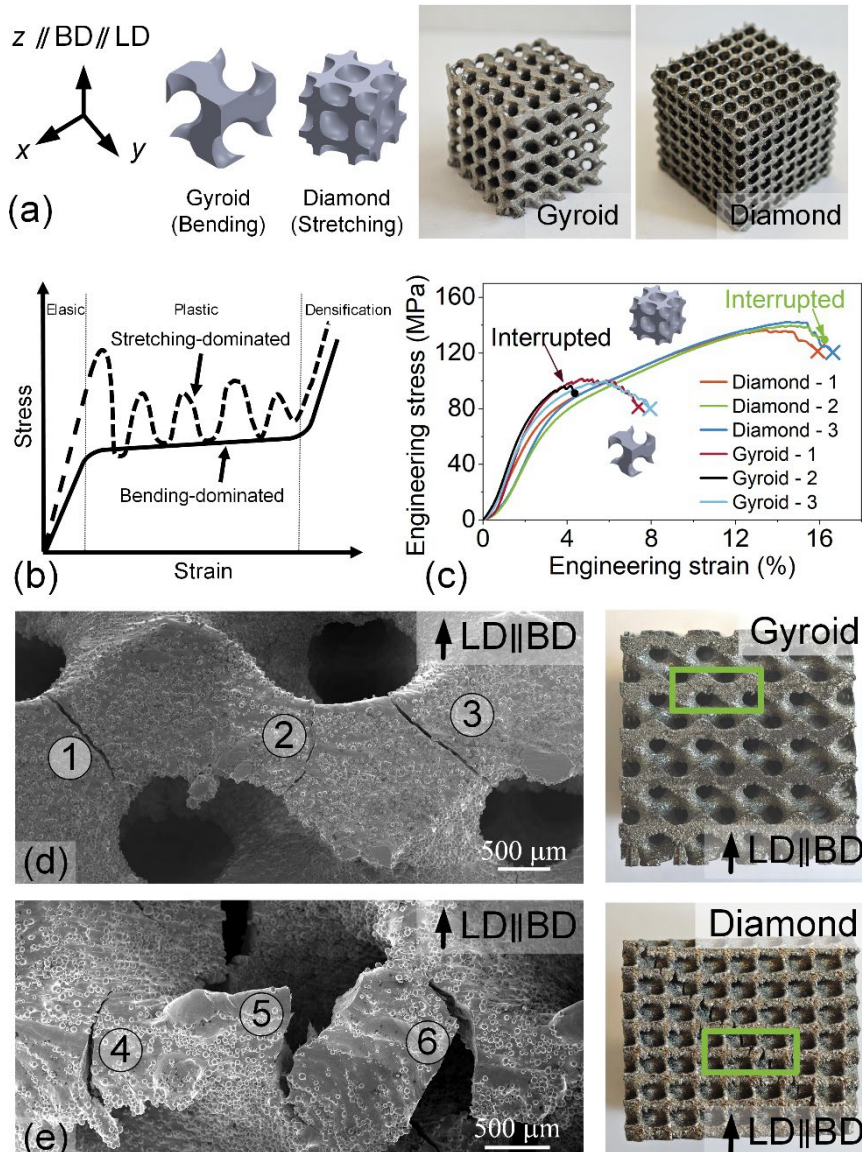


Figure 5.4 (a) Geometric model and as-fabricated samples; (b) Schematic diagram of bending-dominated and stretching-dominated behavior of ductile metallic metamaterials, reproduced from [20,28]; (c) Engineering stress-strain curves of Gyroid and Diamond samples under uniaxial compression from fracture tests; (c) Profiles of interrupted samples; and crack formation in (d) Gyroid network and (e) Diamond shell structures and the selected area are marked by green rectangular box.

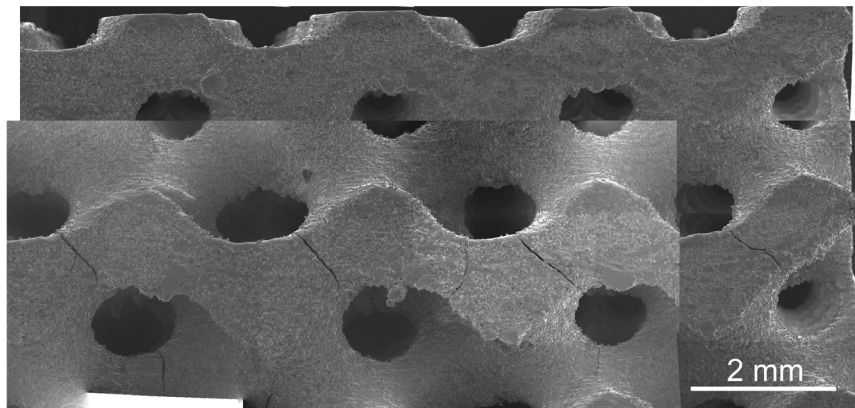


Figure 5.5 Crack initialization on the surface of Gyroid structures.

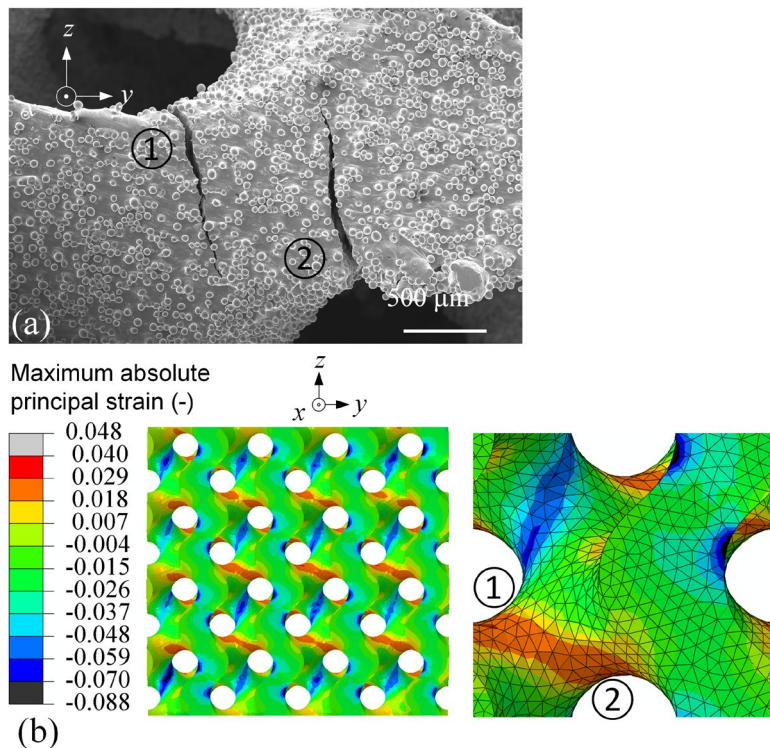


Figure 5.6 Cracks initialization in the internal unit cells: (a) SEM image from interrupted tests and (b) numerical results.

5.4.2. Origin of premature fracture

For these reversed phenomena from uniaxial compression, our hypothesis is that the tension-compression asymmetry of base NiTi leads to the premature failure of the as-fabricated structures. The asymmetric behavior between tension and compression in the as-fabricated bulk samples is compared in Figure 5.7 (a). Using the same parameters for manufacturing bulk samples, the compressive sample demonstrates stress-induced martensitic transformation at 54 °C. In the initial cycle, it shows significant compressive deformation capacity with a maximum strain of 8.3%. In the stabilized cycle, the bulk sample exhibits a maximum strain of 5.6% and a transformation strain of 3.7%. In contrast, the tensile sample only achieves a maximum strain of 4.0%, which is the best data in repeating tests. Cyclic tension tests reveal suppressed superelasticity, characterized by a recoverable strain of 1.75% and a narrow hysteresis area. Recent studies have demonstrated that Ni-rich NiTi with compressive superelasticity can be achieved across a broad process window, but the process window for tensile superelasticity is more limited [29,30]. For tensile superelasticity, careful adjustment of Ni concentration and texture [31,32], or improvements through heat treatment promoting Ni_4Ti_3 precipitation [33], are required. The suppressed tensile superelasticity observed in our as-fabricated samples is consistent with the above findings.

5

To test our hypothesis, the numerical results of the multi-cell model were computed based on data from the first cycle as shown in Table 5.1 and Table 5.2. The maximum principal stresses for these structures are illustrated in Figure 5.7 (b), with a colormap indicating compressive and tensile principal strain. Under uniaxial compression along the macroscopic [100] direction, the Gyroid network structure, due to its bending-dominated behavior and non-slender geometry, exhibits high tensile principal strain. In contrast, the Diamond shell structure is less sensitive to tensile strain under the same loading conditions. Figure 5.7 (c) shows the equivalent transformation strains for the Gyroid and Diamond structures. In the Gyroid structure, transformation localization forms in both compressive and tensile areas, but these transformation regions remain isolated. In the Diamond shell structure, martensitic transformations are interconnected along the compressive loading direction under uniaxial compression. By comparing the interrupted experiments (Figure 5.4 (c)(d)) and numerical results Figure 5.7 (b), the observed crack initiations in both structures correspond to areas of concentrated tensile stress. Therefore, the cracks at the millimeter scale in both structures are initiated from tensile stress areas. Under uniaxial compression with the same macroscopic loading, the Gyroid structure is more susceptible to crack initiation due to the tensile sensitivity of bending-dominated behavior.

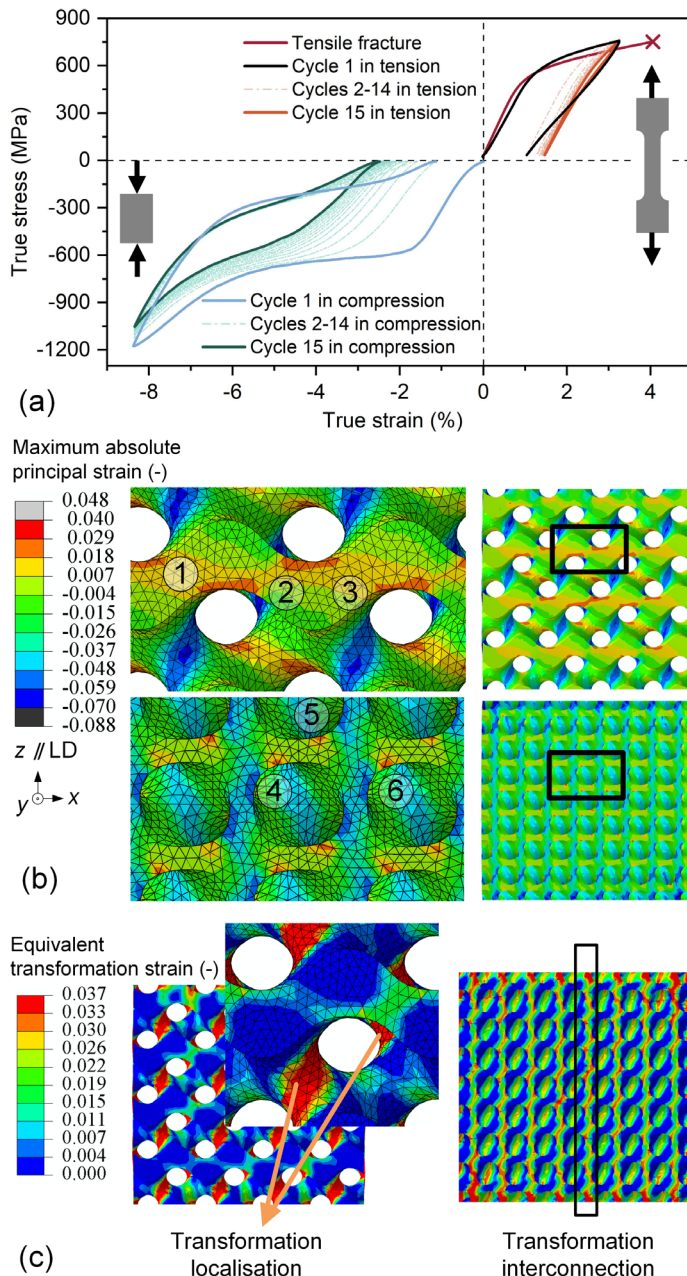


Figure 5.7 (a) Tension-compression asymmetry of base NiTi; (b) Maximum absolute principal strain; (c) Equivalent transformation strain of the Gyroid and Diamond structures under uniaxial compression at maximum loading.

Table 5.1 Thermo-mechanical properties of base NiTi used in numerical models.

E_A (MPa)	E_M (MPa)	ν_A (-)
41327	49889	0.33
ν_M (-)	Maximum transformation strain (-)	Start stress in forward transformation under tension (MPa)
0.33	0.037	460
C_s^{fwd} (MPa K ⁻¹)	Start stress in forward transformation (MPa)	Finish stress in forward transformation (MPa)
8.2	470	900
C_s^{rev} (MPa K ⁻¹)	Start stress in reverse transformation (MPa)	Finish stress in reverse transformation (MPa)
8.2	530	100

Table 5.2 Plastic properties of base NiTi used in numerical models (from Chapter 6).

True stress (MPa)	True strain (-)	True stress (MPa)	True strain (-)
1642	0.081	1908	0.111
1759	0.087	1916	0.117
1827	0.093	1918	0.123
1867	0.099	1917	0.129
1893	0.105		

From a macroscopic view of the structures in Figure 5.8, the final failure of both structures exhibits a shear banding along the macroscopic (110) plane. Clear brittle fracture characteristics are observed on the fracture surfaces, as shown in Figure 5.8 (a) and (b). At high magnification of river-like patterns, some dimples were observed, indicating ductile damage during crack propagation. However, the size and distribution of these micro-dimples suggest that ductile damage is not the dominant mechanism in crack formation and propagation [9].

In the Diamond shell structure, continuous fracture surfaces are observed along the macroscopic {110} planes, with two distinct regions identified in Figure 5.8 (b): cleavage river patterns and tearing ridges in the tensile area, and a smooth shear plane. Cracks initially form in the tensile region, and once stability is lost as the cracks propagate, the entire Diamond structure collapses along the continuous shear plane [20,21]. In the Gyroid structure, two discrete fracture surfaces are intersected as shown in Figure 5.8 (d). Cracks form in the

tensile region due to low tensile strength. The rapid propagation of these cracks creates two fracture planes, and the intersection of these planes leads to the failure of a unit cell.

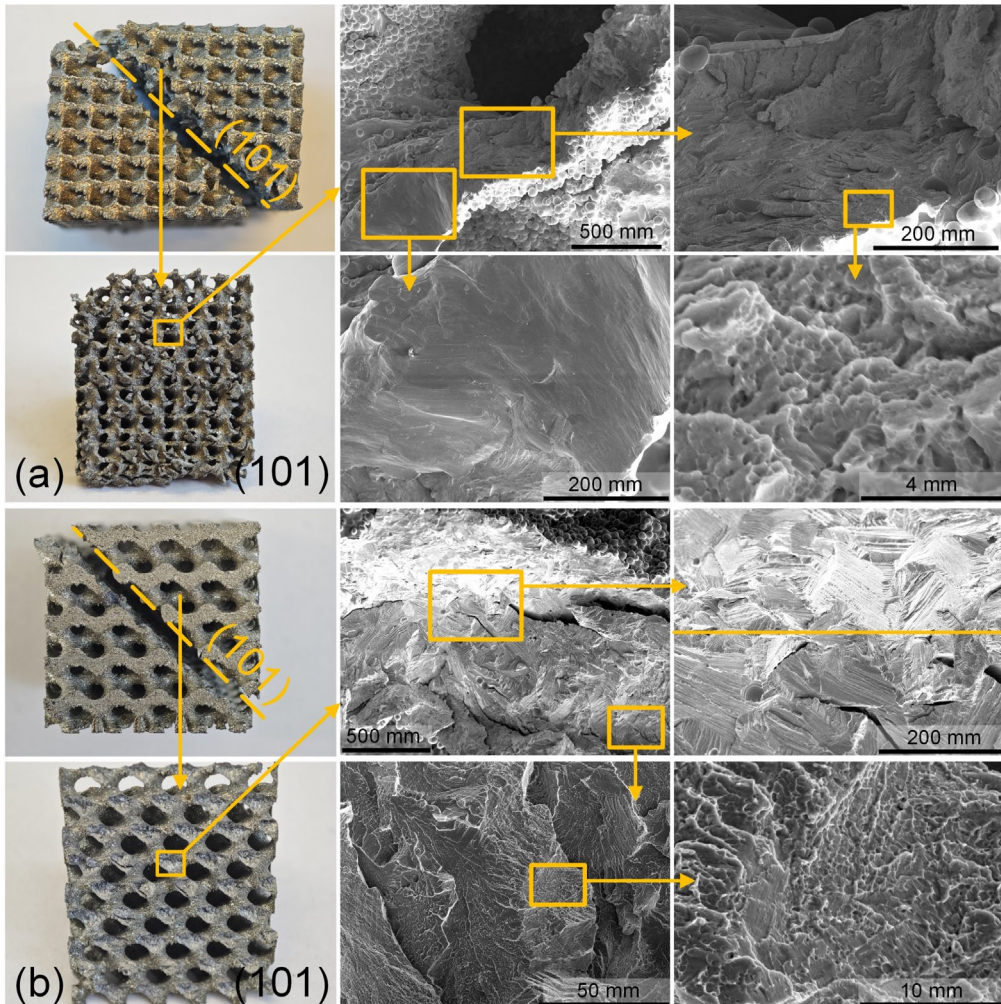


Figure 5.8 Fracture analysis of (a) Gyroid and (b) Diamond structures.

The EBSD characterization on the macroscopic (100) plane//BD of the Diamond shell structure and Gyroid network structure is shown in Figure 5.9 (a), with a colormap corresponding to BD in the inverse pole figure (IPF). Since the slip system for the B2 phase is $\{110\}<001>$, the Taylor factors with loading direction along the building direction are plotted in Figure 5.9 (b) and (f). In the Diamond shell structure, grains with smaller Taylor

factors are primarily presented near the edges, as shown in the extracted grains (Figure 5.9 (g)). This leads to unstable deformation near the edges, consistent with the simulated results where tensile stress is concentrated in these areas.

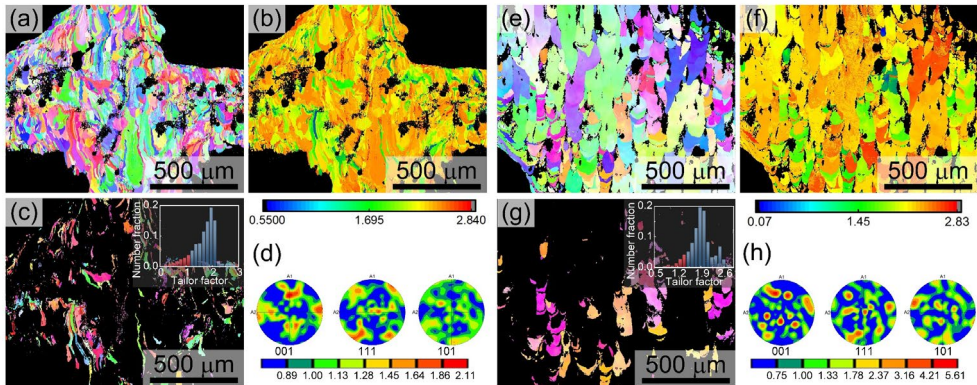


Figure 5.9 EBSD maps with inverse pole figure: (a) Diamond shell and (e) Gyroid network; Taylor factors for (b) Diamond shell and (f) Gyroid network; extracted grains with low Taylor factor values highlighted in red for (c) Diamond shell and (g) Gyroid network; and pole figure for (d) Diamond shell and (h) Gyroid network, with sample direction corresponding to the building direction.

5

The deformation modes of TPMS structures are typically defined by a generalized stiffness-properties relationship [5], assuming homogeneity and tension-compression symmetry in the base NiTi. However, experimental results reveal that the tension-compression asymmetry of base NiTi reverses the structural stability of these two structures. In this study, structural compliance was restricted to evaluate the true deformation capacity driven by reversible martensitic transformation. Large deformation in tensile regions cannot be achieved through either the initiation of martensitic transformation (transformation strain) or the limited slip system (plastic strain).

5.4.3. Heat treatments

Microstructural inhomogeneity (as discussed in Chapter 4) [13,34], and premature fracture have been identified as challenges that should be addressed for engineering application of NiTi metamaterials and structures. To simultaneously mitigate these issues, heat treatment was employed to enhance the superelasticity by introducing Ni_4Ti_3 precipitates in the Diamond shell structured NiTi. Homogenization followed by aging is applied to release

residual stress, homogenize microstructure and introduce Ni_4Ti_3 strengthening precipitates, to satisfy the assumption of homogeneity in mechanical metamaterials.

As shown in Figure 5.10 (a) and (b), the as-fabricated NiTi exhibits a relatively higher critical stress for stress-induced transformation (~ 65 MPa) compared to the heat-treated NiTi (~ 50 MPa). This difference can be attributed to the precipitation of Ni_4Ti_3 (Figure 5.10 (e)), which reduces the Ni content in the NiTi matrix and decreases the critical stress required for transformation [35]. Furthermore, the higher hardening rate observed in the heat-treated NiTi when the engineering strain exceeds 4.5%, as well as its larger recoverable strain ratio after unloading (72%) compared to the as-fabricated NiTi (35%), both suggest that Ni_4Ti_3 precipitates play a key role [33,36]: Enhancing dislocation slip resistance in both the austenite and stress-induced martensite phases, preventing plastic deformation even at higher stress levels (180 MPa). This enhanced slip resistance contributes to the superior superelasticity of the heat-treated NiTi. In contrast, the as-fabricated NiTi, lacking sufficient precipitation strengthening (Figure 5.10 (d)), cannot maintain stress-induced martensitic transformation alone with increasing strain and is accompanied by plastic deformation, resulting in a lower hardening rate when the strain exceeds 4.5%. Model-experiment consistency in superelastic response is successfully achieved in AM superelastic metamaterials, as mechanical metamaterials were initially defined as materials designed through mechanically homogenized models. Moreover, the premature fracture in Gyroid network structures was mitigated (Figure 5.11).

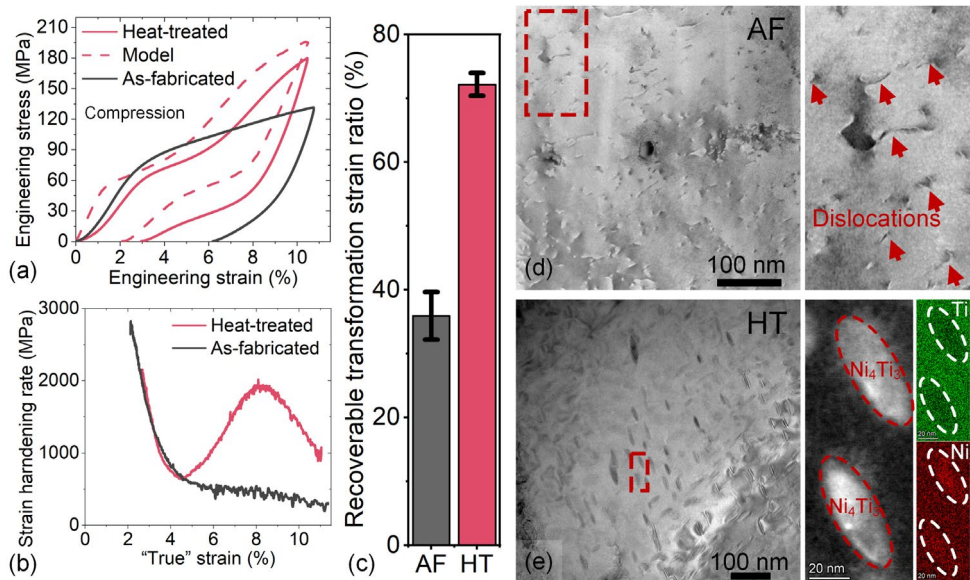


Figure 5.10 (a) Engineering stress-strain curves, (b) strain hardening rates during loading, (c) recoverable transformation strain ratios for as-fabricated (AF) and heat-treated (HT) Diamond shell structured NiTi; (d) bright-field transmission electron microscope (TEM) images showing dislocations in as-fabricated sample and (e) TEM images along with scanning transmission electron microscope (STEM) images and energy-dispersive X-ray spectra (STEM-EDS).

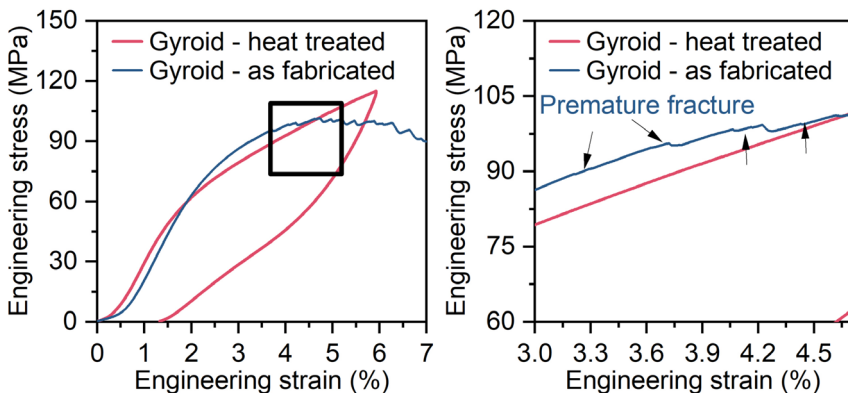


Figure 5.11 Comparison of engineering stress-strain curve for as-fabricated and heat-treated Gyroid network structure.

5.5. Conclusions

In summary, this chapter shows that the premature fracture of Ni-rich NiTi metamaterials originates from the low deformation ability of base material to accommodate the tensile stress. The tension-compression asymmetry changes the structural stability of bending- and stretching-dominated structures. For the first time, we achieved model-experiment consistency in superelastic metamaterials with a recoverable plateau-like response and second hardening. The heat treatment following L-PBF is crucial for microstructural homogenization and introducing Ni_4Ti_3 precipitates in Ni-rich NiTi metamaterials. These insights can facilitate the design of new metamaterial architectures that better exploit the superelastic properties of NiTi alloys under complex loading conditions.

Appendix A

Two types of measurement errors usually lead to the overestimation of the deformation recoverability of Ni-rich NiTi metamaterials. As shown in Figure 5.A1, the actual recoverable strain of the as-fabricated Diamond shell structure is only 4%, but it reaches about 9% when data is collected without using an extensometer. These results are consistent with the earlier findings of Zhong et al. [32], which highlight the importance of using an extensometer for accurate data acquisition when testing the actual performance of superelastic structures [35].

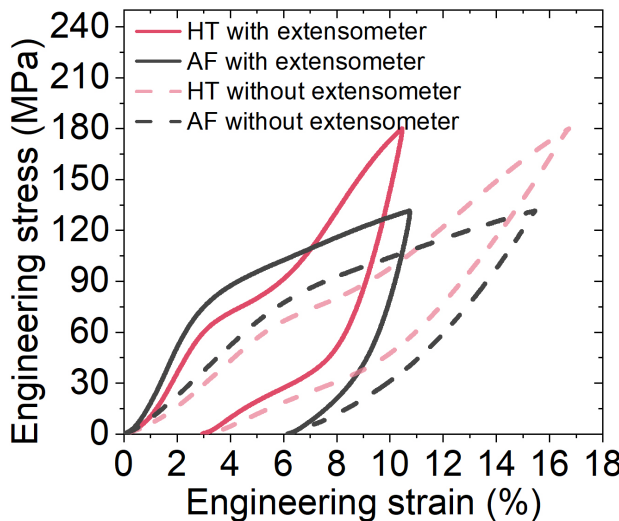


Figure 5.A1 Comparison of stress-strain curves of Diamond shell structures measured with and without using extensometer.

Comparative studies on Gyroid network structures with a relative density of 0.1 are shown in Figure 5.A2. The deformation recoverability is attributed to structural compliance, even when the martensitic transformation is suppressed, as shown in Figure 5.A2 (a) and (b). The quasi-linear response of the Gyroid network structure with a relative density of 0.1 is primarily attributed to elastic deformation and structural compliance, as martensitic transformation is actually suppressed. Therefore, the Gyroid network structure with low relative density is not considered further in this Chapter (Figure 5.A2 (c)).

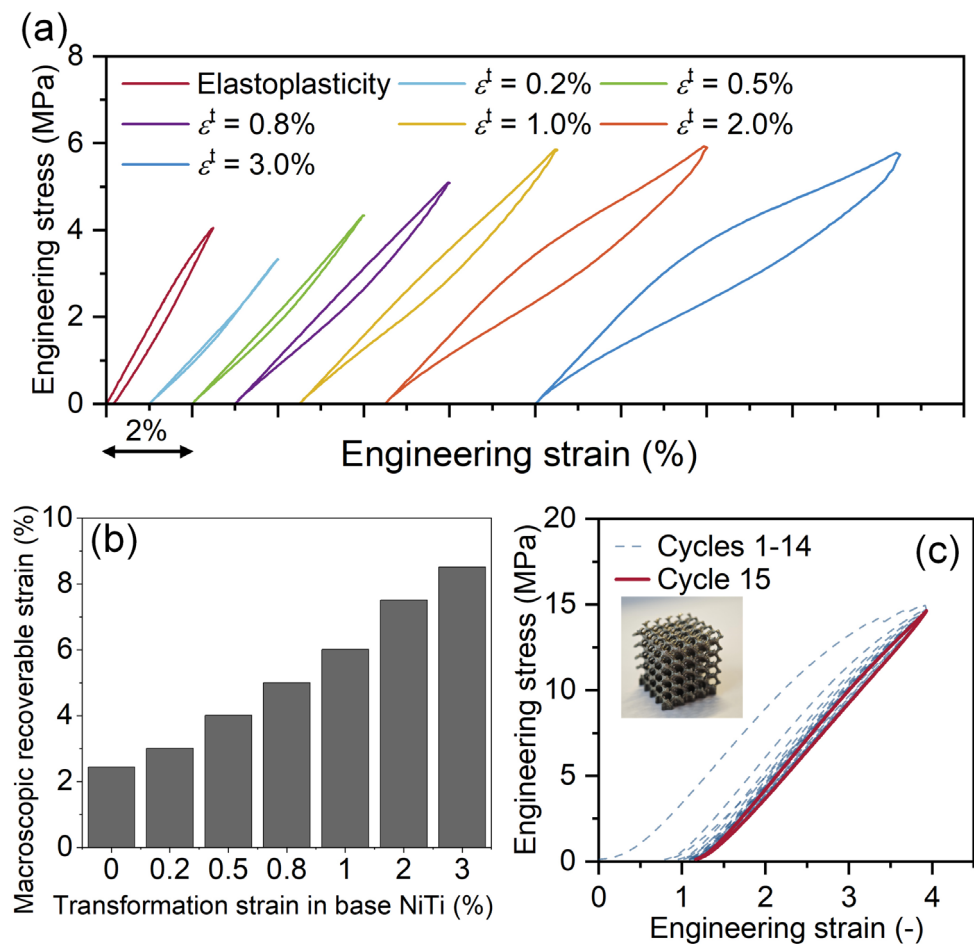


Figure 5.A2 Deformation recoverability caused by structural compliance: (a) stress-strain curve from numerical models, (b) recoverable macroscopic strain, and (c) experiments validation

Appendix B Table of notation

Structural parameters	
\emptyset	Level-set function of triply periodic minimum surfaces
c	Level-set value of triply periodic minimum surfaces
L	Size (edge length) of a unit cell
NiTi constitutive model	
$\Delta\epsilon$	increment of total strain
$\Delta\epsilon^{\text{el}}$	elastic strain increment
$\Delta\epsilon^{\text{tr}}$	increment of equivalent transformation strain
$\Delta\epsilon^{\text{pl}}$	equivalent plastic strain
G^{tr}	Transformation flow potential
ξ_s	Martensitic volume fraction
σ	Cauchy stress tensor

References

[1] Z. Xiong, M. Li, S. Hao, Y. Liu, L. Cui, H. Yang, C. Cui, D. Jiang, Y. Yang, H. Lei, Y. Zhang, Y. Ren, X. Zhang, J. Li, 3D-Printing Damage-Tolerant Architected Metallic Materials with Shape Recoverability via Special Deformation Design of Constituent Material, *ACS Appl. Mater. Interfaces* 13 (2021) 39915–39924. <https://doi.org/10.1021/acsami.1c11226>.

[2] X. Li, H. Wang, L. Sun, X. Wang, Y. Pan, M. Zhou, X. Guo, 3D Chiral Energy-Absorbing Structures with a High Deformation Recovery Ratio Fabricated via Selective Laser Melting of the NiTi Alloy, *ACS Appl. Mater. Interfaces* (2023). <https://doi.org/10.1021/acsami.3c13270>.

[3] Q. Liu, S. Ghodrat, K.M.B. Jansen, Design and modelling of a reversible shape memory alloy torsion hinge actuator, *Mater. Des.* 237 (2024) 112590. <https://doi.org/10.1016/j.matdes.2023.112590>.

[4] Y. Yang, Y. Wang, Snapping for 4D-Printed Insect-Scale Metal-Jumper, *Adv. Sci.* 2307088 (2023) 1–10. <https://doi.org/10.1002/advs.202307088>.

[5] Z. Yan, J. Zhu, E. Borisov, T. Riemsdag, S. Paul, M. Hermans, J. Jovanova, V. Popovich, Superelastic response and damping behavior of additively manufactured Nitinol architected materials, *Addit. Manuf.* 68 (2023) 103505. <https://doi.org/10.1016/j.addma.2023.103505>.

[6] S. Dadbakhsh, M. Speirs, J.P. Kruth, J. Van Humbeeck, Influence of SLM on shape memory and compression behaviour of NiTi scaffolds, *CIRP Ann. - Manuf. Technol.* 64 (2015) 209–212. <https://doi.org/10.1016/j.cirp.2015.04.039>.

[7] B. Haghgouyan, C. Hayrettin, T. Baxevanis, I. Karaman, D.C. Lagoudas, Fracture toughness of NiTi—Towards establishing standard test methods for phase transforming materials, *Acta Mater.* 162 (2019) 226–238. <https://doi.org/10.1016/j.actamat.2018.09.048>.

[8] S. Gollerthan, M.L. Young, A. Baruj, J. Frenzel, W.W. Schmahl, G. Eggeler, Fracture mechanics and microstructure in NiTi shape memory alloys, *Acta Mater.* 57 (2009) 1015–1025. <https://doi.org/10.1016/j.actamat.2008.10.055>.

[9] Y. Cui, X. Zeng, V.B.C. Tan, Z. Zhang, Experimental and numerical studies of NiTi dynamic fracture behaviors under the impact loading, *Int. J. Mech. Sci.* 235 (2022) 107724. <https://doi.org/10.1016/j.ijmecsci.2022.107724>.

[10] A.L. McKelvey, Fatigue-crack propagation behavior in the shape-memory and superelastic alloy nitinol, *Metall. Mater. Trans. A* 32A (1999) 2001–743.

[11] T. Tancogne-Dejean, A.B. Spierings, D. Mohr, Additively-manufactured metallic micro-lattice materials for high specific energy absorption under static and dynamic loading, *Acta Mater.* 116 (2016) 14–28. <https://doi.org/10.1016/j.actamat.2016.05.054>.

[12] O. Al-Ketan, R.K. Abu Al-Rub, Multifunctional Mechanical Metamaterials Based on Triply Periodic Minimal Surface Lattices, *Adv. Eng. Mater.* 21 (2019) 1–39. <https://doi.org/10.1002/adem.201900524>.

[13] Z. Yan, J.N. Zhu, D. Hartl, T. Riemsdag, S.P. Scott, R. Petrov, M. Hermans, J. Jovanova, V. Popovich, Correlation between microstructural inhomogeneity and architectural design in additively manufactured NiTi shape memory alloys, *Virtual Phys. Prototyp.* 19 (2024) 1–20. <https://doi.org/10.1080/17452759.2024.2396065>.

[14] P.A. Michailidis, N. Triantafyllidis, J.A. Shaw, D.S. Grummon, Superelasticity and stability of a shape memory alloy hexagonal honeycomb under in-plane compression, *Int. J. Solids Struct.* 46 (2009) 2724–2738. <https://doi.org/10.1016/j.ijsolstr.2009.03.013>.

[15] X. Yu, J. Zhou, H. Liang, Z. Jiang, L. Wu, Mechanical metamaterials associated with stiffness, rigidity and compressibility: A brief review, *Prog. Mater. Sci.* 94 (2018) 114–173. <https://doi.org/10.1016/j.pmatsci.2017.12.003>.

[16] L.J. Gibson, M.F. Ashby, *Cellular Solids: Structure and Properties*, Cambridge University Press, 1997. <https://books.google.nl/books?id=IySUR5sn4N8C>.

[17] N.A. Fleck, V.S. Deshpande, M.F. Ashby, Micro-architected materials: Past, present and future, *Proc. R. Soc. A Math. Phys. Eng. Sci.* 466 (2010) 2495–2516. <https://doi.org/10.1098/rspa.2010.0215>.

[18] A. du Plessis, S.M.J. Razavi, M. Benedetti, S. Murchio, M. Leary, M. Watson, D. Bhate, F. Berto, Properties and applications of additively manufactured metallic cellular materials: A review, *Prog. Mater. Sci.* 125 (2022) 100918. <https://doi.org/10.1016/j.pmatsci.2021.100918>.

[19] J.A. Shaw, D.S. Grummon, J. Foltz, Superelastic NiTi honeycombs: fabrication and experiments, *Smart Mater. Struct.* 16 (2007) S170–S178. <https://doi.org/10.1088/0964-1726/16/1/S17>.

[20] O. Al-Ketan, R. Rowshan, R.K. Abu Al-Rub, Topology-mechanical property relationship of 3D printed strut, skeletal, and sheet based periodic metallic cellular materials, *Addit. Manuf.* 19 (2018) 167–183. <https://doi.org/10.1016/j.addma.2017.12.006>.

[21] O. Al-Ketan, R. Rezgui, R. Rowshan, H. Du, N.X. Fang, R.K. Abu Al-Rub, Microarchitected Stretching-Dominated Mechanical Metamaterials with Minimal Surface Topologies, *Adv. Eng. Mater.* 20 (2018) 1–15. <https://doi.org/10.1002/adem.201800029>.

[22] N. Qiu, Y. Wan, Y. Shen, J. Fang, Experimental and numerical studies on mechanical properties of TPMS structures, *Int. J. Mech. Sci.* 261 (2024) 108657. <https://doi.org/10.1016/j.ijmecsci.2023.108657>.

[23] A. Jones, M. Leary, S. Bateman, M. Easton, TPMS Designer: A tool for generating and analyzing triply periodic minimal surfaces, *Softw. Impacts* 10 (2021) 100167. <https://doi.org/10.1016/j.simpa.2021.100167>.

[24] F. Auricchio, R.L. Taylor, J. Lubliner, Shape-memory alloys: macromodelling and numerical simulations of the superelastic behavior, *Comput. Methods Appl. Mech. Eng.* 146 (1997) 281–312. [https://doi.org/10.1016/S0045-7825\(96\)01232-7](https://doi.org/10.1016/S0045-7825(96)01232-7).

[25] F. Auricchio, R.L. Taylor, Shape-memory alloys: modelling and numerical simulations of the finite-strain superelastic behavior, *Comput. Methods Appl. Mech. Eng.* 143 (1997) 175–194. [https://doi.org/10.1016/S0045-7825\(96\)01147-4](https://doi.org/10.1016/S0045-7825(96)01147-4).

[26] J.N. Zhu, E. Borisov, X. Liang, E. Farber, M.J.M. Hermans, V.A. Popovich, Predictive analytical modelling and experimental validation of processing maps in additive manufacturing of nitinol alloys, *Addit. Manuf.* 38 (2021) 101802. <https://doi.org/10.1016/j.addma.2020.101802>.

[27] T. Maconachie, M. Leary, B. Lozanovski, X. Zhang, M. Qian, O. Faruque, M. Brandt, SLM lattice structures: Properties, performance, applications and challenges, *Mater. Des.* 183 (2019) 108137. <https://doi.org/10.1016/j.matdes.2019.108137>.

[28] M. Benedetti, A. du Plessis, R.O. Ritchie, M. Dallago, S.M.J. Razavi, F. Berto, Architected cellular materials: A review on their mechanical properties towards fatigue-tolerant design and fabrication, *Mater. Sci. Eng. R Reports* 144 (2021) 100606. <https://doi.org/10.1016/j.mser.2021.100606>.

[29] S. Saedi, N. Shayesteh Moghaddam, A. Amerinatanzi, M. Elahinia, H.E. Karaca, On the effects of selective laser melting process parameters on microstructure and thermomechanical response of Ni-rich NiTi, *Acta Mater.* 144 (2018) 552–560. <https://doi.org/10.1016/j.actamat.2017.10.072>.

[30] N. Shayesteh Moghaddam, S. Saedi, A. Amerinatanzi, A. Hinojos, A. Ramazani, J. Kundin, M.J. Mills, H. Karaca, M. Elahinia, Achieving superelasticity in additively manufactured NiTi in compression without post-process heat treatment, *Sci. Rep.* 9 (2019) 1–11. <https://doi.org/10.1038/s41598-018-36641-4>.

[31] D. Han, X. Ren, Y. Zhang, X. Yu, X. Gang, C. Luo, Y. Min, Lightweight auxetic metamaterials: Design and characteristic study, *Compos. Struct.* 293 (2022) 115706. <https://doi.org/10.1016/j.compstruct.2022.115706>.

[32] S. Zhong, L. Zhang, Y. Li, X. Chen, S. Chai, G. Li, H. Liu, C. Guo, X. Wang, D. Zhang, J. Lu, Superelastic and robust NiTi alloys with hierarchical microstructures by laser powder bed fusion, *Addit. Manuf.* 90 (2024) 104319. <https://doi.org/10.1016/j.addma.2024.104319>.

[33] H.Z. Lu, H.W. Ma, W.S. Cai, X. Luo, Z. Wang, C.H. Song, S. Yin, C. Yang, Stable tensile recovery strain induced by a Ni₄Ti₃ nanoprecipitate in a Ni50.4Ti49.6 shape memory alloy fabricated via selective laser melting, *Acta Mater.* 219 (2021) 117261. <https://doi.org/10.1016/j.actamat.2021.117261>.

[34] H. Vashishtha, P. Jamshidi, A. Vrettou, A. Karez, M. Goode, H. Deyhle, A. James, S. Ahmad, C. Reinhard, M.M. Attallah, D.M. Collins, Microscale stress-geometry interactions in an additively manufactured NiTi cardiovascular stent: A synchrotron dual imaging tomography and diffraction study, *Mater. Charact.* 213 (2024) 114016. <https://doi.org/10.1016/j.matchar.2024.114016>.

[35] H. Sehitoglu, I. Karaman, R. Anderson, X. Zhang, K. Gall, H.J. Maier, Y. Chumlyakov, Compressive response of NiTi single crystals, *Acta Mater.* 48 (2000) 3311–3326. [https://doi.org/10.1016/S1359-6454\(00\)00153-1](https://doi.org/10.1016/S1359-6454(00)00153-1).

[36] Y. Cao, X. Zhou, D. Cong, H. Zheng, Y. Cao, Z. Nie, Z. Chen, S. Li, N. Xu, Z. Gao, W. Cai, Y. Wang, Large tunable elastocaloric effect in additively manufactured Ni–Ti shape memory alloys, *Acta Mater.* 194 (2020) 178–189. <https://doi.org/10.1016/j.actamat.2020.04.007>.

6

Tunable transformation stress-temperature relation in superelastic metamaterials

This chapter investigates the transformation stress-temperature relationship of Ni-rich NiTi superelastic metamaterials. In metallic metamaterials, energy absorption typically relies on the unrecoverable deformation of ductile metals; however, achieving energy absorption using recoverable deformation has not been fully explored. The practical use of superelasticity is often restricted by the temperature dependence and anisotropy of transformation stress. To address this, a numerical model of the temperature-dependent and anisotropic superelasticity in the Diamond shell structures was developed. Building on Chapter 5, numerical predictions were validated by large deformation compression and superelastic responses of heat-treated samples, showing a relative difference of less than 15% in maximum stress and transformation stresses. The recoverable plateau-like response in the macroscopic stress-strain curves originates from the interconnection of transformation localization into a continuous transformation region under uniaxial compression along the macroscopic [100] direction. A low transformation stress-temperature slope for the forward transformation of 0.9 MPa/°C was achieved. Cyclic stability was achieved through hinder dislocation motion using Ni_4Ti_3 precipitates, and specific energy absorption of 3.5 J/g can be obtained in cyclic compression tests. This chapter completes the model-manufacturing strategy for superelastic metamaterials through the microstructural and structural design of NiTi-based metamaterials.

This chapter is based on a journal paper to be submitted.

6.1. Introduction

According to the Gibson-Ashby theory and study of truss-based lattice materials by Deshpande et al. [1], the effective properties of mechanical metamaterials can be defined by the mesoscopic deformation mechanisms of unit cell architecture [1–3]. It is now known that based on the elastoplasticity theory of ductile metals, mechanical properties of metamaterials such as the anisotropic elasticity, yield strength, failure, and energy absorption can be controlled by unit cell architecture and relative density [4–6]. Within the continuum thermodynamical framework, phenomenological constitutive models of shape memory alloys have been well established for the computation of mechanical behaviors of NiTi structures with complex configurations [7–10]. By combining both, i.e. incorporating the transformation stress into the mechanical behavior of metamaterials, the effective transformation stress can be controlled by unit cell architecture and relative density [11–13].

Numerous studies have reported on the model-based design and computation of NiTi metamaterials, as well as experimental investigation on the compressive properties of NiTi metamaterials. However, achieving superelasticity in additively manufactured (AM) samples is still challenging. The early successful cases of 2D honeycombs produced through conventional manufacturing methods were reported by Shaw et al. [14] and Michailidis [12]. In previous chapters, we identified two mechanisms responsible for the partial superelasticity observed in as-fabricated Ni-rich NiTi metamaterials. The first mechanism is the microstructural inhomogeneity at the mesoscale, which impacts mesoscale deformation and the macroscopic response [15]. The second mechanism is the tension-compression asymmetry, particularly the low deformation limit to accommodate tensile stress in as-fabricated NiTi, which results in low structural stability and premature fracture [16]. Consequently, the recoverable plateau-like response after the initial elastic stage and the second stage of hardening by martensite (or densification) is not observed in L-PBF samples of superelastic metamaterials [15,16]. Instead, as-fabricated samples typically exhibit a pseudo-linear or ‘leaf-shaped’ response, characterized by low recoverable deformation and narrow hysteresis. An improved agreement between models and experiments is rarely reported.

Recent studies on L-PBF of NiTi structures have found that the microstructure in as-fabricated samples is influenced by geometrical parameters such as strut diameter and shell thickness [17–20]. On the one hand, the functionality and localized properties of NiTi are highly dependent on this microstructure and its composition [21]. On the other hand, when complex structures are under loading conditions such as tension, compression, shearing, and bending, they undergo stress-induced localized transformation. The localized functionalities of NiTi and the stress-induced localized transformation in complex structures do not align with design models, complicating the achievement of expected performance. This

inconsistency poses challenges in defining the effective properties of metamaterials, even with careful control over the relative density in the model and the actual process parameters in additive manufacturing [15,22].

To mitigate these challenges in the L-PBF process, a heat treatment has been proposed to homogenize and enhance the properties of NiTi. Early research has shown that heat treatment can effectively enhance the superelasticity of Ni-rich NiTi alloys. Lu et al. reported a stable tensile recovery strain in NiTi after heat treatment, attributed to the dislocation saturation around Ni_4Ti_3 precipitates [23]. Similarly, Cao et al. achieved a stable electrocaloric effect in additively manufactured NiTi after heat treatment [24]. Vashishtha et al. highlighted that the presence of highly heterogeneous phases and localized transformation was observed in a NiTi stent with a shape memory effect [25]. Additional successful cases include the work of Finazzi et al., who developed a heat treatment strategy involving L-PBF, followed by heat treatment and chemical etching, which improved the maximum recoverable strain to 5% in NiTi micro-struts [26].

Thus, this chapter focuses on achieving an effective transformation stress-temperature relationship for superelastic metamaterials through the synergistic interaction between mesostructure and microstructure. The theoretical superelastic response of Diamond shell structures is modeled, taking into account the temperature-dependent transformation behavior. A heat treatment is proposed to achieve consistency between modeled and experimental superelastic responses. The macroscopic functional response is discussed, with an analysis of the mesoscopic deformation of the Diamond structures.

6

6.2. Computational models

Finite element analyses were conducted to investigate the anisotropic transformation stress, mesoscopic deformation, energy dissipation of Ni-rich NiTi metamaterials. Unit-cell models with periodic boundary conditions were used to show theoretically superelasticity behavior. Multi-cell models were developed to understand the large deformation under uniaxial compression.

6.2.1. Base constitutive relation

We chose the Auricchio superelasticity model with the plasticity model [27,28]. The elastic properties are defined based on the martensitic volume ξ_s fraction by using the rule of mixtures. The total strain increment is assumed to be the sum of increment in elastic strain $\Delta\boldsymbol{\varepsilon}^{\text{el}}$, the increment in transformation strain $\Delta\boldsymbol{\varepsilon}^{\text{tr}}$ and the increment in plastic strain $\Delta\boldsymbol{\varepsilon}^{\text{p}}$:

$$\Delta\boldsymbol{\varepsilon} = \Delta\boldsymbol{\varepsilon}^{\text{el}} + \Delta\boldsymbol{\varepsilon}^{\text{tr}} + \Delta\boldsymbol{\varepsilon}^{\text{pl}}. \quad (6.1)$$

Both the increment in transformation strain and plastic strain follow a Drucker-Prager type function, with martensitic transformation driven by martensitic volume fraction ξ and plastic hardening driven by the equivalent plastic strain $\bar{\varepsilon}^{\text{p}}$. The relation between critical stress and temperature during the forward and reverse transformation is defined through phenomenological constant $C_s^{\text{fwd}} = d\sigma_s^{\text{fwd}} / dT$ [29]. All material properties used were calibrated based on uniaxial compression tests on heat-treated bulk samples under quasi-static conditions, using a one-dimensional reduction of the material model (Figure 6.1). The experimental details are shown in section 6.3.3, and more details are provided in Appendix A.

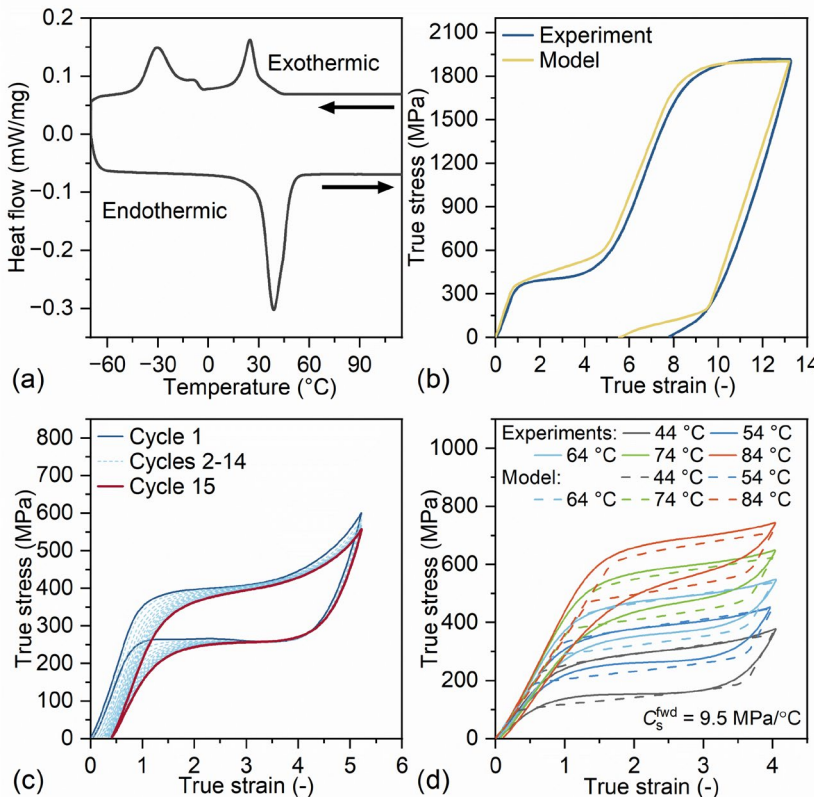


Figure 6.1 Characterization data of the NiTi bulk material used in the numerical model: (a) Differential Scanning Calorimetry (DSC) results for heat-treated samples, (b) comparison between experimental and computed large deformation response under uniaxial compression, (c) cyclic compression test results, and (d) temperature dependence of superelasticity.

6.2.2. Unit cell model with periodic boundary conditions

The geometry of the selected surfaces is described by the following level-set functions [30]:

$$\mathcal{O}_D(x, y, z) = \cos(X) \cos(Y) \cos(Z) + \sin(X) \sin(Y) \sin(Z) = c . \quad (6.2)$$

where $X = (2\pi k/l)x$, $Y = (2\pi k/l)y$, and $Z = (2\pi k/l)z$. k represents the number of unit cells in each direction, and l is the dimension of the entire surface. This study uses a unit cell size of 5 mm and a configuration of $4 \times 4 \times 4$ (64) unit cells to consider the periodicity. The designed samples have dimensions of 20 mm \times 20 mm \times 20 mm. The Diamond shell structure was generated by thickening a surface into a shell structure with a nominal relative density ranging from 0.1 to 0.5. Geometric operations were performed using an open-source package in Matlab 2021a and converted to STL format [31]. To further predict the inelastic response on different orientation, the unit cell model with orthogonal periodicity can be rotated with faces normal to the [100], [101], and [111] loading directions. The rotation vectors can be given as follows:

$$\boldsymbol{\Gamma}_{100} = \left\{ \begin{bmatrix} 1 \\ 0 \\ 0 \end{bmatrix}, \begin{bmatrix} 0 \\ 1 \\ 0 \end{bmatrix}, \begin{bmatrix} 0 \\ 0 \\ 1 \end{bmatrix} \right\} . \quad (6.3)$$

$$\boldsymbol{\Gamma}_{101} = \left\{ \begin{bmatrix} -1 \\ 1 \\ 0 \end{bmatrix} / \sqrt{2}, \begin{bmatrix} 0 \\ 1 \\ 0 \end{bmatrix}, \begin{bmatrix} 0 \\ 1 \\ 1 \end{bmatrix} / \sqrt{2} \right\} . \quad (6.4)$$

$$\boldsymbol{\Gamma}_{111} = \left\{ \begin{bmatrix} 1 \\ 1 \\ 1 \end{bmatrix} / \sqrt{3}, \begin{bmatrix} 1 \\ -1 \\ 0 \end{bmatrix} / \sqrt{2}, \begin{bmatrix} 1 \\ 1 \\ -2 \end{bmatrix} / \sqrt{6} \right\} . \quad (6.5)$$

6

As shown in Figure 6.2 (a), the edge lengths are reconstructed for periodicity after rotation. They are $(\sqrt{2}, \sqrt{2}, 1)$ for the [101] rotation and $(\sqrt{3}, \sqrt{2}, \sqrt{6})$ for the [111] rotation. Periodic boundary conditions were applied to the structure. The triangular files were imported into Altair HyperMesh 2023 and meshed with first-order tetrahedral elements (C3D4) sized between 0.08 mm and 0.16 mm to balance accuracy and efficiency. Symmetry constraints on paired surfaces enforced displacement differences equivalent to those of corresponding dummy nodes. Cyclic displacement loadings for uniaxial, pure shear, and triaxial loading were applied to the dummy nodes as shown in Figure 6.2 (b). The thermal boundary conditions were defined using constant temperatures of 44, 54, 64, 74, and 84 °C. The implicit solver in Abaqus/Standard 2019 is used to perform all unit-cell simulations.

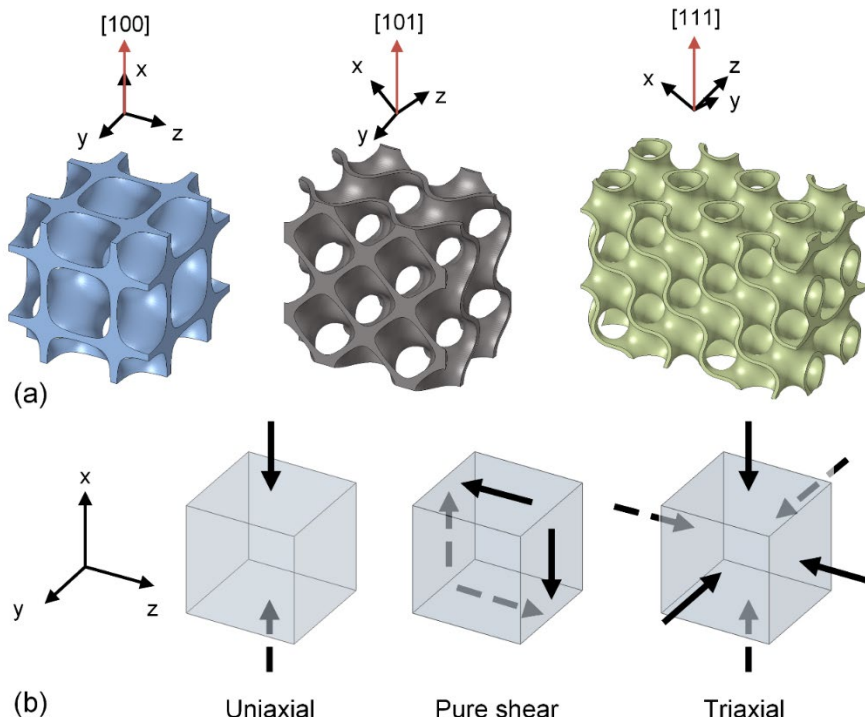


Figure 6.2 (a) Unit cell models under [100], [101] and [111] loading directions and (b) uniaxial, pure shear and triaxial displacement boundary conditions.

6.2.3. Estimation of inelastic deformation

The engineering stress-strain curves were extracted from the reaction force and displacement of dummy nodes in numerical results. The effective martensitic fraction is defined by the volumetric average of all nodes:

$$\bar{\xi} = \frac{1}{V} \int_V \xi_s dV. \quad (6.6)$$

Following the method used to estimate the elastic limit, where local strain evolves linearly with the imposed macroscopic strain, the effective start transformation stress at the forward transformation of NiTi metamaterials can be estimated from unit cell models. In this context, the effective transformation stress is numerically defined as the point when 10% of the elements begin martensitic transformation, with a martensite volume fraction of 1%. By generalizing the Gibson-Ashby model from ideal elastoplastic materials to ideal elasticity-

transformation materials, the effective transformation stress during the forward transformation can be described as:

$$\sigma^{\text{fwd}}(T) = k \left(\bar{\rho} \right)^p \sigma_s^{\text{fwd}}(T), \text{ with } \sigma_s^{\text{fwd}}(T) = \sigma_s^{\text{fwd}}(T_0) - C_s^{\text{fwd}}(T - T_0). \quad (6.7)$$

The effective transformation stress-temperature relation can be controlled by the relative density assuming a constant Clausius-Clayperon relation across base NiTi:

$$C^{\text{fwd}} = k \left(\bar{\rho} \right)^p C_s^{\text{fwd}}. \quad (6.8)$$

6.2.4. Multi-cell models

In the case of large deformation compression with plastic damage, the unit-cell models are expected to be invalid for capturing macroscopic deformation, as asymmetrical behavior is observed in the transformation-plasticity stages. For experimental validation, multi-cell models were developed to investigate the interaction between progressive transformations and plasticity. The multi-cell model was meshed using tetrahedron elements (C3D4), with approximately 2,400,000 elements for samples having relative densities of 0.15, 0.20, and 0.25. The structures were compressed using a stiff push rod, modeled by two rigid planes, with a defined contact between the surfaces and a tangential coefficient of 0.2. The bottom plate was fixed using a reference point, while the boundary condition of the top plate was modeled with a linear ramp displacement, reaching a maximum compressive displacement of 2.4 mm. The simulations were performed using an Abaqus/Explicit 2019 solver. Semi-automatic mass scaling was used with 2,500,000 steps to complete the simulations after the monitoring the kinetic energy.

6.3. Experimental methods

6.3.1. Additive manufacturing and heat treatments

The as-fabricated samples were manufactured using laser-powder bed fusion (Aconity 3D Midi) in a high-purity argon-filled chamber. The powder feedstock consisted of commercial Ni_{51.4}Ti_{48.6} powder, produced through gas atomization. Cylindrical bulk samples, measuring 13 mm in diameter and 20 mm in height, were manufactured using consistent process parameters. Optimized process parameters, including a laser power of 400 W, scanning speed of 1250 mm/s, hatch distance of 0.120 mm, layer thickness of 0.030 mm, and a stripe scanning strategy with a 67.5° rotation, were used to produce defect-free bulk samples and crack-free structures [32]. Diamond shell structures with the nominal relative density of

0.15, 0.20, and 0.25 were chosen for the experiments. A two-step heat treatment was conducted: a solution treatment at 1000°C for 60 minutes, followed by air cooling for 20 minutes, and an aging treatment at 450°C for 90 minutes, followed by air cooling to room temperature. All samples were sealed in vacuum quartz ampoules to prevent oxidation during the heat treatment. The experimental samples are labeled as follows: D20-AF for the as-fabricated Diamond shell structure with a nominal relative density of 0.2 and D15-HT, D20-HT, and D25-HT for the heat-treated samples with relative densities of 0.15, 0.2 and 0.25.

6.3.2. Characterization

After standard sanding and polishing of metallic samples, electron backscatter diffraction (EBSD) samples were prepared using electropolishing (Struers LectroPol5 with Struers A3 liquid) on the macroscopic (010) cross-section aligned with the building direction (BD). The schematic diagram of the EBSD samples is illustrated in the Appendix B. Texture analysis was conducted using a scanning electron microscopy (SEM) equipped with an (EBSD) detector (Helios G4) with a step size of 1.5 μm for coarse scanning and 0.2 μm for fine scanning. The Kikuchi pattern was stored in the fine scanning and reindexed using the NLPAR module of EDAX OIM Analysis 8. Grains with less than 5 data points and a confidence index less than 0.05 are removed from EBSD data. The phase analysis was conducted using X-ray diffraction (XRD) with a Bruker D8 Advance diffractometer (Cu $\text{K}\alpha$ radiation), with a step size of 0.043° and a counting time of 4 seconds per step. Three-dimensional atom probe tomography (3D APT) analysis was implemented on a LEAP 6000XR in ultraviolet laser-pulsed mode at a pulse power of 50 pJ and a pulse frequency of 200 kHz.

6.3.3. Thermal analysis and thermo-mechanical tests

Differential scanning calorimetry (DSC, TA Instruments DSC250) was employed at a heating/cooling rate of 10 °C/min over a temperature range of −70 to +150 °C. DSC samples with dimensions of 5.0×5.0×1.0 mm^3 were taken from the center of the Diamond shell structure.

Bulk samples measuring 4 × 4 × 6 mm^3 were produced using electrical discharge machining (EDM) from cylindrical samples. Quasi-static compression tests were conducted using a universal mechanical testing machine (Zwick Z100) equipped with a heating chamber. First, a large deformation compression test was performed with one cycle and a maximum displacement of 1 mm, at a temperature of 54 °C. Cyclic compression tests, comprising 15 cycles, were conducted at 54 °C until the superelastic response stabilized. Quasi-static

compression tests were subsequently conducted on the same sample after cyclic “training” at temperatures of 44, 54, 64, 74, and 84 °C. The displacement of the characterized sample was measured using a contact extensometer.

The cyclic compressive tests on superelastic metamaterials were conducted at a constant temperature of 54 °C. Displacement and engineering strain were measured using a contact extensometer. Large deformation compression contains 1 cycle, whereas the cyclic compression tests contain 15 cycles, corresponding to the number used in the characterization experiments. Displacement-controlled loading was applied, with a maximum displacement of 2.4 mm for large deformation compression and 1.5 mm for cyclic compression, at a strain rate of $5 \times 10^{-4} \text{ s}^{-1}$. The single-cycle compression was conducted on the trained samples at temperatures of 44, 54, 64, 74, and 84 °C.

The residual deformation of the as-compressed samples was measured using a thermal mechanical analyzer (PerkinElmer TMA400) at a heating and cooling rate of 10 °C/min. Samples were machined from the corresponding as-fabricated, heat-treated, and compressed Diamond metamaterials.

6.4. Results

6.4.1. Anisotropic superelasticity and scaling of transformation stress

In this section, the superelastic response under uniaxial, pure shear, and hydrostatic loading was compared in Figure 6.3. Under all loading conditions, the plateau-like stress monotonically increases with temperature (Figure 6.3 (a)-(c)). We found that transformation localization inevitably occurs in all loading conditions due to stress concentration. By comparing macro- and meso-level analyses, we observe that structural compliance is influenced by both the loading conditions and transformation localization. Strain localization under pure shear leads to higher compliance and a narrower hysteresis (Figure 6.3 (b) and (e)). Under hydrostatic loading, reduced transformation localization corresponds to higher stiffness and a broader hysteresis in the macroscopic response (Figure 6.3 (c) and (f)).

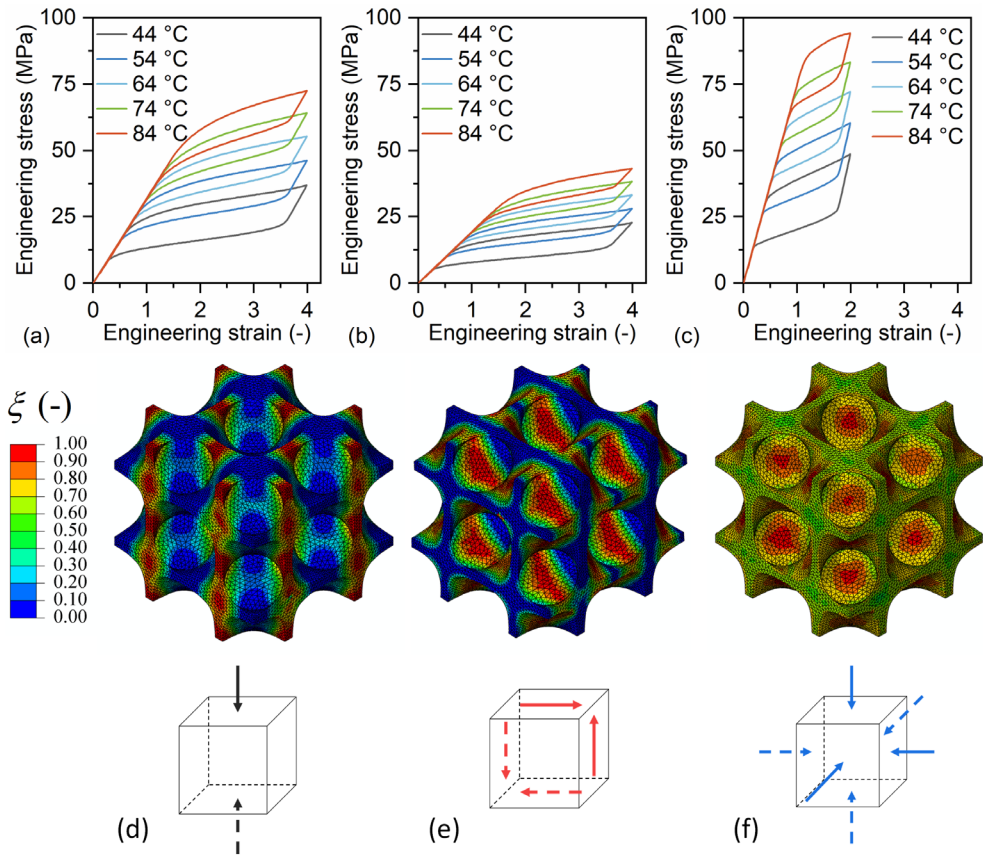


Figure 6.3 Theoretical engineering stress-strain curves and martensitic fraction ξ of the Diamond shell structure with a relative density of 0.2 under (a), (d) uniaxial loading, (b), (e) pure shear loading, and (c), (f) hydrostatic loading.

The anisotropic transformation stress of superelastic shell structures is shown in the form of an inverse pole figure (IPF) in Figure 6.4. The horizontal comparison in Figure 6.4 indicates that the anisotropy of superelastic shell structures remains unchanged with increasing temperature. Increasing the temperature from A_f to a higher value does not affect the structural stability if plasticity is not considered. The anisotropy of superelastic shell structures changes when the relative density increases from 0.15 to 0.5. At the lowest relative density of 0.15, the [100] unit cell exhibits higher transformation stress. However, as the relative density increases, this higher transformation stress shifts to the [011] unit cell. These observations are based on a phenomenological model of shape memory alloys. A more

detailed analysis, including model–experiment comparisons, is provided in the following section.

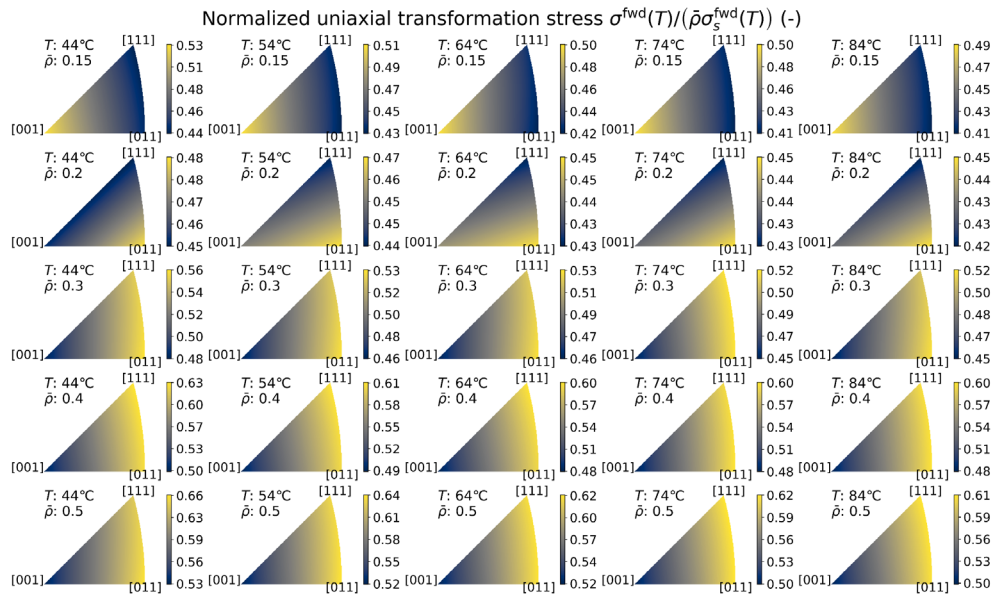


Figure 6.4 Anisotropic analysis of effective transformation stress (Temperature increases from left to right, and relative density increases from top to bottom).

6

6.4.2. Manufacturing strategy of superelastic metamaterials

The cyclic compression response of the as-fabricated sample was compared with that of the heat-treated sample D20-HT, as shown in Figure 6.5. In as-fabricated samples, the macroscopic critical stress decreases with lower energy input, resulting in a recoverable strain of only 3.0% after cyclic compression. Unlike previous references indicating that plasticity in ductile metallic metamaterials can be achieved through L-PBF [4-6], only partial superelasticity was observed in the as-fabricated samples. Despite the broad process window for achieving superelasticity in bulk samples, full superelastic structures could not be fabricated using the same process parameters. This partial superelasticity is associated with microstructural inhomogeneity at the mesoscale, tension-compression asymmetry, and residual-stress-induced martensite [15].

Heat treatment is a critical step for inducing superelasticity in Ni-rich NiTi structures following L-PBF [16]. After the heat treatment, a recoverable stress plateau, a second hardening stage, and a recoverable strain of 8% are observed. By comparing as-fabricated samples with the heat-treated samples in Figure 6.5 (a) and (b), it is evident that the heat-

6.4. Results

treated samples exhibit an effective transformation stress due to the recoverable plateau-like response following the initial elastic regime.

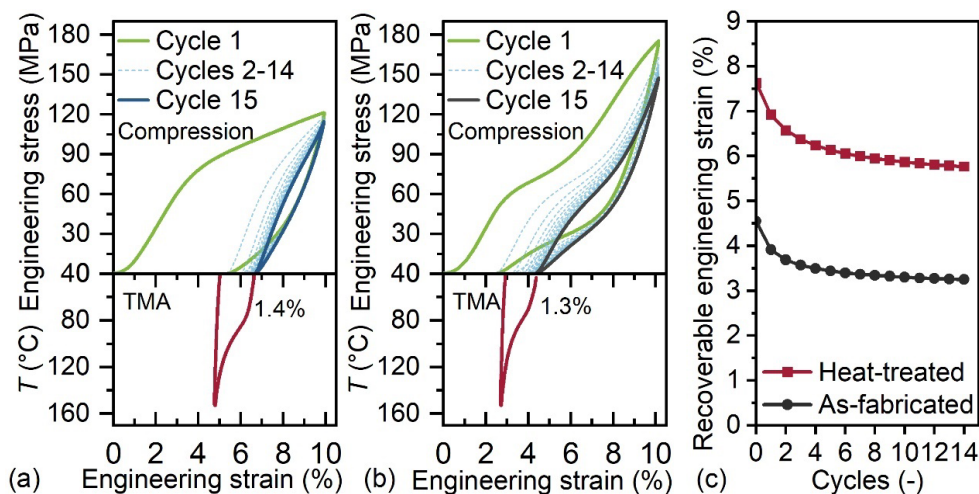


Figure 6.5 Comparison of engineering stress-strain curves from cyclic compression with temperature-strain curves from the TMA test for (a) D20-AF, (b) D20-HT, and (c) the cyclic stability of both samples.

6.4.3. Experimental characterization of superelastic metamaterial

The XRD patterns for as-fabricated and heat-treated samples are compared in Figure 6.6 (a). The main phase at room temperature in the D20-AF sample is the B2 cubic phase, with minor B19' which is induced by residual stress. In the heat-treated samples, overlapped peaks for the B2 phase and R phase are observed at about 42.5° at room temperature. At the same time, R phase peaks of (212) direction can be observed at about 52°.

As shown in Figure 6.6 (b), the as-fabricated Diamond sample exhibits a single B19'-B2 transformation during heating and a reverse B19'-B2 transformation during cooling. Due to the compositional inhomogeneity, transformation temperature peaks in thermal-induced transformation are broadened, with a weak transformation peak. As shown in Figure 6.6 (b), the heat-treated D20 sample experiences a multistage transformation from B2-R1, R1-R2 and R2-B19' during cooling. During heating, single peaks from B19'-B2 are observed. For heat-treated D15 and D25 samples, thermally induced transformation B2-R-B19' was observed during cooling, and overlapping transformation peaks from B19'-R, and R-B2 were observed during heating.

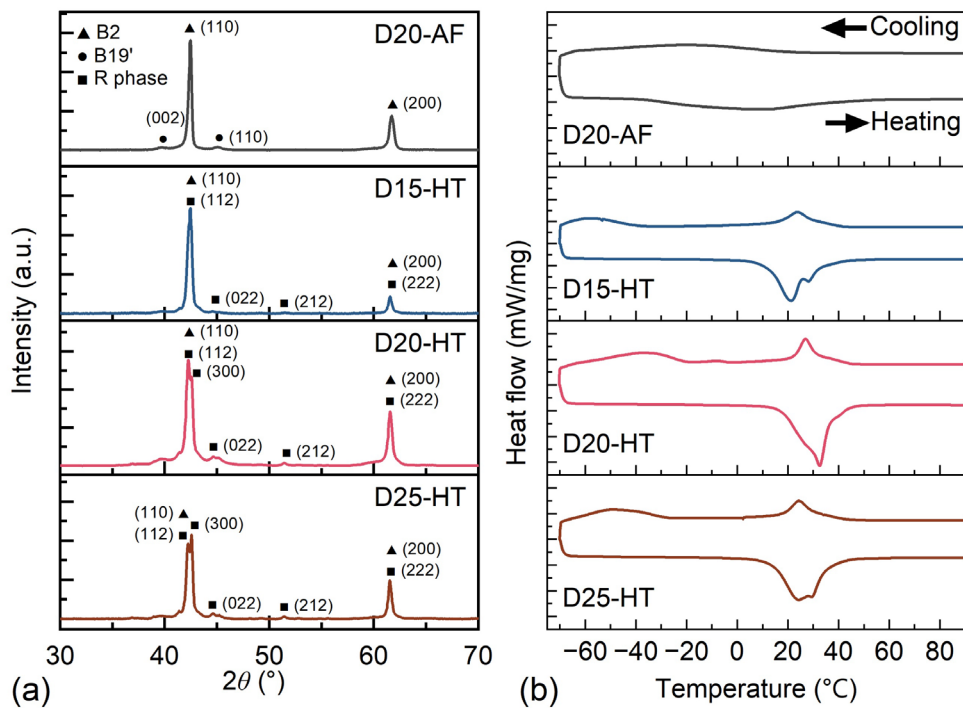


Figure 6.6 (a) XRD pattern at room temperature and (b) DSC curves of D20-AF, D15-HT, D20-HT, and D25-HT samples.

6

Figure 6.7 (a) and (b) present the macroscopic engineering stress-strain curves under large deformation compression, comparing numerical and experimental results. Overall, good agreement is observed between the numerical predictions and experimental data. For strains between 6% and 12%, the relative difference between the experimental results and numerical predictions is less than 10%. The experimental curves show higher stiffness and plateau stress compared to the numerical predictions. Additionally, unlike the linear elastic stage observed in the numerical model for austenite, the superelastic samples exhibit an increase in stiffness during the elastic stage. This discrepancy is attributed to dimensional imperfections and an inhomogeneous texture in the as-fabricated samples. This reasonable validation of the simulation highlights the necessity of applying a heat treatment to the as-fabricated samples when using a phenomenological base model in numerical simulations.

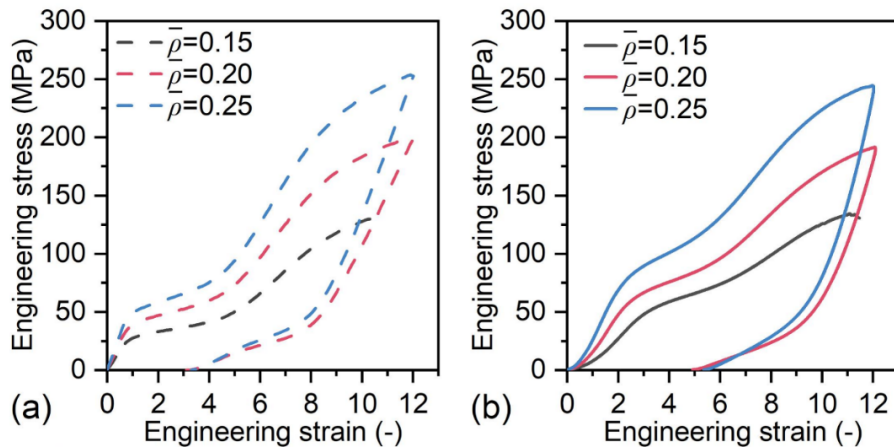


Figure 6.7 Engineering stress-strain response of D20-HT: (a) numerical results and (b) experimental validation.

To experimentally determine the superelastic domain under uniaxial compression, macro-, and mesoscopic analyses were compared to understand the superelastic limit of the experimental samples. The macroscopic response of the superelastic metamaterials, arising from the elastic-transformation-elastic-plastic behavior of the constituent NiTi, can be generalized into seven distinct deformation stages (Figure 6.8 (c)). After the elastic limit of austenite, a plateau-like response was observed due to forward martensitic transformation. This was followed by a second hardening stage, attributed to the elastic deformation of martensite, and eventually post-yielding plasticity. Upon unloading, the structure exhibited an elastic recovery, followed by plateau-like recovery due to the reverse martensitic transformation. The martensite volume fraction and equivalent plastic strain for the corresponding deformation stages of the Diamond structure with a relative density of 0.2 are shown in Figure 6.7, Figure 6.8 (a), and (b). During loading in the forward transformation stage, martensitic transformation is initiated due to strain localization and progressively interconnects into continuous regions. At this stage, plastic deformation was not observed. As martensitic transformation built up along the compressive direction, a plateau-like response was obtained. Following this, a second hardening stage occurred (Stage 3), driven by the elastic deformation of martensite and offset by the reduced stiffness of the transformation regions. The initial yield stress and plastic response in the post-yielding plastic stage were defined using the tangential line of the second hardening stage. The macroscopic deformation was primarily due to plastic deformation in damaged areas.

The elastic stiffness resulted from the combined elasticity of the martensite and untransformed austenite regions. The deformation was recovered due to the reverse martensitic transformation. The structural stability is attributed to the interconnection of transformation localization into a continuous transformation region under uniaxial compression along the macroscopic [100] direction (Figure 6.8 (a)). Post-yield plasticity is attributed to shear bands along the macroscopic [110] direction. Thus, the superelastic limit is defined based on the localized yielding, as the accumulation of plastic deformation will cause the final collapse of the structure.

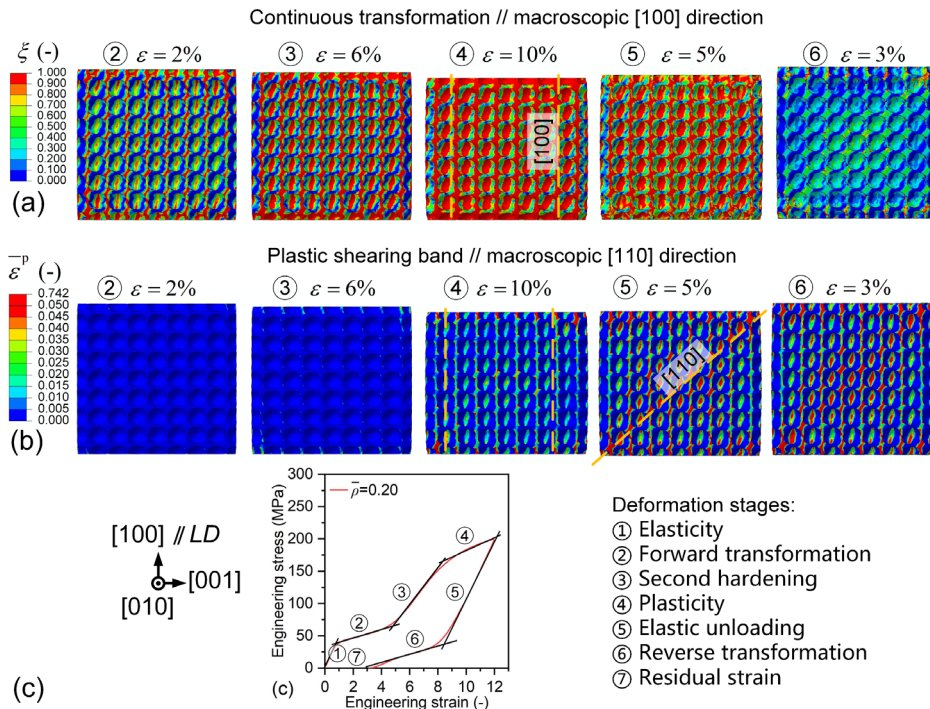


Figure 6.8 Contour map of (a) martensite volume fraction and (b) equivalent plastic strain in multi-cell models of D20-HT, and (c) deformation stages in superelastic metamaterials.

6.5. Discussion

6.5.1. Cyclic stability

It is observed in Figure 6.8 that residual strain partly results from the localized yielding induced shear band. Further investigation through EBSD-TMA-EBSD experiments is needed to discuss the cyclic stability within the superelastic limit. The transformation localization of a unit cell is shown in Figure 6.9 (a), highlighting two zoomed-in regions that illustrate both a low martensitic fraction and a high martensitic fraction. The inverse pole figure with a color map corresponding to the building direction (IPF-BD) of the region with the low martensitic fraction, is shown in Figure 6.9 (b). After 15 cycles of cyclic compression, the main phase in this area is B2 austenite with a random texture. No obvious martensitic transformation occurred in this region during uniaxial compression along the macroscopic [100] direction. Thus, residual B19' martensite is not observed in this region before (Figure 6.9(b)) and after thermal mechanical analysis (TMA), as shown in Figure 6.9(c) and Figure 6.5(b). The IPF-BD of the transformation region corresponding to the high martensitic fraction in the numerical model is shown in Figure 6.9 (d). Numerous non-indexed areas are observed in this region after cyclic compression. To better understand the phase distribution in the non-indexed areas, the phases present in a selected area after fine scanning and reindexing is shown in Figure 6.9 (f)-(j). Residual martensite with an area fraction of 13.6% was recorded, and the corresponding IPF-BD of the B2 phase and B19' phase are shown in Figure 6.9 (g) and (h). A residual B19' phase with [100] texture parallel to the building direction (BD) was observed in the D20-HT sample after cyclic compression.

The temperature-engineering strain curves of the as-compressed D20-HT samples are shown in Figure 6.5. The residual strain of the D20-HT sample recovered by 1.3% as the temperature increased to 150°C. After the TMA test, an EBSD was performed on the same area, as shown in Figure 6.9 (f)-(j). The non-indexed areas in regions with high martensitic fraction decreased after the TMA test. In the zoomed-in figure, it was found that the residual martensite had recovered after the TMA test, and the main phase is B2 austenite (Figure 6.9 (i) and (j)).

In summary, the first source of residual deformation is the local yielding induced plastic shear banding (Figure 6.8 (b)). The second source of residual deformation is the residual martensite in the continuous transformation region that is induced by transformation degradation (Figure 6.9 (b)). This part of residual deformation can be recovered by increasing the temperature to 150 °C.

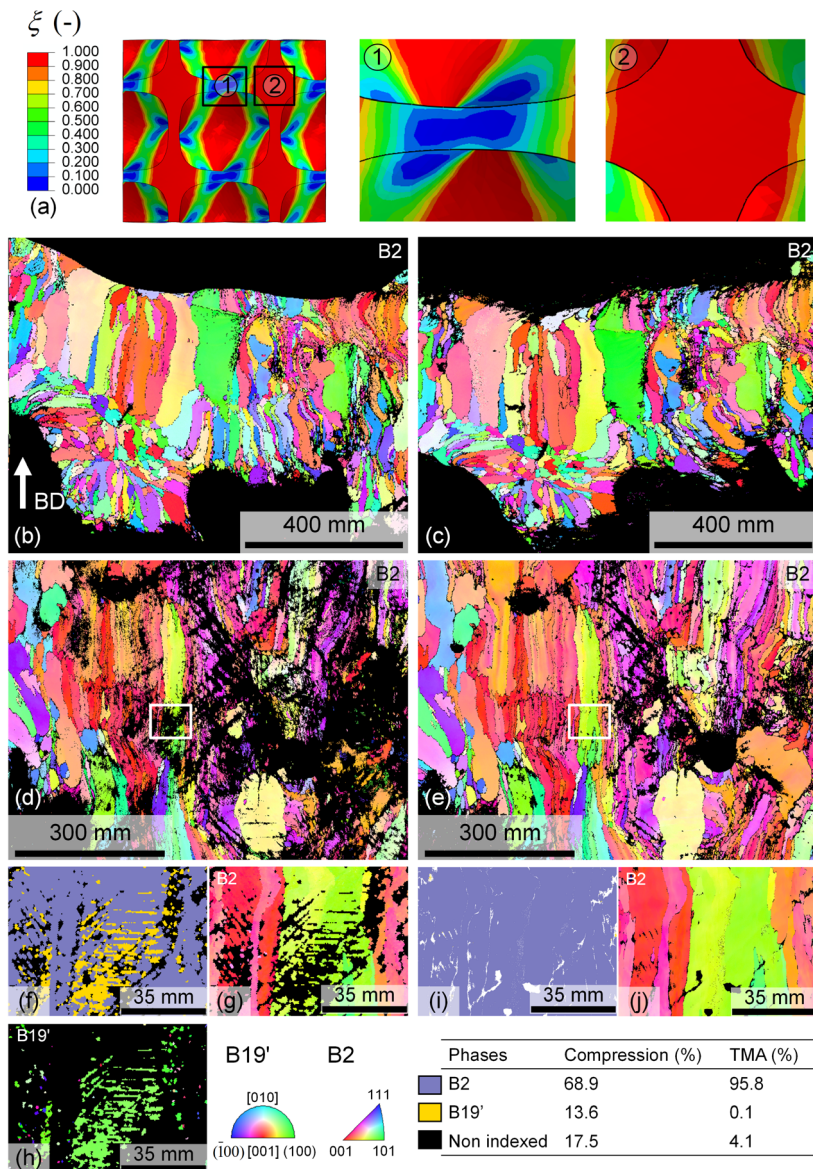


Figure 6.9 Sources of residual deformation: (a) IPF-BD of the selected area corresponding to low martensite fraction, (b) transformation localization during uniaxial compression, (c) IPF-BD of the selected area corresponding to a high martensite fraction, (d) phases, (e)IPF-BD of austenite and (f) IPF-BD of martensite in the zoomed-in area; (g) IPF-BD of selected area after TMA, (h) phases and (i) IPF-BD of austenite in the selected zoomed-in area.

After obtaining validation on large deformation responses, the superelastic domain was determined experimentally. The elastoplastic behavior of metamaterials was extended for NiTi metamaterials by incorporating a phenomenological model of shape memory alloys. The D15-HT, D20-HT, and D25-HT samples were “trained” through 15 cycles at 54°C, as shown in Figure 6.10 (a)-(c). Due to the accumulation of residual martensite, the superelastic curves show hardening and functional degradation after cyclic compression. As illustrated in Figure 6.10 (e), the cyclic stability of superelastic metamaterials is independent of the relative density of the structure. Consequently, the microstructure characterization on D20-HT sample can be generalized into other densities.

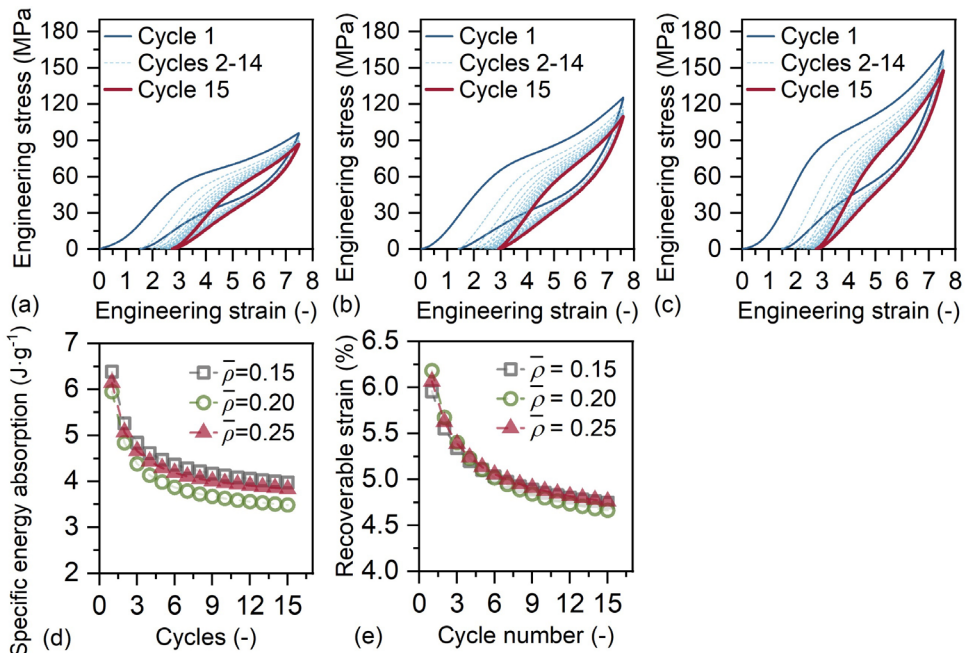


Figure 6.10 Cyclic stability of Diamond samples: (a–c) cyclic compression in the superelastic range for D15-HT, D20-HT, and D25-HT, respectively; (d) specific energy absorption; and (e) recoverable strain.

The obtained cyclic stability can be attributed to solution homogenization and the precipitation of Ni_4Ti_3 (Figure 6.11) found in this study, which reduce the Ni content in the NiTi matrix and lower the critical stress needed for transformation. As a result, the assumption of homogenization in the phenomenological model becomes valid after solution treatment. The larger recoverable strain after unloading indicates that Ni_4Ti_3 precipitates play a key role by enhancing dislocation slip resistance in both the austenite and stress-induced

martensite phases, thus preventing plastic deformation even at higher stress levels. This reinforced slip resistance ultimately leads to superior superelasticity in the heat-treated NiTi.

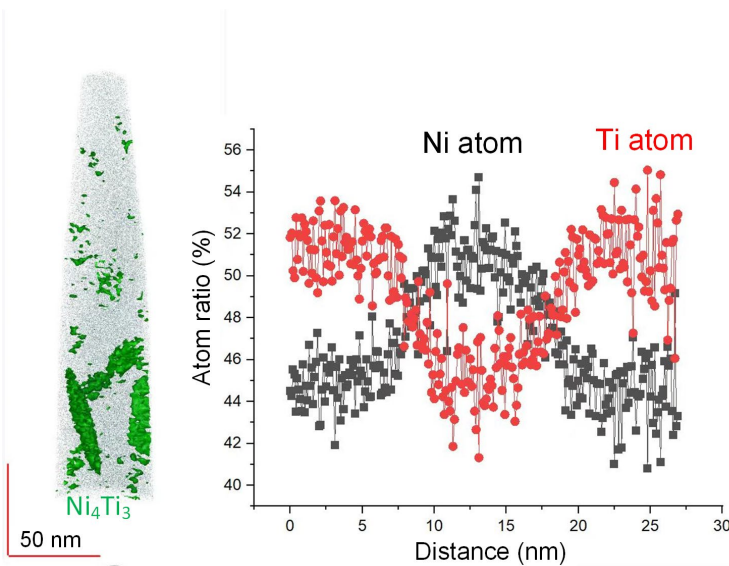


Figure 6.11 Atom probe tomography characterization of Ni_4Ti_3 precipitates in D20-HT sample.

6

Due to the dissipative nature of the reversible martensitic transformation, the closed integration of the engineering stress-strain curve was used to calculate the specific energy absorption (SEA) φ of NiTi metamaterials with recoverable deformation:

$$\varphi = \frac{\Delta W}{\rho}, \text{ with } \Delta W = \oint \sigma^- d\epsilon^- . \quad (6.9)$$

For large deformation compression, the dissipated energy is cumulatively composed of transformation dissipation and plastic dissipation. A maximum engineering strain of 7.5% is chosen to evaluate the SEA in Figure 6.10. Under cyclic compression, the plastic dissipation induced by plastic banding can be omitted, so energy absorption with recoverable deformation can be finally achieved in superelastic metamaterials. Superelastic metamaterials maintain a high level of energy dissipation across 15 cycles. A SEA of 3.5 J/g can be obtained after cyclic compression deformation. Unlike metamaterials primarily designed for energy absorption through plastic deformation, superelastic metamaterials offer the advantage of reusability. They can endure cyclic deformation while maintaining effective energy dissipation.

6.5.2. Effective transformation stress-temperature relationship

Figure 6.12 (a)-(c) demonstrates the engineering stress-strain curves of the “trained” Diamond metamaterials at 44-84°C. The transformation stress-temperature relationships from experiments and numerical models are compared in Figure 6.12 (d). The results show that the effective transformation stress can be controlled by adjusting the relative density of the unit cell. Additionally, isolating the temperature term from the critical stress reveals that the slope of the transformation stress-temperature relationship is also tunable by relative density, as shown in Figure 6.12 (f).

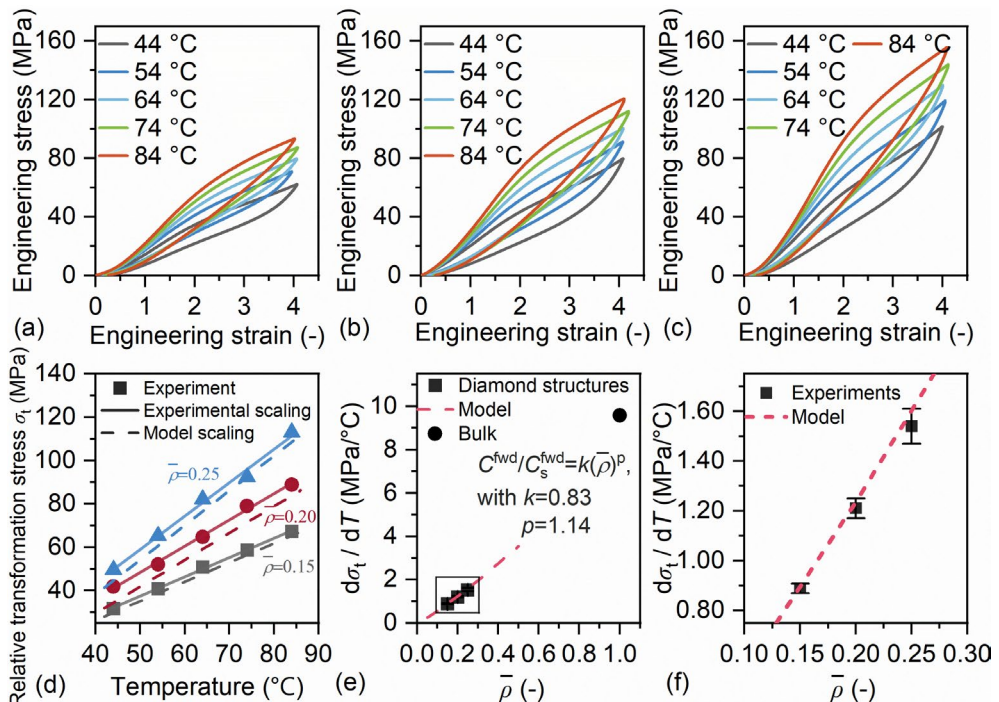


Figure 6.12 Effective transformation stress-temperature relationship in Ni-rich NiTi Diamond shell structures: (a)-(c) Temperature dependence of superelasticity in D15-HT, D20-HT, and D25-HT; (d) Transformation stress-temperature relationship; (e)-(f) Corresponding slopes of the transformation stress-temperature curves.

The influence of relative density and temperature was validated in Figure 6.12 (d) and (f). Overall, good agreement was observed between the numerical and experimental results for the effective transformation stress-temperature relationship. The differences between the

experimentally measured and numerically predicted transformation stress are within 15%, with the experimental values being slightly higher. These differences can be attributed to the influence of dimensional imperfections and transformation hardening after cyclic compression. Figure 6.12 (f) compares the transformation stress-strain curves from experiments and numerical predictions, showing that the predicted values lie within the error bars of the experimental results. A low transformation stress-temperature coefficient of 0.9 MPa/°C can be achieved through structure design and relative density, compared to 9.5 MPa/°C for bulk samples (Figure 6.12 (e)).

We found that achieving superelastic metamaterials requires a synergistic interaction between the unit-cell structure and the microstructure. The programmability of the effective transformation stress-temperature relation depends on the relative density of the unit-cell structure. Furthermore, complete superelasticity demands careful control of both the homogenized microstructure and the precipitation of Ni_4Ti_3 .

6.6. Conclusions

In this chapter, superelastic NiTi metamaterials were successfully modeled and manufactured, demonstrating consistency between the models and experiments. Additionally, it was demonstrated that the transformation stress-temperature relationship can be effectively controlled by adjusting the relative density of the material. The following conclusions can be drawn:

- In theoretical superelastic response, numerical models were developed to predict the transformation stress-temperature relation and anisotropy of superelastic metamaterials with a Diamond shell topology.
- The heat treatment is a critical step to ensure reasonable agreement between numerical models and experiments. The differences between the experimentally measured and numerically predicted transformation stress are within 15%, with the experimental values being slightly higher. The effective transformation stress can be controlled by the relative density of the unit cell. The effective transformation stress-temperature coefficient can also be controlled by unit cell design, reducing the value from 9.5 MPa/°C for bulk materials to 0.9 MPa/°C by tuning relative density.
- The mesoscopic deformation mechanism of the Diamond shell is the interaction of martensitic transformation and plasticity. The recoverable plateau-like response in the macroscopic stress-strain curves originated from the interconnection of transformation localization into a continuous transformation region under uniaxial compression along the

macroscopic [100] direction. Post-yielding plasticity in the macroscopic stress-strain curves is related to plastic shear bands formed along the [110] direction. EBSD reveals that the residual deformation comes from residual martensite in the transformable region, which can be recovered by further increasing the temperature.

- Specific energy absorption of 3.5 J/g can be obtained after cyclic compression deformation. Unlike metamaterials designed with plastic dissipation for energy absorption, superelastic metamaterials offer the advantages of reusability and sustainability, as they can withstand cyclic deformation while maintaining effective energy dissipation.

This chapter demonstrates that both microstructural design and structural design must be considered simultaneously to achieve consistency between theoretical and experimental superelastic structures and metamaterials.

Appendix A Thermomechanical properties for numerical models

Thermomechanical properties of base NiTi after heat treatments are shown in Table 6.A1-A3. Stress-free transformation temperatures are measured using the tangential line from the DSC data (Figure 6.1 (a)). The properties of constituent NiTi are measured through uniaxial compression until the true strain of 13.5%, with a one-dimensional reduction of the Auricchio model [27,28]. Data from Cycle 1 was used for the calibration of large deformation compression as shown in Figure 6.1 (b). For small deformation calibration, the bulk samples were first trained at a maximum true strain of 5.5% over 15 cycles as shown in Figure 6.1 (c). The calibration was based on data recorded during Cycle 15, at which point the superelastic response stabilized and property degradation became negligible. The transformation stress-temperature relation is calibrated at five different temperatures and 9.5 MPa/°C is estimated in bulk samples after heat treatment (Figure 6.1 (d)). All the thermomechanical properties used in the current chapter are listed in Table 6.A1-A3. By comparing the numerical and experimental results, we observe good agreement. The experimentally measured and numerically predicted stress-strain curves closely overlap in the large deformation range. The predicted maximum stress is within 5% of the experimental results, indicating that the chosen constitutive model provides a reasonable approximation of the stress-strain behavior of additively manufactured NiTi after heat treatment. For strains between 1% and 4%, the temperature-dependent behavior of the heat-treated bulk samples is validated, with stress differences within 8%.

6

Table 6.A1 Thermo-mechanical properties of the constituent NiTi used in the multi-cell model.

E_A (MPa)	E_M (MPa)	n_A	ν_M	ε^{tr} (-)	T_0 (°C)
45400	41566	0.33	0.33	0.038	54
Start transformation stress for forward transformation (MPa)	Start transformation stress for reverse transformation (MPa)			$C_s^{fwd} = \frac{d\sigma_s^{fwd}}{dT}$ (MPa K ⁻¹)	
324	603				9.5
Finish transformation stress for forward transformation (MPa)	Finish transformation stress for reverse transformation (MPa)			$C_s^{rev} = \frac{d\sigma_s^{res}}{dT}$ (MPa K ⁻¹)	
212	10				9.5

Table 6.A2 Plastic properties of the constituent NiTi used in multi-cell model.

True stress (MPa)	True strain (-)
1642	0.081
1759	0.087
1827	0.093
1867	0.099
1893	0.105
1908	0.111
1916	0.117
1918	0.123
1917	0.129

Table 6.A3 Thermomechanical properties of the constituent NiTi used for the unit-cell model.

E_A (MPa)	E_M (MPa)	n_A	ν_M	ε^{tr} (-)	T_0 (°C)
35659	43655	0.33	0.33	0.038	54
Start transformation stress for forward transformation (MPa)	Start transformation stress for reverse transformation (MPa)			$C_s^{fwd} = \frac{d\sigma_s^{fwd}}{dT}$ (MPa K ⁻¹)	
315	480				9.5
Finish transformation stress for forward transformation (MPa)	Finish transformation stress for reverse transformation (MPa)			$C_s^{rev} = \frac{d\sigma_s^{rev}}{dT}$ (MPa K ⁻¹)	
290	190				9.5

Appendix B Supplementary details on parameter optimization and characterization

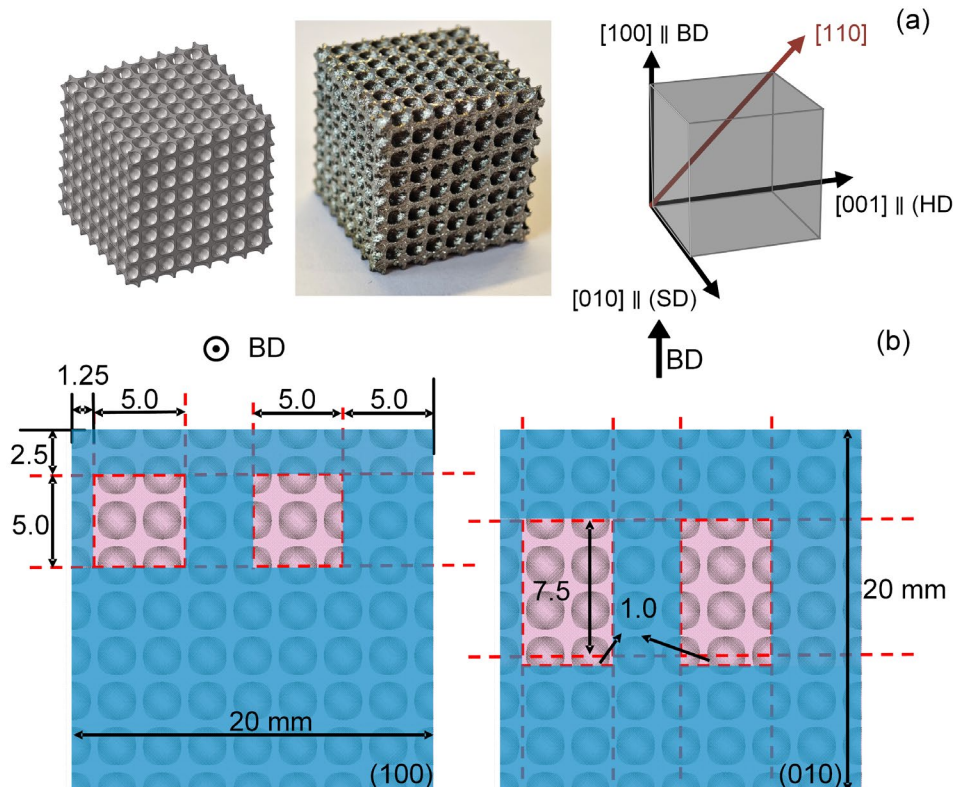


Figure 6.B1 Location of samples for TMA-EBSD and DSC characterization.

Parameter optimization is an essential first step in achieving superelastic samples. Initially, process parameters were selected based on a process map that identified suitable conditions for fabricating bulk samples without cracks or delamination [32]. However, when these parameters were applied to structural samples, cracking issues emerged at sharp edges and nodes. Many of the parameters initially suitable for bulk samples were no longer stable when applied to structural geometries, significantly narrowing the effective process window. The narrowed process window for superelastic structures were determined to manufacture sample without macroscopic cracking and delamination. Process parameters, including a laser power of 400 W, scanning speed of 1250 mm/s, hatch distance of 0.120 mm, layer thickness of 0.030 mm, and a stripe scanning strategy with a rotation angle of 67.5°, successfully produced defect-free bulk samples and crack-free TPMS structures. Additional

comparative parameter sets were also tested: the medium power (MP) set included a laser power of 300 W, scanning speed of 1250 mm/s, and hatch distance of 0.100 mm, while the low power (LP) set consisted of a laser power of 200 W, scanning speed of 900 mm/s, and hatch distance of 0.100 mm. Cyclic compression tests performed on Diamond shell structures fabricated with these representative parameter sets are presented in Figure 6.B2. By reducing the heat input from 88.9 J/mm³ (Figure 6.B2 (a)) to 80 J/mm³ (MP set in Figure 6.B2 (b)) and 74 J/mm³ (LP set in Figure 6.B2 (c)), a lower transformation stress was observed in the initial loading cycle. Nevertheless, only partial superelasticity could be achieved in the as-fabricated samples.

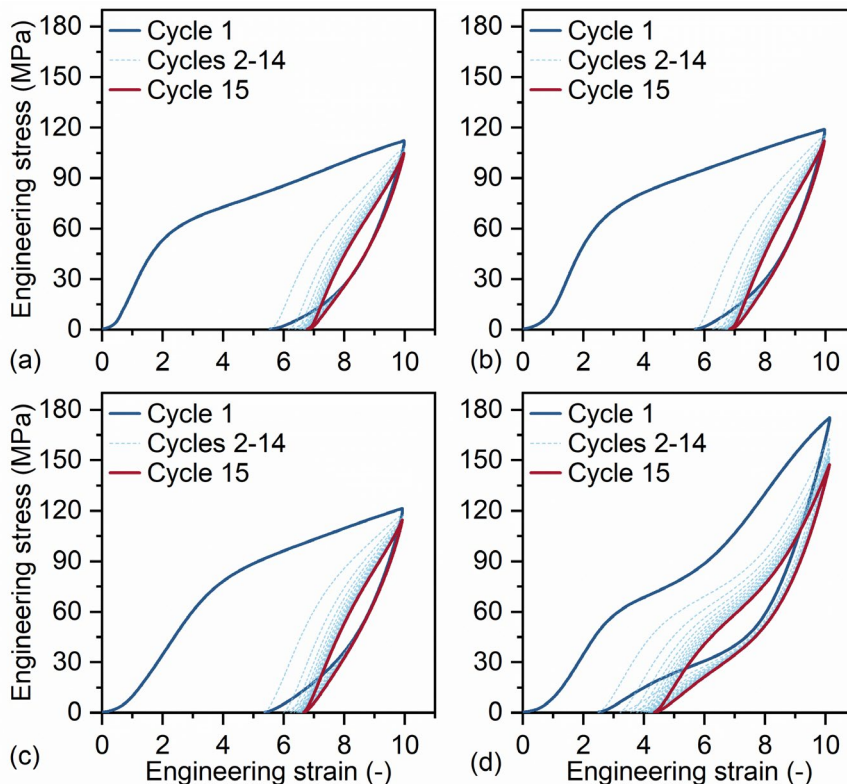


Figure 6.B2 Comparison of engineering stress-strain curves of as-fabricated and heat treated samples: (a) D20-LP, (b) D20-MP, (c) D20-HP, and (d) D20-HT.

Appendix C Table of notation

Structural parameters	
\emptyset	Level-set function of triply periodic minimum surfaces
$\bar{\rho}$	Relative density of mechanical metamaterial
ρ	Density of mechanical metamaterial
c	Level-set value of triply periodic minimum surfaces
L	Size (edge length) of a unit cell
Γ	Rotation matrix
V	Volume of superelastic metamaterials
NiTi constitutive model	
$\Delta\epsilon$	Increment of total strain
$\Delta\epsilon^{\text{el}}$	Elastic strain increment
$\Delta\epsilon^{\text{tr}}$	Increment of equivalent transformation strain
$\Delta\epsilon^{\text{pl}}$	Equivalent plastic strain
C_s^{fwd}	Slope for transformation stress-temperature relation of NiTi
ξ_s	Martensitic volume fraction of NiTi
σ_s^{fwd}	Transformation stress during forward transformation of NiTi
T	Ambient temperature
Properties of superelastic metamaterials	
$\bar{\xi}$	Effective martensitic fraction
σ^{fwd}	Martensitic volume fraction of superelastic metamaterials
k, p	Coefficient for Gibson-Ashby model
C^{fwd}	Transformation stress during forward transformation of superelastic metamaterial
φ	Specific energy absorption
ΔW	Dissipated energy
$\bar{\sigma}$	Effective stress
$\bar{\epsilon}$	Effective strain

References

[1] V.S. Deshpande, N.A. Fleck, M.F. Ashby, Effective properties of the octet-truss lattice material, *J. Mech. Phys. Solids* 49 (2001) 1747–1769. [https://doi.org/10.1016/S0022-5096\(01\)00010-2](https://doi.org/10.1016/S0022-5096(01)00010-2).

[2] L.J. Gibson, M.F. Ashby, Mechanics of Three-Dimensional Cellular Materials., *Proc. R. Soc. London, Ser. A Math. Phys. Sci.* 382 (1982) 43–59. <https://doi.org/10.1098/rspa.1982.0088>.

[3] M.F. Ashby, The properties of foams and lattices, *Philos. Trans. R. Soc. A Math. Phys. Eng. Sci.* 364 (2006) 15–30. <https://doi.org/10.1098/rsta.2005.1678>.

[4] T. Tancogne-Dejean, A.B. Spierings, D. Mohr, Additively-manufactured metallic micro-lattice materials for high specific energy absorption under static and dynamic loading, *Acta Mater.* 116 (2016) 14–28. <https://doi.org/10.1016/j.actamat.2016.05.054>.

[5] C. Bonatti, D. Mohr, Smooth-shell metamaterials of cubic symmetry: Anisotropic elasticity, yield strength and specific energy absorption, *Acta Mater.* 164 (2019) 301–321. <https://doi.org/10.1016/j.actamat.2018.10.034>.

[6] J.B. Berger, H.N.G. Wadley, R.M. McMeeking, Mechanical metamaterials at the theoretical limit of isotropic elastic stiffness, *Nature* 543 (2017) 533–537. <https://doi.org/10.1038/nature21075>.

[7] D. Lagoudas, D. Hartl, Y. Chemisky, L. MacHado, P. Popov, Constitutive model for the numerical analysis of phase transformation in polycrystalline shape memory alloys, *Int. J. Plast.* 32–33 (2012) 155–183. <https://doi.org/10.1016/j.ijplas.2011.10.009>.

[8] W. Zaki, Z. Moumni, A three-dimensional model of the thermomechanical behavior of shape memory alloys, *J. Mech. Phys. Solids* 55 (2007) 2455–2490. <https://doi.org/10.1016/j.jmps.2007.03.012>.

[9] C. Cisse, W. Zaki, T. Ben Zineb, A review of constitutive models and modeling techniques for shape memory alloys, *Int. J. Plast.* 76 (2016) 244–284. <https://doi.org/10.1016/j.ijplas.2015.08.006>.

[10] M. Simoes, C. Braithwaite, A. Makaya, E. Martínez-Pañeda, Modelling fatigue crack growth in shape memory alloys, *Fatigue Fract. Eng. Mater. Struct.* 45 (2022) 1243–1257. <https://doi.org/10.1111/ffe.13638>.

[11] Z. Yan, J. Zhu, E. Borisov, T. Riemslag, S. Paul, M. Hermans, J. Jovanova, V. Popovich, Superelastic response and damping behavior of additively manufactured Nitinol

architected materials, *Addit. Manuf.* 68 (2023) 103505. <https://doi.org/10.1016/j.addma.2023.103505>.

[12] P.A. Michailidis, N. Triantafyllidis, J.A. Shaw, D.S. Grummon, Superelasticity and stability of a shape memory alloy hexagonal honeycomb under in-plane compression, *Int. J. Solids Struct.* 46 (2009) 2724–2738. <https://doi.org/10.1016/j.ijsolstr.2009.03.013>.

[13] A. Cebrian Carcavilla, W. Zaki, Effective Superelastic Domains of Schwarz Primitive Shape Memory Alloy Lattices Subjected to Cyclic Loading, *Adv. Eng. Mater.* 25 (2023) 1–18. <https://doi.org/10.1002/adem.202300432>.

[14] J.A. Shaw, D.S. Grummon, J. Foltz, Superelastic NiTi honeycombs: fabrication and experiments, *Smart Mater. Struct.* 16 (2007) S170–S178. <https://doi.org/10.1088/0964-1726/16/1/S17>.

[15] Z. Yan, J.N. Zhu, D. Hartl, T. Riemslag, S.P. Scott, R. Petrov, M. Hermans, J. Jovanova, V. Popovich, Correlation between microstructural inhomogeneity and architectural design in additively manufactured NiTi shape memory alloys, *Virtual Phys. Prototyp.* 19 (2024) 1–20. <https://doi.org/10.1080/17452759.2024.2396065>.

[16] Z. Yan, J.-N. Zhu, Y.-C. Yang, H. Brouwer, T. Riemslag, J.R. Jinschek, M. Hermans, J. Jovanova, V. Popovich, Origin of premature fracture and enhancement of superelasticity in laser additively manufactured Ni-rich NiTi metamaterials, *Scr. Mater.* 259 (2025) 116558.

[17] G. Carlucci, L. Patriarca, A.G. Demir, J.N. Lemke, A. Coda, B. Previtali, R. Casati, Building Orientation and Heat Treatments Effect on the Pseudoelastic Properties of NiTi Produced by LPBF, *Shape Mem. Superelasticity* 8 (2022) 235–247. <https://doi.org/10.1007/s40830-022-00391-0>.

[18] H. Jiang, X. Wang, R. Xi, G. Li, H. Wei, J. Liu, B. Zhang, S. Kustov, K. Vanmeensel, J. Van Humbeeck, G. Zhao, Size effect on the microstructure, phase transformation behavior, and mechanical properties of NiTi shape memory alloys fabricated by laser powder bed fusion, *J. Mater. Sci. Technol.* 157 (2023) 200–212. <https://doi.org/10.1016/j.jmst.2023.02.026>.

[19] P. Delroisse, P.J. Jacques, E. Maire, O. Rigo, A. Simar, Effect of strut orientation on the microstructure heterogeneities in AlSi10Mg lattices processed by selective laser melting, *Scr. Mater.* 141 (2017) 32–35. <https://doi.org/10.1016/j.scriptamat.2017.07.020>.

[20] A. Fardan, U. Klement, H. Brodin, E. Hryha, Effect of Part Thickness and Build Angle on the Microstructure, Surface Roughness, and Mechanical Properties of Additively Manufactured IN-939, *Metall. Mater. Trans. A Phys. Metall. Mater. Sci.* 54 (2023) 1792–1807. <https://doi.org/10.1007/s11661-022-06940-7>.

[21] M. Elahinia, N. Shayesteh Moghaddam, M. Taheri Andani, A. Amerinatanzi, B.A. Bimber, R.F. Hamilton, Fabrication of NiTi through additive manufacturing: A review, *Prog. Mater. Sci.* 83 (2016) 630–663. <https://doi.org/10.1016/j.pmatsci.2016.08.001>.

[22] N.M. della Ventura, C.Q. Dong, S.A. Messina, R.R. Collino, G.H. Balbus, S.P. Donegan, J.D. Miller, D.S. Gianola, M.R. Begley, Heterogeneity in millimeter-scale Ti-6Al-4V lattice primitives: Challenges in defining effective properties for metamaterial design, *Mater. Des.* 238 (2024). <https://doi.org/10.1016/j.matdes.2024.112695>.

[23] H.Z. Lu, H.W. Ma, W.S. Cai, X. Luo, Z. Wang, C.H. Song, S. Yin, C. Yang, Stable tensile recovery strain induced by a Ni₄Ti₃ nanoprecipitate in a Ni50.4Ti49.6 shape memory alloy fabricated via selective laser melting, *Acta Mater.* 219 (2021). <https://doi.org/10.1016/j.actamat.2021.117261>.

[24] Y. Cao, X. Zhou, D. Cong, H. Zheng, Y. Cao, Z. Nie, Z. Chen, S. Li, N. Xu, Z. Gao, W. Cai, Y. Wang, Large tunable elastocaloric effect in additively manufactured Ni–Ti shape memory alloys, *Acta Mater.* 194 (2020) 178–189. <https://doi.org/10.1016/j.actamat.2020.04.007>.

[25] H. Vashishtha, P. Jamshidi, A. Vrettou, A. Karez, M. Goode, H. Deyhle, A. James, S. Ahmad, C. Reinhard, M.M. Attallah, D.M. Collins, Microscale stress-geometry interactions in an additively manufactured NiTi cardiovascular stent: A synchrotron dual imaging tomography and diffraction study, *Mater. Charact.* 213 (2024) 114016. <https://doi.org/10.1016/j.matchar.2024.114016>.

[26] V. Finazzi, F. Berti, L. Petrini, B. Previtali, A.G. Demir, Additive manufacturing and post-processing of superelastic NiTi micro struts as building blocks for cardiovascular stents, *Addit. Manuf.* 70 (2023). <https://doi.org/10.1016/j.addma.2023.103561>.

[27] Z. Yan, J.-N. Zhu, Y.-C. Yang, H. Brouwer, T. Riemslag, J.R. Jinschek, M. Hermans, J. Jovanova, V. Popovich, Origin of premature fracture and enhancement of superelasticity in laser additively manufactured Ni-rich NiTi metamaterials, *Scr. Mater.* 259 (2025) 116558.

[27] F. Auricchio, R.L. Taylor, Shape-memory alloys: modelling and numerical simulations of the finite-strain superelastic behavior, *Comput. Methods Appl. Mech. Eng.* 143 (1997) 175–194. [https://doi.org/10.1016/S0045-7825\(96\)01147-4](https://doi.org/10.1016/S0045-7825(96)01147-4).

[28] F. Auricchio, R.L. Taylor, J. Lubliner, Shape-memory alloys: macromodelling and numerical simulations of the superelastic behavior, *Comput. Methods Appl. Mech. Eng.* 146 (1997) 281–312. [https://doi.org/10.1016/S0045-7825\(96\)01232-7](https://doi.org/10.1016/S0045-7825(96)01232-7).

[29] J. Xia, Y. Noguchi, X. Xu, T. Odaira, Y. Kimura, M. Nagasako, T. Omori, R. Kainuma, Iron-based superelastic alloys with near-constant critical stress temperature dependence, *Science* (80-.). 369 (2020) 855–858. <https://doi.org/10.1126/science.abc1590>.

[30] N. Qiu, Y. Wan, Y. Shen, J. Fang, Experimental and numerical studies on mechanical properties of TPMS structures, *Int. J. Mech. Sci.* 261 (2024) 108657. <https://doi.org/10.1016/j.ijmecsci.2023.108657>.

[31] A. Jones, M. Leary, S. Bateman, M. Easton, TPMS Designer: A tool for generating and analyzing triply periodic minimal surfaces, *Softw. Impacts* 10 (2021) 100167. <https://doi.org/10.1016/j.simpa.2021.100167>.

[32] J.N. Zhu, E. Borisov, X. Liang, E. Farber, M.J.M. Hermans, V.A. Popovich, Predictive analytical modelling and experimental validation of processing maps in additive manufacturing of nitinol alloys, *Addit. Manuf.* 38 (2021) 101802. <https://doi.org/10.1016/j.addma.2020.101802>.

7

General discussion, conclusions, and recommendations

7

7.1. General discussion

The aim of this doctoral project was to design and additively manufacture superelastic metamaterials capable of recovering large deformation and energy absorption. Superelasticity occurs under applied stress when the material is in the temperature range of stable austenite. Superelasticity allows NiTi to undergo significant deformation during loading (up to 10% strain) with full shape recovery upon unloading.

Laser powder bed fusion (L-PBF) can be used to manufacture structures and metamaterials with complex geometry. The laser beam scans a certain trajectory over a thin layer of powder, consolidating the powder by melting and subsequent solidification. This procedure is repeated until the final part is produced in a layer-by-layer fashion. L-PBF parameters for example, laser power and scanning speed dictate the dimensions of the melt pool and, combined with the geometry of the structures, affect the resulting microstructure. It should be emphasized that the microstructure and thus the localized properties obtained in the as-fabricated structures are strongly dependent on the design of the unit cell structure. To obtain macroscopic superelasticity, martensitic transformation in NiTi is required and the successful additive manufacturing of the structures is needed.

The accurate numerical prediction in the design of metamaterials appeared to be a challenge. A mismatch between models and experiments was found in uniaxial compression behavior. Therefore, the primary objective of this research was to bridge this gap by developing a model-manufacturing-properties methodology.

To improve the model-experiment consistency, research questions particularly related to the (effective) martensitic transformation of NiTi were addressed. Although only one independent variable, i.e. the unit cell architecture or relative density, was varied, it strongly affected multiple dependent metallurgical aspects and finally also the macroscopic response, including macroscopic homogenized response and microstructure. These dependent variables are interrelated, making it challenging to establish clear qualitative or quantitative relationships between these variables and the relative densities. Therefore, these relationships were investigated across three length scales. The effective properties at the macroscale, the base material properties and structural deformation mechanisms at the mesoscale, and the metallurgical microstructures, including precipitation behavior at the microscale are considered in this work.

Building on the concept of designing materials based on mesoscale structures, Chapter 3 investigated the mechanically homogenized properties of superelastic metamaterials. An analytical and a parametric finite element study using a phenomenological superelasticity model was conducted to predict the mesoscopic deformation and theoretical effective properties of the octet and BCC truss-based metamaterials. After comparing theoretical

predictions with the actual behavior of superelastic metamaterials, the research discusses two multiscale problems. The first problem is the microstructural inhomogeneity, resulting from the L-PBF process, which is discussed in Chapter 4. A second problem arises from the tension-compression asymmetry, which is detailed in Chapter 5.

In Chapter 3, two main conclusions were drawn at the macroscale level. First, the effective mechanical properties of superelastic metamaterials can be derived by generalizing the elastoplastic behavior by incorporating the phenomenological model of shape memory alloys. In subsequent research and discussion in the thesis, this extension of the model was applied. By comparing typical octet and BCC unit cell architectures, it was found that octet structures with stretching-dominated deformation exhibit a broader stress hysteresis due to the larger transformable volume of NiTi. In contrast, BCC structures with bending-dominated deformation enhance the compliance of NiTi, but are more sensitive to transformation localization. A second conclusion, based on the model-experiment comparisons of as-fabricated samples, was that only partial superelasticity with narrow hysteresis was achieved in these samples due to low deformation recoverability (2.8%) and premature fracture. Unlike the straightforward modeling and experimental validation of elastoplastic metamaterials in previous studies, the modeled superelastic response in NiTi metamaterials could only be validated for small deformations after cyclic compression testing on metamaterials. Process-induced microstructural variation was found to significantly influence the macroscopic response of Ni-rich NiTi metamaterials. This mismatch highlighted that achieving superelastic metamaterials requires precise control over microstructures across multiple length scales. This second conclusion led to the next phase of the study, investigating microstructural inhomogeneity as one of the key reasons for the narrow hysteresis and low deformation.

Chapter 4, focusing on microstructural inhomogeneity and partial superelasticity, describes that the mesoscopic melt pool behavior is significantly influenced by geometrical parameters at the macroscale. Two reasons are specifically identified, i.e. the laser turn region and the edge effect. At the region where the laser trajectory changes direction, localized heat accumulation takes place, while the edges of the structures cause variations in heat dissipation. Both effects contribute to changes in texture and localized thermomechanical properties. This indicates that the relative density of metamaterial is not merely a geometrical parameter controlling the effective properties of mechanically homogenized superelastic metamaterials, but also is an external parameter influencing the microstructure and localized thermomechanical properties of NiTi. It was shown that although identical process parameters were used in the L-PBF process, variations in relative density introduced additional dependent variables, for instance, grain size and elemental composition distribution. These local variations present challenges in defining the actual effective

properties of superelastic metamaterials, as the general assumptions of homogeneous material properties are not satisfied. Consequently, the derived structure–property relationships have to be changed into the interdependent relation of structure–metallic microstructure–effective properties. While it was found that inhomogeneous transformation temperatures account for the pseudo-linear response with narrow hysteresis, the mechanism underlying premature fracture remained unclear. This particular aspect is addressed in Chapter 5.

Focusing on premature fracture in Chapter 5, the study showed that this issue was attributed to the low tensile deformation capacity of the NiTi, which could not sufficiently accommodate the high stresses in the regions that experience tensile stress. As large deformation can not be achieved through martensitic transformation or dislocation slip systems, were only partial superelasticity and low deformation recoverability observed in the as-fabricated samples. The tension-compression asymmetry led to a change in the structural stability of bending- and stretching-dominated structures, reversing the classical Gibson-Ashby theory as shown in Figure 5.4.

To address the multiscale challenges identified in Chapters 4 and 5, a heat treatment was proposed, introducing Ni_4Ti_3 precipitates that enhance superelastic behavior by increasing slip resistance in both austenite and martensite phases. The heat treatment consisted of a first step to homogenize the microstructure and release residual stresses. This satisfies the necessary assumptions of homogenization in the phenomenological modeling of NiTi. The second step involved an aging heat treatment, which mitigates tension-compression asymmetry and thereby improves the superelasticity of the NiTi. By applying the heat treatment, the effects of dependent variables induced by geometrical aspects during the printing process were significantly reduced. This approach simplifies the structure–metallic microstructure–effective properties relationship caused by the printing process to the structural–effective properties relationship modeled in Chapter 3. Qualitative consistency between the model and experimental results was thus successfully achieved in the macroscopic response curves.

In Chapter 6, the relationship between structure and effective properties is quantitatively described as the controllable transformation stress-temperature behavior of superelastic metamaterials. Numerical and experimental results show the effective transformation stress-temperature slope was successfully reduced from 9.5 MPa/°C in bulk NiTi samples to as low as 0.9 MPa/°C in Diamond shell structures with a theoretical relative density of 0.15. The macroscopic superelastic response showed a recoverable plateau-like behavior, a second hardening stage, and post-yielding plasticity. The observed plateau-like response across superelastic metamaterials with varying relative densities suggests that the problem of

controlling the microstructure was successfully addressed. Designed properties through mesoscopic structures can be achieved in experiments.

At the macroscale, the plateau-like response is linked to transformation localization and continuous transformation at the mesoscale along the macroscopic (100) direction. Post-yielding plasticity at the macroscale corresponds to plastic shear banding along the macroscopic (110) direction under compressive loading. These findings conclude our study that the family of mechanical metamaterials can be extended to superelastic metamaterials with effective martensitic transformation. Macroscopic mechanical properties can be tuned through mechanism-based mesoscopic deformation, provided that microstructure and nanoscale precipitates are carefully controlled using heat treatments. This study highlights the necessity of addressing multiscale challenges in the additive manufacturing of Ni-rich NiTi structures and metamaterials.

The results presented in this research establish a robust foundation for the development and application of NiTi structures and metamaterials across a wide range of engineering fields. By addressing multiscale challenges such as microstructural inhomogeneity and tension-compression asymmetry, this study shows that computation-based design and additive manufacturing can create functional NiTi structures and metamaterials with highly tunable thermomechanical properties and responses. These advancements enable the design of NiTi-based structures optimized for recoverable large deformation and energy dissipation, directly addressing the demands of applications in medical devices (such as stents and orthodontic tools), aerospace components (like actuators and adaptive structures), and robotics (including soft robotics). Furthermore, the proposed model-manufacturing-testing methodology lays the framework for future innovations in NiTi metamaterials, offering a pathway to customizable solutions for complex mechanical and functional requirements in extreme and adaptive environments. This work not only contributes to the theoretical understanding of NiTi superelastic behavior but also accelerates its practical adoption in cutting-edge technologies.

7.2. General conclusions

The following conclusions can be drawn from the studies at different scales:

- At the macroscale, the effective properties of superelastic metamaterials can be derived by generalizing the elastoplastic behavior into incorporating a phenomenological model of shape memory alloys with reversible martensitic transformation.

- Microstructural inhomogeneity and tension-compression asymmetry were identified as the two multiscale challenges for achieving superelastic NiTi metamaterials. These challenges arise from variable interdependencies across length scales.
- Microstructural inhomogeneity is attributed to changing boundary conditions during L-PBF at the mesoscale, which is influenced by geometrical parameters such as relative density at the macroscale. This multiscale dependency can inversely result in low martensitic transformation at the mesoscale and partial superelasticity at the macroscale.
- Tension-compression asymmetry is a critical factor in the premature fracture and stability of NiTi superelastic structures. Large deformation in the tensile region of the structures cannot be achieved through martensitic transformation or dislocation slip systems.
- A post-printing heat treatment, including solution homogenization and aging, is crucial for addressing these two problems by homogenizing the microstructure and introducing Ni_4Ti_3 precipitates.
- The effective transformation stress-temperature relationship and effective martensitic transformation can be controlled by adjusting the relative density of the unit cell. The differences between the experimentally measured and numerically predicted transformation stress are within 15%, with the experimental values being slightly higher. This study successfully achieves a transformation stress-temperature slope of 0.9 MPa/ $^{\circ}\text{C}$ in superelastic Ni-rich NiTi metamaterials.
- The proposed model-manufacturing-testing strategy can be applied to customize the design and production of NiTi-based structures and metamaterials. This work lays a foundation for advanced engineering applications, such as energy absorption systems, medical stents, and adaptive structures for different industries, including aerospace, mechanical and maritime.

7.3. Recommendations

In this thesis, both the modeling and experimental investigation of superelastic NiTi metamaterials were explored. While multiscale research questions related to (effective) martensitic transformation were addressed, the following aspects are recommended for future studies:

As initially discussed in Figure 2.5, the application of NiTi and other SMAs relies on simple geometry such as wire, foil, tube and spring. Through the findings obtained in this research, the scope of potential applications has significantly broadened. Specifically, Functionally Graded Metamaterials (FGMs), which combine multiple unit cells with varied superelastic characteristics, can be designed and additively manufactured to provide tailored mechanical responses in specific locations within a structure. By employing FGMs composed of carefully selected and spatially arranged unit cells, it becomes feasible to create location-specific mechanical properties and optimize structural performance beyond simple damping applications as shown in Figure 7.1. For instance, integrating multiple types of superelastic unit cells in a gradient manner allows for precise control of stress distribution and deformation mechanisms within complex structural systems. A conceptual schematic demonstrating the superposition of diverse unit cells into a graded metamaterial architecture is presented to illustrate these possibilities in automobiles, military vehicles, marine vessels, and diverse infrastructure systems.

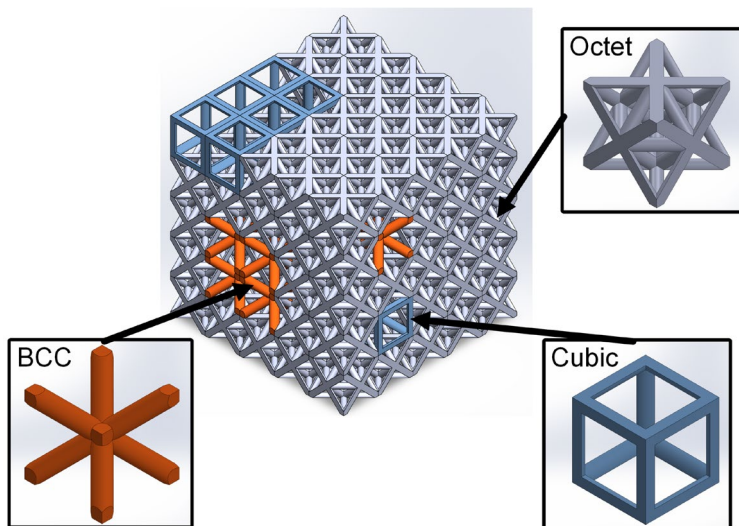


Figure 7.1 Schematic diagram illustrating the application of superelastic metamaterials with functionally graded properties for energy absorption.

Process parameter optimization is a critical initial step toward manufacture metamaterials samples. Initially, process parameters were chosen according to a process map that identified suitable conditions for producing bulk samples without cracking or delamination. However, upon applying these parameters to metamaterial samples, issues with cracking appeared at the sharp edges and nodes. Many parameters that were initially effective

for bulk samples became unsuitable when applied to structural geometries, thereby greatly restricting the usable processing window as shown in Figure 6.B2. Despite optimizing various processing parameters, the as-fabricated samples only exhibited partial superelasticity. This underscores the necessity for further exploration into developing processing windows specific for metamaterials and investigating post-processing heat treatments.

The heterogeneous microstructure, resulting from the L-PBF process, is a significant challenge in developing NiTi structures and metamaterials for engineering applications. Although solution annealing can homogenize the microstructure to some extent at the mesoscale, it cannot control the crystallographic texture. Texture control is linked to the remelting and solidification processes in laser powder bed fusion and cannot be achieved through heat treatment alone. Therefore, further research is required to in-situ control texture during additive manufacturing of complex geometries in NiTi structures. This is important when melt pool behavior is affected by both process parameters (heat input) and external geometry (heat dissipation). A new parameter optimization scheme that considers geometrical effects in texture control should be developed.

Tensile superelasticity is significant in most structural applications but remains a challenge in the L-PBF of superelastic NiTi. To date, reliable manufacturing strategies to consistently produce tensile superelasticity have yet to be achieved, and the fracture mechanisms under tensile loading remain unclear. Tensile superelasticity is critical for engineering applications involving NiTi structures and metamaterials. Failure mechanisms in tensile superelasticity (especially for millimeter-scale samples) could be investigated using in-situ EBSD and TKD analysis. To achieve tensile superelasticity applicable in different industrial sectors, we need to develop a robust manufacturing protocol.

In the computational design of NiTi structures, the multiscale problem requires further investigation. Phenomenological constitutive models, based on generalized plasticity theory, can predict thermo-mechanical behavior using macroscopic experimental data; however, they do not account for microstructure sensitivity. Crystallographic plasticity models can consider micromechanics of NiTi alloys, but they are computationally intensive and inefficient for structural design applications. Along with heterogeneous microstructure in as-fabricated samples, a more efficient and accurate model-manufacturing strategy is needed for scale bridging in L-PBF-produced NiTi structures.

Porosity and geometrical inaccuracies are another challenge in the L-PBF of NiTi structures and metamaterials. The optimized parameters for bulk samples are not necessarily optimized parameters for structures and metamaterials. Current solutions incorporate porosity and geometric inaccuracies into models to improve prediction accuracy. However,

the mechanisms underlying porosity formation in L-PBF of metamaterials remain unclear and require further study. Hot isostatic pressing (HIP) is an effective post-processing method to significantly reduce internal porosity and improve the structural integrity of NiTi components produced via additive manufacturing. However, the impact of HIP on the microstructure evolution, phase transformation behavior, and ultimately the superelastic response of NiTi structures still requires systematic investigation. Additionally, surface roughness induced by additive manufacturing leads to stress concentration, accelerating fatigue crack initiation and reducing the fatigue life of NiTi structures. Applying suitable post-processing methods such as sand blasting or electrochemical polishing can significantly enhance surface finish and thus improve fatigue resistance.

Curriculum Vitae

Zhaorui Yan

Born on 08 November 1993 in Guangdong, China

Education

Apr. 2021 – Present PhD Researcher in Mechanical Engineering

 Delft University of Technology, Delft, the Netherlands

Sep. 2016 – Jun. 2019 MSc in Mechanical Manufacture and Automation

 Dalian University of Technology, Dalian, China

Sep. 2012 – Jun. 2016 BSc in Process Equipment and Control Engineering

 Dalian University of Technology, Dalian, China

List of publications

Journal papers as first author

1. **Z. Yan**, J.N. Zhu, H. Brouwer, T. Riemslag, M. Hermans, J. Jovanova, V. Popovich, Tunable transformation stress-temperature relation in additively manufactured superelastic metamaterials (To be submitted).
2. **Z. Yan**, J.N. Zhu, Y.C Yang, H. Brouwer, T. Riemslag, J. R. Jinschek, M. Hermans, J. Jovanova, V. Popovich, Origin of Premature Fracture and Enhancement of Superelasticity in Laser Additively Manufactured Ni-rich NiTi Metamaterials, *Scripta Materialia.* 259 (2025) 116558.
3. **Z. Yan**, J.N. Zhu, D. Hartl, T. Riemslag, S.P. Scott, R. Petrov, M. Hermans, J. Jovanova, V. Popovich, Correlation between microstructural inhomogeneity and architectural design in additively manufactured NiTi shape memory alloys, *Virtual Physical Prototyping.* 19 (2024).
4. **Z. Yan**, J.N. Zhu, E. Borisov, T. Riemslag, S. Paul, M. Hermans, J. Jovanova, V. Popovich, Superelastic response and damping behavior of additively manufactured Nitinol architectured materials, *Additive Manufacturing.* 68 (2023) 103505.

Journal papers as co-author

1. J.N. Zhu, Z. Li, E. Rahimi, **Z. Yan**, Z. Ding, A. Mol, V. Popovich, Enhancing corrosion resistance through crystallographic texture control in additively manufactured superelastic NiTi alloy, *Corros. Sci.* 251 (2025) 112929.
2. J.N. Zhu, **Z. Yan**, Y.C. Yang, Z. Ding, M. J. M. Hermans, J. R. Jinschek, V. Popovich, Functionally graded nickel–titanium shape memory alloys produced by in-situ additive manufacturing, *Scripta Materialia.* 255 (2025) 116351.
3. W. Liu, G. Hu, **Z. Yan**, B. Liu, T. Wang, Z. Lyu, Thermal effect on microstructure and mechanical properties in directed energy deposition of AISI 316L, *The International Journal of Advanced Manufacturing Technology.* 134(7) (2024) 3337-3353.
4. J.N. Zhu, W. Zhu, E. Borisov, X. Yao, T. Riemslag, C. Goulas, A. Popovich, **Z. Yan**, F. D. Tichelaar, D. P. Mainali, Effect of heat treatment on microstructure and functional properties of additively manufactured NiTi shape memory alloys, *Journal of Alloys and Compounds.* 967 (2023) 171740.

5 Z.J. Tang, W. Liu, L.N. Zhu, Z.C. Liu, **Z.R. Yan**, D. Lin, Z. Zhang, H.C. Zhang, Investigation on coaxial visual characteristics of molten pool in laser-based directed energy deposition of AISI 316L steel, *Journal of Materials Processing Technology*. 290 (2021) 116996.

Conferences

1. **Z. Yan**, J. Jovanova, M.J.M. Hermans and V.A. Popovich. Unraveling Tension-Compression Asymmetry in Additively Manufactured NiTi TPMS Structures. ECCOMAS Congress 2024 – Oral presentation.
2. **Z. Yan**, J. Jovanova, M.J.M. Hermans and V.A. Popovich. Evolution of microstructure in additively manufactured NiTi architected materials. AAMS 2023 - Oral presentation.
3. **Z. Yan**, J. Jovanova, M.J.M. Hermans and V.A. Popovich. Energy dissipation and damping of additively manufactured Nitinol lattice structures under compressive loading. EMMC18 – Oral presentation.

Acknowledgements

Completing this dissertation has been a journey filled with challenges, personal growth, and generous support from many individuals, to whom I wish to express my deepest gratitude.

First and foremost, I would like to sincerely thank my promoter, Dr. Vera Popovich, whose guidance, encouragement, and trust have been invaluable throughout my research. Her confidence in my abilities and the freedom she provided allowed me to pursue my ideas and explorations with assurance. I am equally grateful to my promoter, Dr. Marcel Hermans, whose encouragement and sense of humor have provided motivation and enjoyment during my PhD journey. His insightful advice, critical thinking and inspiring discussions have continually propelled my work forward. Special thanks also go to Dr. Jovana Jovanova, whose brainstorming sessions and open discussions inspired my innovative and conceptual designs. All three supervisors have profoundly shaped my academic development and have served as role models in my professional career.

I extend my appreciation to the members of my thesis committee, Prof. Matthijs Langelaar, Prof. Leo Kestens, Prof. Maurizio Vedani, Prof. Ian Gibson, and Dr. Pouliumi Dey, for their valuable insights and constructive feedback, which greatly enhanced the quality of this thesis.

I wish to thank Ton Riemslag, Elise Reinton, Sean Scott, and Raymond Dekker for their assistance with mechanical testing and the design of experimental setups. Their essential contributions were critical to the success of my research. I am grateful to Jia-Ning Zhu for the insightful discussions on NiTi alloys and for the fruitful outcomes of our close collaboration in tackling numerous technical challenges. I would like to thank Hans Brouwer for his pivotal contribution in designing and conducting the heat treatment experiments, which played a vital role in this research. I am particularly grateful to Richard Huizenga for his extensive help with XRD measurements and data analysis. I also extend my thanks to Kees Kwakernaak for his assistance with numerous SEM-EBSD experiments. I also wish to thank Darren Hartl, Xiaohui Liang, and Jiaxiang Yi for their valuable suggestions and support in developing the computational framework for shape memory alloys. Additionally, my gratitude goes to Durga Mainali for his expertise in DSC measurements and for his troubleshooting support during microstructural characterization. I would like to thank Remko Seijffers for his generous help and technical support throughout the course of my research. Finally, I would like to thank Prof. Roumen Petrov for his valuable guidance on EBSD analysis and crystallography.

I am immensely grateful to my colleagues and friends for their companionship and support throughout this PhD journey. My sincere thanks extend to my current and former colleagues: Virgínia, Quanxin, José, Tim, Arjun, Gautham, Fei, Yan, Zixiong, Aswin, Chrysoula, and Iftikhar.

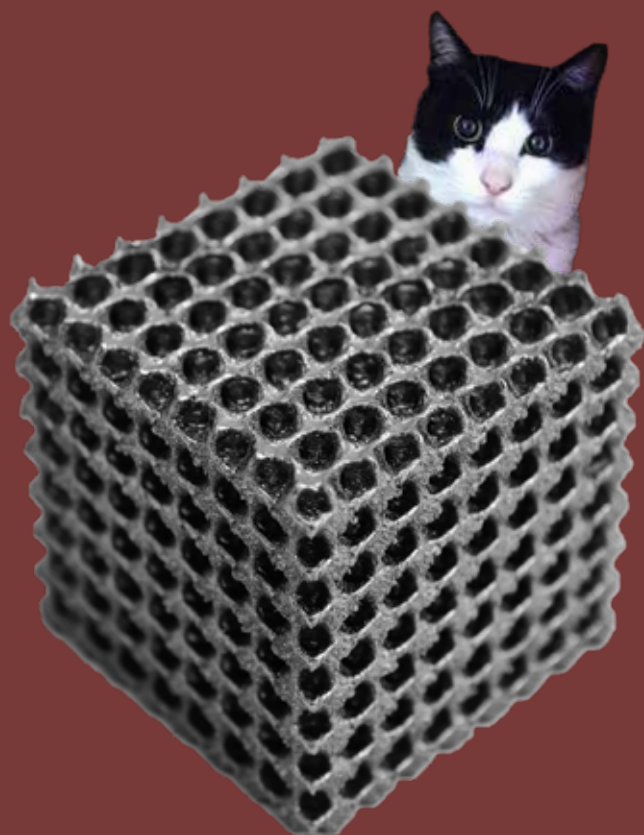
I would also like to express my appreciation to my friends in Delft for their warm companionship and continuous support during my time here, especially Xiaohui, Dingshan, Ziyu, Zhaoying, Keer, Jiaxiang, Yuliu, Kai Liu, Yaqi, Ji Cheng, Hao Ma, Sifeng and Yang Yang, for all the wonderful moments we have shared. My office-mates, Jia-Ning, Gaojie, and Dongil, deserve special mention for our daily conversations and shared laughter. Additionally, I warmly thank my badminton friends for making leisure time enjoyable. Special thanks to Xiaohui, Jia-Ning, and Dingshan for the exciting moments we shared while playing MOBA games.

I gratefully acknowledge the financial support provided by the China Scholarship Council, which made this research possible. My heartfelt thanks go to all individuals who generously contributed their knowledge, skills, and experiences to this research project. Finally, I sincerely thank Dr. Che Zhu, Dr. Weiwei Liu, and Prof. Hong-Chao Zhang, who initially inspired me and guided my path into the world of scientific research.

Above all, my deepest gratitude goes to my family, especially my parents and grandmother, for their unwavering belief in me. Their constant support, encouragement, and care throughout my PhD journey have been a source of strength and motivation. I am also deeply thankful for the love and guidance they have given me throughout my life, which have shaped who I am today.

“空谈误国，实干兴邦”
——邓小平

“Empty talk harms the nation; practical action helps it thrive.”
—Deng Xiaoping



 **TU**Delft